Tackling Coupled Problems in Porous Media: Development of Numerical Models and an Open Source Simulator

Vom Stuttgart Research Centre for Simulation Technology
und der Fakultät Bau- und Umweltingenieurwissenschaften
der Universität Stuttgart genehmigte Habilitationsschrift

vorgelegt von

Dr. rer. nat. Bernd Flemisch
aus
Augsburg

Hauptberichter:	Prof. Dr.-Ing. Rainer Helmig
1. Mitberichter:	Prof. Dr. rer. nat. Thomas Ertl
2. Mitberichter:	Prof. Dr. rer. nat. Christian Rohde
3. Mitberichter:	Prof. Mary F. Wheeler, Ph.D.

Tag der mündlichen Prüfung: 18. Juli 2013

Institut für Wasser- und Umweltsystemmodellierung
Lehrstuhl für Hydromechanik und Hydrosystemmodellierung
2013

Acknowledgments

This habilitation thesis is based on work that was carried out between the years 2007 and 2013, mainly at the Department of Hydromechanics and Modelling of Hydrosystems (LH2), University of Stuttgart. Coming from the field of applied mathematics, I am happy that I could adapt my interpretation of "applied" during these 6.5 years and play a part in the amazing research work in porous media flow and transport modeling undertaken in our group and in collaboration with other research groups.

Numerous people contributed to the realization of this thesis in many different ways. First of all, I would like to mention Rainer Helmig, our group head and head of the reviewing board for this thesis. I thank him deeply for his support in all matters of my work. In particular, for his encouragement to write this thesis and for providing me with the necessary freedom to actually get it done. And in general for being the main driver behind the wonderful and unique working environment at the LH2 that I could become a part of. I also would like to thank the other reviewers for their careful reading of this thesis, the writing of the reports and the interesting discussion in the colloquium: Mary Wheeler from UT Austin as well as Thomas Ertl and Christian Rohde from the University of Stuttgart.

To a large extent, this thesis assembles results that have been previously achieved and published with several co-authors. I want to express my sincere gratitude to all of them for the inspiration they gave me, the discussions we had and the pleasant and fruitful collaboration: from the LH2, these are Katherina Baber, Holger Class, Melanie Darcis, Anozie Ebigbo, Karin Erbertseder, Jochen Fritz, Rainer Helmig, Andreas Lauser, Klaus Mosthaf, Jennifer Niessner, Philipp Nuske, Alex Tatomir and Markus Wolff; from outside our group, these are Ivar Aavatsmark, Mike Celia, Helge Dahle, Geir Eigestad, Yaqing Fan, Sarah Gasda, Ton Leijnse, Steffen Müthing, Halvor Nilsen, Jan Nordbotten, Gillian Pickup, Karsten Pruess, Iryna Rybak, Bernd Wiese and Barbara Wohlmuth.

The computational results in this thesis that come from our working group at the LH2 have been achieved with the open-source porous-media simulator DuMu$^{\text{x}}$. I had the pleasure to initiate and co-develop this simulator and want to thank all other developers and users for contributing to the project. Moreover, DuMu$^{\text{x}}$ would not have been possible without its underlying framework DUNE. I am heavily indebted to all DUNE developers and want to express my sincere gratitude and appreciation for their great work. In particular, I want to thank Peter Bastian, Robert Klöfkorn, Steffen Müthing, Rebecca Neumann and Oliver Sander for their strong support and help for our work.

This thesis was also influenced by the research visits that I could make during the last years. I am thankful to Xavier Sanchez-Vila and Jesús Carrera for hosting my stay at the UPC in Barcelona during which I wrote the chapter on locally conservative discretization methods. I enjoyed very much my travels to Norway and want to thank Kristin Flornes, Knut-Andreas Lie and Atgeirr Rasmussen for enabling my research visits to IRIS in Bergen and SINTEF in Oslo, as well as Jan Nordbotten for organizing two wonderful meetings in Geilo. My special thanks goes to Mary Wheeler for hosting a very nice stay in her research group in Austin, Texas.

The successful completion of my habilitation will equip me with the venia legendi for the

academic subject "Simulationstechnik." I am happy to be the first person to receive the permission to teach this particular subject. This was of course driven by the DFG-funded Cluster of Excellence "Simulation Technology" which has been established at the University of Stuttgart in 2007. I would like to thank the SimTech-affiliated people that helped to form this strong research community and to widen my understanding of computational science and engineering. I am especially grateful to Wolfgang Ehlers, the coordinator of SimTech, for his support for my habilitation project.

I enjoyed the privilege of being happy to go to work (pretty much) every working day in the last 6.5 years. As mentioned above, the environment and atmosphere at the LH2 combine cutting-edge research and every-day amusement in a truly unique and pleasant way. I want to thank all my colleagues for contributing to this experience. I am particularly grateful to my current and former officemates Holger Class, Anozie Ebigbo and Jochen Fritz. Moreover, our research work is strongly facilitated by persons managing our administrative and financial issues: my thank goes to Prudence Lawday and Maria Costa for organizing our group in this perspective.

Finally, I would like to thank my family and friends for their ever-lasting support of my academic career and for equipping me with a rich, joyful and unmatchable private life. I would like to express my deepest gratitude to Lorena whose sincere love still illuminates my life every day; and to our new-born daughter Nuria who rocks my world in the most pleasant way.

Stuttgart, July 2013 Bernd Flemisch

Contents

Deutsche Zusammenfassung

Strömungs- und Transportprozesse in porösen Medien sind die dominierenden Vorgänge für eine Vielzahl geologischer, technischer und biologischer Systeme. Für die Beschreibung vieler interessanter und wichtiger Anwendungen reicht ein einzelnes mathematisches und darauf basierendes numerisches Modell, das nur eine Skala und einen physikalischen Vorgang berücksichtigt, nicht aus, und die Kopplung zweier oder mehrerer Modelle ist erforderlich. Die Entwicklung solcher gekoppelter numerischer Modelle stellt große Herausforderungen auf konzeptioneller, analytischer und algorithmischer Ebene. Das Ziel dieser Habilitationsschrift ist die Beschreibung einiger dieser Herausforderungen und das Aufzeigen von Lösungsmöglichkeiten für die Probleme, die durch sie gestellt werden. Die Arbeit gliedert sich in drei Teile:

A Modellkopplung,

B Lokal erhaltende Diskretisierungsverfahren,

C Open-Source Poröse-Medien-Simulation.

Jeder Teil ist in drei Kapitel untergliedert. Die meisten Kapitel (1-3, 5, 6, 8, 9) basieren auf bereits veröffentlichten Zeitschriftenartikeln oder Buchkapiteln. Das Layout und die Notation dieser Kapitel wurden vereinheitlicht, der Inhalt wurde bei den meisten aber nicht verändert, um ihre Eigenständigkeit beizubehalten. Zwei Kapitel (4 und 7) wurden für diese Habilitationsschrift neu geschrieben. Im Folgenden wird ein Überblick über jeden Teil und dessen Kapitel gegeben, und die Inhalte in den Kontext dieser Arbeit gesetzt.

Part A *Modellkopplung* behandelt ungekoppelte und gekoppelte Modelle für Strömungs- und Transportvorgänge in porösen Medien im Allgemeinen und beschreibt einige dieser Modelle im Detail. **Kapitel 1** *Mathematische und numerische Modelle für poröse Medien* dient hauptsächlich zur Einführung von Konzepten und Notation für die Modellierung von Strömungs- und Transportvorgängen in porösen Medien. So werden die relevanten Skalen definiert und das Konzept des repräsentativen Elementarvolumens eingeführt. Grundlegende Definitionen wie die von Phasen und Komponenten werden gegeben, zusammen mit den fundamentalen Fluid- und Matrix-Eigenschaften und den Konstitutivbeziehungen, die die Interaktion von Fluiden und Matrix und die Gesetze für das Phasengleichgewicht beschreiben. Die Bilanzgleichungen für Mehrphasenströmung in porösen Medien auf der Darcy-Skala werden aus dem Reynolds-Transport-Theorem hergeleitet, einschließlich der Behandlung teilweise mischbarer Phasen und nichtisothermer Strömung. Spezielles Augenmerk wird auf die Entwicklung entkoppelter Modellformulierungen gerichtet, die mit semi-impliziten Lösungstrategien behandelt werden können. Die Notwendigkwit von Mehrskalen- und Mehrphysik-Ansätzen wird durch eine Beschreibung der Anforderungen an die Simulation von CO_2-Speicherszenarien illustriert. Der Stand der Technik für Hochskalierungs- und Mehrskalen-Methoden wird besprochen und ein Beispiel einer Mehrskalen-Methode auf adaptiv verfeinerten Gittern präsentiert. Der Begriff der Mehrphysik-Methode ist in diesem Kapitel auf Techniken beschränkt, die einen

effizienten Umgang mit einer unterschiedlichen Anzahl an relevanten Phasen oder Komponenten in unterschiedlichen Teilen des Simulationsgebiets erlauben. Zwei Anwendungen einer solchen Mehrphysik-Methode für die Strömung zweier teilweise mischbarer Phasen auf adaptiven Gittern und Teilgebieten werden diskutiert.

Kapitel 2 *Klassifizierung von und Übersicht über Modelkopplungs-Ansätze* erweitert den Blick über die in Kapitel 1 behandelten Mehrskalen- und Mehrphysik-Methoden hinaus. Modellkopplungskonzepte werden in zeitliche und räumliche Konzepte unterteilt, und die räumlichen Konzepte weiter in Mehrprozess-, Mehrskalen-, Mehrdimensions- und Mehrabteilungs-Konzepte. Die Bezeichnung Mehrprozess bezieht sich auf die Volumenkopplung unterschiedlicher Modellgleichungen auf einer Skala für die Beschreibung mehrerer physikalischer Vorgänge, wohingegen der Begriff Mehrskalen die Volumenkopplung möglicherweise unterschiedlicher Modellgleichungen auf mehr als einer Skala für die Beschreibung eines einzelnen physikalischen Vorgangs bezeichnet. Mehrdimensional steht für die Volumen- oder Oberflächenkopplung möglicherweise unterschiedlicher Modellgleichungen für die Beschreibung physikalischer Vorgänge auf Teilgebieten von unterschiedlicher effektiver Dimension, und Mehrabteilung bezeichnet die Oberflächenkopplung möglicherweise unterschiedlicher Modellgleichungen für die Beschreibung physikalischer Vorgänge auf Teilgebieten von gleicher Dimension. Einige herkömmliche räumliche Kopplungsansätze werden entsprechend dieser Kategorien klassifiziert und vorgestellt. Eine Möglichkeit der sequenziellen zeitlichen Kopplung wird detaillierter vorgestellt, bei der Zeitspannen entsprechend der darin dominierenden Prozesse identifiziert werden und für jede Spanne ein geeignetes Modell gewählt wird. Beispiele aus der Bodensanierung und der CO_2-Speicherung werden präsentiert.

Von großem Interesse für viele Anwendungen sind Gebiete, die zu einem Teil aus einem porösen Medium bestehen und in deren anderem Teil eine freie Strömung vorherrscht. Dieses Thema ist Gegenstand von **Kapitel 3** *Kopplung Freie Strömung – Poröses Medium*. Es wird eine Mehrabteilungs-Kopplung für die nichtisotherme Strömung zweier Komponenten präsentiert, die in zwei Fluidphasen innerhalb des porösen Mediums und in einer Phase in der Region freier Strömung vorkommen können. Das mathematische Modell für die Strömungs- und Transportvorgänge im porösen Medium basiert auf dem Darcy-Gesetz, für die freie Strömung hingegen werden die (Navier-)Stokes-Gleichungen verwendet. Es wird eine detaillierte Beschreibung der Modelle auf den Teilgebieten gegeben. Der wesentliche Beitrag des Kapitels ist die Entwicklung des Kopplungskonzepts, das mit nichtisothermer teilweise mischbarer Strömung und einem Zweiphasensystem im porösen Medium umgehen kann. Es basiert auf der Stetigkeit von Flüssen und der Annahme thermodynamischen Gleichgewichts, und benutzt die Beavers-Joseph-Saffman-Bedingung. Die phänomenologischen Erklärungen für das Modell werden im Detail beschrieben. Das Modell ist in der Lage, Evaporations- und Kondensationsprozesse am Interface zu berücksichtigen. In einem ersten numerischen Beispiel wird es dafür eingesetzt, die durch Wind beeinflusste Evaporation aus dem Boden zu modellieren.

Lokal erhaltende Diskretisierungsverfahren, wie in **Teil B** behandelt, sind ein fundamentaler Bestandteil angemessener numerischer Modelle für Strömungs- und Transportprozesse in porösen Medien. **Kapitel 4** ist einer *Übersicht über lokal erhaltende Diskretisierungsverfahren* (LED) gewidmet. Zunächst wird als Modellproblem die Massenbilanz für die stationäre Strömung einer inkompressiblen Fluidphase formuliert. Der Begriff der lokalen Erhaltung wird definiert und die Diskretisierung des Rechengebiets formalisiert. Die einzelnen LED werden gemäß ihres Ursprungs als Kontrollvolumen-, Finite-Differenzen- oder Finite-Elemente-Methode kategorisiert und beschrieben. Als Kontrollvolumen-Methode sind dies

im einzelnen die Zweipunkt- und die Mehrpunkt-Flussapproximation sowie die Diskrete-Dualität-Finite-Volumen-Methode. Mimetische finite Differenzen, ebenso wie gemischte, unstetige und stetige Galerkin-, Least-Squares- und Kontrollvolumen-Finite-Elemente-Methoden, werden vorgestellt. Einige der LED werden zusätzlich zu ihrer klassischen Beschreibung in den beiden Rahmen der gemischten Finite-Elemente- und der mimetischen Finite-Differenzen-Methode interpretiert. Das Kapitel wird mit einem Vergleich der diskutierten Methoden abgeschlossen, der unter anderem auf die Art und Anzahl der verwendeten Druck- und Fluss-Freiheitsgrade sowie auf die Anforderungen an das Simulationsgitter eingeht.

Ein spezifisches LED wird in **Kapitel 5** *Eine MPFA-Methode für die Behandlung tensorieller relativer Permeabilitäten* vorgestellt. Gewöhnlicherweise werden für die Modellierung von Mehrphasenströmung in porösen Medien skalare relative Permeabilitäten in die Darcy-Gleichung eingesetzt. Im Falle anisotropisch strukturierter Heterogenitäten jedoch können auch diejenigen hochskalierten Parameter anisotrop sein, die nicht nur vom porösen Medium sondern auch von den Fluid-Fluid- oder Fluid-Fluid-Matrix-Wechselwirkungen abhängen. Das Kapitel präsentiert eine Methode für die Modellierung inkompressibler, isothermer und unmischbarer Zweiphasenströmung unter Berücksichtigung anisotroper absoluter und relativer Permeabilitäten. Im Rahmen eines semi-impliziten Lösungsverfahrens wird eine Mehrpunkt-Flussapproximation mit einer speziellen Upwind-Strategie kombiniert. Sowohl das Potenzial der Methode als auch die Relevanz anisotroper relativer Permeabilitäten werden mit Hilfe mehrerer Tests demonstriert. Dafür wird ein poröses Medium gewählt, das auf der feinen Skala heterogen aber isotrop ist und für welches gemittelte homogene aber anisotrope Parameter bekannt sind. Vergleiche zeigen, dass die vorgestellte Methode die Auswirkungen der Anisotropie in den grobskaligen Parametern gut abbildet und das anisotrope Verhalten der feinskaligen Lösung in guter Übereinstimmung modelliert. Dies wird sowohl für einen advektions- als auch für einen diffusionsdominierten Fall demonstriert. Darüber hinaus wird gezeigt, dass Nebendiagonaleinträge in den relativen Permeabilitäts-Tensoren einen entscheidenden Einfluss auf die Fluidverteilung haben können.

Ein anderes LED ist Gegenstand von **Kapitel 6** *Numerische Untersuchung einer mimetischen Finite-Differenzen-Methode.* Zunächst wird eine spezifische mimetische Finite-Differenzen-Methode kurz vorgestellt. Diese Methode wird anschließend anhand einer Serie wohldefinierter zweidimensionaler Benchmark-Probleme getestet. Die Art der Permeabilitäts-Tensoren reicht von homogen und isotrop bis heterogen und anisotrop. Außerdem werden viele unterschiedliche Rechengitter getestet, bestehend aus Dreieckselementen, uniformen Rechteckselementen oder verzerrten Viereckselementen, oder auch nichtkonforme Gitter mit hängenden Knoten. Die Qualität der diskreten Lösungen wird anhand mehrerer Kennzahlen ausgewertet. Unter anderem werden für die Tests, die auf einer analytischen Lösung basieren, die Diskretisierungsfehler in Druck und Geschwindigkeit berechnet. Außerdem wird zum Beispiel in allen Tests überprüft, ob die Masse global erhalten wird. Die eingesetzte Methode löst die Mehrheit der Benchmark-Probleme mit überzeugender Genauigkeit und Robustheit. Auch dadurch, dass sie relativ leicht implementiert werden kann, erscheint die Methode sehr vielversprechend für den Einsatz in ingenieursrelevanten Anwendungen.

Ein numerisches Modell wird durch seine Implementierung in Form von Programmcode realisiert. **Teil C** *Open-Source Poröse-Medien-Simulation* beschäftigt sich mit der Idee, diesen Programmcode mit Hilfe von Open-Source-Entwicklungsprinzipien und -techniken zu entwickeln. Er beginnt mit **Kapitel 7** *Open Source in rechnergestützten Ingenieurswis-*

senschaften. Anfangs wird eine Motivation für die Entwicklung von Open-Source-Code in der Wissenschaft gegeben. Diese besteht aus drei Argumenten: Reproduzierbarkeit als ein fundamentaler Bestandteil der wissenschaftlichen Methode verpflichtet zur Freigabe entsprechenden Quellcodes, die Qualität und das Anwendungsspektrum des Codes werden verbessert, und die Zusammenarbeit mit Partnern aus Industrie und Wissenschaft wird vereinfacht. Als nächstes werden, nach einer Vorstellung der Free Software Foundation und der Open Source Initiative, die Definitionen von freier und Open-Source-Software präsentiert und diskutiert. Es wird ein Überblick über existierende Poröse-Medien-Simulatoren gegeben und auf deren Anwendungsspektren, Lizenzierungsmethoden, verwendete Programmiersprachen und zugrundeliegende Diskretisierungsverfahren eingegangen. Als Abschluss des Kapitels werden notwendige und nützliche Infrastruktur-Komponenten für Open-Source-Projekte vorgestellt: Versionskontrolle, Datenbewahrung, Webseite, Mailingliste, Service-Ticket-System, automatisiertes Testen und Projektanalyse.

Kapitel 8 präsentiert *DuMu^x: ein Open-Source Poröse-Medien-Simulator.* DuMu^x ist ein Open-Source-Simulator für Strömungs- und Transportprozesse in porösen Medien, basierend auf DUNE, der "Distributed and Unified Numerics Environment." Sein wesentliches Ziel ist die Bereitstellung eines nachhaltigen und konsistenten Rahmenwerks für die Implementierung und Anwendung von Modellkonzepten, Konstitutivbeziehungen, Diskretisierungen und Lösern. Das Kapitel gibt einen Überblick über DuMu^x mit Hauptaugenmerk auf Software-verwandte Aspekte. Nachdem sowohl die Vision als auch das Konzept und die Design-Ideen eingeführt wurden, werden die von allen DuMu^x-Modellen verwendeten gemeinsamen Strukturen vorgestellt: Materialsystem, Simulationskontrolle und Property-System. Es werden mehrere zur Verfügung stehende numerische Modelle diskutiert, von isothermer, einkomponentiger, Einphasenströmung bis hin zu nichtisothermer, mehrkomponentiger Mehrphasenströmung. Ausgewählte Beispiele illustrieren die Möglichkeiten für die Mehrskalenmodellierung und den parallelen Einsatz.

Aus einem anderen Blickwinkel wird die Notwendigkeit für Open-Source-Simulatoren in **Kapitel 9** *Unsicherheiten in der praktischen Simulation von CO_2-Speicherung* beleuchtet. Der Einfluss dreier unterschiedlicher Ansätze für die Reduktion der Freiheitsgrade in praktischer Simulation von CO_2-Speicherung wird untersucht: reduzierte Physik, Hochskalierung und nichtkonvergierte Diskretisierungen. Eine Benchmark-Studie wird benutzt, um die Auswirkung der Anwendungen dieser Strategien auf die Resultate numerischer Simulationen durch verschiedene Expertengruppen darzustellen. Um die Bandbreite der Untersuchung einzugrenzen, wurde die geometrische und geologische Beschreibung des Speicheraquifers weitestgehend vereinfacht. Die unterschiedlichen Strategien für die Freiheitsgradreduktion führen auf signifikant große Abweichungen in den Antworten auf wesentliche Fragestellungen. Außerdem gibt es einen großen Interpretationsspielraum, wenn komplexe Simulationsergebnisse in eine für Entscheidungsträger nutzbare vereinfachte Form gebracht werden sollen. Die Erfahrungen aus dieser Studie führen zu dem Schluss, dass selbst für hoch-idealisierte Problemstellungen die Antworten auf wichtige, für die CO_2-Speicherung relevante, Fragestellungen mit numerischen Simulationsmethoden nicht mit ausreichender Genauigkeit vorhergesagt werden können. Diese Erkenntnis verdeutlicht unter anderem die Notwendigkeit für Echtzeitüberwachung und Modellkalibrierung während des Injektionsvorgangs.

Diese Habilitationsschrift wird mit einem *Fazit und Ausblick* abgeschlossen. Die Konklusionen der einzelnen Kapitel werden zusammengefasst und in den Kontext der Arbeit gesetzt. Zusätzlich werden einige Vorschläge für die zukünftige Forschung gemacht.

Overview

Flow and transport processes in porous media are the governing processes in a large variety of geological, technical and biological systems. For many interesting and important applications, these processes cannot be treated in an isolated manner or adequately described by means of a single-scale, single-physics mathematical model, and the coupling of two or more models is required. The development of coupled numerical models poses severe challenges on the conceptual, analytical and computational level. This habilitation thesis aims to describe a number of these challenges and solve some of the problems they pose. It is divided into three parts:

A Model Coupling,

B Locally Conservative Discretization Methods,

C Open-Source Porous-Media Simulation.

Each part is divided into three chapters. Most of the chapters (1-3, 5, 6, 8, 9) are based on previously published journal articles and book chapters. While the styles and notations have been unified, the content of most of these chapters has not been altered in order to keep them self-contained. Two chapters (4 and 7) have been created anew for the purpose of this thesis. In the following, an overview of each part and its chapters is provided and their content put into the context of this thesis.

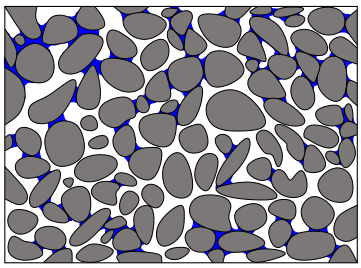

Part A *Model Coupling* deals with uncoupled and coupled porous-media models in general and describes some of these models in detail. **Chapter 1** *Mathematical and Numerical Models for Porous Media* is used primarily for the introduction of notions and concepts for modeling flow and transport processes in porous media. In particular, the relevant scales are defined and the concept of a representative elementary volume is introduced. Basic definitions like the notions of phases and components are provided, together with the essential fluid and matrix parameters and constitutive relations describing fluid-matrix interactions and laws for fluid-phase equilibria. On the Darcy scale, the balance equations for multi-phase flow in porous media are derived by applying the Reynolds transport theorem, including compositional and non-isothermal flow. Special emphasis is placed on the derivation of decoupled model formulations that can be treated by semi-implicit solution schemes. The necessity for multi-scale and multi-physics approaches is illustrated by describing the requirements for CO_2 storage simulation. The state of the art of upscaling and multi-scale methods is reviewed and an example of a multi-scale method on adaptive grids is presented. In this chapter, the notion of multi-physics methods is primarily restricted to techniques that are able to deal efficiently with different numbers of relevant phases and components in different parts of the domain. Two applications of such a multi-physics method for two-phase compositional flow on adaptive grids and subdomains are discussed.

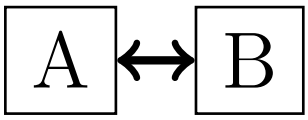

Chapter 2 *Classification and Review of Model Coupling Approaches* broadens the scope beyond the multi-scale and multi-physics methods treated in Chapter 1. Model coupling concepts are divided into temporal and spatial coupling concepts; the latter are subdivided into multi-process, multi-scale, multi-dimensional, and multi-compartment coupling strategies. While multi-process refers to the volume coupling of different model equations on the same scale for the description of multiple physical phenomena, multi-scale indicates the volume coupling of potentially different model equations on more than one scale for the description of the same physical phenomena. Multi-dimensional indicates the volume or surface coupling of potentially different model equations describing physics on subdomains of different dimensionality, while multi-compartment stands for the surface coupling of potentially different model equations describing physics on subdomains of the same dimensionality. Several standard spatial coupling approaches are classified and reviewed according to these categories. A more detailed discussion is devoted to sequential temporal coupling, where time periods with different process regimes are identified, and an appropriate model is chosen for each period. Examples from soil remediation and CO_2 storage are presented.

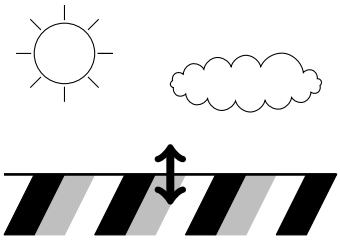

Domains composed of a porous part and an adjacent free-flow region are of special interest in many fields of application. This subject matter is treated in **Chapter 3** *Free-Flow – Porous-Media Coupling*. It presents a multi-compartment coupling for two-component non-isothermal flow with two phases inside the porous medium and one phase in the free-flow region. The mathematical modeling of flow and transport phenomena in porous media is based on Darcy's law whereas, in free-flow regions, the (Navier–)Stokes equations are used. A detailed description of the employed subdomain models is given. The main contribution is the developed coupling concept which is able to deal with compositional flow and a two-phase system in the porous medium. It is based on the continuity of fluxes and the assumption of thermodynamic equilibrium, and uses the Beavers-Joseph-Saffman condition. The phenomenological explanations leading to the model are laid out in detail. The model can account for evaporation and condensation processes at the interface and is used to model evaporation from soil influenced by a wind field in a first numerical example.

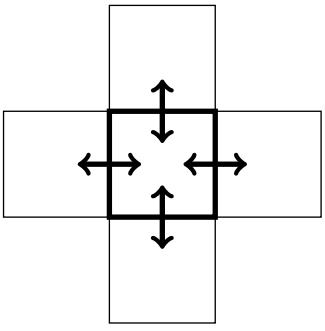

Locally Conservative Discretization Methods, as treated in **Part B**, are a fundamental ingredient of reasonable numerical models for porous media flow and transport processes. **Chapter 4** is dedicated to a *Review of Locally Conservative Discretization Methods* (LCM). First, the single-phase incompressible and stationary mass balance equation is formulated as a prototype model problem. The notion of locally conservative is given, and the discretization of the computational domain if formalized. The individual LCM, grouped into control volume, finite difference and finite element methods, are introduced and reviewed by means of their traditional description. In particular, two-point and multi-point flux approximation and the discrete-duality finite-volume method are discussed as instances of control-volume methods. Mimetic finite differences are presented, as well as mixed, discontinuous Galerkin, continuous Galerkin, least-squares, and control-volume finite-element methods. In addition to their classic description, some of the LCM

are interpreted within the frameworks of mixed finite element and mimetic finite difference methods. The chapter concludes with a comparison of the methods discussed, regarding the discrete pressure and velocity spaces, mesh requirements and number of degrees of freedom.

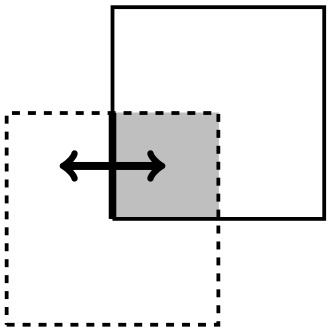

A specific LCM is presented in **Chapter 5** *An MPFA Method for the Treatment of Tensorial Relative Permeabilities*. While multi-phase flow in porous media is most commonly modeled by adding a scalar relative permeability into the Darcy equation, anisotropically structured heterogeneities can result in anisotropy of upscaled parameters, which not only depend on the solid structure but also on fluid-fluid or fluid-fluid-solid interaction. The chapter presents a method for modeling incompressible, isothermal, immiscible two-phase flow, which accounts for anisotropic absolute and relative permeabilities. Multipoint flux approximation (MPFA) is combined with an appropriate upwinding strategy in the framework of a sequential solution algorithm. Different tests demonstrate the capabilities of the method and motivate the relevance of anisotropic relative permeabilities. To this end, a porous medium is chosen, which is heterogeneous but isotropic on a fine scale and for which averaged homogeneous but anisotropic parameters are known. Comparison shows that the anisotropy in the large-scale parameters is well accounted for by the method and agrees with the anisotropic distribution behavior of the fine-scale solution. This is demonstrated for both the advection dominated as well as the diffusion dominated case. Further, it is shown that off-diagonal entries in the relative permeability tensor can have a significant influence on the fluid distribution.

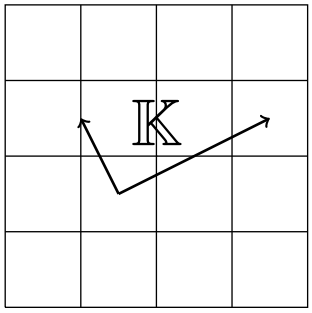

Another LCM is the topic of **Chapter 6** *Numerical Investigation of a Mimetic Finite Difference Method*. First, a particular mimetic finite difference method is briefly presented. This method is tested by solving a series of well-defined benchmark problems in two dimensions. The types of permeability tensors range from homogeneous isotropic to heterogeneous anisotropic. The computational grids may be simplicial, uniform rectangular, distorted quadrilateral, or nonconforming with hanging nodes. Several measures are used to evaluate the quality of the discrete solutions. For the tests that are based upon an analytical solution, the discretization errors in the pressure and the velocity are calculated. Moreover, the validity of global mass conservation is checked in all tests. The proposed method solves the majority of the benchmark problems with convincing accuracy and robustness. It appears to be most promising for tackling real applications, also because of the ease of implementation.

A numerical model is realized by its implementation in the form of computer code. **Part C** *Open-Source Porous-Media Simulation* deals with the idea of developing such a computer code by means of open-source development techniques. It starts with **Chapter 7** *Open Source in Computational Science and Engineering*. A motivation for developing open-source code in academia is provided first. It consists of three basic arguments: providing access to source code is mandatory as reproducibility is fundamental to the scientific method, code quality and applicability can be expected to increase, and collab-

orations with industrial or academic partners are greatly facilitated. Next, the definitions of free and open-source software are provided and discussed, together with an introduction of the Free Software Foundation and the Open Source Initiative. An overview of existing porous media simulators is presented, highlighting their capabilities, licensing policies, programming languages employed, and underlying discretization techniques. To round off, necessary and useful infrastructure components for open-source projects are listed: revision control, code hosting, website, mailing list, issue tracking, automated testing, and project analysis.

Chapter 8 presents *DuMu^x: an Open-Source Porous-Media Simulator*. DuMu^x is a free and open-source simulator for flow and transport processes in porous media, based on the Distributed and Unified Numerics Environment DUNE. Its main intention is to provide a sustainable and consistent framework for the implementation and application of model concepts, constitutive relations, discretizations, and solvers. The chapter provides an overview of DuMu^x with the focus on software-related aspects. After the vision as well as concept and design ideas have been introduced, the common structures that are used by DuMu^x models are presented: material system, simulation control, and property system. Several available numerical models are discussed, ranging from isothermal single-phase single-component to non-isothermal multi-phase multi-component. Selected examples highlight the multi-scale and the parallel capabilities.

The necessity for open-source simulators is illustrated from a different point of view in **Chapter 9** *Uncertainties in the Practical Simulation of CO_2 Storage*. It reports on the impact of three distinct approaches to make the practical simulation of CO_2 storage computationally tractable: reduced physics, upscaling, and non-converged discretizations. Compounding these different strategies, a benchmark study is used to try to assess the impact of an expert group on the results of the numerical simulations. In order to restrict the scope of the investigation, the geometric and geological description of the storage aquifer was simplified to the greatest extent possible. The different strategies applied to simplify the problem lead to significantly deviating answers when addressing relevant storage questions. Furthermore, there is room for interpretation when complex simulation results are simplified to the type of higher-level information sought in decision making processes. Our experience leads us to conclude that answers to important questions relating to CO_2 storage cannot be predicted convincingly with satisfactory accuracy with numerical simulation tools, even for highly idealized problems. This emphasizes the need for real-time monitoring and history matching during injection operations.

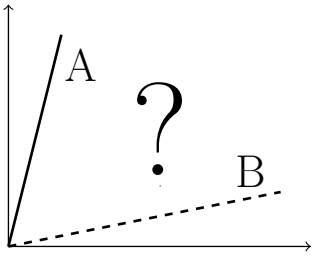

This thesis closes with a *Conclusion and Outlook*. The conclusions of the individual chapters are summarized and put into the context of the thesis. Moreover, several suggestions for future research are given.

Part A

Model Coupling

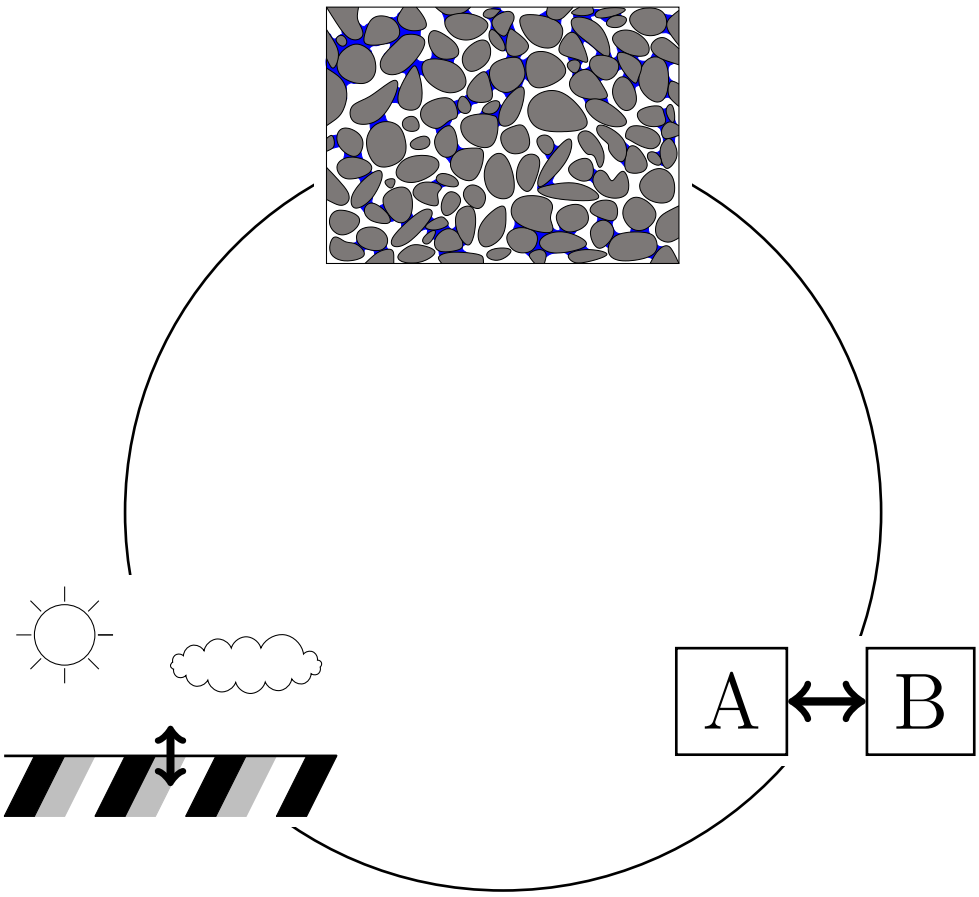

1 Mathematical and Numerical Models for Porous Media

Bibliographic Note: The content of this chapter is based on the following original article [Helm 10]: R. Helmig, J. Niessner, B. Flemisch, M. Wolff, J. Fritz (2010): Efficient modeling of flow and transport in porous media using multi-physics and multi-scale approaches. *Handbook of Geomathematics*, Springer, pp. 417–458.

Summary Flow and transport processes in porous media including multiple fluid phases are the governing processes in a large variety of geological and technical systems. In general, these systems include processes of different complexity occurring in different parts of the domain of interest. The different processes mostly also take place on different spatial and temporal scales. It is extremely challenging to model such systems in an adequate way accounting for the spatially varying and scale-dependent character of these processes. In this work, we give a brief overview of existing upscaling, multi-scale, and multi-physics methods, and we present mathematical models and model formulations for multi-phase flow in porous media including compositional and non-isothermal flow. Finally, we show simulation results for two-phase flow using a multi-physics and a multi-scale method.

1.1 Introduction

In a hydrological, technical or biological system, various processes occur in different parts of the general modeling domain. These processes must be considered on different space and time scales, and they require different model concepts and data. Highly complex processes may take place in one part of the system necessitating a fine spatial and temporal resolution, while in other parts of the system, physically simpler processes take place allowing an examination on coarser scales. For an overview and categorization of concepts for temporal and spatial model coupling we refer to [Helm 13].

Figure 1.1 shows a sketch of an exemplary porous media system including various important length scales and different types of physical processes. The heterogeneous structure in porous media is depending strongly on the spatial scale (see, for example, [Nies 07]). The traditional approach resolves the underlying structure on one scale, which has to be fine enough if an accurate description is desired. **Multi-scale** algorithms regard scales separately. The connection between two scales is made by up- and downscaling approaches. In Figure 1.1, this is exemplarily visualized by integrating local heterogeneous information via upscaling techniques into the global flow problem. Much research has been done to upscale either pressure or saturation equation in two-phase flow or include the different scales directly in the numerical scheme by using multi-scale finite volumes or elements, see, for example, [E 03c, E 03a, Chen 03b, Hou 97, Jenn 03, Durl 91, Rena 97, Efen 00, Efen 02, Chen 03a].

In contrast to an a-priori decision about the model complexity undertaken in traditional methods, **multi-physics** approaches allow to apply different model concepts in different

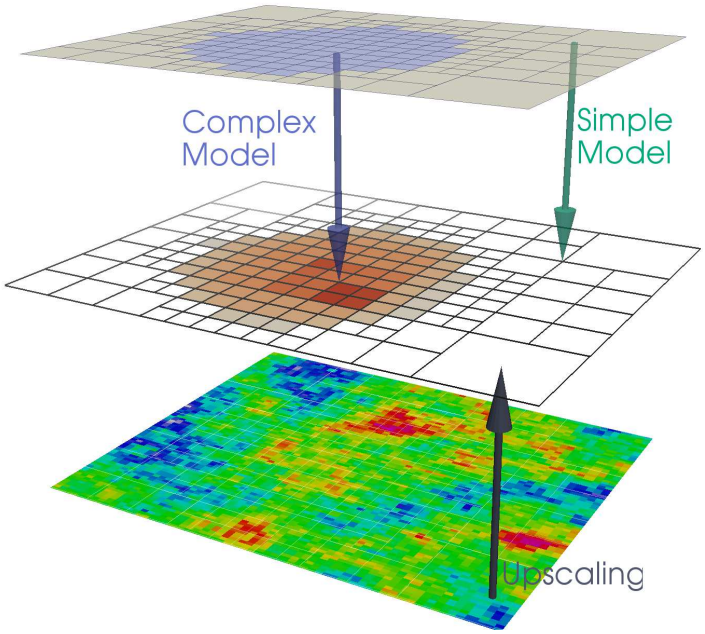

Figure 1.1: A general physical system where different processes occur in different parts of a domain and on different scales.

subdomains. In the upper half of Figure 1.1, the red plume in the middle of the domain can be simulated by accounting for a multitude of physical processes, whereas the surroundings are approximated by a simpler model abstraction. In this respect, research has advanced in the context of domain decomposition techniques (see, for example, [Whee 99, Yoto 02]) and in the context of mortar finite element techniques that allow multi-physics as well as multi-numerics coupling (see, for example, [Pesz 02]). The advantage of multi-scale multi-physics algorithms is on one side that the appropriate model can be applied at will for each specific scale or physical process. On the other hand, they allow to save computing time or make the computation of very complex and large systems possible that could otherwise not be numerically simulated, at least not in that level of detail.

In the following, as an example application, the storage of carbon dioxide (CO_2) in a deep geological formation will be studied and multi-scale as well as multi-physics aspects in space and time will be identified. Please note that multi-scale and multi-physics aspects are relevant in a large number of additional applications, not only in geological systems, but also in biological (for example, treatment of brain tumors) and technical (for example, processes in polymer electrolyte membrane fuel cells) systems. Thus, multi-scale multi-physics techniques developed for geological applications can be transferred to a broad range of other problems.

Concerning CO_2 storage, different storage options are commonly considered that are shown in Figure 1.2, which is taken from [IPCC 05]. According to that figure, possible storage possibilities are given by depleted oil and gas reservoirs, use of CO_2 in the petroleum industry in order to enhance oil and gas recovery or – in a similar spirit – in order to improve the methane production by injection of CO_2. Besides, deep saline formations represent possible storage places, either onshore or offshore. When injecting carbon dioxide, processes take place on highly different spatial and temporal scales. Concerning spatial scales, the processes in the vicinity of the CO_2 plume are very complex including phase change, chemical reactions etc. But usually, the interest lies on the effect of the CO_2

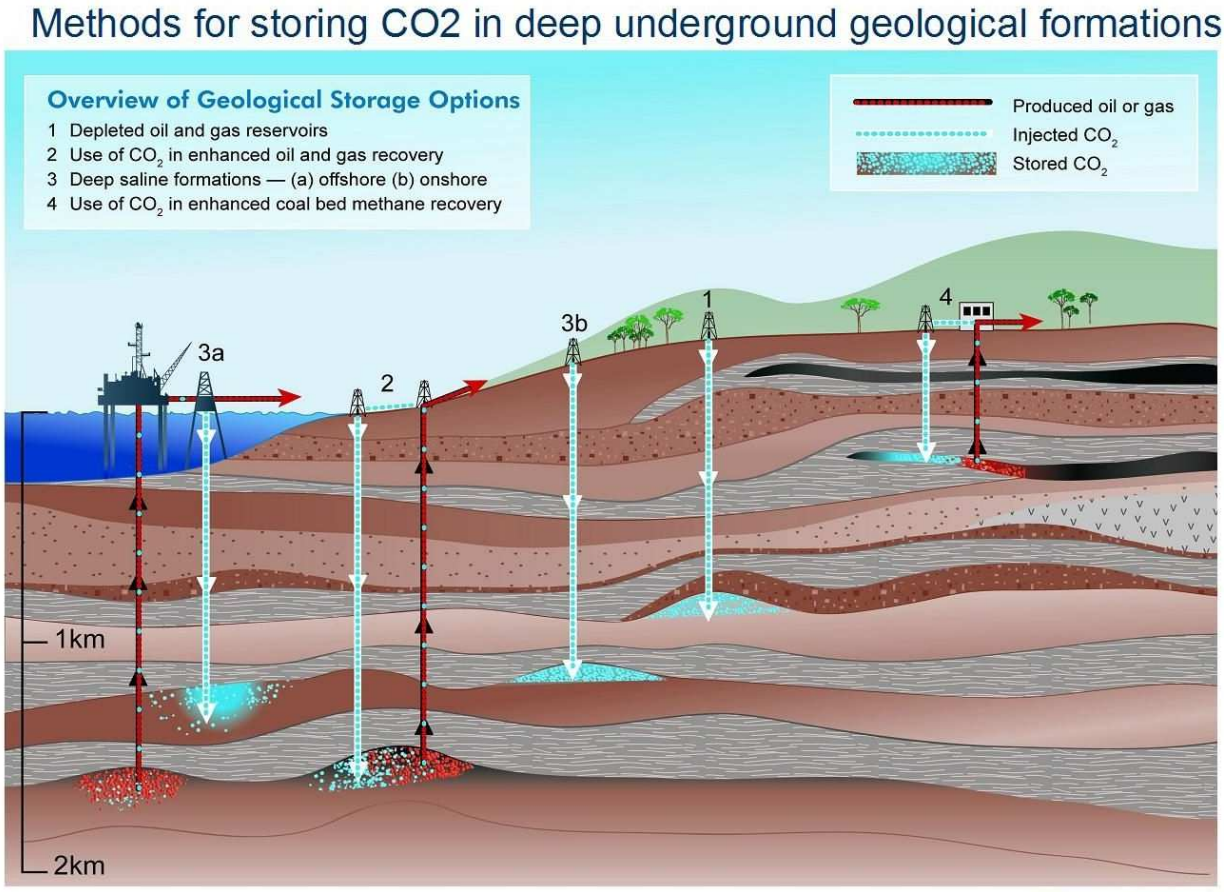

Figure 1.2: Carbon dioxide storage scenarios from IPCC special report on carbon capture and storage, [IPCC 05].

injection on larger domains, especially if it is to be investigated whether CO_2 is able to migrate to the surface or not. In the vicinity of the CO_2 plume, processes of much higher complexity and much higher fine-scale dependence occur than in the remaining part of the domain. This aspect prescribes both the spatial multi-scale and the spatial multi-physics character of this application: around the CO_2 plume, processes have to be resolved on a fine spatial scale in order to be appropriately accounted for. In the rest of the domain of interest, processes may be resolved on a coarser spatial scale. Additionally, the processes occurring in the plume zone and in the non-plume zone are different: While complex two-phase multi-component processes including reaction need to be considered near the plume, a single-phase system may be sufficient in other parts of the domain.

With respect to temporal scales we consider Figure 1.3, which is again taken from [IPCC 05]. In the early time period, i.e. few years after the CO_2 injection ceased, the movement of the CO_2 is determined by advection-dominated multi-phase flow (viscous, buoyant, and capillary effects are relevant). In a later time period, when the CO_2 has reached residual saturation everywhere, dissolution and diffusion processes are most decisive for the migration of the carbon dioxide. Eventually, in the very long time range of thousands of years, it is to be expected that the CO_2 will be bound by chemical reactions.

This chapter is structured as follows: In Section 1.2, we define the relevant scales considered in this work and give an overview of multi-scale and of multi-physics techniques. Next,

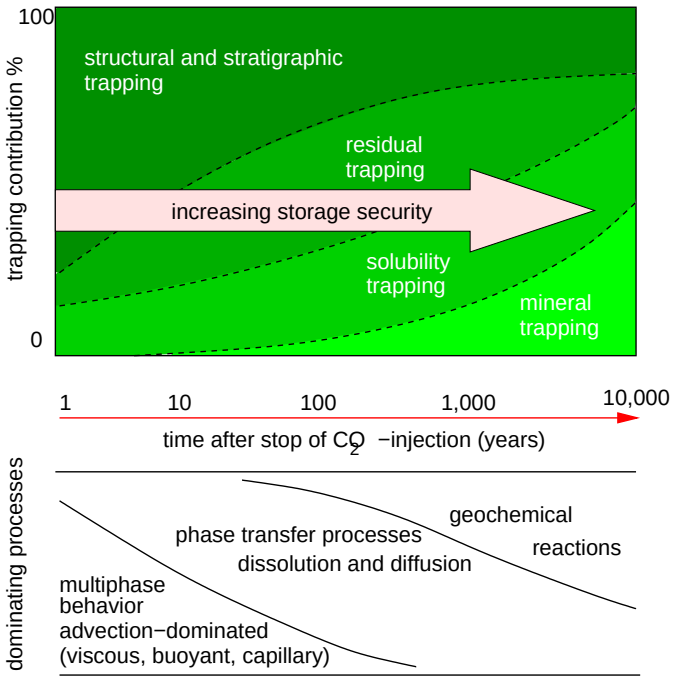

Figure 1.3: Time scales of carbon dioxide sequestration, [IPCC 05].

in Section 1.3, the mathematical model for flow and transport in porous media is described including non-isothermal flow and different mathematical formulations. In Section 1.4, the numerical solution procedures for both decoupled and coupled model formulations are explained. In Section 1.5, we present two different applications of multi-physics and of multi-scale algorithms. Finally, we conclude in Section 1.6.

1.2 State of the Art

We want to give a brief introduction into existing multi-scale methods and into methods for scale transfer. First, general definitions of different important scales are given (Section 1.2.1) to point out which are the scales considered in the following sections. Afterwards, we give a very general overview of basic approaches for upscaling and different kinds of multi-scale methods (Section 1.2.2), and a short introduction to multiphysics methods (Section 1.2.3).

1.2.1 Definition of Scales

In order to design an appropriate modeling strategy for particular problems, it is important to consider the spatial and temporal scales involved, and how the physical processes and parameters of the system relate to these scales.

A careful definition of relevant length scales can clarify any investigation of scale considerations, although such definitions are a matter of choice and modeling approach [Hris 97]. In general, we define the following length scales of concern: the molecular length scale, which is of the order of the size of a molecule; the microscale, or the minimum continuum length scale on which individual molecular interactions can be neglected in favor of an ensemble average of molecular collisions; the local scale, which is the minimum continuum

length scale at which the microscale description of fluid movement through individual pores can be neglected in favor of averaging the fluid movement over a representative elementary volume (REV) – therefore this scale is also called the REV-scale; the mesoscale, which is a scale on which local scale properties vary distinctly and markedly; and the megascale or field-scale. Measurements or observations can yield representative information across this entire range of scales, depending on the aspect of the system observed and the nature of the instrument used to make the observation. For this reason, we do not specifically define a measurement scale.

Figure 1.4 graphically depicts the range of spatial scales of concern in a typical porous medium system. It illustrates two important aspects of these natural systems: several orders of magnitude in potentially relevant length scales exist, and heterogeneity occurs across the entire range of relevant scales. A similar range of temporal scales exists as well, from the pico-seconds over which a chemical reaction can occur on a molecular length scale to the centuries or milleniums of concern in the long-term storage of greenhouse gases or atomic waste.

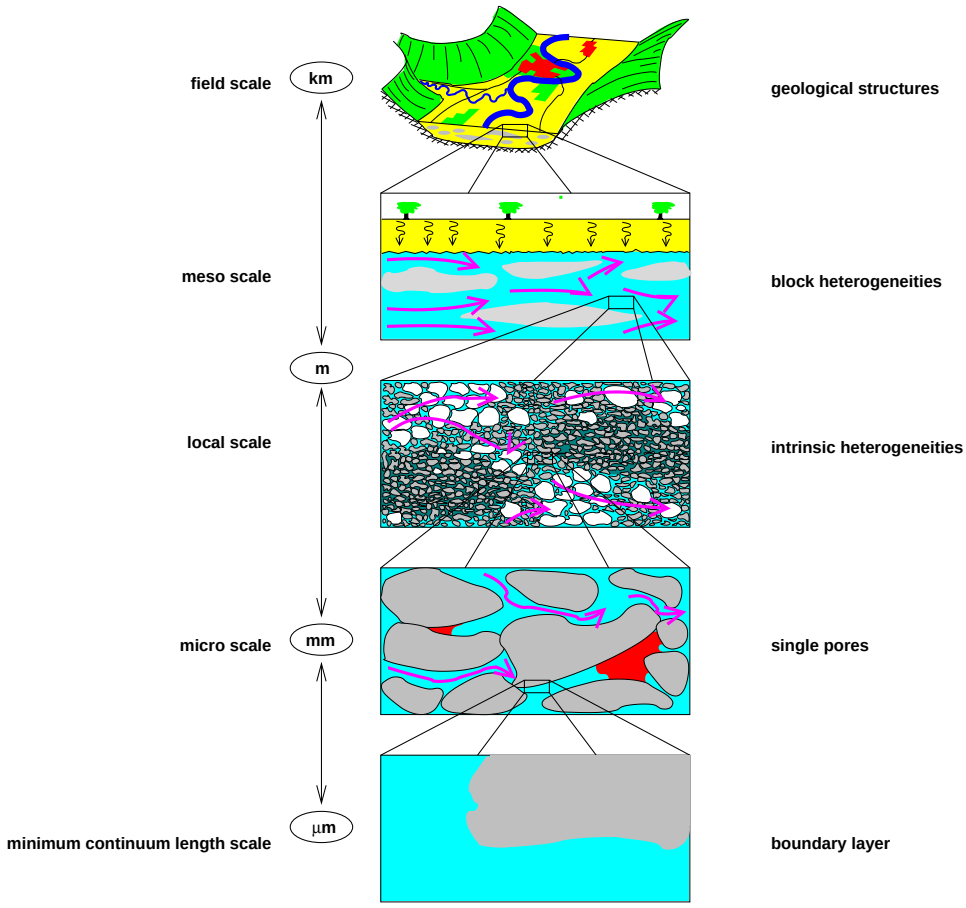

Figure 1.4: Different scales for flow in porous media

When looking at the REV-scale, we average over both fluid–phase properties and solid–phase properties. In Figure 1.5, we schematically show the averaging behavior on the example of the porosity. While averaging over a representative elementary volume (REV), we assume that the averaged property P does not oscillate significantly. In Figure 1.5 this is the case in the range of r_{min} to r_{max}, so an arbitrarily shaped volume V with an inscribed sphere with radius r_{min} and a circumscribed sphere with radius r_{max} can be chosen as REV.

Accordingly, we do not assume any heterogeneities on the REV-scale. For our model, we assume that the effects of the sub–REV–scale heterogeneities are taken into account by effective parameters.

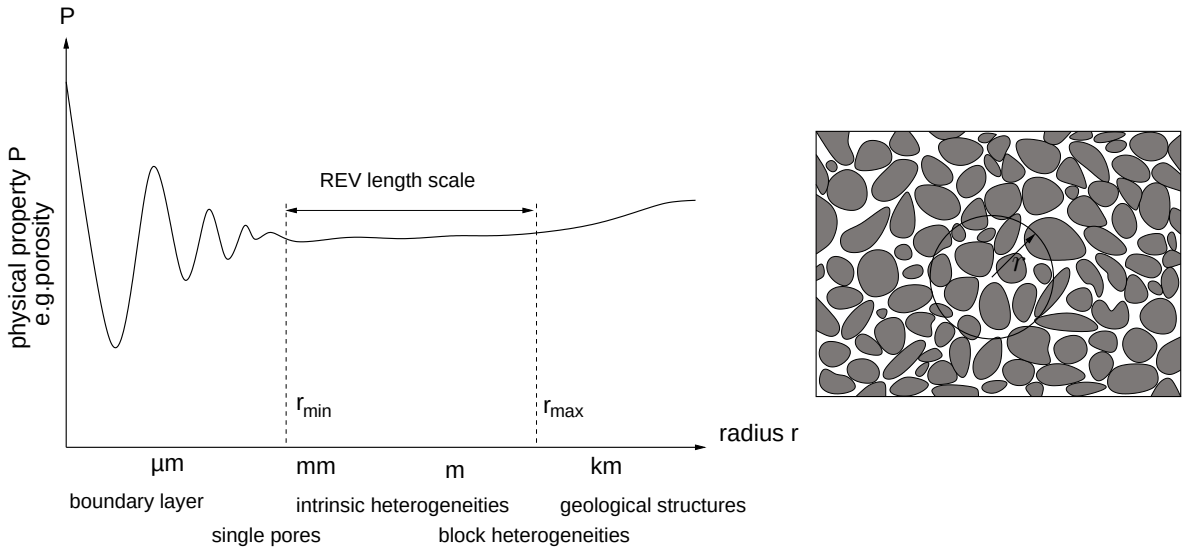

Figure 1.5: Different scales for flow in porous media (schematically for Figure 1.4)

The scales of interest in this work are the meso-scale (which we also call fine scale) and the mega-scale (for us, the coarse scale).

1.2.2 Upscaling and Multi-Scale Methods

In multi-scale modeling, more than one scale is involved in the modeling as the name implies. In general, each pair of scales is coupled in a bidirectional way, where the coarser scale contains the finer scale. This means that upscaling and downscaling methods have to be provided. Upscaling is a transition of the finer to the coarser scale and downscaling vice-versa. Both kinds of operators are generally needed. Only special applications with weak coupling between the scales allow for a mono-directional coupling and thus, only upscaling or only downscaling operators.

Classical upscaling strategies comprise the method of asymptotic expansions (homogenization) and volume averaging. Usually, the fine-scale informations which get lost due to averaging are accounted for by effective parameters in the upscaled equations. For downscaling, the typical methodology is to specify boundary conditions at the boundaries of a coarse-grid block and solve a fine-grid problem in the respective domain. The boundary conditions are obtained either directly from the coarse-scale problem or coarse-scale results are rescaled to fine-scale properties using fine-scale material parameters. In the latter case, fine-grid boundary conditions can be specified along the boundaries of the downscaling domain. In the following, we provide a brief overview of common upscaling techniques and of multi-scale methods.

Upscaling Methods

Effective Coefficients This method the coarse scale equations to be a priori known, for example by assuming the same kind of equation than at the fine scale. In that case the

problem is to find upscaled or averaged effective model parameters to describe the physical large scale behavior properly. This method is very commonly applied to upscale the single-phase flow equation in porous media. Effective parameters like the transmissibility are obtained by the solution of local fine-scale problems which can be isolated from the global problem (local upscaling) or coupled to the global problem (local-global upscaling) (for example, see [Durl 91] or [Chen 03a]).

Pseudo Functions This method follows the idea of effective coefficients described before. The question is how to determine effective parameters like coarse-scale relative permeabilities, mobilities or fractional flow functions, which depend on the primary variables and therefore vary in time. One possibility, which is for example discussed in [Bark 97] and [Darm 02], is the use of pseudo functions. Most likely, these functions are calculated from the solution of a fine-scale multi-phase flow problem (for example, see [Chen 06a]). Detailed investigations on appropriate boundary conditions for the solution of the local fine scale problems can be found in [Wall 02a] and [Wall 02b].

Volume Averaging/Homogenization Methods Coarse scale equations may be derived from known fine-scale equations applying volume averaging or homogenization methods. Application of this methods for porous media flow can be found in, for example, [Whit 98, Gray 93, Quin 88, Efen 00, Efen 02, Saez 89, Panf 00] . Depending on the assumptions, different kinds of new coarse-scale parameters or functions occur in the upscaled equations accounting for fine-scale fluctuations which get lost due to the averaging. The problem is to find upscaled or averaged effective model parameters or functions which describe the physical large-scale behavior properly. It is a common approach to assume the fine-scale equations to be valid also on the coarse scale. In this case, application of volume averaging or homogenization methods can give information about the underlying and simplifying assumptions.

Numerical Upscaling Assuming the coarse-scale equations to be known, the problem is to find upscaled or averaged effective model parameters or functions which describe the physical large-scale behavior properly. A flexible tool for calculating effective coefficients is provided by numerical upscaling techniques where representative fine-scale problems are solved to approximate the coarse-scale parameters. Generally, two types of method can be distinguished: Global methods and local methods. Local methods choose sub-domains of a size much smaller than the global scale (for example, the size of one coarse grid block). Examples of local upscaling techniques for single-phase parameters like permeabilities or transmissibilities or two-phase parameters like phase permeabilities can be found in, for example, [Durl 91, Pick 96, Wall 02a, Wall 02b, Efen 04]. Global methods choose sub-domains of the size of the model domain. Examples for such methods are the pseudo function approaches (see, for example, [Kyte 75, Ston 91, Bark 97, Darm 02].

Multi-Scale Methods

Homogeneous Multi-Scale Methods Homogeneous multi-scale methods inherently give approximate solutions on the micro-scale. They consist of the traditional numerical approaches to deal with multi-scale problems, like, for example, multi-grid methods, [Bram 93, Brig 00, Stub 01, Trot 01], multi-resolution wavelet methods, [Catt 03, He 08,

Jang 04, Urba 09], multi-pole techniques, [Gira 06, Of 07, Torn 08, Yao 08], or adaptive mesh refinement, [Ains 00, Babu 01, Mull 03]. Due to the usually enormous number of degrees of freedom on this scale, this direct numerical solution of real-world multiple scale problems is impossible to realize even with modern supercomputers.

Heterogeneous Multi-Scale Methods The heterogeneous multi-scale method (HMM), [E 07], proposes general principles for developing accurate numerical schemes for multiple problems, while keeping costs down. It was first introduced in [E 03b], and clearly described in [E 03c]. The general goal of the HMM, as in other multi-scale type methods, is to capture the macroscopic behavior of multi-scale solutions without resolving all the fine details of the problem. The HMM does this by selectively incorporating the microscale data when needed, and exploiting the characteristics of each particular problem.

Variational Multi-Scale Method In [Hugh 95, Hugh 98], Hughes et al. present the variational multi-scale method that serves as a general framework for constructing multi-scale methods. An important part of the method is to split the function space into a coarse part, which captures low frequencies, and a fine part, which captures the high frequencies. An approximation of the fine-scale solution is computed and it is used to modify the coarse-scale equations. In recent years, there have been several works on convection-diffusion problems using the variational multi-scale framework, see, for example, [Codi 01, Hauk 01, Juan 05], and it has also been applied as a framework for multi-scale simulation of multi-phase flow through porous media, see, for example, [Juan 08a, Kees 08, Nord 09a, Calo 11].

Multi-Scale Finite-Volume Method The underlying idea is to construct transmissibilities that capture the local properties of the differential operator. This leads to a multi-point discretization scheme for the finite volume solution algorithm. The transmissibilities can be computed locally and therefore this step is perfectly suited for massively parallel computers. Furthermore, a conservative fine-scale velocity field can be constructed from the coarse-scale pressure solution. Over the recent years, the method became able to deal with increasingly complex equations, [Haji 08, Jenn 06, Lee 08, Luna 06, Luna 07, Luna 08].

Multi-Scale Finite-Element Method Another multi-scale method, the multi-scale finite element method, was presented in 1997, [Hou 97]. The theoretical foundation is based on homogenization theory. The main idea is to solve local fine-scale problems numerically in order to use these local solutions to modify the coarse-scale basis functions. There has been a lot of work on this method over the last decade, see, for example, [Aarn 06, Aarn 08b, Arbo 07, Efen 07, Kim 07, Kipp 08].

Multi-Scale Methods and Domain Decomposition By comparing the formulations, the authors of [Nord 08] observe that the multi-scale finite volume method is a special case of a non-overlapping domain decomposition preconditioner. They go on to suggest how the more general framework of domain decomposition methods can be applied in the multi-scale context to obtain improved multi-scale estimates. Further work on multi-scale modelling of flow through porous media using a domain-decomposition preconditioner can be found in [Galv 10, Sand 11].

Vertical Equilibrium Methods Vertical equilibrium methods are special kinds of multi-scale methods. An upscaled model is derived through vertical integration of the three-dimensional governing equations for two-phase flow under the assumptions of vertical equilibrium, complete gravity segregation, and a sharp-interface between the two phases. The resulting model is a two-dimensional model for flow in the lateral directions only. The underlying assumptions are sufficiently justified in many CO_2 sequestration scenarios, which currently are the main application areas of vertical equilibrium models. Formulations with [Gasd 09] and without [Gasd 11a] upscaling of convective mixing exist.

Adaptive Upscaling Methods Numerical upscaling methods (see Section 1.2.2) can be extended to (adaptive) local-global methods. Boundary conditions for the solution of the local fine-scale problems are determined from the global coarse-scale solution via a downscaling step. Depending on the model, the physical regime and the required accuracy, the effective parameters may have to be recalculated each time the global solution changes considerably (see, e.g., [Chen 03a, Chen 06a, Chen 09, Chen 13]). Combining upscaling and downscaling, (adaptive) local–global methods can be viewed as multi-scale methods.

1.2.3 Multi-Physics Methods

In general, the term multi-physics is used whenever processes which are described by different sets of equations interact and thus are coupled within one global model. The coupling mechanisms can in general be divided into volume (or vertical) coupling and surface (or horizontal) coupling. In this sense, the multi-scale approaches introduced before could be interpreted as vertical coupling approaches. Moreover, a large variety of multi-continua models exist. Here, the model domain is physically the same for the different sets of equations, and the exchange is usually performed by means of source and sink terms. Within the context of porous media, most well-known multi-continua models include the double porosity models, [Arbo 89, Ryzh 07], and the MINC method, [Prue 85, Smit 99].

In contrast to that, horizontal coupling approaches divide the model domain into subdomains sharing common interfaces. The coupling is achieved by enforcing appropriate interface conditions. In physical terms, these interface conditions should state thermodynamic equilibrium, while in mathematical terms, they often correspond to the continuity of primal and dual variables, like, for example, pressure and normal velocity. Examples for surface coupling are discrete fracture approaches, [Diet 05], or the coupling of porous media flow and free flow domains, [Beav 67, Disc 02, Gira 09, Jage 09, Layt 03]. While these two examples couple different types of flow regimes, we will in our study concentrate on the coupling of different processes inside one porous media domain. A good overview of such multiphysics methods can be found in [Whee 02]. In [Albo 99], the authors present an interface concept to couple two-phase flow processes in different types of porous media. The coupling of different models for one, two or three-phase flow incorporating an iterative non-linear solver to ensure the interface coupling conditions was presented in [Pesz 00].

1.3 Mathematical Models for Flow and Transport Processes in Porous Media

We introduce the balance equations of flow and transport processes in porous media by means of an REV concept, i.e. on our fine scale. These equations may be upscaled in a subsequent step using one of the techniques of Section 1.2.2 or used in a multi-scale technique of Section 1.2.2. After establishing the necessary physical background, the equations for isothermal multi-phase flow processes are derived, both for the case of immiscible fluids as well as for miscible fluids. Furthermore, we give an introduction to different decoupled formulations of the balance equations paving the way for specialized solution schemes discussed in the following section. Finally, an extension to non-isothermal processes is provided.

1.3.1 Preliminaries

After stating the basic definitions of phases and components, the essential fluid and matrix parameters are introduced. Parameters and constitutive relations describing fluid-matrix interactions are discussed, and some common laws for fluid phase equilibria are reviewed.

Basic Definitions

Phases If two or more fluids fill a volume (for example, the pore volume), are immiscible and separated by a sharp interface, each fluid is called a phase of the multi-phase system. Formally, the solid matrix can also be considered as a phase. If the solubility effects are not negligible, the fluid system has to be considered as a compositional multi-phase system.

A pair of two different fluid phases can be divided into a wetting and a non-wetting phase. Here, the important property is the contact angle θ between fluid-fluid interface and solid surface (Figure 1.6). If the contact angle is acute, the phase has a higher affinity to the solid and is therefore called wetting, whereas the other phase is called non-wetting.

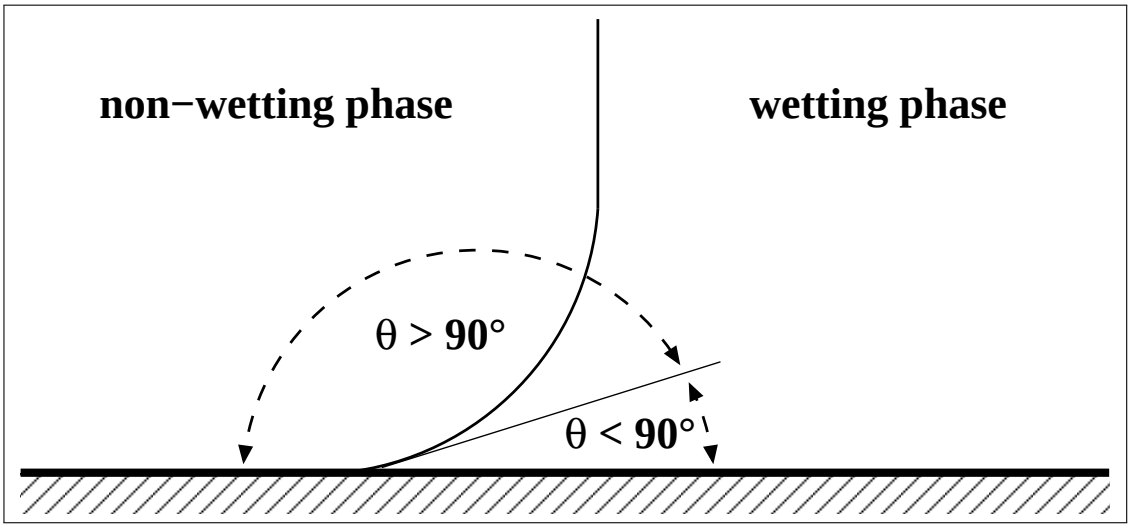

Figure 1.6: Contact angle between a wetting and a non-wetting fluid.

Components A phase usually consists of several components which can either be pure chemical substances, or consist of several substances which form a unit with constant physical properties, such as air. Thus, it depends on the model problem which substances or mixtures of substances are considered as a component. The choice of the components is essential, as balance equations for compositional flow systems are in general formulated with respect to components.

Fluid Parameters

Compositions and Concentrations The composition of a phase α is described by fractions of the different components contained in the phase. *Mass fractions* X_α^κ give the ratio of the mass $mass_\kappa$ of one component κ to the total mass of phase α,

$$X_\alpha^\kappa = \frac{m^\kappa}{\sum_\kappa m^\kappa}\,. \tag{1.1}$$

From this definition, it is obvious that the mass fractions sum up to unity for each phase,

$$\sum_\kappa X_\alpha^\kappa = 1. \tag{1.2}$$

A concept which is widely used in chemistry and thermodynamics, are *mole fractions* which phase-wise relate the number of molecules of one component to the total number of components. Mole fractions are commonly denoted by lower case letters and can be calculated from mass fractions via the molar mass M^κ by

$$x_\alpha^\kappa = \frac{X_\alpha^\kappa / M^\kappa}{\sum_\kappa X_\alpha^\kappa / M^\kappa} \tag{1.3}$$

Both, mole fractions and mass fractions are dimensionless quantities. *Concentration* is the mass of a component per volume of the phase, and thus obtained by multiplying the mass fraction of the component by the density of the phase, $C_\alpha^\kappa = \varrho_\alpha X_\alpha^\kappa$, which yields the SI unit $\mathrm{kg/m^3}$.

Density The density ϱ relates the mass m of an amount of a substance to the volume v which is occupied by it:

$$\varrho = \frac{m}{v}. \tag{1.4}$$

The corresponding unit is $\mathrm{kg/m^3}$. For a fluid phase α, it general depends on the phase pressure p_α and temperature T, as well as on the composition x_α^κ of the phase,

$$\varrho_\alpha = \varrho_\alpha(p_\alpha, T, x_\alpha^\kappa). \tag{1.5}$$

Since the compressibility of the solid matrix as well as its temperature-dependence can be neglected for many applications, one can often assign a constant density to solids.

For liquid phases, the dependence of density on the pressure is usually very low and the contribution by dissolved components is not significant. Thus, the density can be assumed to be only dependent on temperature, $\varrho_\alpha = \varrho_\alpha(T)$. For isothermal systems, the temperature is constant in time and thus, the density of the liquid phase is also constant in time.

The density of gases is highly dependent on temperature as well as on pressure.

Viscosity Viscosity is a measure for the resistance of a fluid to deformation under shear stress. For Newtonian fluids, the fluid shear stress τ is proportional to the temporal deformation of an angle γ, namely, $\tau = \mu\,\partial\gamma/\partial t$. The proportionality factor μ is called dynamic viscosity with the SI unit $\mathrm{N}\cdot\mathrm{s}/\mathrm{m}^2 = \mathrm{kg}/(\mathrm{m}\cdot\mathrm{s})$. In general, the viscosity of liquid phases is primarily determined by their composition and by temperature. With increasing temperature, the viscosity of liquids decreases. Contrarily, the viscosity of gases increases with increasing temperature (see, for example, [Atki 94]).

Matrix Parameters

Porosity A porous medium consists of a solid matrix and the pores. The dimensionless ratio of the pore space within the REV to the total volume of the REV is defined as porosity ϕ,

$$\phi = \frac{\text{volume of pore space within the REV}}{\text{total volume of the REV}}. \tag{1.6}$$

If the solid matrix is assumed to be rigid, the porosity is constant and independent of temperature, pressure or other variables.

Intrinsic Permeability The intrinsic permeability characterizes the inverse of the resistance of the porous matrix to flow through that matrix. Depending on the matrix type, the permeability may have different values for different flow directions which in general yields a tensor $\mathbb{K}$ with the unit m^2.

Parameters Describing Fluid-Matrix Interaction

Saturation The pore space is divided and filled by the different phases. In the macroscopic approach, this is expressed by the saturation of each phase α. This dimensionless number is defined as the ratio of the volume of phase α within the REV to the volume of the pore space within the REV:

$$S_\alpha = \frac{\text{volume of phase } \alpha \text{ within the REV}}{\text{volume of the pore space within the REV}}. \tag{1.7}$$

Assuming that the pore space of the REV is completely filled by the fluid phases α, the sum of the phase saturations must be equal to one,

$$\sum_\alpha S_\alpha = 1. \tag{1.8}$$

If no phase transition occurs, the saturations change due to displacement of one phase by another phase. However, a phase can in general not be fully displaced by another, but a certain saturation will be held back, which is called *residual saturation* . For a wetting phase, a residual saturation occurs if parts of the displaced wetting phase are held back in the finer pore channels during the drainage process (see Figure 1.7, left hand side). On the other side, a residual saturation for the non-wetting phase may occur if bubbles of the displaced non-wetting phase are trapped by surrounding wetting phase during the imbibition process (see Figure 1.7, right hand side). Therefore, a residual saturation may

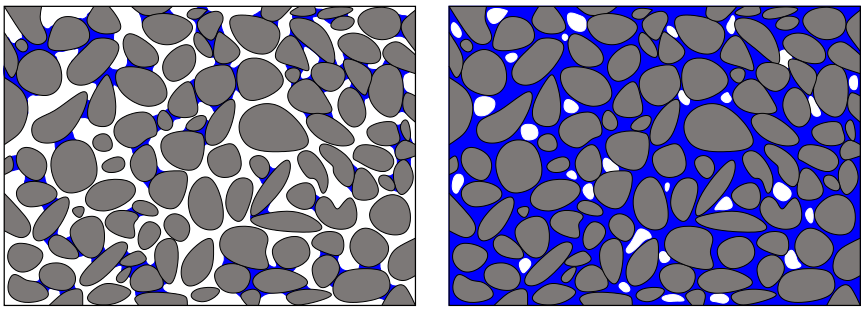

Figure 1.7: Residual saturations of the wetting and non-wetting phase, respectively

depend on the pore geometry, the heterogeneity and the displacement process, but also on the number of drainage and imbibition cycles. If the saturation of a phase S_α is smaller than its residual saturation, the relative permeability (Section 1.3.1) of phase α is equal to zero which means that no flux of that phase can take place. This implies that a flux can only occur, if the saturation of a phase α lies between the residual saturation and unity ($S_{r\alpha} \leq S_\alpha \leq 1$). With the residual saturation, an effective saturation for a two phase system can be defined in the following way:

$$S_e = \frac{S_w - S_{rw}}{1 - S_{rw}}, \qquad S_{rw} \leq S_w \leq 1. \tag{1.9}$$

Alternatively, in many models the following definition is used:

$$S_e = \frac{S_w - S_{rw}}{1 - S_{rw} - S_{rn}}, \qquad S_{rw} \leq S_w \leq 1 - S_{rn}. \tag{1.10}$$

Which definition has to be used, depends on the way the capillary pressure and the relative permeability curves are obtained, as explained below. Further considerations on the use of effective saturations are made in [Helm 97].

Capillarity Due to interfacial tension, forces occur at the interface of two phases. This effect is caused by interactions of the fluids on the molecular scale. Therefore, the interface between a wetting and a non-wetting phase is curved and the equilibrium at the interface leads to a pressure difference between the phases called capillary pressure p_c:

$$p_c = p_n - p_w, \tag{1.11}$$

where p_n is the non-wetting phase and p_w the wetting phase pressure. In a macroscopic consideration, an increase of the non-wetting phase saturation leads to a decrease of the wetting phase saturation, and, according to microscopic considerations, to the retreat of the wetting fluid to smaller pores. It is common to regard the macroscopic capillary pressure as a function of the saturation,

$$p_c = p_c(S_w), \tag{1.12}$$

the so-called capillary pressure-saturation relation. The simplest way to define a capillary pressure-saturation function is a linear approach:

$$p_c(S_e(S_w)) = p_{c,max}(1 - S_e(S_w)). \tag{1.13}$$

The most common p_c-S_w-relations for a twophase system are those of Brooks and Corey and van Genuchten .

In the Brooks–Corey model,

$$p_c(S_e(S_w)) = p_d S_e(S_w)^{-\frac{1}{\lambda}}, \qquad p_c \leq p_d, \tag{1.14}$$

the capillary pressure is a function of the effective Saturation S_e. The entry pressure p_d represents the minimum pressure needed for a non-wetting fluid to enter a porous medium initially saturated by a wetting fluid. The parameter λ is called pore-size distribution index and usually lies between 0.2 and 3.0. A very small λ-parameter describes a single size material, while a very large parameter indicates a highly non-uniform material.

The parameters of the Brooks–Corey relation are determined by fitting to experimental data. The effective saturation definition which is used in this parameter fitting is also the one to choose for later application of the respective capillary pressure or relative permeability function.

Relative Permeability Flow in porous media is strongly influenced by the interaction between the fluid phase and the solid phase. If more than one fluid phase fill the pore space, the presence of one phase also disturbs the flow behavior of another phase. Therefore, the relative permeability $k_{r\alpha}$ which can be considered as a scaling factor is included into the permeability concept. Considering a two fluid phase system, the space available for one of the fluids depends on the amount of the second fluid within the system. The wetting phase, for example, has to flow around those parts of the porous medium occupied by non-wetting fluid, or has to displace the non-wetting fluid to find new flow paths. In a macroscopic view, this means that the cross-sectional area available for the flow of a phase is depending on its saturation. If the disturbance of the flow of one phase is only due to the restriction of available pore volume caused by the presence of the other fluid, a linear correlation for the relative permeability can be applied,

$$k_{rw}(S_e(S_w)) = S_e(S_w), \tag{1.15}$$

$$k_{rn}(S_e(S_w)) = 1 - S_e(S_w). \tag{1.16}$$

This formulation also implies that the relative permeability becomes zero if the residual saturation, representing the amount of immobile fluid, is reached.

In reality, one phase usually not only influences the flow of another phase just by the restriction in available volume, but also by additional interactions between the fluids. If capillary effects occur, the wetting phase, for example, fills the smaller pores if the saturation is small. This means that in case of an increasing saturation of the wetting phase, the relative permeability k_{rw} has to increase slowly if the saturations are still small and it has to increase fast if the saturations become higher, since then the wetting phase begins to fill the larger pores. For the non-wetting phase the opposite situation is the case. Increasing the saturation, the larger pores are filled at first causing a faster rise of k_{rn}. At higher saturations the smaller pores become filled which slows down the increase of the relative permeability. Therefore, correlations for the relative permeabilities can be defined using the known capillary pressure-saturation relationships (see [Helm 97] for details). Besides capillary pressure effects also other effects might occur.

As an example, the Brooks–Corey model is defined as

$$k_{\mathrm{rw}}(S_{\mathrm{e}}(S_{\mathrm{w}})) = S_{\mathrm{e}}(S_{\mathrm{w}})^{\frac{2+3\lambda}{\lambda}}, \tag{1.17}$$

$$k_{\mathrm{rn}}(S_{\mathrm{e}}(S_{\mathrm{w}})) = (1 - S_{\mathrm{e}}(S_{\mathrm{w}}))^2 \left(1 - S_{\mathrm{e}}(S_{\mathrm{w}})^{\frac{2+\lambda}{\lambda}}\right), \tag{1.18}$$

where λ is the empirical constant from the Brooks–Corey $p_{\mathrm{c}}(S)$-relationship (Equation 1.14). These relative permeabilities do not sum up to unity as for the linear relationship. This is caused by the effects described before, and means that one phase is slowed down stronger by the other phase as it would be only due to the restricted volume available for the flow.

Extended Darcy's Law

In a macroscopic treatment (we are on our fine scale) of porous media, Darcy's law, which was originally obtained experimentally for single phase flow, can be used to calculate averaged velocities using the permeability. For multi-phase systems, extended Darcy's law incorporating relative permeabilities is formulated for each phase (see [Helm 97, Sche 74] for details):

$$\mathbf{v}_\alpha = \frac{k_{\mathrm{r}\alpha}}{\mu_\alpha}\mathbb{K}(-\,\mathbf{grad}\, p_\alpha + \varrho_\alpha \mathbf{g}), \tag{1.19}$$

where $k_{\mathrm{r}\alpha}$ is the relative permeability dependent on saturation, and $\mathbb{K}$ the intrinsic permeability dependent on the porous medium, μ_α the dynamic fluid viscosity, p_α the phase pressure and ϱ_α the phase density, while $\mathbf{g}$ is the gravity vector. The mobility of a phase is defined as $\lambda_\alpha = k_{\mathrm{r}\alpha}/\mu_\alpha$. Note that in equation (1.19), the pressure in phase α is used which is important, since the pressure of different phases can differ due to capillarity. The product of the relative and the intrinsic permeability $k_{\mathrm{r}\alpha}\mathbb{K}$ is often called total permeability $\mathbb{K}_{\mathrm{t}}$ or effective permeability $\mathbb{K}_{\mathrm{e}}$.

Laws for Fluid-Phase Equilibria

We give a short summary of common physical relationships, which govern the equilibrium state between fluid phases and thus, the mass transfer processes, i.e. the exchange of components between phases. While a variety of other relationships can be found in literature, only Dalton's law, Raoult's law, as well as Henry's law are treated here.

Dalton's Law Dalton's Law states that the total pressure of a gas mixture equals the sum of the pressures of the gases that make up the mixture, namely,

$$p_{\mathrm{g}} = \sum_{\kappa} p_{\mathrm{g}}^{\kappa}, \tag{1.20}$$

where p_{g}^{κ} is the pressure of a single component κ, the partial pressure, which is by definition the product of the mole fraction of the respective component in the gas phase and the total pressure of the gas phase, i.e.,

$$p_{\mathrm{g}}^{\kappa} = x_{\mathrm{g}}^{\kappa} p_{\mathrm{g}}. \tag{1.21}$$

Raoult's Law Raoult's law describes the lowering of the vapor pressure of a pure substance in a solution. It relates the vapor pressure of components to the composition of the solution under the simplifying assumption of an ideal solution. The relationship can be derived from the equality of fugacities, see [Prau 67]. According to Raoult's law, the vapor pressure of a solution of component κ is equal to the vapor pressure of the pure substance times the mole fraction of component κ in phase α.

$$p_{\mathrm{g}}^{\kappa} = x_{\alpha}^{\kappa} p_{\mathrm{vap}}^{\kappa} \tag{1.22}$$

Here, $p_{\mathrm{vap}}^{\kappa}$ denotes the vapor pressure of pure component κ which is generally a function of temperature.

Henry's Law Henry's law is valid for ideally diluted solutions and ideal gases. It is especially used for the calculation of the solution of gaseous components in liquids. Considering a system with gaseous component κ, a linear relationship between the mole fraction x_{α}^{κ} of component κ in the liquid phase and the partial pressure p_{g}^{κ} of κ in the gas phase is obtained,

$$x_{\alpha}^{\kappa} = H_{\alpha}^{\kappa} p_{\mathrm{g}}^{\kappa}. \tag{1.23}$$

The parameter H_{α}^{κ} denotes the Henry coefficient of component κ in phase α, which is dependent on temperature, $H_{\alpha}^{\kappa} = H_{\alpha}^{\kappa}(T)$.

Figure 1.8 shows the range of applicability of both Henry's law and Raoult's law for a binary system, where component 1 is a component forming a liquid phase, for example, water, and component 2 is a component forming a gaseous phase, for example, air. One can see that for low mole fractions of component 2 in the system (small amounts of dissolved air in the liquid phase), Henry's law can be applied whereas for mole fractions of component 1 close to 1 (small amounts of vapor in the gas phase), Raoult's law is the appropriate description. In general, the solvent follows Raoult's law as it is present in excess, whereas the dissolved substance follows Henry's law as it is highly diluted.

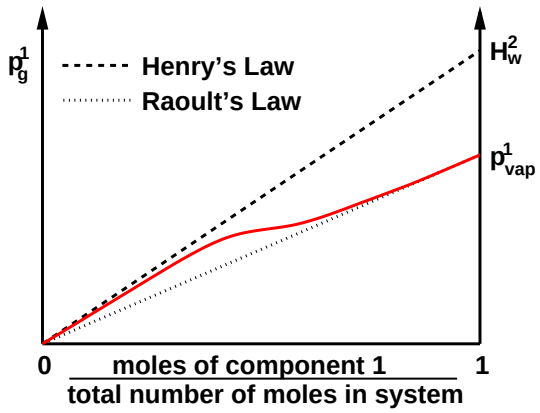

Figure 1.8: Applicability of Henry's law and Raoult's law for a binary gas–liquid system (after [Lude 00]).

The Reynolds Transport Theorem

A common way to derive balance equations in fluid dynamics is to use the Reynolds transport theorem, (for example, [Whit 03, Helm 97]), named after the British scientist Osborne

Reynolds. Let E be an arbitrary property of the fluid (for example, mass, energy, momentum) that can be obtained by the integration of a scalar field e over a moving control volume V,

$$E = \int_V e \, \mathrm{d}V \, . \tag{1.24}$$

The Reynolds transport theorem states that the temporal derivative of the property in a control volume moving with the fluid can be related to local changes of the scalar field by

$$\frac{\mathrm{d}E}{\mathrm{d}t} = \frac{\mathrm{d}}{\mathrm{d}t} \int_V e \, \mathrm{d}V = \int_V \frac{\partial e}{\partial t} + \operatorname{div}(e\mathbf{v}) \, \mathrm{d}V. \tag{1.25}$$

For a general balance equation, we require a conservation of the property E. Thus the property can only change due to sinks and sources, diffusion or dissipation:

$$\frac{\mathrm{d}E}{\mathrm{d}t} = \int_V \frac{\partial e}{\partial t} + \operatorname{div}(e\mathbf{v}) \, \mathrm{d}V = \int_V q^{\mathrm{e}} - \operatorname{div} \mathbf{w} \, \mathrm{d}V, \tag{1.26}$$

where $\mathbf{w}$ is the diffusive flux of e and q^{e} is the source per unit volume.

1.3.2 Multi-Phase Flow

We derive the mass balance equations for the immiscible and the compositional case. Both derivations are based on the general balance equation (1.26) and the insertion of extended Darcy's law (1.19) for the involved velocities.

The Immiscible Case

According to the specifications provided in Section 1.3.1, the mass of a phase α inside a control volume V can be expressed by

$$m_\alpha = \int_V \phi S_\alpha \varrho_\alpha \, \mathrm{d}V. \tag{1.27}$$

Under the assumption that the phases are immiscible, the total mass $m_\alpha = \int_V m_\alpha \, \mathrm{d}V$ is conserved, i.e. $\mathrm{d}m_\alpha / \mathrm{d}t = 0$ in the absence of external sources. Using the general balance equation (1.26), this mass conservation can be rewritten as

$$\int_V \frac{\partial (\phi \varrho_\alpha S_\alpha)}{\partial t} + \operatorname{div}(\phi S_\alpha \varrho_\alpha \mathbf{v}_{a\alpha}) \, \mathrm{d}V = \int_V \varrho_\alpha q_\alpha \, \mathrm{d}V \, . \tag{1.28}$$

We emphasize that the diffusive flux is assumed to be zero, since for the motion of phases on an REV scale, no diffusion or dispersion processes are considered. Coarse-scale approaches may, however, include additional dispersive terms to counterbalance the loss of fine-scale informations on the coarse scale. The control volume considered for the transport theorem moves with $\mathbf{v}_{a\alpha}$, which is related to the Darcy velocity $\mathbf{v}_\alpha$ by

$$\mathbf{v}_\alpha = \phi S_\alpha \mathbf{v}_{a\alpha}. \tag{1.29}$$

Inserting (1.29) into (1.28) yields the integral balance equation for a single phase α in a multi-phase system

$$\int_V \frac{\partial\left(\phi\varrho_\alpha S_\alpha\right)}{\partial t} + \operatorname{div}\left(\varrho_\alpha \mathbf{v}_\alpha\right) \mathrm{d}V = \int_V \varrho_\alpha q_\alpha \,\mathrm{d}V \,, \tag{1.30}$$

Rewriting this equation in differential form and inserting extended Darcy's law (1.19) yields a system of n_α partial differential equations (with n_α the number of phases),

$$\frac{\partial\left(\phi\varrho_\alpha S_\alpha\right)}{\partial t} = -\operatorname{div}\left(\varrho_\alpha \lambda_\alpha \mathbb{K}\left(-\mathbf{grad}\, p_\alpha + \varrho_\alpha \mathbf{g}\right)\right) + \varrho_\alpha q_\alpha. \tag{1.31}$$

Under isothermal conditions, the system (1.31) of n_α partial differential equations is already closed. In particular, the parameters ϕ, $\mathbb{K}$, $\mathbf{g}$ are intrinsic, and q_α are given source terms. The densities ϱ_α are functions of pressure and the known temperature only, and the mobilities λ_α only depend on the phase saturations. The remaining n_α constitutive relations for the $2n_\alpha$ unknowns S_α, p_α are the closure relation (1.8) and the $n_\alpha - 1$ capillary pressure-saturation relationships (1.12).

The Compositional Case

We now allow that each phase is made up of different components which can also be partially dissolved in the other phases. Inserting the total concentration per component,

$$C^\kappa = \phi \sum_\alpha \varrho_\alpha S_\alpha X_\alpha^\kappa, \tag{1.32}$$

into the general balance equation (1.26), and applying the same considerations on the velocities as in Section 1.3.2 yields

$$\int_V \frac{\partial C^\kappa}{\partial t} + \sum_\alpha \operatorname{div}\left(\varrho_\alpha X_\alpha^\kappa \mathbf{v}_\alpha\right) \mathrm{d}V = \int_V q^\kappa \,\mathrm{d}V \,, \tag{1.33}$$

Rewriting this in differential form and inserting the extended Darcy law (1.19), we obtain a set of n^κ partial differential equations (with n^κ the number of components),

$$\frac{\partial C^\kappa}{\partial t} = -\sum_\alpha \operatorname{div}\left(\varrho_\alpha X_\alpha^\kappa \lambda_\alpha \mathbb{K}\left(-\mathbf{grad}\, p_\alpha + \varrho_\alpha \mathbf{g}\right)\right) + q^\kappa. \tag{1.34}$$

We remark that the immiscible case (1.31) can be easily derived from (1.34) as a special case. In particular, immiscibility can be equally expressed as X_α^κ being known and constant with respect to space and time. By eventually regrouping and renaming the components with respect to the fixed phase compositions, we can furthermore assume that each component is associated with a distinct phase and $X_\alpha^\kappa = 1$ holds for this particular phase α, whereas it equals zero for all other phases. This directly leads to (1.31).

In general, we are left with n^κ partial differential equations (1.34) for the $2n_\alpha + n^\kappa n_\alpha$ unknowns $p_\alpha, S_\alpha, X_\alpha^\kappa$. Considering (1.8) and (1.12) as in the immiscible case, and additionally the closure relations (1.2), yields $2n_\alpha$ constraints. The remaining $n^\kappa(n_\alpha - 1)$ constraints have to be carefully chosen from the laws for fluid phase equilibria, see Section 1.3.1.

1.3.3 Decoupled Formulations

It is often advantageous to reformulate the mass balance equations (1.31) or (1.34) into one elliptic or parabolic equation for the pressure and one or more hyperbolic-parabolic transport equations for the saturations or concentrations, respectively. In particular, this reformulation allows to employ multi-scale or discretization approaches which are especially developed and suited for the corresponding type of equation, and to combine them in various ways. Furthermore, a sequential or iterative solution procedure reduces the amount of unknowns in each solution step. In the following, we introduce these decoupled formulations for the immiscible and for the miscible case.

The Immiscible Case

The reformulation of the multi-phase mass balance equations (1.31) into one pressure equation and one or more saturation equations was primarily derived in [Chav 76], where the author just called it *a new formulation* for two-phase flow in porous media. Due to the introduction of the idea of fractional flows this formulation is usually called fractional flow formulation.

Pressure Equation A pressure equation can be derived by summation of the phase mass balance equations. After some reformulation, a general pressure equation can be written as follows:

$$\sum_\alpha S_\alpha \frac{\partial \phi}{\partial t} + \operatorname{div} \mathbf{v}_\mathrm{t} + \sum_\alpha \frac{1}{\varrho_\alpha} \left(\phi S_\alpha \frac{\partial \varrho_\alpha}{\partial t} + \mathbf{v}_\alpha \cdot \mathbf{grad}\, \varrho_\alpha \right) - \sum_\alpha q_\alpha = 0, \tag{1.35}$$

with the following definition of a total velocity:

$$\mathbf{v}_\mathrm{t} = \sum_\alpha \mathbf{v}_\alpha. \tag{1.36}$$

Inserting extended Darcy's law (1.19) into (1.36) yields

$$\mathbf{v}_\mathrm{t} = -\lambda_\mathrm{t} \mathbb{K} \left(\sum_\alpha f_\alpha \mathbf{grad}\, p_\alpha - \sum_\alpha f_\alpha \varrho_\alpha \mathbf{g} \right). \tag{1.37}$$

where $f_\alpha = \lambda_\alpha / \lambda_\mathrm{t}$ is the fractional flow function of phase α and $\lambda_\mathrm{t} = \sum_\alpha \lambda_\alpha$ is the total mobility. In the following, different possibilities to reformulate this general pressure equation for two-phase flow are shown. There also exist fractional flow approaches for three phases, which are not further considered here. For details, we refer to, for example, [Suk 08].

Global Pressure Formulation for Two-Phase Flow Defining a global pressure p such that $\mathbf{grad}\, p = \sum_\alpha f_\alpha \mathbf{grad}\, p_\alpha$ (see below), equation (1.37) can be rewritten as a function of p:

$$\mathbf{v}_\mathrm{t} = -\lambda_\mathrm{t} \mathbb{K} \left(\mathbf{grad}\, p - \sum_\alpha f_\alpha \varrho_\alpha \mathbf{g} \right) \tag{1.38}$$

Inserting (1.38) into (1.35) yields the pressure equation related to the global pressure.

For a domain Ω with boundary $\Gamma = \Gamma_\mathrm{D} \cup \Gamma_\mathrm{N}$, where Γ_D denotes a Dirichlet and Γ_N a Neumann boundary, the boundary conditions are:

$$\begin{aligned} p &= p_\mathrm{D} \quad \text{on} \quad \Gamma_\mathrm{D} \qquad \text{and} \\ \mathbf{v}_\mathrm{t} \cdot \mathbf{n} &= q_\mathrm{N} \quad \text{on} \quad \Gamma_\mathrm{N}. \end{aligned} \tag{1.39}$$

This means that a global pressure has to be found on a Dirichlet boundary which can lead to problems, as the global pressure is no physical variable and thus can not be measured directly. Following [Chav 86], the global pressure is defined by

$$p = \frac{1}{2}\left(p_\mathrm{w} + p_\mathrm{n}\right) - \int_{S_\mathrm{c}}^{S_\mathrm{w}} \left(f_\mathrm{w}(S_\mathrm{w}) - \frac{1}{2}\right) \frac{\mathrm{d}p_\mathrm{c}}{\mathrm{d}S_\mathrm{w}}(S_\mathrm{w})\, \mathrm{d}S_\mathrm{w}, \tag{1.40}$$

where S_c is the saturation satisfying $p_\mathrm{c}(S_\mathrm{c}) = 0$. This definition makes sure that the global pressure is a smooth function and thus is easier to handle from a numerical point of view. However, as shown, for example, in [Binn 99], an iterative solution technique is required for more complex (realistic) conditions, where a phase pressure might be known at a boundary. It becomes also clear, that $p = p_\mathrm{w} = p_\mathrm{n}$, if the capillary pressure between the phases is neglected.

Phase Pressure Formulation for Two-Phase Flow A pressure equation can also be further derived using a phase pressure which is a physically meaningful parameter in a multi-phase system. Investigations of a phase pressure fractional flow formulation can for example be found in [Chen 06c] and a formulation including phase potentials has been used in [Hote 08].

Exploiting equation (1.11), equation (1.37) can be rewritten in terms of one phase pressure. This yields a total velocity in terms of the wetting phase pressure as:

$$\mathbf{v}_\mathrm{t} = -\lambda_\mathrm{t}\mathbb{K}\left(\mathbf{grad}\, p_\mathrm{w} + f_\mathrm{n}\, \mathbf{grad}\, p_\mathrm{c} - \sum_\alpha f_\alpha \varrho_\alpha \mathbf{g}\right), \tag{1.41}$$

and in terms of a non-wetting phase pressure as:

$$\mathbf{v}_\mathrm{t} = -\lambda_\mathrm{t}\mathbb{K}\left(\mathbf{grad}\, p_\mathrm{n} - f_\mathrm{w}\, \mathbf{grad}\, p_\mathrm{c} - \sum_\alpha f_\alpha \varrho_\alpha \mathbf{g}\right), \tag{1.42}$$

Substituting $\mathbf{v}_t$ in the general pressure equation (1.35) by equation (1.41) or (1.42) yields the pressure equations as function of a phase pressure.

In analogy to the global pressure formulation, the following boundary conditions can be defined:

$$\begin{aligned} p_\mathrm{w} &= p_\mathrm{D} \quad \text{on} \quad \Gamma_\mathrm{D} \qquad \text{or} \\ p_\mathrm{n} &= p_\mathrm{D} \quad \text{on} \quad \Gamma_\mathrm{D} \qquad \text{and} \\ \mathbf{v}_\mathrm{t} \cdot \mathbf{n} &= q_\mathrm{N} \quad \text{on} \quad \Gamma_\mathrm{N}. \end{aligned} \tag{1.43}$$

It is important to point out that we now have a physically meaningful variable, the phase pressure, instead of the global pressure. So boundary conditions at Dirichlet boundaries can be defined directly, if a phase pressure at a boundary is known.

Saturation Equation We derive the transport equation for the saturation depending on whether a global or a phase pressure formulation is used. In the first case, a possibly degenerated parabolic-hyperbolic equation is derived, which is quite weakly coupled to the pressure equation. In the second case, a purely hyperbolic equation is obtained with a stronger coupling to the corresponding pressure equation.

Global Pressure formulation for Two-Phase Flow In the case of a global pressure formulation a transport equation for saturation related to the total velocity $\mathbf{v}_t$ has to be derived from the general multi-phase mass balance equations (1.35). With the definition of the capillary pressure (1.11), the extended Darcy's law (1.19) can be formulated for a wetting and a non-wetting phase as:

$$\mathbf{v}_{\mathrm{w}} = -\lambda_{\mathrm{w}}\mathbb{K}(\mathbf{grad}\, p_{\mathrm{w}} - \varrho_{\mathrm{w}}\mathbf{g}) \tag{1.44}$$

and

$$\mathbf{v}_{\mathrm{n}} = -\lambda_{\mathrm{n}}\mathbb{K}(\mathbf{grad}\, p_{\mathrm{w}} + \mathbf{grad}\, p_{\mathrm{c}} - \varrho_{\mathrm{w}}\mathbf{g}). \tag{1.45}$$

Solving (1.45) for $\mathbb{K}\,\mathbf{grad}\, p_{\mathrm{w}}$ and inserting it into Equation (1.44) yields:

$$\mathbf{v}_{\mathrm{w}} = \frac{\lambda_{\mathrm{w}}}{\lambda_{\mathrm{n}}}\mathbf{v}_{\mathrm{n}} + \lambda_{\mathrm{w}}\mathbb{K}\left(\mathbf{grad}\, p_{\mathrm{c}} + (\varrho_{\mathrm{w}} - \varrho_{\mathrm{n}})\mathbf{g}\right). \tag{1.46}$$

With $\mathbf{v}_{\mathrm{n}} = \mathbf{v}_{\mathrm{t}} - \mathbf{v}_{\mathrm{w}}$, (1.46) can be reformulated as the fractional flow equation for $\mathbf{v}_{\mathrm{w}}$:

$$\mathbf{v}_{\mathrm{w}} = \frac{\lambda_{\mathrm{w}}}{\lambda_{\mathrm{w}} + \lambda_{\mathrm{n}}}\mathbf{v}_{\mathrm{t}} + \frac{\lambda_{\mathrm{w}}\lambda_{\mathrm{n}}}{\lambda_{\mathrm{w}} + \lambda_{\mathrm{n}}}\mathbb{K}\left(\mathbf{grad}\, p_{\mathrm{c}} + (\varrho_{\mathrm{w}} - \varrho_{\mathrm{n}})\mathbf{g}\right), \tag{1.47}$$

which can be further inserted into the wetting phase mass balance equation leading to a transport equation for the wetting phase saturation related to $\mathbf{v}_{\mathrm{t}}$:

$$\frac{\partial(\phi\varrho_{\mathrm{w}}S_{\mathrm{w}})}{\partial t} + \operatorname{div}\left(\varrho_{\mathrm{w}}\left(f_{\mathrm{w}}\mathbf{v}_{\mathrm{t}} + f_{\mathrm{w}}\lambda_{\mathrm{n}}\mathbb{K}\left(\mathbf{grad}\, p_{\mathrm{c}} + (\varrho_{\mathrm{w}} - \varrho_{\mathrm{n}})\mathbf{g}\right)\right)\right) - \varrho_{\mathrm{w}}q_{\mathrm{w}} = 0. \tag{1.48}$$

Some terms of (1.48) can be reformulated in dependence on the saturation (see [Helm 97] for details). For incompressible fluids and a porosity which does not change in time, the saturation equation of a two-phase system can then be formulated showing the typical character of a transport equation as

$$\begin{aligned}\phi\frac{\partial S_{\mathrm{w}}}{\partial t} + \left(\mathbf{v}_{\mathrm{t}}\frac{\mathrm{d}f_{\mathrm{w}}}{\mathrm{d}S_{\mathrm{w}}} + \frac{\mathrm{d}(f_{\mathrm{w}}\lambda_{\mathrm{n}})}{\mathrm{d}S_{\mathrm{w}}}\mathbb{K}(\varrho_{\mathrm{w}} - \varrho_{\mathrm{n}})\mathbf{g}\right)\cdot\mathbf{grad}\, S_{\mathrm{w}} \\ + \operatorname{div}\left(\bar{\lambda}\mathbb{K}\frac{\mathrm{d}p_{\mathrm{c}}}{\mathrm{d}S_{\mathrm{w}}}\,\mathbf{grad}\, S_{\mathrm{w}}\right) - q_{\mathrm{w}} + f_{\mathrm{w}}q_{\mathrm{t}} &= 0,\end{aligned} \tag{1.49}$$

where $q_{\mathrm{t}} = q_{\mathrm{w}} + q_{\mathrm{n}}$.

Similarly, an equation for the non-wetting phase saturation can be derived which can be written in its final form as:

$$\frac{\partial(\phi\varrho_{\mathrm{n}}S_{\mathrm{n}})}{\partial t} + \operatorname{div}\left(\varrho_{\mathrm{n}}\left(f_{\mathrm{n}}\mathbf{v}_{\mathrm{t}} - f_{\mathrm{n}}\lambda_{\mathrm{w}}\mathbb{K}\left(\mathbf{grad}\, p_{\mathrm{c}} - (\varrho_{\mathrm{n}} - \varrho_{\mathrm{w}})\mathbf{g}\right)\right)\right) - \varrho_{\mathrm{n}}q_{\mathrm{n}} = 0. \tag{1.50}$$

Phase Pressure Formulation for Two-Phase Flow Obviously, for the phase pressure formulation the saturation can be calculated directly from the mass balance equations (1.35), leading to

$$\frac{\partial\left(\phi\varrho_{\mathrm{w}}S_{\mathrm{w}}\right)}{\partial t}+\operatorname{div}(\varrho_{\mathrm{w}}\mathbf{v}_{\mathrm{w}})=q_{\mathrm{w}} \tag{1.51}$$

for the wetting phase of a two-phase system and to

$$\frac{\partial\left(\phi\varrho_{\mathrm{n}}S_{\mathrm{n}}\right)}{\partial t}+\operatorname{div}(\varrho_{\mathrm{n}}\mathbf{v}_{\mathrm{n}})=q_{\mathrm{n}}, \tag{1.52}$$

where the phase velocities can be calculated using extended Darcy's law.

A nice feature of the global pressure formulation is that the two equations (pressure equation and saturation equation) are only weakly coupled through the presence of the total mobility and the fractional flow functions in the pressure equation. These are dependent on the relative permeabilities of the phases and thus dependent on the saturation. This also holds for the phase pressure formulation. However, in this formulation the coupling is strengthened again due to the additional capillary pressure term in the pressure equation.

The Compositional Case

Similarly to the fractional flow formulations for immiscible multi-phase flow, decoupled formulations for compositional flow have been developed. However, dissolution and phase changes of components affect the volume of mixtures, compromising the assumption of a divergence-free total velocity field. In [Acs 85, Tran 89], a pressure equation for compositional flow in porous media based on volume conservation is presented. The derivation as done in [Odyc 08] is based on the constraint that the pore space always has to be filled by some fluid i.e., the volume of the fluid mixture $v_{\mathrm{t}}=\sum_{\alpha}v_{\alpha}[\mathrm{m}^3/\mathrm{m}^3]$ has to equal the pore volume,

$$v_{\mathrm{t}}=\phi\,. \tag{1.53}$$

To capture transient processes, both sides of the volume balance are approximated in time by a Taylor series:

$$v_{\mathrm{t}}\left(t\right)+\Delta t\frac{\partial v_{\mathrm{t}}}{\partial t}+\mathcal{O}\left(\Delta t^2\right)=\phi\left(t\right)+\Delta t\frac{\partial\phi}{\partial t}+\mathcal{O}\left(\Delta t^2\right)\,. \tag{1.54}$$

In the isothermal case, the fluid volume changes in time if there are variations of pressure or a change of mass. If latter is expressed in terms of the total concentration C^{κ} as introduced in Equation 1.32, we get

$$\frac{\partial v_{\mathrm{t}}}{\partial t}=\frac{\partial v_{\mathrm{t}}}{\partial p}\frac{\partial p}{\partial t}+\sum_{\kappa}\frac{\partial v_{\mathrm{t}}}{\partial C^{\kappa}}\frac{\partial C^{\kappa}}{\partial t}\,, \tag{1.55}$$

Inserting equation (1.55) in (1.54), neglecting the higher order terms, reordering under the assumption of an incompressible porous medium $\frac{\partial\phi}{\partial t}=0$ yields

$$\frac{\partial v_{\mathrm{t}}}{\partial p}\frac{\partial p}{\partial t}+\sum_{\kappa}\frac{\partial v_{\mathrm{t}}}{\partial C^{\kappa}}\frac{\partial C^{\kappa}}{\partial t}=\frac{\phi-v_{\mathrm{t}}}{\Delta t}\,. \tag{1.56}$$

For the change of total concentration in time, we include the compostional conservation equation 1.34. The term on the ride side in Equation 1.56 arises if non-iterated secondary

variables such as density lead to minor violations of Equation 1.53. Details on the treatment of this term of volume error can be found in [Frit 12, Pau 12].

1.3.4 Non-Isothermal Flow

The consideration of non-isothermal flow processes involves an additional conservation property: energy. This is expressed as internal energy inside a unit volume which consists of the internal energies of the matrix and the fluids:

$$U = \int_V \phi \sum_\alpha \left(\varrho_\alpha S_\alpha u_\alpha\right) + \left(1-\phi\right) \varrho_\mathrm{s} c_\mathrm{s} T \, \mathrm{d}V \,, \tag{1.57}$$

where the internal energy is assumed to be a linear function of temperature T above a reference point. Then c_s denotes the heat capacity of the rock and u_α is the specific internal energy of phase α. The internal energy in a system is increased by heat fluxes into the system and by mechanical work done on the system

$$\frac{\mathrm{d}U}{\mathrm{d}t} = \frac{\mathrm{d}Q}{\mathrm{d}t} + \frac{\mathrm{d}W}{\mathrm{d}t} \,. \tag{1.58}$$

Heat flows over the control volume boundaries by conduction, which is a linear function of the temperature gradient and occurs in direction of falling temperatures

$$\frac{\mathrm{d}Q}{\mathrm{d}t} = \int_\Gamma -\mathbf{n} \cdot \left(-\lambda_\mathrm{s} \, \mathbf{grad}\, T\right) \mathrm{d}\Gamma = \int_V \mathrm{div}\left(\lambda_\mathrm{s} \, \mathbf{grad}\, T\right) \mathrm{d}V \,. \tag{1.59}$$

The mechanical work done by the system (and therefore decreasing its energy) is volume changing work. It is done when fluids flows over the control volume boundaries against a pressure p

$$\frac{\mathrm{d}W}{\mathrm{d}t} = \int_\Gamma -p \left(\mathbf{n} \cdot \mathbf{v}\right) \mathrm{d}\Gamma = \int_V -\mathrm{div}\left(p\mathbf{v}\right) \mathrm{d}V \,. \tag{1.60}$$

The left hand side of equation (1.58) can be expressed by the Reynolds transport theorem, where the velocity of the solid phase equals zero,

$$\frac{\mathrm{d}U}{\mathrm{d}t} = \int_V \frac{\partial}{\partial t} \left(\phi \sum_\alpha \left(\varrho_\alpha S_\alpha u_\alpha\right) + \left(1-\phi\right) \varrho_\mathrm{s} c_\mathrm{s} T \right) \mathrm{d}V + \int_\Gamma \mathbf{n} \cdot \sum_\alpha \left(\varrho_\alpha u_\alpha \mathbf{v}_\alpha\right) \mathrm{d}\Gamma. \tag{1.61}$$

Using the definition of specific enthalpy $h = u + p/\varrho$, the second term on the right hand side of equation (1.61) and the right hand side of equation (1.60) can be combined and equation (1.58) can be rewritten to

$$\int_V \frac{\partial}{\partial t} \left(\phi \sum_\alpha \left(\varrho_\alpha S_\alpha u_\alpha\right) + \left(1-\phi\right) \varrho_\mathrm{s} c_\mathrm{s} T \right) \mathrm{d}V = \int_\Gamma \mathbf{n} \cdot \left(\lambda_\mathrm{s} \, \mathbf{grad}\, T - \sum_\alpha \left(\varrho_\alpha h_\alpha \mathbf{v}_\alpha\right) \right) \mathrm{d}\Gamma \tag{1.62}$$

or in differential form as

$$\frac{\partial}{\partial t} \left(\phi \sum_\alpha \left(\varrho_\alpha S_\alpha u_\alpha\right) + \left(1-\phi\right) \varrho_\mathrm{s} c_\mathrm{s} T \right) = \mathrm{div} \left(\lambda_\mathrm{s} \, \mathbf{grad}\, T - \sum_\alpha \left(\varrho_\alpha h_\alpha \mathbf{v}_\alpha\right) \right) . \tag{1.63}$$

1.4 Numerical Solution Approaches

After establishing the continuous models, it remains to choose numerical discretization and solution schemes. We will only very briefly address this question for the fully coupled balance equations (1.31) or (1.34) in Section 1.4.1, our main emphasis here is on the decoupled systems, which will be treated in Section 1.4.2.

1.4.1 Solution of the Fully Coupled Equations

One possibility to calculate multi-phase flow is to directly solve the system of equations given by the balances (1.31) or (1.34). These mass balance equations are usually non-linear and strongly coupled. Thus, we also call this the *fully coupled* multi-phase flow formulation. After space discretization, the system of equations one has to solve can be written as:

$$\frac{\partial}{\partial t}\mathbf{M}(\underline{u}) + \mathbf{A}(\underline{u}) = \mathbf{R}(\underline{u}), \tag{1.64}$$

where $\mathbf{M}$ consists of the accumulation terms, $\mathbf{A}$ includes the internal flux terms and $\mathbf{R}$ is the right hand side vector which comprises Neumann boundary flux terms as well as source or sink terms. An implicit time discretization is applied to (1.64) that results in a *fully implicit* formulation. Usually, the implicit Euler method is chosen. All resulting equations have to be solved simultaneously due to the strong coupling. Therefore, a linearization technique has to be applied. The most common solution method is the Newton-Raphson algorithm [Aziz 89, Denn 96].

Advantages of the fully coupled formulation and the implicit method respectively are that it includes the whole range of physical effects (capillarity, gravity,...) without having additional effort; that it is quite stable; and that it is usually not very sensitive to the choice of the time step size. The disadvantage is that a global system of equations, which is twice as large as for a single phase pressure equation if two-phase flow is calculated (and even larger in the non-isothermal case or including more phases), has to be solved *several* times during each time step, dependent on the number of iterations the linearization algorithm needs to converge.

1.4.2 Solution of the Decoupled Equations

As before, we split our considerations into the immiscible and the miscible case.

The Immiscible Case

As their name implies, decoupled formulations decouple the system of equations of a multi-phase flow formulation to some extent. In the immiscible case, the result is an equation for pressure and additional transport equations for one saturation (see Section 1.3.3) in the case of two-phase flow or several saturations if more phases are considered. The new equations are still weakly coupled due to the saturation dependent parameters like relative permeabilities or capillary pressure in the pressure equation and the pressure dependent parameters like density and viscosity in the saturation transport equation. Nevertheless, in many cases it is possible to solve this system of equations sequentially. Numerically, this is usually done by using an IMPES scheme (IMplicit Pressure - Explicit Saturation), which was first introduced in [Shel 59, Ston 61]. Therefore, the pressure equation is solved

first implicitly. From the resulting pressure field the velocity field can be calculated and inserted into the saturation equation which is then solved explicitly.

One major advantage of the decoupled formulation is that it allows for different discretizations of the different equations. For the pressure equation, it is of utmost importance that its solution admits the calculation of a locally conservative velocity field. There are various discretization methods meeting this requirement, like finite volumes with two-point or multi-point flux approximation, [Aava 02, Aava 08, Cao 08, Eige 05, Klau 06b], mixed finite elements, [Alle 92, Brez 91, Huan 00, Mazz 06, Srin 92], or mimetic finite differences, [Bern 05, Brez 05a, Brez 05b, Hyma 02, Shas 96]. Moreover, it is also possible to use discretizations with non-conservative standard velocity fields, and employ a post-processing step to reconstruct a locally conservative scheme. This has been investigated for discontinuous Galerkin methods in [Bast 03], while for standard Lagrangian finite elements, it is possible to calculate equilibrated fluxes known from a posteriori error estimation, [Ains 00].

Similarly, there exists a variety of discretization methods for the solution of the transport equation(s), ranging from standard upwind finite volume approaches, [Eyma 00, LeVe 02], over higher order discontinuous Galerkin methods with slope limiter, [Cock 89a, Cock 89b, Ghos 09, Hote 04], the modified method of characteristics, [Chen 02, Daws 89, Doug 99, Ewin 84], and the Eulerian-Lagrangian localized adjoint method, [Ewin 94, Ewin 96, Herr 93, Russ 90, Wang 02], up to streamline methods [Juan 08b, Matr 06, Olad 08].

The IMPES scheme can be very efficient, since a system of equations with only n unknowns, where n is the number of degrees of freedom for the discretization of the pressure equation, has to be solved only once in the pressure step. In comparison, several solutions of a system of equations with m unknowns have to be calculated in the fully coupled scheme, where m is usually at least twice as large as n. However, there are strong restrictions with respect to the choice of the time step size. Stability analyses of the IMPES scheme can be found in, for example, [Aziz 79, Russ 89, Coat 03a, Coat 03b]. The scheme is conditionally stable if for each grid cell i

$$c_{\mathrm{CFL}} = \Delta t \frac{F_i}{\phi_i V_i} \leq 1 \tag{1.65}$$

where c_{CFL} is the CFL-number, Δt is the time-step size, V the volume of the cell and ϕ the porosity. The CFL-volume-flux F_i of cell i can be defined as

$$F_i = \max(F_{i,\mathrm{in}}, F_{i,\mathrm{out}}) \tag{1.66}$$

where $F_{i,\mathrm{in}}$ is the sum of all CFL-volume-fluxes q_j that enter and $F_{i,\mathrm{out}}$ of the fluxes that leave cell i through face j:

$$F_{i,\mathrm{in}} = \sum_j q_{j,\mathrm{in}}, \qquad F_{i,\mathrm{out}} = \sum_j q_{j,\mathrm{out}}. \tag{1.67}$$

Equation 1.65 states that the volume obtained by multiplying F_i with Δt must not exceed the pore volume in cell i. In the one-dimensional case, this condition is the well-known Courant–Friedrichs–Lewy CFL-condition:

$$c_{\mathrm{CFL}} = \Delta t \frac{v_i}{\phi \Delta x} \leq 1. \tag{1.68}$$

From Equation 1.65 it follows that a stable time step can be estimated as:

$$\Delta t = c_{\mathrm{CFL}} \min\left(\frac{\phi_i V_i}{F_i}\right), \qquad c_{\mathrm{CFL}} \leq 1. \tag{1.69}$$

There exist varies approaches for the estimation of F_i which differ for different kinds of transport equations and for varying complexity of the physical processes. One straightforward approach for calculating F_i is to define the fluxes $q_{\alpha j}$ to be the face fluxes:

$$q_j = \sum_{\alpha} |\mathbf{v}_{\alpha j} \cdot \mathbf{n}_j A_j| \tag{1.70}$$

where $\mathbf{n}_j$ and A_j are face normal and face area. However, it is important that, for $c_{\mathrm{CFL}} = 1$, this approach guarantees stability of the IMPES scheme but only leads to a physically correct solution if a linear hyperbolic transport equation is solved. In this case, the displacement front is a shock moving with constant velocity. If the transport equation is non-linear hyperbolic or parabolic, the front velocity varies with saturation and diffusive transport may occur. In this case, the CFL-number has to be less than one. To avoid the kind of heuristic choice of c_{CFL}, stability analyses provides theoretically based estimates for F_i. If capillary pressure and gravity are neglected, $F_{i,\mathrm{in}}$ and $F_{i,\mathrm{out}}$ can be estimated as derived in [Aziz 79] or [Coat 03b] using:

$$q_j = \left| \left(\frac{df_{\mathrm{w}}}{dS_{\mathrm{w}}}\right)_j \sum_{\alpha} \mathbf{v}_{\alpha j} \cdot \mathbf{n}_j A_j \right|. \tag{1.71}$$

In this approach the derivative of the wetting-phase-fractional-flow function $\frac{df_{\mathrm{w}}}{dS_{\mathrm{w}}}$ accounts for the non-linearity of the movement of the fluid fronts. Thus, the CFL-number can be chosen as $c_{\mathrm{CFL}} = 1$. For the general case, including capillary pressure and gravity, an IMPES stability criterion is derived in [Coat 03a], which also accounts for countercurrent flow. It is originally derived for three-phase flow but can be reduced for the simplified case of two-phase flow. The volume fluxes $F_{i,\mathrm{in}}$ and $F_{i,\mathrm{out}}$ are then estimated from Equation 1.67 by substituting q_j by:

$$q_j = t_j \left(f_{\mathrm{n}j} \left(\frac{d\lambda_{\mathrm{w}}}{dS_{\mathrm{w}}}\right)_j |\Delta\Phi_{\mathrm{w}}|_j \right. \tag{1.72}$$

$$\left. - f_{\mathrm{w}j} \left(\frac{d\lambda_{\mathrm{n}}}{dS_{\mathrm{w}}}\right)_j |\Delta\Phi_{\mathrm{n}}|_j - f_{\mathrm{w}j}\lambda_{\mathrm{n}j} \left(\frac{dp_{\mathrm{c}}}{dS_{\mathrm{w}}}\right)_j \right), \tag{1.73}$$

where t_j is the transmissibility associated with the face j. The efficiency of the explicit scheme mainly depends on the time-step size. If the non-linear coupling between pressure and transport equation or the physically correct approximation of the transport require small time-step sizes, implicit schemes may become more efficient. A comparison between an IMPES scheme and an fully implicit scheme can for example be found in [Slee 93].

The Compositional Case

The decoupled compositional multi-phase flow equations derived in Section 1.3.3 can be solved sequentially according to the IMPES scheme, where it is commonly referred to as

IMPEC scheme, since concentrations are considered in this case. First, the pressure equation (1.56) is solved implicitly to obtain a pressure field and fluid phase velocities which are used to explicitly solve the transport equation (1.34). After each of these pressure-transport sequences, the distribution of total concentrations is known. For the next sequence, phase saturation and component mass fractions are needed. These are gained by performing a phase equilibrium- or so-called flash calculation (see below), which forms the last step of the IMPEC scheme.

Flash Calculations After the evaluation of the transport equation, the total concentrations at each cell or node are known. From these, an overall mass fraction (or feed mass fraction) $z^\kappa = C^\kappa / \sum_\kappa C^\kappa$ of each component inside the mixture is calculated. Now the question is, how the phase mass fractions ν_α can be calculated from this, i.e. how the different components are distributed among the different phases. Therefore, we introduce at first the equilibrium ratios

$$K_\alpha^\kappa = \frac{X_\alpha^\kappa}{X_\mathrm{r}^\kappa}\,, \tag{1.74}$$

which relate the mass fractions of each component in each phase α to its mass fraction in a reference phase r, where K_r^κ obviously always equals unity. The equilibrium ratios can be obtained by using the laws for fluid phase equilibria in section 1.3.1, as described in [Nies 07] or by incorporating a thermodynamic equation of state [Aziz 89, Nghi 84, Mich 07]. In the former case, the equilibrium ratios depend only on pressure and are therefore constant for constant pressure and temperature. The feed mass fraction z^κ can be related to the phase mass fractions X_α^κ via $\nu_\alpha = \frac{C^\kappa}{\sum\limits_\kappa C^\kappa}$ by

$$z^\kappa = \sum_\alpha \nu_\alpha X_\alpha^\kappa\,. \tag{1.75}$$

Combining and rearranging of (1.74) and (1.75) yields

$$X_\mathrm{r}^\kappa = \sum_\kappa \frac{z^\kappa}{\sum\limits_{\alpha \neq \mathrm{r}} K_\alpha^\kappa \nu_\alpha + \nu_\mathrm{r}}, \tag{1.76}$$

and some more steps, which are elaborately described in [Aziz 89], yield a set of $n_\alpha - 1$ equations, known as the Rachford-Rice equation

$$\sum_\kappa \frac{z^\kappa \left(K_\alpha^\kappa - 1\right)}{1 + \sum\limits_{\alpha \neq \mathrm{r}} \left(K_\alpha^\kappa - 1\right) \nu_\alpha} = 0, \qquad \alpha \neq \mathrm{r}, \tag{1.77}$$

which generally has to be solved iteratively for the phase mass fraction ν_α. Only in the case of the same number of phases and components, the Rachford–Rice equation can be solved analytically. Once the phase mass fractions are known, the mass fractions of the components inside the reference phase can be calculated by (1.76) and then lead to the mass fractions inside the other phases via (1.74). Other flash calculation approaches which use so-called reduced equation algorithms and which basically use modified forms of the presented equations are presented in [Wang 95].

1.5 Application of Multi-Physics and Multi-Scale Methods

In the following we present our approach to multi-scale and multi-physics modeling which slightly differs to the methods mentioned before by means of two examples. The common base for both kinds of methods is the use of an h-adaptive grid. This can be combined with numerical upscaling methods to a multi-scale method with regard to scale-dependent heterogeneous parameters or allows the adaptive local treatment of domains of different physical regimes in the sense of a multi-physics approach. This comparably simple approach follows the idea of developing a tool which is above all simple and flexible enough to be easily applied and adapted to complex real-life application. All of the methods and examples that are presented in the following have been implemented into the open-source porous-media simulator DuMu$^{\text{x}}$, [Flem 11].

1.5.1 A Multi-Physics Example

In this section, we introduce a method to couple compositional two-phase flow with single-phase compositional flow as proposed in [Frit 12].The advantage of this coupling is, that for single-phase compositional flow, a simpler pressure equation can be used. Moreover, for single-phase flow, the evaluation of flash calculations can be avoided. The latter becomes ever more interesting when these evaluations require lots of computational power such as in many reservoir engineering problems, where flash calculations may occupy up to 70 % of the total CPU time of a model (see [Sten 93]).

Single-Phase Transport

We want to take a closer look at the equations for the miscible case and assume that only one phase is present. Inserting the definition of the total concentration (1.32) into the component mass balance equation (1.34) for one phase α and applying the chain rule yields

$$\phi \varrho_\alpha X_\alpha^\kappa \frac{\partial S_\alpha}{\partial t} + S_\alpha \varrho_\alpha X_\alpha^\kappa \frac{\partial \phi}{\partial t} + \phi S_\alpha \varrho_\alpha \frac{\partial X_\alpha^\kappa}{\partial t} = -\operatorname{div}\left(\varrho_\alpha X_\alpha^\kappa \mathbf{v}_\alpha\right) + q^\kappa \,. \tag{1.78}$$

The first term on the left hand side equals zero since only one phase is present and thus the saturation always equals unity. Further we assume that phase and matrix compressibilities are of low importance and can be neglected. Then the second and third term on the left hand side cancel out as well. A volumetric source q_α of the present phase with the composition X_Q^κ is introduced and using the definition $q^\kappa = q_\alpha \varrho_\alpha X_Q^\kappa$, with X_Q^κ in the source-flow, we replace the mass source of component κ and write

$$\phi \varrho_\alpha \frac{\partial X_\alpha^\kappa}{\partial t} = \frac{\partial C^\kappa}{\partial t} = -\varrho_\alpha \operatorname{div}\left(X_\alpha^\kappa \mathbf{v}_\alpha\right) + q_\alpha \varrho_\alpha X_Q^\kappa \,. \tag{1.79}$$

This is the mass balance equation for the compositional transport in a single phase. The same assumptions can be applied to the compositional pressure equation. For incompressible flow, the derivatives of volume with respect to mass equal the reciprocal of the phase density, i.e. $\frac{\partial}{v_t}/\partial C^\kappa = 1/\varrho_\alpha$. Inserting this identity into equation (1.56), setting the derivative of volume with respect to pressure to zero (incompressible flow) and applying the chain

rule to the divergence term, we get

$$\sum_{\kappa} \frac{1}{\varrho_\alpha} \left(X_\alpha^\kappa \varrho_\alpha \operatorname{div} \mathbf{v}_\alpha + \varrho_\alpha \mathbf{v}_\alpha \cdot \mathbf{grad}\, X_\alpha^\kappa + X_\alpha^\kappa \mathbf{v}_\alpha \cdot \mathbf{grad}\, \varrho_\alpha \right) = \sum_{\kappa} \frac{1}{\varrho_\alpha} q^\kappa \,. \tag{1.80}$$

By definition, the sum of the mass fractions X_α^κ inside one phase equals unity, thus the second term in parenthesis cancels out. Furthermore, the gradient of the density equals zero due to the incompressibility. Again introducing the volumetric source term as above, yields the pressure equation for incompressible single phase compositional flow, which can as well be derived from equation (1.35):

$$\operatorname{div} \mathbf{v}_\alpha = q_\alpha \tag{1.81}$$

We note here that dropping the assumption of incompressibility only slightly complicates equation 1.81, which still provides an efficiency potential compared to equation (1.56) ([Frit 12]).

Model Coupling

Consider a spatial integration of equation (1.56) as is done for any numerical discretization. Then the unit of the terms is easily discovered to be volume over time. This basically reveals the physical aspect of the equation, namely the conservation of total fluid volume as also described in Section 1.3.3. The same consideration holds for equation (1.81), which makes sense since it is derived from the compositional pressure equation. The associated transport equations also have a common physical relevance: the conservation of mass.

The clear relation of the multi-phase compositional and single phase transport model and the possibility to use the same primary variables (as indicated in equation (1.79)) open the way to couple both models. This makes it possible to fit the model to the actual problem and use a sophisticated and accurate model in a subdomain of special interest, whereas a simpler model can be used in the rest of the domain. Consider for example a large hydrosystem which is fully saturated with water except at a spill of non aqueous phase liquid (NAPL) as displayed in Figure 1.9. The components of the NAPL are solvable in water and contaminate it. To model the dissolution of the components in the water, only a small area around the NAPL spill has to be discretized by a compositional two-phase model. The spreading of the contaminants in the larger part of the domain can in contrary be simulated using a single-phase transport model. The advantage in coupling the two models in this domain is that in large parts, the costly equilibrium calculations and evaluation of volume derivatives can be avoided.

Practical Implementation

The practical implementation of the multi-physics scheme proposed in the preceding sections is done by exploiting the similarity of the equations. Since both pressure equations have the same dimensions and the same unknowns, both can be written into one system of equations. The entries in the stiffness matrix and right hand side vector are evaluated using either equation (1.56) if the control volume is situated inside the subdomain or the equation (1.81) in the other parts of the domain. Equation (1.56) can also be set up properly at the internal boundary of the subdomain, since all coefficients can be determined. The coefficients concerning the phase which is not present outside the subdomain just have

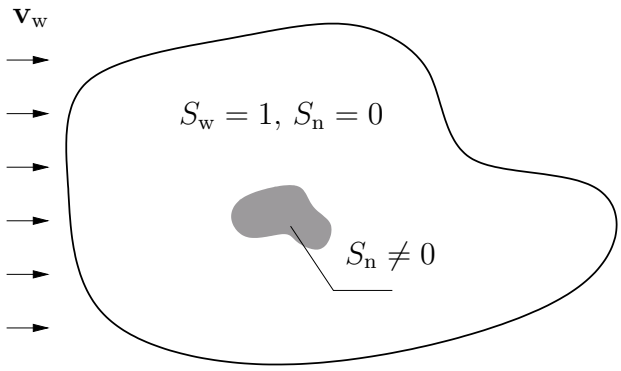

Figure 1.9: Multi-physics problem example taken from [Frit 12]

to be set to zero for the outer elements which makes all terms concerning this phase vanish at the boundary. Also the transport equation is well defined at the boundary. Since only one phase is present outside the subdomain, the mobility coefficient in equation (1.34) will equal zero for all other phases and the multi-phase compositional mass balance will boil down to equation (1.79) at the interface.

Implicitly the coupling conditions are already contained in the presented scheme: first, mass fluxes have to be continuous across the subdomain boundary and second, phase velocities have to be continuous across the subdomain boundary. Since only one phase is present outside the subdomain, it is obvious that the second condition requires that only this one phase may flow across the subdomain boundary. Another effect that has to be considered is demixing. Solubilities usually depend on pressure. If a phase is fully saturated with a certain component and then moves further downstream, where the pressure is lower, the solubility decreases and demixing occurs. If the solubility is exceeded outside the subdomain this effect is not represented. These two considerations show the crucial importance of an adequate choice of the subdomain. On the one hand, we want the subdomain to be as small as possible to obtain an economic model, on the other hand, it must be chosen large enough to prevent errors. Especially in large and heterogeneous simulation problems, it is unlikely to determine a proper subdomain in advance, so an automatic adaption is sought. As the most logical scheme, we propose to choose all cells with more than one phase and – since demixing occurs predominantly here – all directly adjacent cells to be part of the subdomain. At the end of each time step, the choice is checked and superfluous cells are removed and necessary cells are added. This quite easy decomposition can only be expected to be successful in the case of an explicit solution of the transport equations. In particular, the fulfillment of the CFL-condition guarantees that no modeling error will occur, since information is transported at most one cell further in one time step.

As example for the described subdomain adaptivity see Figure 1.10. Displayed is nearly residual air that moves slightly upward before it is dissolved in water. The subdomain is marked by black squares. In the upper row, the initial subdomain and its expansion due to demixing after 100 time steps can be seen. In the lower row, one can actually see that cells also get removed from the subdomain and that it moves and finally vanishes with the air phase.

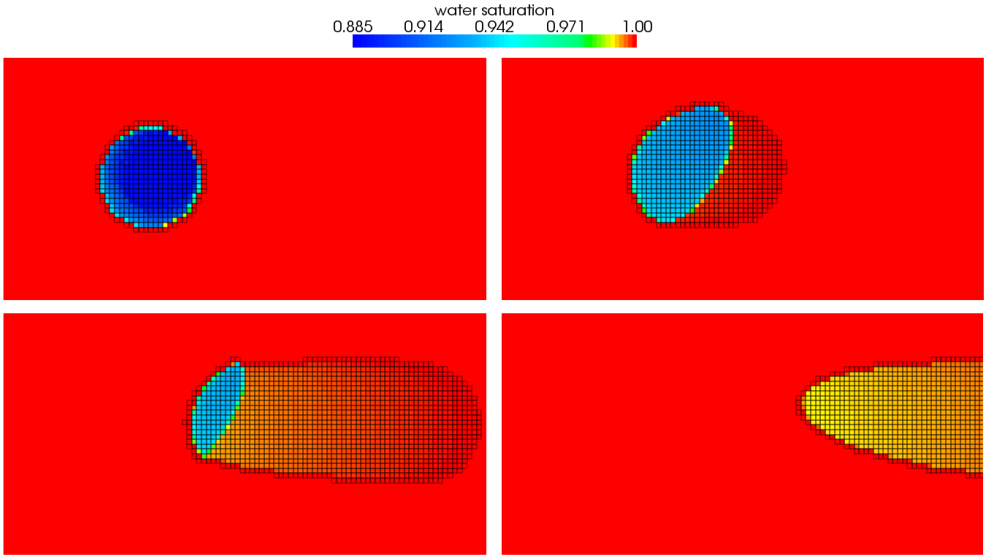

Figure 1.10: Dissolution of residual air in water. In black squares: adaptive subdomain at initial conditions, after 100, 200 and 300 time steps, respectively. taken from [Frit 12]

Application Example

To demonstrate the performance of the multi-physics approach and to compare it to the full compositional two-phase model on a real life problem, we chose a benchmark problem from carbon-dioxide storage as presented in [Eige 09] and [Clas 09]. Carbon dioxide is injected at a depth of 2960 to 3010 meter into a saline aquifer over a time period of 50 years, while injection is stopped after 25 years. The given spatial discretization spans 54756 control volumes. Figure 1.11 shows the results of the simulation. The results of the multi-physics approach compared to the model on full complexity show good agreement, the integral indicators proposed in the benchmark agree as well. In fact, observable differences are largely caused by truncation errors (volume error) in the post-injection phase, and not by the multi-physics framework. After 25 years, the complex subdomain covers roughly 3% of total cells, expanding to roughly 4.5% after 50 years.

1.5.2 A Multi-Scale Example

As a multi-scale example flow through a layer of the three-dimensional geological model (model 2) of the SPE 10 benchmark study [Chri 01] is simulated. The permeability and porosity fields of layer 15 (top formation), are shown in Figure 1.12 (a) and (b). Capillary pressure and gravity are neglected and the fluids are assumed to be incompressible. The fine-scale relative permeabilities are calculated using quadratic laws

$$k_{\mathrm{rw}} = S_{\mathrm{w}}^2 \tag{1.82}$$

$$k_{\mathrm{rn}} = (1 - S_{\mathrm{w}})^2 \tag{1.83}$$

and the fluid viscosities are $\mu_{\mathrm{w}} = 10^{-3}$ kg/(ms) and $\mu_{\mathrm{n}} = 5 \times 10^{-3}$ kg/(ms). As shown in Figure 1.12 (c) the domain is initially saturated by a non-wetting phase (for example, oil) and water infiltrates from the southern domain boundary driven by a pressure gradient in y-direction. At the remaining sides no-flow boundary conditions are applied. On the fine

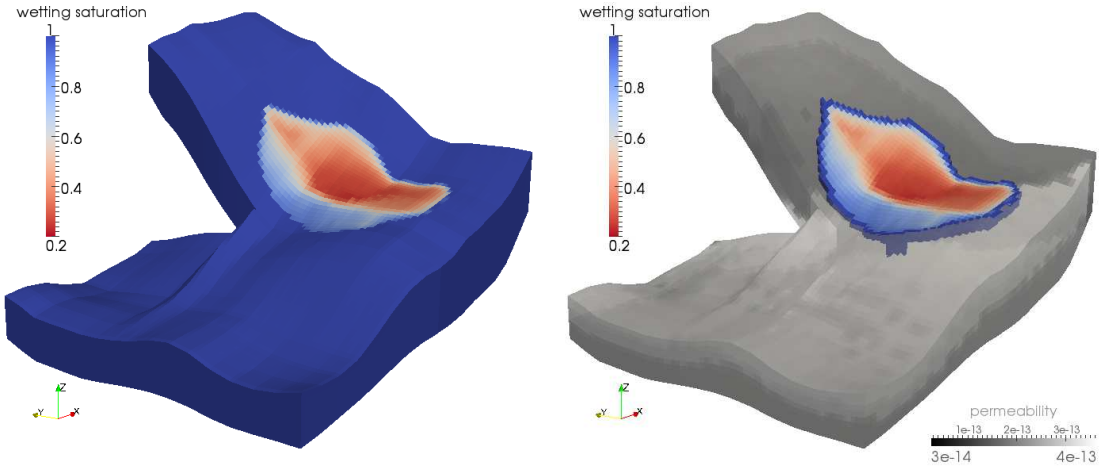

Figure 1.11: Results for the Johannsen formation benchmark after 50 years. Left: full compositional two-phase model, right: multi-physics approach, depicting only the most complex subdomain

scale, the domain is discretized by a grid of 128 × 256 cells and on the coarse scale by a grid of 4 × 8 cells, leading to a hierarchic refinement factor of 5.

The Multi-Scale Approach

The multi-scale model is described in detail in [Wolf 13b]. It solves a decoupled system of equations for incompressible isothermal two-phase flow like introduced in Section 1.3.3. Effective coarse scale permeabilities are calculated for the coarsest grid level (4 × 8 cells) from the fine-scale distribution (Figure 1.12) applying the method of [Wen 03] which enables the construction of full permeability tensors. For the solution of the local fine-scale problems effective flux boundary conditions derived in [Wall 02a] and [Wall 02b] are used. The multi-scale concept is straightforward: We combine an h-adaptive grid method with the numerical upscaling approach, where the adaptive grid can be interpreted as a kind of global downscaling. Wherever possible, the grid consists of level zero cells (coarse scale), otherwise it can be refined up to the highest level (fine scale). Only one level difference is allowed between neighboring cells. This leads to a transfer region if there is more than one level difference between the fine scale and the coarse scale. At the highest level, the fine-scale parameters can be used directly. At all other levels, we use the upscaled parameters calculated for the zeroth grid level. The grid is adapted using a nonconforming refinement strategy with hanging nodes. For a correct approximation of fluxes at hanging nodes, a multi-point flux approximation method (MPFA) is used [Aava 08, Wolf 13a, Faig 13]).

Numerical Results

Some results of the simulation of the previously described problem setup are shown in Figures 1.13 and 1.14. For both the distribution of the saturation and of the total velocity magnitude the multi-scale result (b) agrees very well with the fine-scale reference solution (a). It can be observed that a preferred flow path exists which leads to the development of a large-scale finger. The preferred flow paths are very well accounted for by the grid adaptation scheme as can be seen in Figure 1.14 (c) where the grid at the simulation end is

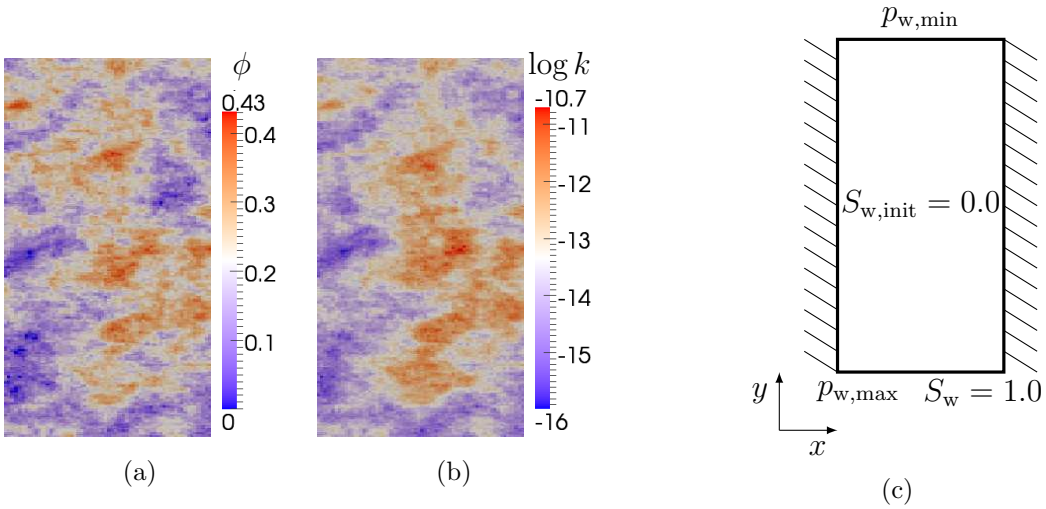

Figure 1.12: Porosity (a) and permeability (b) distribution according to layer 15 of the SPE10 benchmark model 2 (top formation), and problem setup (c).

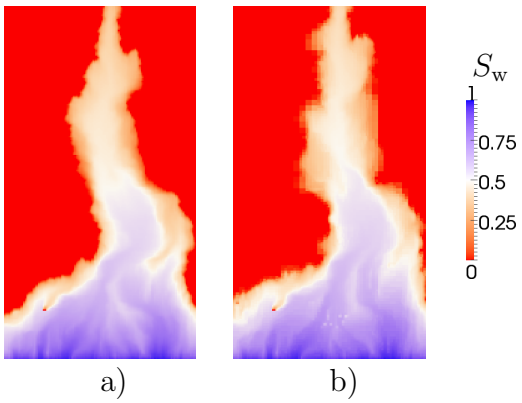

Figure 1.13: Saturation distribution of the fine-scale simulation (a) and the multi-scale simulation (b) at $t = 1.5 \times 10^8$ s.

plotted. For an accurate approximation the resolving of the large scale flow paths as well as the local front propagation is important. In this example adaptation indicators based on local saturation gradients and on the total velocity are applied. Considering the grid (Figure 1.14 (c)), it is obvious that the number of degrees of freedom can be reduced and hence the efficiency increased significantly by the multi-scale method.

1.6 Conclusion

In this work, we have given an overview of multi-scale and multi-physics methods for flow and transport processes in porous media. Therefore, we defined relevant scales and gave an overview of multi-scale and of multi-physics methods. We introduced the mathematical model for compositional non-isothermal multi-phase flow and transport in porous media and discussed possible reformulations. Based on that, decoupled and coupled numerical solution strategies are discussed. In a next part, applications examples of multi-physics and of multi-scale models were given. This work is meant to give an overview of existing multi-scale

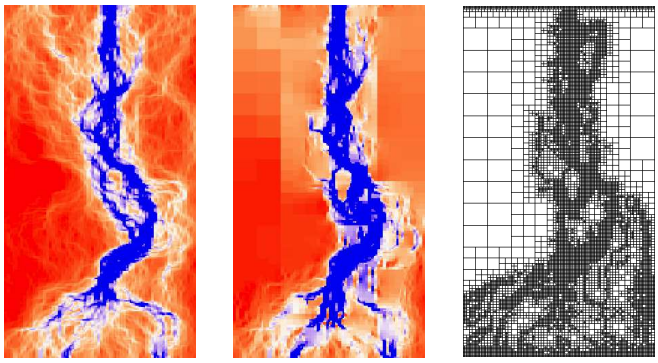

(a) (b) (c)

Figure 1.14: Total velocity distribution of the fine-scale simulation (a) and the multi-scale simulation (b) at $t = 1.5 \times 10^8$ s, and the corresponding adapted grid.

and multi-physics approaches for multi-phase flow problems in porous media. Examples are given in order to illustrate the effectiveness and applicability of these algorithms.

Future work needs to be done to include more complex processes in the multi-scale and multi-physics algorithms in order to allow for the modeling of highly complex real-life systems. Also, the development of upscaling techniques and the upscaling of the complex equations is a crucial issue. Coupling techniques need to be improved to allow for a physically based coupling of different multi-physics domains and for the coupling across scales. Numerical methods need to be improved in order to allow for moving meshes if the multi-physics domains move during a simulation and multi-scale multi-physics algorithms need to allow for the application of different numerical schemes for the solution of different physical processes (multi-numerics).

In conclusion, we state that the development and application of multi-scale and multi-physics techniques allows to model highly complex physical problems in large domains that could otherwise not be solved numerically.

2 Classification and Review of Model Coupling Approaches

Bibliographic Note: The content of this chapter is based on the following original article [Helm 13]: R. Helmig, B. Flemisch, M. Wolff, A. Ebigbo, H. Class (2013): Model coupling for multiphase flow in porous media. *Advances in Water Resources* **51**, pp. 52–66.

Summary Numerical models for flow and transport in porous media are valid for a particular set of processes, scales, levels of simplification and abstraction, grids etc. The coupling of two or more specialized models is a method of increasing the overall range of validity while keeping the computational costs relatively low. Several coupling concepts are reviewed in this article with a focus on the authors' work in this field. The concepts are divided into temporal and spatial coupling concepts, of which the latter is subdivided into multi-process, multi-scale, multi-dimensional, and multi-compartment coupling strategies. Examples of applications for which these concepts can be relevant include groundwater protection and remediation, carbon dioxide storage, nuclear-waste disposal, soil dry-out and evaporation processes as well as fuel cells and technical filters.

2.1 Introduction

The description of the flow of multiple fluid phases through a material which consists of a solid and interconnected pore space is highly relevant in several fields of application. This includes environmental and geological applications such as groundwater protection and remediation, (enhanced) oil recovery, nuclear-waste disposal, carbon dioxide storage, dry-out and evaporation processes etc., but also technical systems such as the flow of water and gas in fuel cells or filters. In all of these examples, a quantitative prediction of flow and transport on strongly varying spatial and temporal scales is required and typically achieved with mathematical and numerical models. A need for model coupling arises for two basic reasons: (i) The relevant spatial and temporal scales, in particular for some geological applications such as CO_2 storage and nuclear waste disposal, are very large, and computational costs need to be reduced by adapting the complexities of the applied (sub-)models. (ii) The processes of the overall problem are in some cases described by different sets of equations, for example, if different compartments of hydrosystems interact with each other. An example is the problem of water evaporation and dry out of soils due to wind in arid regions. This chapter gives a review of coupling concepts and multi-scale approaches with a focus on the authors' contribution in this field.

2.1.1 Scales

As outlined in [Helm 10], several characteristic length scales can be identified on which the relevant flow processes can be described. A basic differentiation is made here between (i) the pore scale, at which the fluids, solid, and interfaces can explicitly be accounted for, (ii)

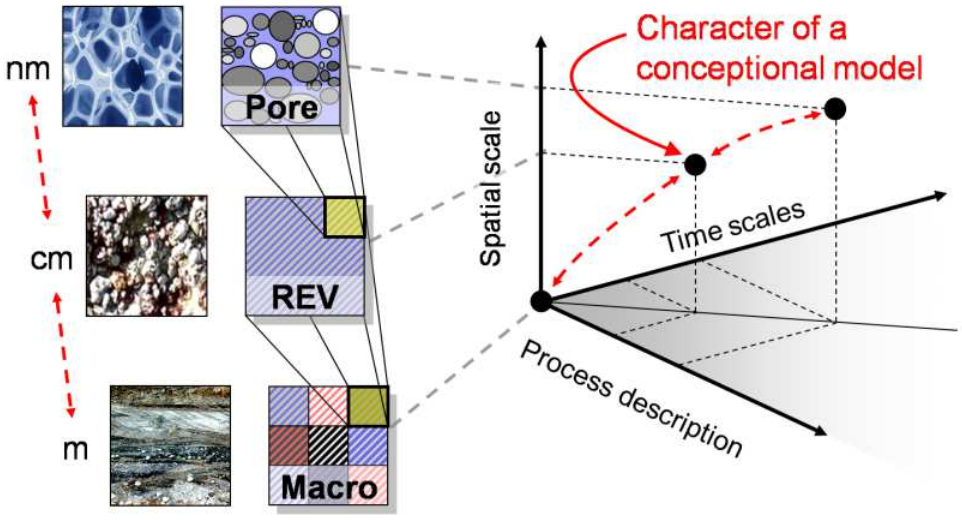

Figure 2.1: Several characteristic length and time scales can be identified when considering flow and transport in porous media. Model concepts need to be developed with respect to the temporal and spatial scales at which the flow processes occur.

the REV (or fine) scale, at which effective properties and functions are sufficient to describe flow in a representative elementary volume (REV), and (iii) the macro (or coarse) scale, which is typically determined by the size of grid blocks of a computational simulation – see Figure 2.1. The models considered in this article are based on the REV scale and the macro scale, which will also be referred to as the fine and coarse scales, respectively.

2.1.2 Modeling Challenges

The modeling applications mentioned previously pose several challenges to numerical models, some of which are listed below:

- Geological applications are often characterized by their very large spatial and temporal scales. For example, geological formations relevant for oil recovery or CO_2 storage may extend several hundreds of kilometers; in the storage of nuclear waste, processes of interest continue even after millennia.
- They are usually also characterized by a small region in which complex physical processes take place as compared to the simpler processes in the rest of the domain.
- Heterogeneities exist on all the scales considered here. Obviously, the effects of fine-scale heterogeneities have to be accounted for on the coarse scale.
- The rate at which processes occur can vary significantly. For the underground storage of CO_2, there is a strong difference in flow velocities during and after injection.
- Due to a general scarcity of geological data, there is a high degree of uncertainty. Methods for the quantification of uncertainties require several possible realizations of the underlying deterministic numerical model.

Due to computational-cost constraints, efficient methods are necessary if the above modeling challenges are to be met. One way of improving efficiency is specification. Making a

model concept specific to a problem of given complexity and/or scale can boost efficiency without affecting accuracy. Such models can then be coupled to address a complex and realistic problem.

2.1.3 Outline

This article gives an overview of the model-coupling strategies which are currently in the focus of research. Before describing coupling strategies, the basic mathematical models which describe multiphase and compositional flow in porous media are given in Section 2.2. Then the coupling strategies are divided in Section 2.3 into various categories which are partly overlapping or in a smooth transition to each other: spatial coupling methods (volume coupling, surface coupling, see Figure 2.2), in which case regions of the spatial domain are identified with differing characteristic model complexities or where equations of different character are solved on different scales etc. Section 2.4 focuses on temporal coupling where processes have different characteristics in time such that model complexity can be adapted in the entire domain (or in parts, if multiple coupling approaches are useful) over time. Finally, Section 2.5 summarizes the perspectives of model coupling for future research and application to current challenging engineering problems.

2.2 Mathematical Models for Multi-Phase Flow

Mathematical and numerical formulations of the equations which govern multiphase flow in porous media are briefly introduced with the aim of setting a basis on which the coupling strategies operate.

2.2.1 Governing Equations

The governing equations are generally derived by balancing such quantities as mass, momentum, and energy. These equations are given on the REV (fine) scale. The pore scale is not considered, and the macro (coarse) scale is achieved by upscaling. More comprehensive descriptions of these equations have been given, for example, by [Helm 10, Chen 97, Mill 98, Gerr 05].

Balance equations for the mass of a component in a system which consists of more than one fluid phase generally have the following form:

$$\frac{\partial}{\partial t}\left(\phi \varrho_\alpha S_\alpha X_\alpha^\kappa\right) + \operatorname{div}(\phi \varrho_\alpha S_\alpha X_\alpha^\kappa \mathbf{u}_\alpha + \mathbf{J}_\alpha^\kappa) = I_\alpha^\kappa + q_\alpha^\kappa, \tag{2.1}$$

where ϱ is density, ϕ is porosity, S is fluid-phase saturation, X is mass fraction, $\mathbf{u}$ is velocity, $\mathbf{J}$ is diffusive flux, I is interphase mass exchange, and q stands for external sources and sinks. The subscripts κ and α denote the component and the phase, respectively. In addition to the solid phase, a general system may consist of an aqueous (w), a non-aqueous (n), and a gas (g) phase as well as N components:

$$\kappa \in \{1, 2, \ldots, N\}; \quad \alpha \in \{\mathrm{w}, \mathrm{n}, \mathrm{g}\}. \tag{2.2}$$

Given the constraints and definitions

$$\begin{aligned} &\sum_{\kappa} \mathbf{J}_{\alpha}^{\kappa} = \mathbf{0}, \quad \sum_{\kappa} X_{\alpha}^{\kappa} = 1, \quad \sum_{\kappa} I_{\alpha}^{\kappa} = I_{\alpha}, \quad \sum_{\kappa} q_{\alpha}^{\kappa} = q_{\alpha}, \\ &\sum_{\alpha} I_{\alpha}^{\kappa} = 0, \quad \sum_{\alpha} S_{\alpha} = 1, \quad \sum_{\alpha} q_{\alpha}^{\kappa} = q^{\kappa}, \end{aligned} \tag{2.3}$$

it is convenient to sum up the balance equations either over all components in each phase, which gives one equation for each phase

$$\frac{\partial}{\partial t}\left(\phi \varrho_{\alpha} S_{\alpha}\right) + \operatorname{div}(\phi \varrho_{\alpha} S_{\alpha} \mathbf{u}_{\alpha}) = I_{\alpha} + q_{\alpha}, \tag{2.4}$$

or over all phases, which gives one equation for each component

$$\sum_{\alpha} \frac{\partial}{\partial t}\left(\phi \varrho_{\alpha} S_{\alpha} X_{\alpha}^{\kappa}\right) + \sum_{\alpha} \operatorname{div}\left(\phi \varrho_{\alpha} S_{\alpha} X_{\alpha}^{\kappa} \mathbf{u}_{\alpha} + \mathbf{J}_{\alpha}^{\kappa}\right) = q^{\kappa}. \tag{2.5}$$

The Extended Darcy Equation As noted by [Mill 98], a separate momentum balance equation is usually not considered. Instead, the flux of a fluid phase $\mathbf{v}_{\alpha}$ is approximated with the extended Darcy equation

$$\mathbf{v}_{\alpha} = \phi S_{\alpha} \mathbf{u}_{\alpha} = -\frac{k_{\mathrm{r}\alpha}}{\mu_{\alpha}} \mathbb{K}\left(\mathbf{grad}\, p_{\alpha} - \varrho_{\alpha} \mathbf{g}\right), \tag{2.6}$$

where $\mathbb{K}$ is the intrinsic permeability of the porous medium, k_{r} is relative permeability, μ is viscosity, and $\mathbf{g}$ is the gravitational vector.

Fickian Diffusion For the applications considered here, the diffusive flux can adequately be described with a Fickian approach, i.e.

$$\mathbf{J}_{\alpha}^{\kappa} = -\mathbb{D}_{\alpha}^{\kappa}\, \mathbf{grad}(\varrho_{\alpha,\mathrm{mol}} x_{\alpha}^{\kappa}), \tag{2.7}$$

where $\mathbb{D}_{\alpha}^{\kappa}$ is a diffusion tensor, $\varrho_{\alpha,\mathrm{mol}}$ is the molar density of phase α and x_{α}^{κ} the respective mole fraction of component κ in this phase.

Capillary Pressure and Relative Permeability The orientation of the interfaces between two fluids in the pores is controlled by interfacial tension [Core 94]. Interfacial tension leads to a pressure difference between the two phases, i.e. capillary pressure. On the REV scale, it is often assumed to be a function of saturation,

$$p_{\mathrm{c},\alpha\beta}(S_{\alpha}) = p_{\beta} - p_{\alpha}. \tag{2.8}$$

In this case, β denotes the fluid with the lower affinity to the solid. Similarly, the reduced permeability of a fluid phase as a result of the presence of other phases, i.e. relative permeability, is also typically taken to be a function of saturation. There are equations with which $p_{\mathrm{c}}-S$ and $k_{\mathrm{r}}-S$ relationships can be expressed. However, these relationships are not unique. Special models have been developed to handle hysteretic effects. Alternative approaches, which tend to be more general, try to avoid hysteresis altogether.

2.2.2 Fully Implicit and Semi-Implicit Models

The nature of the mass balance equations (Equations (2.4) or (2.5)) depends on the character of the application under consideration. The $p_c - S$ and $k_r - S$ relations usually introduce very strong non-linearities and can impose a strong coupling between the balance equations. The equations are parabolic. The balance between the advective and diffusive (due to capillary diffusion and hydrodynamic dispersion) parts of the equations can significantly change their character.

Several environmental applications – for example, groundwater remediation, flow in the vadose zone, CO_2 storage in geological formations, radionuclide transport in waste repositories – have to be described with equations that are highly non-linear, strongly coupled, and parabolic. In such cases, the equations are often solved simultaneously in a fully implicit way.

Other applications allow certain assumptions under which the mass balance equations can readily be reformulated into one elliptic pressure equation and one hyperbolic saturation equation for each phase. This *fractional flow formulation* results in equations which are weakly coupled and can be solved sequentially in a semi-implicit way.

Fractional Flow Formulation The fractional flow formulation is typically used in applications which are strongly dominated by advection, occur over large spatial scales, and have very limited mutual dissolution. As such, the effects of miscibility, capillarity, and compressibility (if a gas is not involved) are often neglected. If these assumptions are accounted for in Equation (2.4) and the equations for both phases are added, one obtains the pressure equation:

$$\operatorname{div} \mathbf{v}_t = \sum_\alpha q_\alpha / \varrho_\alpha, \tag{2.9}$$

where $\mathbf{v}_t$ is the total velocity, defined as

$$\mathbf{v}_t = \sum_\alpha \mathbf{v}_\alpha = -\lambda_t \mathbb{K} \left(\sum_\alpha f_\alpha \left(\mathbf{grad}\, p_\alpha - \varrho_\alpha \mathbf{g} \right) \right), \tag{2.10}$$

and $\lambda_\alpha = k_{r\alpha}/\mu_\alpha$ is the phase mobility, $f_\alpha = \lambda_\alpha / \lambda_t$ is the phase fractional flow function, and $\lambda_t = \sum_\alpha \lambda_\alpha$ is the total mobility.

Inserting these definitions in Equation (2.4) gives the saturation equation for each phase:

$$\phi \frac{\partial S_\alpha}{\partial t} + \operatorname{div}(f_\alpha \mathbf{v}_t) = q_\alpha / \varrho_\alpha. \tag{2.11}$$

While the phase velocities are determined with the pressure equation, the saturation equation describes the movement of the fluids. These equations are only weakly coupled and can be solved sequentially. Hence, different discretization and solution techniques can be applied to the equations depending on their character. This is very advantageous when considering the coupling of models of different scales, complexity, and/or character.

Note that the fractional flow formulation is not limited by the assumptions made here [Chen 97, see, for example,]. However, the strong difference in the characters of the equations is partly lost if the restrictions are loosened. For example, as stated in [Gerr 05], Equation (2.9) becomes parabolic if compressibility is accounted for, and Equation (2.11) loses its strictly hyperbolic character if capillary effects are not negligible.

2.3 Classification and Review of Spatial Model-Coupling Approaches

Model coupling is needed whenever a system or formulation is defined on multiple domains, possibly coinciding, involving dependent variables that cannot be eliminated on the equation level [Hame 99]. A possible classification of model-coupling approaches is sketched in Figure 2.2. It is based on the observation that coupling mechanisms can be divided

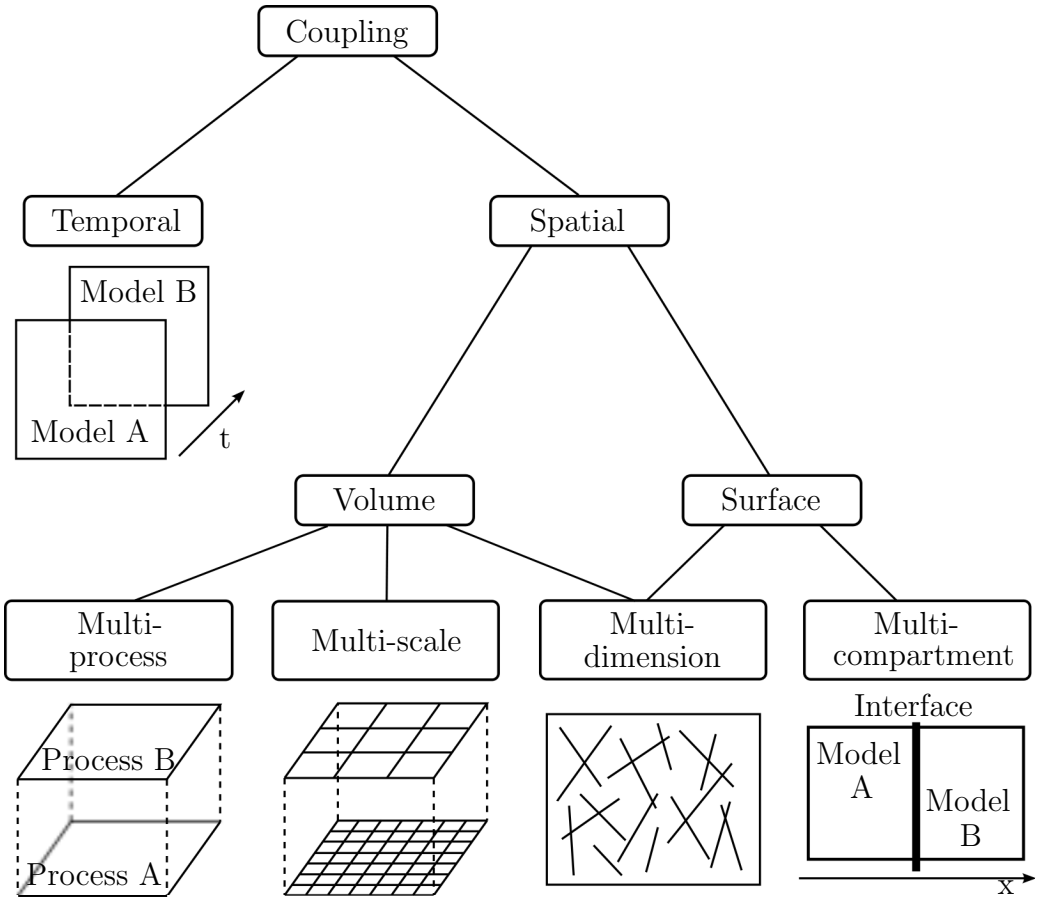

Figure 2.2: Classification of model-coupling approaches.

into three categories: volume, surface, and temporal. A volume coupling occurs if the d-dimensional spatial domains of interest for each of the dependent variables overlap. A surface coupling is given if these domains share a common $(d-1)$-dimensional interface. If the temporal domain of interest can be split into subdomains and each time span requires a different model, we speak of temporal coupling.

A further subdivision of the volume and surface coupling approaches now yields the following classical coupled systems:

- Multi-process: volume coupling of different model equations on the same scale for the description of multiple physical phenomena;
- Multi-scale: volume coupling of potentially different model equations on more than one scale for the description of the same physical phenomena;

- Multi-dimensional: volume or surface coupling of potentially different model equations describing physics on subdomains of different dimensionality;
- Multi-compartment: surface coupling of potentially different model equations describing physics on subdomains of the same dimensionality.

While temporal coupling is described in more detail in Section 2.4, the above-mentioned classical coupling approaches are reviewed in the following sections. Since these approaches and their further subdivisions constitute research fields in their own right, we restrict ourselves to a rather exemplary selection of references which should facilitate the access to a particular topic for an interested reader, but which is far from being complete. Moreover, we can describe only a subset of coupled models for porous media flow, omitting, for example, the coupling of well models and reservoir models, or the coupling of reservoir models and seismic models.

2.3.1 Multi-Process Approaches

The defining feature of a multi-process model is that the model domain is physically the same for the different sets of equations. Within the context of porous media, most well-known multi-process models include the addition of heat transfer, geomechanical and geochemical effects, as well as multi-porosity models.

Heat Transfer

Probably the most common occurrence of a multi-process model in porous media modeling is the coupled system of flow and transport of fluid phases and thermal energy, see Figure 2.3. In addition to the phase mass balances (2.4) or the component mass balances (2.5), one

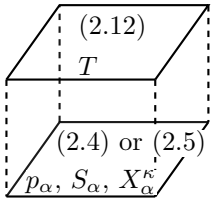

Figure 2.3: Heat transfer: Mass balances (2.4) or (2.5) with unknowns p_α, S_α (X_α^κ) coupled to an energy balance (2.12) with unknown T.

has to solve one or more balances of internal energy, depending on whether local thermal equilibrium is assumed or not. For example, if local thermal equilibrium is assumed, this balance is of the form

$$\frac{\partial}{\partial t}\left(\phi \sum_\alpha (\varrho_\alpha u_\alpha S_\alpha) + (1-\phi)\,\varrho_\mathrm{s} c_\mathrm{s} T\right) - \operatorname{div}\left(\sum_\alpha (\varrho_\alpha h_\alpha \mathbf{v}_\alpha) - \lambda_\mathrm{pm}\,\mathbf{grad}\,T\right) = q_h, \quad (2.12)$$

where T is the temperature, u_α and h_α stand for the internal energy and the enthalpy of the fluid phases, and the density ϱ_s, the heat capacity c_s, and the thermal conductivity λ_pm are properties of the porous medium. The potentially strong bidirectional coupling is described by

- (2.4), (2.5) → (2.12): There is an obvious dependence on the phase saturations S_α, and also the thermal conductivity λ_{pm} is saturation-dependent in general. Clearly, the Darcy velocity $\mathbf{v}_\alpha$ depends on the pressure p_α, on the saturation S_α via the relative permeability $k_{\text{r}\alpha}$, and possibly on the composition of the phases, i.e. on the mass fractions X_α^κ, via the viscosity μ_α. Moreover, the density ϱ_α depends on the pressure p_α and possibly the phase composition, and the phase enthalpy h_α also depends on the phase composition.
- (2.12) → (2.4), (2.5): The densities ϱ_α and the viscosities μ_α can be strongly temperature-dependent.

Literature on the modeling of heat transfer processes in porous media is vast and would require a review paper of its own. We therefore only point to the recent review paper [Inge 10], the textbooks [Niel 06, Kavi 95], the book series [Ingh 98], and the review articles in [Vafa 00].

Geomechanics

A broad and important field of application for coupled models of flow and geomechanics is found in reservoir engineering. Due to fluid production or fluid injection, large pressure changes occur leading to a change of hydraulic properties and deformations of rock matrix. The literature on geomechanics and rock mechanics is also very detailed. Among the most well-known textbooks specific to this topic are [Zoba 07, Jaeg 07, Fjae 08].

Geomechanical processes can be very complex. Depending on the stress–strain behavior, the processes can be classified, for example, as linear elastic, visco-elastic, or visco-plastic. In particular, larger strains lead to deviations from the most simple case of linear elasticity. Also, rock failure (tensile failure, shear failure) cannot be described by a linear-elastic model, since it is always associated with plastic deformations. Since every deviation from linear elasticity requires a higher complexity of the mathematical descriptions and constitutive relations, many models only consider linear elastic deformation. Geomechanics in porous media has to take into account both fluids and rock matrix, see Figure 2.4. Therefore, the concept of effective stress, introduced in 1923 by Terzaghi and generalized

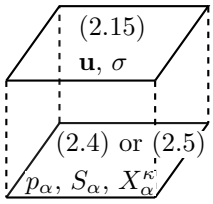

Figure 2.4: Geomechanics: Mass balances (2.4) or (2.5) with unknowns p_α, S_α (X_α^κ) coupled to a momentum balance (2.15) with unknowns $\mathbf{u}$, $\mathbb{S}$.

by Biot in 1941, is commonly used:

$$\mathbb{S}' = \mathbb{S} - \alpha p_{\text{eff}} \mathbb{I}, \tag{2.13}$$

where $\mathbb{S}$ and $\mathbb{S}'$ are the tensors of stress and effective stress, and $\alpha = 1 - K_{\text{b}}/K_{\text{g}}$ is the Biot parameter which approaches one for highly porous materials, where the elastic modulus of the soil grains K_{g} is much larger than K_{b} of the bulk volume. The effective pressure

p_{eff} is computed from the phase pressures and corresponding saturations (w: wetting; n: non-wetting) via

$$p_{\text{eff}} = S_{\text{n}} p_{\text{n}} + S_{\text{w}} p_{\text{w}}. \tag{2.14}$$

The balance equation for linear momentum can be formulated as

$$\operatorname{div} \mathbb{S} + \varrho_b \mathbf{g} = 0 \tag{2.15}$$

with ϱ_b representing the bulk density and time derivatives neglected due to a quasi-static assumption.

The coupling of flow and transport with geomechanics can be realized with different numerical approaches. The simplest method is a one-way coupling approach, where the results of the flow and transport steps are given to the geomechanics part [Prei 11, Vida 09]. Other authors use explicitly coupled, partially coupled, or iteratively coupled sequential or even fully coupled schemes to solve geomechanics together with flow. The stronger the coupling, the higher the demand on robustness and computational resources. Literature on such coupling approaches is vast on this topic and we refer here without claiming to be complete to [Sett 01, Long 02, Rutq 03, Lewi 91, Rohm 10]. In particular, we like to refer to [Kim 11a, Kim 11b] for a detailed analysis when sequential coupling strategies for hydromechanical-geomechanical simulations including capillary effects work and when they fail.

Modeling geomechanical effects like deformation and stresses requires typically large domains. The underlying equation behaves elliptic and is strongly influenced by boundary conditions, i.e. the modeled properties at the edges of the modeled domains. A fixed deformation value at the boundary can affect the stresses in the domain. For example, if a boundary, where zero deformation is prescribed is too close, it may lead to an overestimation of uplift or subsidence in the domain. However, the work of, for example, [Darc 12] showed for the case of CO_2 storage that, depending on the question of interest, it may still be that flow and transport require an even larger spatial scale than local geomechanical effects.

(Bio-)Geochemistry

Chemical reactions, sometimes due to (micro-)biological activity, can be a very important part of a subsurface multiphase flow system. To account for this, reactive transport models are often coupled to multiphase flow models. Any of the phases can transport chemical or biological species which may undergo reactions on their own or with other species, upon mixing. Examples of such reactions [Lee 01, as given by] include aqueous speciation and redox reactions, precipitation/dissolution, and interface reactions. Systems in which the coupling of multiphase flow and (bio-)geochemical reactions is relevant can be found in CO_2 sequestration, reservoir souring, natural attenuation, radioactive waste repositories etc.

Each reactive chemical species is a component of one or more phases and can be accounted for with a mass balance equation as in Equation (2.5). Potential reactions are accounted for by the source/sink term, see Figure 2.5:

$$q^{\kappa} = \hat{q}^{\kappa} + r^{\kappa}. \tag{2.16}$$

Here, $\hat{q}^{\kappa}$ represents external sources and sinks. The reaction term r^{κ} can be a function of

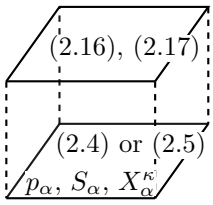

Figure 2.5: Geochemistry: Reactive source term (2.16), (2.17) in the mass balances (2.4) or (2.5).

several variables and parameters:

$$r^\kappa = r^\kappa(X^\kappa_\alpha, p_\alpha, S_\alpha, T, t, \ldots). \tag{2.17}$$

A model which describes (bio-)geochemical reactions couples to a multiphase flow (and/or heat transfer, geomechanics) model through r^κ which:

- can be dependent on pressure and saturation, temperature or on the mixing between two or more components.
- may have an effect on flow parameters such as permeability and porosity (for example, dissolution/precipitation), or may be endo- or exothermic.

For further reading on this topic, the reader is referred to the review papers [Gaus 08, Dent 11] and the references therein, as well as to [Xu 01, Lee 01, Lich 96].

Multi-Porosity Models

The concept of multi-porosity arises when a flow system consists of two or more distinct characteristic media with significantly different flow properties. It is most commonly applied to fractured systems, in which case, the fractures exhibit very fast flow but almost no storage whereas the matrix (in which the fractures are embedded) allow little or no flow but very large storage capacity.

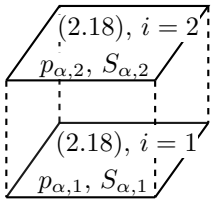

Figure 2.6: Multi-porosity models: Mass balance (2.18) for each continuum i, coupling by exchange terms (2.19).

One defines two or more continua which exist within the same REV and solves separate mass balance equations in each continuum. Each continuum has its own set of parameters (such as porosity and permeability) and variables (such as pressure and saturation). The different equations are coupled by exchange terms e. For example, for immiscible two-phase flow, Equation (2.4) would become

$$\frac{\partial}{\partial t}\left(\phi_i \varrho_{\alpha,i} S_{\alpha,i}\right) + \operatorname{div}(\varrho_{\alpha,i}\mathbf{v}_{\alpha,i}) = \hat{q}_{\alpha,i} + e_\alpha \tag{2.18}$$

for each continuum i, see Figure 2.6. The exchange of mass between two continua is then assumed to be proportional to the difference in potential between the two continua, for example,

$$e_\alpha = \frac{\varrho_\alpha a}{\mu_\alpha}(p_{\alpha,2} - p_{\alpha,1)}. \tag{2.19}$$

The parameter a can depend on, for example, the geometry and the effective permeability of the interface between the continua.

Numerous articles on double-porosity models can be found in the literature, for example, in [Bare 60, Arbo 89, Ryzh 07, Rami 09]. There are several variations and extensions. A prominent example is the so-called MINC (multiple interacting continua) method [Prue 85, Smit 99, Gong 09], in which the blocks of the rock matrix are discretized in a sequence of nested elements. The thermodynamic state of each element or continuum depends on its distance from the nearest fracture. Each continuum can exchange mass and/or heat with neighboring continua. This introduces a transient component to the inter-porosity flow, alleviating one of the biggest drawbacks of the classical double-porosity models.

2.3.2 Multi-Scale Approaches

The discretization of a modal domain usually depends on the relevant length scales. Thus, the smallest length scale which is important determines the discretization resolution. This can lead to very fine grids which, on the one hand, allow the modeling of all relevant effects but, on the other hand, lead to a huge number of degrees of freedom and enormous computational costs. The basic idea of multi-scale models is to decrease the global degrees of freedom while preserving important features of flow and transport processes which can occur on various scales. Roughly two steps can be identified: First, important scales have to be identified. Second, the different scales have to be combined in a multi-scale model such that the global flow problem is solved on a scale as coarse as possible while still accounting for smaller-scale processes. The multi-scale method has to provide scale transfer operators or mechanisms in both directions: from fine scales to coarser scales (upscaling) and from coarse scales to finer scales (downscaling) , see Figure 2.7. However, use of simplified

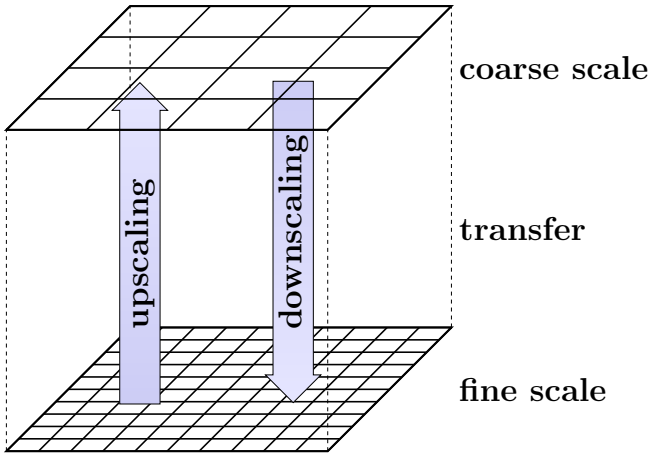

Figure 2.7: Idea of multi-scale modeling: Solve on different scales and transfer information via upscaling and downscaling operators.

methods applying only upscaling or only downscaling operators can be sufficient if the

coupling between the different scales is weak. Let us consider for example a heterogeneous parameter field for which the assumption of scale separation is reasonable. In this case a pure upscaling method can be applied if results are only required in a coarse resolution.

Many of the existing multi-scale methods which are applied to porous-medium flow are developed to deal with elliptic (or parabolic) partial differential equations which arise from a fractional flow formulation (Section 2.2). They are used to solve the pressure equation (2.9) and to reconstruct velocity. Commonly, the set of equations is further simplified to

$$\operatorname{div}\left(-\lambda_{\mathrm{t}}\mathbb{K}\,\mathbf{grad}\,p\right) = \sum_{\alpha} q_{\alpha}, \tag{2.20}$$

$$\phi\frac{\partial S_{\alpha}}{\partial t} + \operatorname{div}(f_{\alpha}\mathbf{v}_{\mathrm{t}}) = q_{\alpha}, \tag{2.21}$$

neglecting capillary pressure, gravity as well as compressibility. Once the elliptic pressure equation (Equation (2.20)) is solved applying a multi-scale method, the transport equation (Equation (2.21)) is often solved explicitly on the fine scale. Many of the existing methods which will be partly reviewed in the following are able to model this simplified system very efficiently and accurately. However, efficient multi-scale methods for modeling both pressure and transport, and for cases in which important physical effects such as capillarity are significant are, to the authors' knowledge, still part of ongoing research.

In the following, we provide a brief overview of common multi-scale methods.

Homogeneous Multi-Scale Methods

Homogeneous multi-scale methods inherently give approximate solutions on the finest scale (grid). Homogeneous, in this context, means that one model is used at different scales. They consist of the traditional numerical approaches to deal with multi-scale problems, for example, multi-grid methods [Bram 93, Brig 00, Stub 01, Trot 01], multi-resolution wavelet methods [Catt 03, He 08, Jang 04, Urba 09], multi-pole techniques [Gira 06, Of 07, Torn 08, Yao 08], or adaptive mesh refinement [Ains 00, Babu 01, Mull 03]. Due to the usually enormous number of degrees of freedom on the fine scale, this direct numerical solution of real-world, multiple-scale problems is often only possible by means of high performance computing.

Heterogeneous Multi-Scale Methods

The general goal of the heterogeneous multi-scale method [E 07] as in other multi-scale-type methods, is to capture the macroscopic behavior of multi-scale solutions without resolving all the fine details of the problem. Compared to homogeneous multi-scale methods, these methods are heterogeneous in the sense that they include the multi-physics nature of multi-scale problems. This means that they provide a general methodology to couple different models which are valid at different scales. The idea is to selectively incorporate smaller-scale data when needed, depending on the characteristics of a particular problem. A key component for the improvement of numerical efficiency is the exploitation of the separation of scales (spatial/temporal). The heterogeneous multi-scale method was first introduced in [E 03b], and clearly described in [E 03c]. To the authors' knowledge, so far, the heterogeneous multi-scale method has not specifically been applied to the problem of multi-phase flow in porous media.

Variational Multi-Scale Method

In [Hugh 95, Hugh 98], Hughes et al. present the variational multi-scale method that serves as a general framework for constructing multi-scale methods. An important part is to split the function space into a coarse part, which captures low frequencies, and a fine part, which captures high frequencies. An approximation of the fine-scale solution is computed and used to modify the coarse-scale equations. There have been several works on convection–diffusion problems using the variational multi-scale framework [Codi 01, Hauk 01, Juan 05, see, for example], and recently it has also been applied as a framework for multi-scale simulation of multi-phase flow through porous media [Juan 05, Juan 08a, Kees 08, Nord 09a, Calo 11].

Multi-Scale Finite-Element Method

Another multi-scale method, the multi-scale finite-element method, was presented in 1997 [Hou 97]. The theoretical foundation is based on the homogenization theory. The main idea is to solve local fine-scale problems numerically in order to use these local solutions to modify the coarse-scale basis functions. Like for standard finite-element methods, a drawback of this method is the violation of the local conservation property. Consequently, in the last decade, the idea of the multi-scale finite-element method has been transferred into the framework of mixed finite-element methods, see Figure 2.8. These mixed, multi-scale

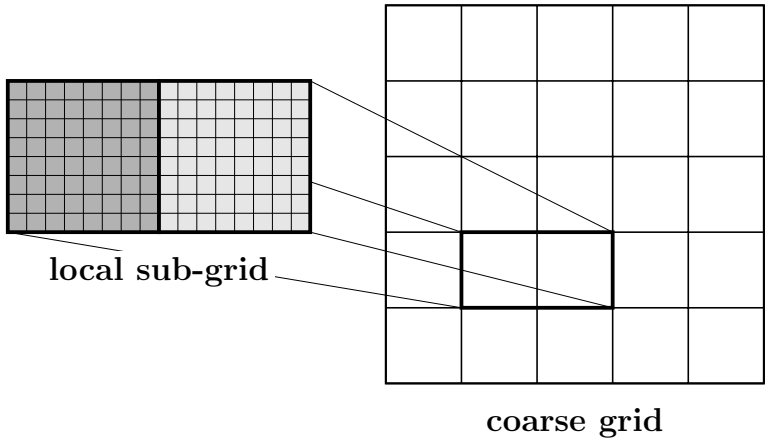

Figure 2.8: Multi-scale mixed-finite-element method: Domain of the local problem for the calculation of the basis function for the middle coarse edge. Fine grid (thin lines), coarse grid (thick lines). In the standard approach, a constant source term q_c is prescribed on the left coarse element (dark shaded), while $-q_c$ is prescribed on the right one.

finite-element methods allow the efficient capture of small-scale effects on the large scale as well as the reconstruction of mass-conserving, fine-scale velocities [Chen 03b, Aarn 06, Aarn 08a, Aarn 08b, Arbo 07, Efen 07, Kim 07, Kipp 08].

Multi-Scale Finite-Volume Method

The multi-scale finite-volume method was introduced in [Jenn 03], motivated by the multi-scale nature of subsurface (porous-medium) flow. The underlying idea is to construct

coarse-scale transmissibilities which account for fine-scale effects and lead to a multi-point approximation for the finite-volume solution algorithm. For the construction of the transmissibilities, sets of basis functions have to be computed from local numerical solutions of fine-scale problems that are associated with dual coarse grid cells, see Figure 2.9. Further sets of local basis functions might be needed, for example, to recon-

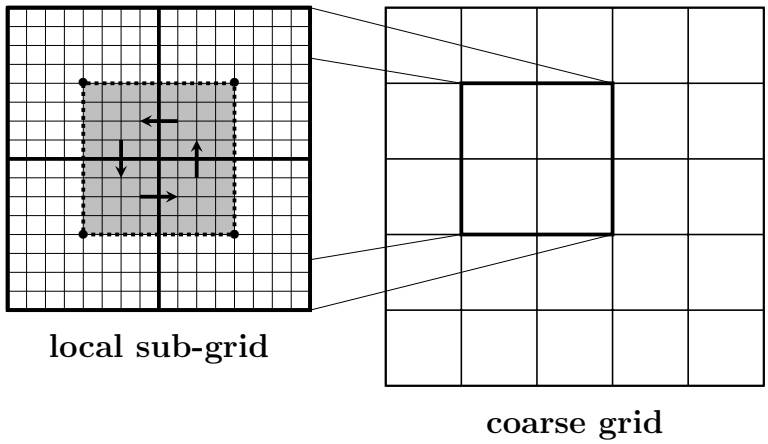

Figure 2.9: Multi-scale finite-volume method: fine grid (thin lines), coarse grid (thick lines), dual coarse grid cell (shaded, dashed lines) associated with the center node.

struct a conservative fine-scale velocity field from the coarse-scale pressure solution. In recent years, the method has become able to deal with increasingly complex equations [Haji 08, Jenn 06, Lee 08, Luna 06, Luna 07, Luna 08]. Further, it has been applied to elliptic (parabolic) pressure equations as well as hyperbolic saturation (transport) equations [Lee 09]. As for many other multi-scale approaches, the quality of the multi-scale results strongly depends on the localization conditions (usually local boundary conditions) used to solve the local fine-scale problems.

Multi-Scale Methods and Domain Decomposition

By comparing the formulations, [Nord 08] observe that the multi-scale finite-volume method is a special case of a non-overlapping domain-decomposition preconditioner. They go on to suggest how the more general framework of domain decomposition methods can be applied in the multi-scale context to obtain improved multi-scale estimates. Further work on multi-scale modeling of flow through porous media using a domain-decomposition preconditioner can be found in [Galv 10, Sand 11].

Vertical Equilibrium Methods

Vertical equilibrium methods are special kinds of multi-scale methods. An upscaled model is derived through vertical integration of the three-dimensional governing equations for two-phase flow under the assumptions of vertical equilibrium, complete gravity segregation, and a sharp-interface between the two phases. The resulting model is a two-dimensional model for flow in the lateral directions only (vertical flow is zero), see Figure 2.10. The underlying assumptions are sufficiently justified in many CO_2 sequestration scenarios, which currently are the main application areas of vertical equilibrium models. Formulations with [Gasd 09] and without [Gasd 11a] upscaling of convective mixing exist.

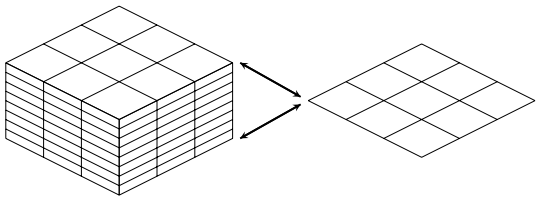

Figure 2.10: Vertical equilibrium methods: upscaling by vertical integration from a three-dimensional to a two-dimensional model.

Adaptive Upscaling Methods

Classical upscaling strategies comprise the method of asymptotic expansions (homogenization) and volume averaging [Whit 98, Gray 93, Panf 00]. Depending on the assumptions which are made during the upscaling step, different kinds of new coarse-scale parameters or functions occur in the upscaled equations. These parameters implicitly include fine-scale information which gets lost due to the averaging. Numerical upscaling methods supply a tool to calculate coarse-scale functions or parameters. They solve representative fine-scale (flow or transport) problems to calculate averaged quantities (such as permeabilities, transmissibilities, pseudo functions etc.). There are both local and global methods. Local methods choose sub-domains of a size much smaller than the global scale (for example, the size of one coarse grid block) and calculate effective parameters locally for each of this sub-domains, see Figure 2.11 [Durl 91, Pick 96, Wall 02a, Wall 02b, Efen 04]. Global meth-

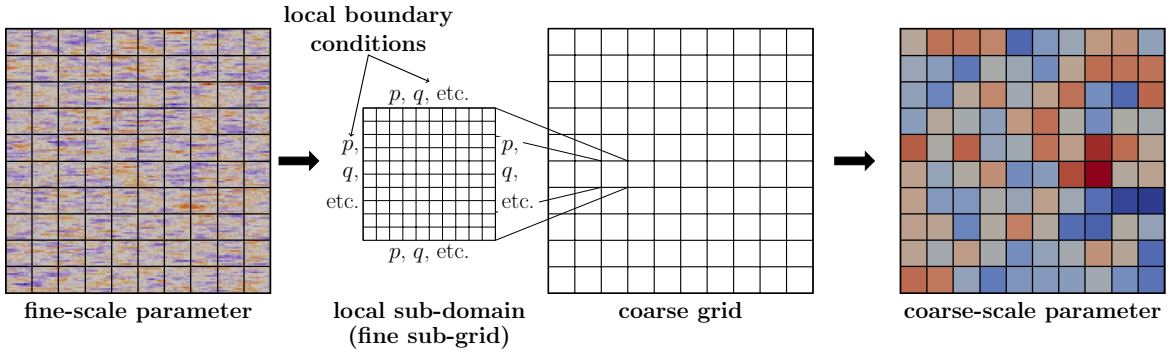

Figure 2.11: Workflow of a local numerical upscaling method: Define local subdomains (for example, coarse grid blocks) – solve local fine-scale flow problems (boundary conditions static – local method, or dynamic – (adaptive) local-global method) – calculate effective coarse scale parameters from local fine-scale solutions.

ods solve representative fine-scale problems on the global scale [Kyte 75, Ston 91]. Local methods can be further extended to (adaptive) local-global methods. In this case a downscaling step is added to the method to approximate local fine-scale boundary conditions from the global coarse-scale solution. Depending on the required accuracy, the effective coarse-scale parameters have to be recalculated each time the global solution changes noticeably [Chen 03a, Chen 06a, Chen 09]. Combining numerical upscaling and downscaling, (adaptive) local–global methods can also be viewed as multi-scale methods.

Moreover, upscaling can also occur in a multi-stage approach, i.e. effective quantities are calculated successively for different scales [Lerd 05, Rhod 09]. Likewise, new upscaling

strategies aim to incorporate pore-scale simulations directly to compute complex multi-phase flow functions or capture small-scale physics in regions where continuum-scale models that are based on REV-averaged results fail, [Holm 10, Batt 11].

2.3.3 Multi-Dimensional Approaches

Whenever the effective dimensionality of a submodel is smaller that of another submodel, the resulting coupled model has to account for submodels of different dimensions. For the full-dimensional submodel, the character of the coupling usually can be seen as surface coupling, while for the lower-dimensional model, one usually speaks of a volume coupling. The two most prominent examples of multi-dimensional coupling in porous-medium flow are discrete fracture approaches and subsurface–surface coupling.

Discrete-Fracture-Matrix Models

In discrete fracture approaches, the geometrical structure of the fractures, i.e. orientation and aperture, is discretely resolved by the grid. If the fractures are modeled with equi-dimensional discretization techniques [Geba 02], one faces a huge number of degrees of freedom. Modeling the fractures as lower-dimensional objects is an alternative approach and subject of many monographs and research papers [Diet 05, Basq 05, Haeg 09, Neun 03, Weat 08, Reic 06, Sand 12].

Under certain assumptions, it is possible to disregard the flow simulation in the surrounding porous medium, which yields an essentially uncoupled problem and is referred to by DFN (discrete fracture networks). Here, we focus on the discrete fracture method (DFM), where flow in both, fracture and matrix, is simulated. Most often, the lower-dimensional fracture network is treated as a porous medium on its own, with defining parameters porosity and permeability which are strongly different from those of the surrounding porous medium. Correspondingly, the same model equations (2.4)–(2.7) are chosen, where the differential operators and the vector fields are interpreted with respect to the fracture tangent plane, and the behavior of the quantities in normal direction, i.e. the upscaling to the full-dimensional fields, is assumed to be known. The coupling between the fracture network and the full-dimensional porous matrix usually is prescribed by a similar exchange term (2.19) as in the double-porosity models, which depends on the pressure difference between fracture and matrix. However, the meaning of the coupling condition (2.19) is slightly different: while it still resembles a volumetric source term for the lower-dimensional fracture, it is closer to an internal boundary condition for the full-dimensional matrix. There are numerous extensions and alternatives to the standard approach. For example, in [Mart 05], a rigorous mathematical derivation of coupling conditions starting from equi-dimensional models is given.

Related to the coupling of a two-dimensional fracture network and a three-dimensional porous matrix are models for the description of a three-dimensional porous medium which completely overlaps a network of one-dimensional entities. These multi-dimensional models can be found for a variety of applications such as root water uptake [Dous 06], mining shafts [Doga 09], or blood vessels and human tissue [DAng 08].

Subsurface-Surface Coupling

Models for the description of subsurface–surface coupling provide another example of multi-dimensional coupling. Most often, the goal here is to understand flow and transport processes in a hydrosystem which consists of rivers and lakes, the unsaturated zone, and, possibly, groundwater aquifers. A good account of research efforts is provided in [Flec 10] and the corresponding special issue on groundwater–surface-water interaction, as well as in [Span 09], to which we would like to add the recent contributions [Shen 10, Suli 10, Weil 11].

For the full-dimensional subsurface flow, the commonly employed model is the Richards equation which is derived from (2.4) by assuming that the air phase is infinitely mobile compared to the water phase. As a consequence, the air-phase pressure is assumed to be known, and only one independent mass balance equation has to be solved for the unknown water-phase pressure or, more traditionally, for the piezometric head. For the lower-dimensional surface flow (one-dimensional for rivers and two-dimensional for lakes), the corresponding model is usually based on a depth-(2d) and width-(1d) integrated form of the Navier–Stokes equations, most prominently, the standard shallow water equations or simplified forms. Like for fracture networks, the coupling is performed by exchanging source and sink terms depending on the pressure difference between the different subdomains (2.19).

While the approaches for discrete-fracture-matrix models and subsurface-surface coupling are conceptually very similar, the main difference is that, in the case of discrete fracture or pipe networks, the porous matrix completely overlaps the lower-dimensional subdomains, whereas, in the case of subsurface–surface coupling, the surface domains can be interpreted as part of the outer boundary of the subsurface domain. This fact greatly simplifies the development and implementation of a coupled numerical model.

2.3.4 Multi-Compartment Approaches

Multi-compartment coupling approaches divide the model domain into subdomains sharing common interfaces. The coupling is achieved by enforcing appropriate interface conditions. In physical terms, these interface conditions should state thermodynamic equilibrium (mechanical, thermal, and chemical equilibrium), while in mathematical terms, they often correspond to the continuity of the employed primal and dual variables, for example, pressure and normal velocity. Examples of surface coupling are the coupling of porous-medium-flow and free-flow domains. In contrast to the subsurface-surface coupling described above, both subdomains are treated in a full-dimensional way. Here, the case of one-phase, one-component flow in both subdomains has been thoroughly investigated, for example, by [Beav 67, Disc 02, Gira 09, Jage 09, Layt 03], see Figure 2.12. Recently, the concept has been extended to cover two-phase, compositional, non-isothermal flow in the porous medium and one-phase, compositional, non-isothermal flow in the free-flow subdomain, [Most 11, Babe 12].

While the aforementioned example couples two different flow regimes, many studies concentrate on the coupling of different processes inside one porous-medium domain. In [Albo 99], the authors present an interface concept to couple two-phase flow processes in different types of porous media. The coupling of different models for one-, two-, or three-phase flow incorporating an iterative non-linear solver to ensure the interface coupling conditions was presented in [Pesz 00]. Usually, the choice of the subdomains is predefined by expert knowledge and fixed for the whole simulation. Algorithms for an adaptive subdomain selection rarely exist. One exception is the work described in [Frit 12], where the

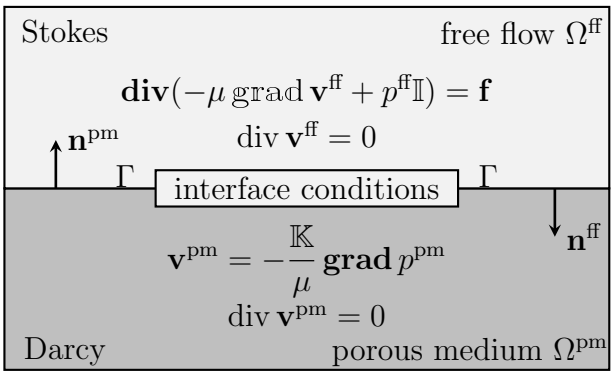

Figure 2.12: Multi-compartment coupling of single-phase single-component isothermal Stokes flow with Darcy flow, [Most 11].

space occupied by each subdomain is automatically adapted in each time step.

2.4 Temporal Coupling

Temporal model-coupling approaches can be divided into two main subcategories: split-operator methods and sequential temporal coupling methods. In Section 2.4.1, we provide a very brief overview of split-operator methods, while in Section 2.4.2, a detailed exposition of sequential temporal coupling approaches is provided by means of two applications.

2.4.1 Split-Operator Methods

Split-operator methods use different approximations for different portions of the overall transient operator. They allow an optimized treatment of the characteristic behavior of the equations, for example, with respect to parabolic (diffusive) or hyperbolic (advective) flow and transport processes or in combination with reactive transport. Different mathematical

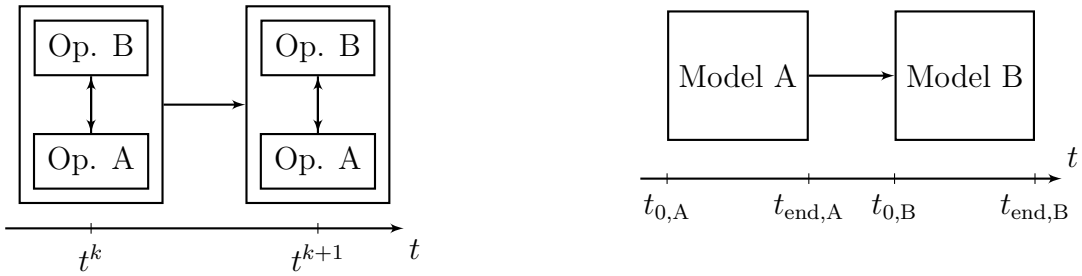

Figure 2.13: Two subcategories of temporal coupling approaches: operator-split methods (left), sequential temporal coupling (right).

behavior can be addressed by tailored numerical methods. For example, strongly hyperbolic processes require schemes such as first-order upwinding to avoid problems with oscillatory solutions, while parabolic processes can be solved robustly with central-differences discretization. The literature provides abundant examples of split-operator approaches, for

example, [Mill 93, Kann 03, Carr 04]. Split-operator approaches differ, for example, in the way the time-stepping procedure is controlled. Whether the coupling of the splitted operators is done just sequentially, iteratively, or with a sub-stepping procedure during a time step influences the required computational efforts and the introduced errors. A comprehensive survey of split-operator concepts was recently conducted by [Gasd 11b].

In contrast to split-operator methods, the temporal coupling idea as introduced below uses temporal adaption of the complexity of the conceptual model due to differences in the complexity of the governing processes, see Figure 2.13. While split-operator methods – even those denoted as sequential split-operator methods – can be viewed as a way to treat different portions of the operator in parallel as simulation time proceeds, the approach in the following section uses coupling of distinct time periods sequentially in time.

2.4.2 Sequential Temporal Coupling: Time Periods with Different Process Regimes

Model coupling in time can be an option to save computational costs when the dominating processes of interest (and relevance) change over time. A sequential coupling of models allows the best-possible temporal adaption to the required processes. In general, the complexity of a mathematical/numerical model should, of course, always be adapted to achieve the necessary accuracy with an acceptable computational effort. Sequential model coupling, as it is proposed here, involves two basic steps: (i) development of criteria which indicate when a coupling is reasonable; (ii) definition of coupling interfaces which transfer the required information between the coupled models.

Distinct time periods must be identified, where different process regimes prevail with respect to a given question of interest. We illustrate this below with two examples.

Example: Soil Remediation

The example addresses infiltration and propagation of non-aqueous phase liquids (NAPLs) in the subsurface and subsequent in-situ remediation, for example, by enhanced soil-air extraction with steam/air injection.

Figure 2.14 gives a schematic illustration of the variable influence of certain processes on this contaminant flow/transport problem over time. The processes after a hypothetical NAPL spill into the unsaturated soil zone include the spreading of the NAPL as a separate phase and as a component within other fluid phases, and a subsequent remediation of the site. Basically, three to four different time periods, dependent on the particular scenario and on the aims of the numerical simulations, can be distinguished in this sample problem: (i) The infiltration of the NAPL occurs on the shortest time scale. The liquid NAPL phase spreads and reaches a state of rest due to capillary trapping or due to structural heterogeneities. The processes are dominated by a multiphase system with liquid NAPL, liquid water, and gas. Neglecting dissolution, evaporation, or adsorption of the NAPL, the processes could be modeled with satisfactory accuracy using an isothermal, three-phase model. (ii) Dissolution and volatilization of the contaminant into the liquid water and into the soil air typically occur on a larger time scale. These processes can become dominant when the fluids are (almost) immobile. However, they are only relevant when diffusive/dispersive spreading compromises drinking-water quality. Modeling these processes requires compositional models. (iia) Chemical and biological degradation of contaminants, natural attenuation, adsorption, and other processes that dilute or reduce the concentration of the

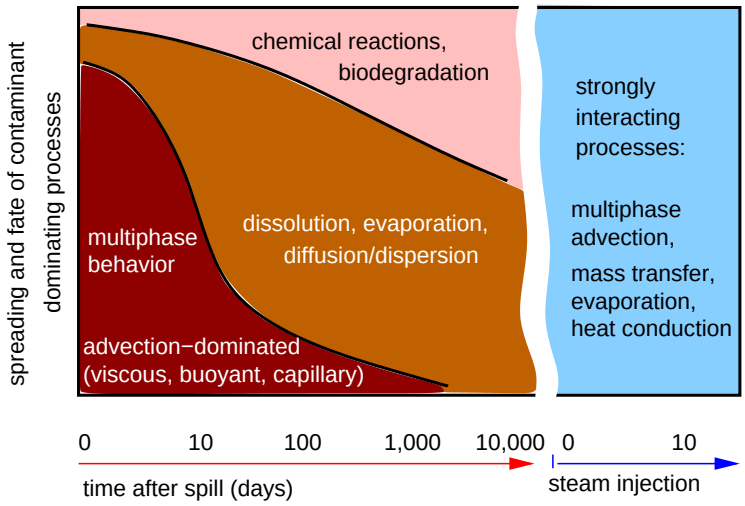

Figure 2.14: Dominating processes on different time scales after a NAPL spill and subsequent steam-injection [Clas 08].

contaminant typically occur on a large time scale. From the viewpoint of saving computationally resources, it might be useful to consider these processes with an additional model adaption in time on an even larger time scale than dissolution and volatilization. (iii) Eventually, if a remediation of such a NAPL-contaminated site is done by thermally enhanced techniques, the processes get their highest degree of complexity. A non-isothermal, multiphase, multicomponent description is then inevitable.

In this example of contaminant spreading, the time scales can be estimated by simple back-of-the-envelope calculations. [Clas 08] suggest for such a system an initial time period of days to weeks, which covers the multiphase flow, advection-dominated regime which lasts until the NAPL spill has reached the groundwater table and approaches a state of rest. Of course, this time depends, besides other factors, mainly on the permeability of the soil. Following the advection-dominated regime, phase transition (evaporation, dissolution) and diffusive spreading will dominate. The diffusion coefficients, the amount of spilled NAPL, and the surface area of the NAPL plume will lead to a time of 10 to 50 years (or even more), before the influence of diffusive spreading reduces, and for example, the background groundwater flow remains the only driving force for further spreading of the contaminant. Time period (iii) is easy to identify with the start of active thermally enhanced recovery.

Example: CO_2 Sequestration

A similar distinction of time periods with different characteristic flow/transport regimes can be obtained in the geologic storage of carbon dioxide. As Figure 2.15 indicates, a natural splitting into different dominating regimes can be obtained by following the time scales on which the different trapping mechanisms contribute to the safety of a storage project. The injection stage is characterized by a multiphase flow system driven by large pressure gradients and strong viscous and buoyant forces. At these early time, in addition to the hydraulic processes, thermal influences can also be important, for example, the Joule-Thompson effect, which leads to a cooling of the reservoir due to the pressure lowering and expansion of CO_2. With time proceeding, the importance of compositional effects increases. CO_2 dissolves in the initially present brine and, since CO_2-enriched brine is

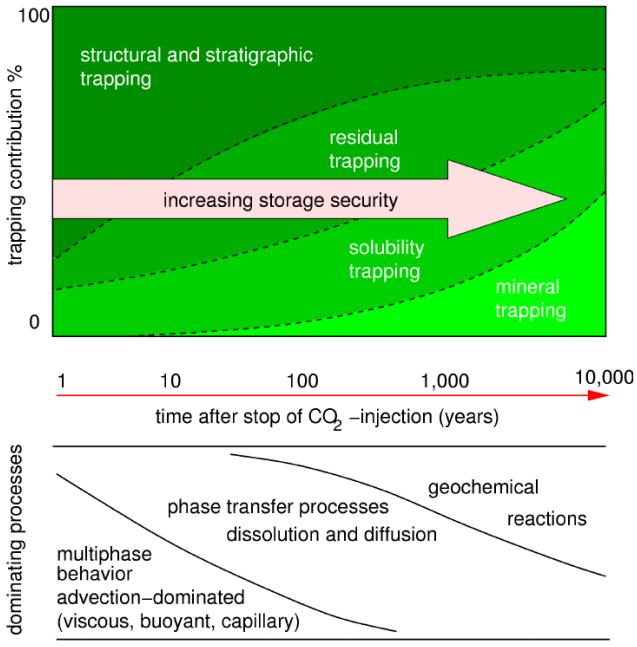

Figure 2.15: Trapping mechanisms and governing processes during and after the injection of CO_2 into saline aquifers (modified after IPCC Special Report, 2005).

heavier, leads to an unstable layering and subsequently triggers convective mixing. The growing surface of the CO_2-phase plume also causes a shift of the governing processes towards compositional effects. Eventually, multiphase flow processes cease, the CO_2 plume becomes immobile and gradually dissolves into the brine. This time period is typically expected to be tens to hundreds of years long. Geochemical processes (like in the previous example bio-degradation and natural dilution effects) can play an important role in a CO_2 storage system but it is difficult to a assign to them a lump-sum time scale, since the individual scenarios, geochemical environment etc. determine the reactions and their kinetics. A detailed discussion of sequential coupling for CO_2 injection scenarios is given by [Darc 11, Darc 12]

2.4.3 Algorithms and Transfer Conditions

The CO_2 storage scenario, as explained before, is chosen here to illustrate the numerical algorithms and transfer conditions for sequential coupling. Let us assume, that an initial period, dominated by multiphase flow, is modeled with a non-isothermal, two-phase flow model (`2pni`) without compositional effects. A second (much larger) time period is subsequently modeled with a non-isothermal, compositional, two-phase, two-component model (`2p2cni`) including CO_2 and brine as phases and components, respectively. The handover of the baton from the `2pni` model to the `2p2cni` model requires a few assumptions and constraints.

The `2pni` model solves for a constant set of primary variables, here the brine-phase pressure p_w, the CO_2 saturation S_n, and the temperature T. The set of primary variables in the `2p2cni` model, however, changes according to the local phase state. The phase state

is an information stored for each control volume and can take the values *only brine phase*, *only CO_2 phase* or *both phases*. If only one phase is present, either brine or CO_2, the value of S_n is trivial (0 or 1), and a mass fraction is used as primary variable. If, for example, the mass fraction of CO_2 in brine reaches the value of maximum solubility X^{κ}_{eq}, a second phase appears, and the primary variable is switched to the CO_2 saturation S_n (Table 2.1). For saturation values of 0.0 and 1.0, the model switches back to *only brine phase* or *only CO_2 phase*, respectively.

Table 2.1: In the `2p2cni` model, the set of primary variables depends on the phase state.

primary variables		
only brine phase	only CO_2 phase	both phases
p_w, $X_w^{CO_2}$, T	p_w, $X_n^{H_2O}$, T	p_w, S_n, T
mass fraction		
only brine phase	only CO_2 phase	both phases
$X_w^{CO_2} < X_{eq}^{CO_2}$	$X_n^{H_2O} < X_{eq}^{H_2O}$	$X_w^{CO_2} = X_{eq}^{CO_2}$ $X_n^{H_2O} = X_{eq}^{H_2O}$

Switching from the `2pni` model to the `2p2cni` model, i.e. coupling the two models, requires transfer of the primary variables at each node of the grid for which the mass of CO_2 must be conserved. In single-phase regions in the `2pni` model, the mass fraction of CO_2 in the brine phase ($X_w^{CO_2}$) or the mass fraction of H_2O in the CO_2-rich phase ($X_n^{H_2O}$) can be initialized with zero in the subsequently applied `2p2cni` model. Where both phases co-exist in the `2pni` model, the CO_2 saturation in the `2p2cni` model needs to be corrected locally after the model coupling, since there is CO_2 mass in the brine phase due to the assumed maximum equilibrium solubility $X_{eq}^{CO_2}$ (Table 2.1). The equality of the CO_2 mass in a given control volume before and after the model coupling leads to the following equation:

$$\{S_n \varrho_n\}_{\texttt{2pni}} = \{S_n X_n^{CO_2} \varrho_n + S_w X_w^{CO_2} \varrho_w\}_{\texttt{2p2cni}} \tag{2.22}$$

$\{S_w\}_{\texttt{2p2cni}}$ can be replaced by inserting the algebraic supplementary conditions for the sum of the saturations (Equation (2.3)) and for the phase pressures (Equation (2.8)). Solving for $\{S_n\}_{\texttt{2p2cni}}$ leads to:

$$\{S_n\}_{\texttt{2p2cni}} = \frac{\{S_n \rho_n\}_{\texttt{2pni}} - \{X_w^{CO_2} \varrho_w\}_{\texttt{2p2cni}}}{\{\varrho_n X_n^{CO_2} - \varrho_w X_w^{CO_2}\}_{\texttt{2p2cni}}} \tag{2.23}$$

The reduced S_n value after this transformation also has an impact on capillary pressure which is lower than modeled with the `2pni` model. As a consequence, the value of CO_2 pressure is also lower. This, in turn, causes a change in the maximum solubility of CO_2 in the brine phase which also has an influence on the brine density. Thus, a few iterations with updated `2p2cni` terms on the right-hand side need to be performed for Equation (2.23).

Around the boundaries of the CO_2 plume, small values of $\{S_n\}_{\texttt{2pni}}$ typically occur. With the aforementioned transformation, this can lead locally to negative $\{S_n\}_{\texttt{2p2cni}}$ in Equation (2.23), which means that there is not enough CO_2 present to reach the maximum

solubility in the brine phase. In this case, the phase state in the `2p2cni` model is set to *only brine phase*, and the CO_2 mass fraction in brine can be calculated as follows:

$$\begin{aligned} \{X_{\mathrm{w}}^{\mathrm{CO}_2} \varrho_{\mathrm{w}}\}_{\texttt{2p2cni}} &= \{S_{\mathrm{n}} \rho_{\mathrm{n}}\}_{\texttt{2pni}} \\ \{X_{\mathrm{w}}^{\mathrm{CO}_2}\}_{\texttt{2p2cni}} &= \frac{\{S_{\mathrm{n}} \varrho_{\mathrm{n}}\}_{\texttt{2pni}}}{\{\varrho_{\mathrm{w}}\}_{\texttt{2p2cni}}} \end{aligned} \tag{2.24}$$

As in Equation (2.23), a few iterations are necessary to take the influence of the resulting CO_2 mass fraction on the value of $\{\varrho_{\mathrm{w}}\}_{\texttt{2p2cni}}$ into account. This method guarantees the conservation of the CO_2 mass in the system, however, due to the modifications in saturation and composition it does not conserve the mass of H_2O.

Thus, it becomes clear that the switching interface between two sequentially coupled models requires the consideration of constraints which are specifically important to the question of interest. In the presented examples, these constraints are the mass conservation of the components CO_2 or NAPL. The propagation and spreading of exactly these components are the aim of modeling, and no mass should be lost or produced by numerical errors.

2.4.4 Discussion: Introduced Errors and Numerical Performance

The two major criteria to justify a sequential model coupling are expressed in the following questions:

- Which errors are introduced when using simpler models during certain time periods?
- How much computation time can be saved by the coupling?

A detailed analysis and investigation of these questions is current work in the group of the authors [Darc 12]. Currently, we have to leave it at a preliminary and brief summarizing discussion.

Finding criteria which identify the best point in time to switch from one model to another involves minimizing the introduced errors and maximizing the saved CPU time. In Figure 2.16, the CPU time is plotted versus the simulation time. The simulation of a one-year injection period and subsequent 1000 years of relaxation takes 10.59 h with the `2p2cni` reference model and 3.19 h with a sequentially coupled model `2pni-2p2cni` on a

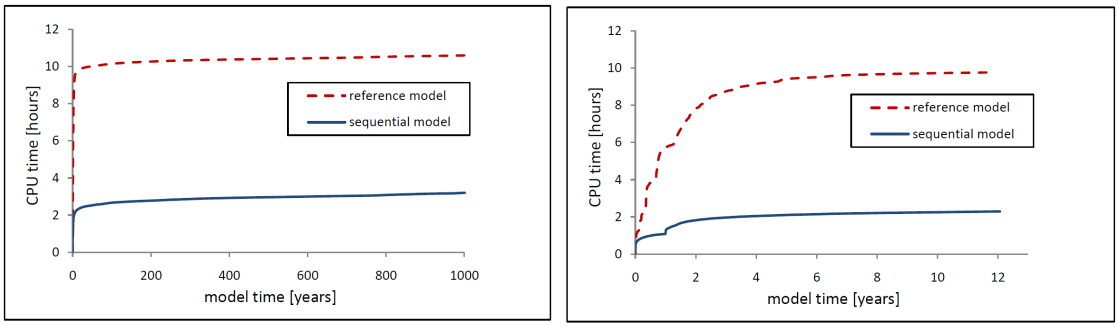

Figure 2.16: CPU time in hours versus simulation time in years for the sequential (`2pni-2p2cni` and the reference (only `2p2cni`) model.

single core of an *Intel Core 2 Duo E6300* processor with 1.86 GHz. In this example, sequential coupling leads to a speed-up of roughly factor 3. As expected, a large speed-up takes place during the injection period, when the less complex `2pni` formulation is applied in the sequential model. Besides other reasons, the reference model is slowed down mainly by the large number of phase switches that occur during this period. Phase switches and primary variable substitution generally reduce the performance of the Newton algorithm applied in each time step.

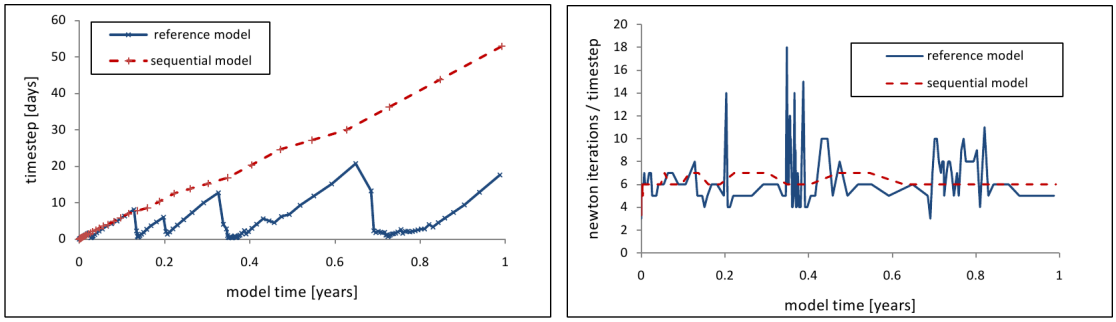

Figure 2.17: Number of newton iterations per time step and time-step size for the sequential and the reference models during the injection period.

This can be seen in the development of time-step size and Newton iterations during model time as shown in Figure 2.17. The sequential model is faster due to fewer non-linear solution steps, but the main differences lie in the much better convergence and the larger time steps of the `2pni` model during the injection period. Even though another setting of the time-step management (for example different accuracy criteria) can have an influence on the exact value of the resulting speed-up factor, the convergence of the compositional model will always be reduced due to the phase switches.

There are other factors that need to be considered, of course. For example, grid refinement or heterogeneities can influence the speed-up factor.

The errors introduced by the use of a simpler model are the other side of the coin. For this example, one could measure it by differences in local CO_2 saturations, mass fractions, pressures etc. The errors introduced by sequential coupling in time are dependent on the time of the coupling and the assumptions in the conceptually simpler model. The tolerable size of errors determines whether this kind of sequential coupling is applicable or not, and at which time the error is tolerable while still computational speed-up is gained. Details and a comprehensive discussion is given in [Darc 12]. It can be shown, for example, that the sequentially coupled model overestimates the propagation of the CO_2 plume since all the CO_2 is in the mobile phase and none can dissolve before the switch to the `2p2cni` model is done. Without going into too much detail, the general conclusions of this example are:

- The model predictions for the distribution of CO_2, both in phase and dissolved in brine, are in excellent agreement when large time periods are considered after the coupling.

- The sequentially coupled approach leads to significant savings of CPU time.

It is commonly known that random processes like the triggering of fingers by instabilities is in reality always dominated by permeability perturbations or local heterogeneities.

Thus, deviations occurring in homogeneous scenarios in the mass fraction distributions of dissolved CO_2 are considered as non-limiting for the applicability of the proposed approach.

As already mentioned, it is of particular importance to develop criteria of 'when' and 'how' such coupling can be done, and what the error introduced by neglecting some of the processes during certain periods is.

2.5 Summary and Perspectives

This review highlights the relevance and diversity of coupling concepts for multi-phase, multi-component flow and transport in porous media. Generally speaking, the need for such concepts arises when one has to deal with very large temporal and spatial scales raising the need for specialized sub-models that require coupling or when different sets of governing equations are valid in the different parts of the overall model domain.

A general classification of coupled models is suggested. To this end, coupling methods are divided into temporal and spatial coupling, the latter of which is subdivided into volume and surface coupling methods. A further classification of the spatial concepts yields multi-process, multi-scale, multi-dimension, and multi-compartment techniques.

These concepts are particularly important for large-scale applications such as groundwater protection, nuclear-waste disposal, CO_2 storage, oil recovery etc. for which the comprehensive evaluation of risk and feasibility typically requires a huge number of simulations. They are also necessary for applications with obvious discontinuities in their domains such as soil dry-out and evaporation processes, fuel cells, fractured media etc.

With respect to the current and future challenges one is faced with in these fields and the continuously improving modeling capabilities, model coupling definitely has great potential. The demand for multiphase flow simulations has become huge, and the implications of decisions taken on their basis may be very severe. For example, for the selection of safe storage sites for nuclear waste, regulators, policy makers, and the society have to rely to a large extent on predictions based on very complex simulations on large domains which extrapolate current data into the distant future.

This review shows that a number of approaches exist on the conceptual level of modeling. However, a lot of development still is necessary to utilize more of the promising benefits. Many coupling approaches are still isolated. An integration of multiple coupling schemes for a particular application is challenging. For example, it might be useful for long-term processes to do a coupling both in space and time.

Further, an adaptive selection of the required physics and scales of consideration is not yet established. Adaptivity requires the formulation of distinct criteria for switching between models of different complexity or scales of consideration. The development of such criteria is difficult and often specific to the problem and the particular question; and the implementation into adaptive coupling algorithms is a research task of its own.

Finally, the challenges are not only on the conceptual level. Very often, practical problems also occur on the technical level, for example, the coupling of different software packages, non-availability of source code, differing programming languages, or problems with software–hardware interaction. A partial solution to these problems can be found by using and developing open-source software packages that allow both coarse- and fine-grained model coupling within one package or to other packages. In particular, two open-source porous-medium simulators have evolved in recent years: DuMu^x, "DUNE for Multi-{Phase, Component, Scale, Physics, ...} flow and transport in porous media" [Flem 11], and the

"Matlab Reservoir Simulation Toolbox" [Lie 12].

If future research can address these issues, achieving better flexibility and model-coupling approaches which promise greater efficiency as well as high accuracy for large-scale/long-term simulations, it is the authors' opinion that the coupling of models will be *the* essential tool for the comprehensive simulation of realistic problems in the area of multiphase flow in porous media.

3 Free-Flow – Porous-Media Coupling

Bibliographic Note: The content of this chapter is based on the following original article [Most 11]: K. Mosthaf, K. Baber, B. Flemisch, R. Helmig, T. Leijnse, I. Rybak, B.I. Wohlmuth (2011): A coupling concept for two-phase compositional porous-medium and single-phase compositional free flow. *Water Resources Research* **47**, W10522.

Summary Domains composed of a porous part and an adjacent free-flow region are of special interest in many fields of application. So far, the coupling of free flow with porous-media flow has been considered only for single-phase systems. Here, we extend this classical concept to two-component non-isothermal flow with two phases inside the porous medium and one phase in the free-flow region. The mathematical modeling of flow and transport phenomena in porous media is often based on Darcy's law, whereas in free-flow regions the (Navier–)Stokes equations are used. In this chapter, we give a detailed description of the employed subdomain models. The main contribution is the developed coupling concept which is able to deal with compositional flow and a two-phase system in the porous medium. It is based on the continuity of fluxes and the assumption of thermodynamic equilibrium, and uses the Beavers-Joseph-Saffman condition. The phenomenological explanations leading to a simple, solvable model which accounts for the physics at the interface are laid out in detail. Our model can account for evaporation and condensation processes at the interface and is used to model evaporation from soil influenced by a wind field in a first numerical example.

3.1 Introduction

Flow and transport processes in domains composed of a porous medium and an adjacent free-flow region appear in a wide range of industrial, environmental and medical applications. In this context, evaporation is an ubiquitous process, since evaporation rates and patterns affect the energy balance of terrestrial surfaces and drive an array of climatic processes. Notwithstanding its prominence for many natural and engineering applications, prediction of evaporative drying rates from porous media remains a challenge due to complex interactions between the porous medium and the free-flow system, the ambient conditions (radiation, humidity, temperature, air velocity, turbulent conditions) at the interface, and the internal porous-medium properties that lead to abrupt transitions and rich flux dynamics (see Figure 3.1).

Modeling such a coupled system while accounting for the ongoing processes in both domains is a challenging task. Often, decoupled or simplified model concepts are used [Dam 00, Schn 10]. In order to examine the limitations of these models and to extend them, a concept for two-phase compositional flow in the unsaturated zone in contact with a single-phase compositional system in the atmosphere is required. Naturally, an energy balance has to be included in order to account for the influence of the temperature on the ongoing processes.

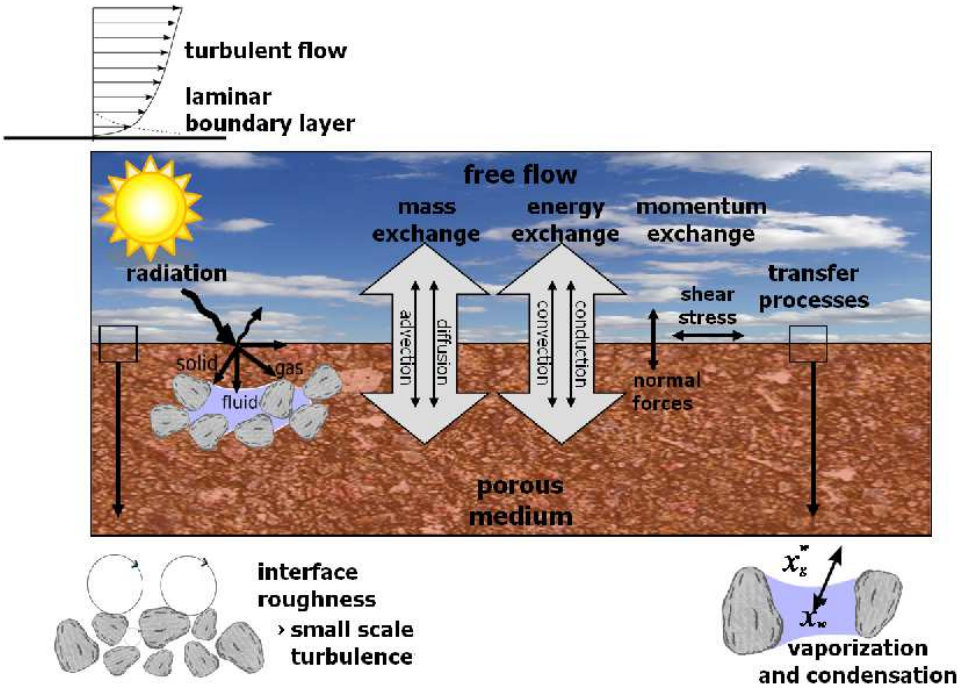

Figure 3.1: Relevant interface processes for evaporation: Solar radiation, small and larger scale turbulence, vaporization and condensation at the interface and exchange fluxes.

In the following, we present a model concept that allows the detailed description of such a coupled compositional non-isothermal two-phase system. In a first step, radiation and the influence of turbulent flow is neglected. This concept is based on existing approaches which, to our knowledge, have so far only been applied to single-phase flow, and which will be briefly reviewed in the following.

3.1.1 Basic Existing Coupling Concepts for Single-Phase Single-Component Flow

On the pore scale, the pore structure is resolved and the same type of equations, the Navier-Stokes equations, are used to describe the flow in the free-flow region and within the pores. On the REV scale, however, the potential theory is applied in the porous medium using Darcy's law and coupling strategies have to be found to couple the two domains. Two basic strategies for the description of mass and momentum transfer in coupled free and porous-medium flow on the Darcy scale can be identified [Jame 09, Shav 09] and are illustrated in Figure 3.2. In the single-domain approach, one set of equations is assumed to be valid in the whole domain and the coupling is realized via a transition zone, where material parameters are varied. In the two-domain approach two sets of equations are used for the subdomains which are coupled in terms of suitable transfer conditions at the interface. The single-domain approach (see Figure 3.3) usually involves the solution of the Brinkman equations in the entire domain [Brin 47]. This model results from a superposition of the Stokes equations and Darcy's law, requiring the introduction of an apparent viscosity inside the porous medium. There is no need to specify coupling conditions between the free-flow region and the porous medium since velocity and stress continuity are automat-

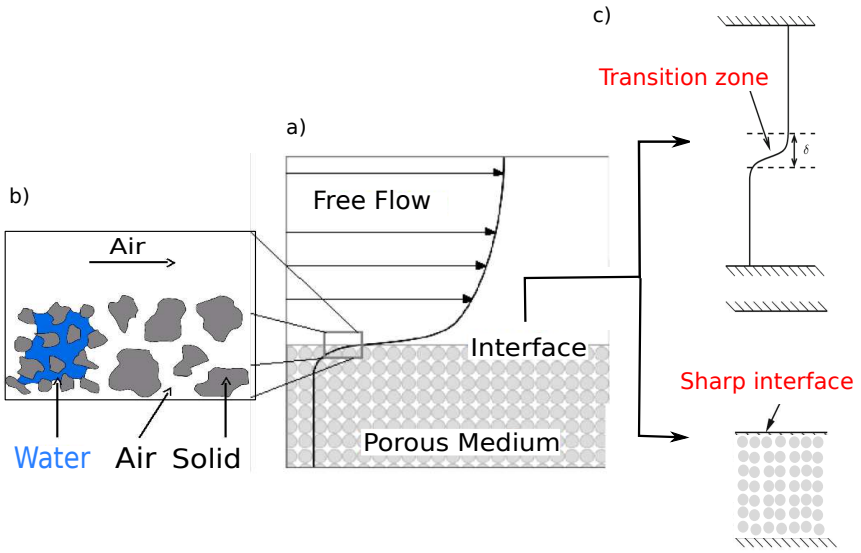

Figure 3.2: Interface descriptions: a) REV scale: velocity profile for coupled free flow (single-phase Stokes equations) and porous-medium flow (multi-phase Darcy's law), b) micro/pore scale: the distribution of all phases and pore sizes is resolved, c) interface description either as a transition zone with continuously varying parameters or as a sharp interface. (after [Chan 09])

ically satisfied. The transition between the two regions is achieved either by specifying the continuous spatial variation of physical properties such as permeability and porosity within an equi-dimensional transition zone or by admitting a discontinuous variation across a lower-dimensional interface. The physical transition zone is usually only a few grain diameters thick [Jame 09]. The choice of the parameters in this zone may decisively influence the results and, generally, it is hardly possible to determine them [Goye 03, Rose 07].

Brinkman/Stokes	**free flow**
$-\,\mathbf{div}\,(\tilde{\mu}\,\mathrm{grad}\,\mathbf{v}) + \mu\mathbb{K}^{-1}\mathbf{v} + \mathbf{grad}\,p = \mathbf{f}$ $\mathrm{div}\,\mathbf{v} = 0$	$\phi = 1$ $\lvert\mathbb{K}\rvert \gg 1$
transition zone	
$-\,\mathbf{div}\,(\tilde{\mu}\,\mathrm{grad}\,\mathbf{v}) + \mu\mathbb{K}^{-1}\mathbf{v} + \mathbf{grad}\,p = \mathbf{0}$ $\mathrm{div}\,\mathbf{v} = 0$	$\phi < 1$ $\lvert\mathbb{K}\rvert \ll 1$
Brinkman/Darcy	**porous medium**

Figure 3.3: Single-domain coupling concept for a single-phase flow system.

The two-domain approach (Figure 3.4) is based on different models in the two subdomains: the Navier-Stokes equations, which in case of low Reynolds numbers can be simplified to the Stokes equations, are applied in the free-flow region and Darcy's law is used in the porous medium. In addition to the subdomain models, suitable coupling conditions have to be specified at the interface. Realistically, processes between free-flow and porous-medium regions are not only interface-driven but the two regions interact via a transition

zone where changes in fluid properties and strong gradients in the driving forces may occur. According to [Hass 89], this transition zone can either be approximated by a simple interface devoid of thermodynamic properties or by an interface that can store and transport mass and other thermodynamic quantities. The simple interface corresponds to continuity of thermodynamic properties at the interface, whereas an interface with thermodynamic properties leads to discontinuities which are then characterized by appropriate conditions involving jump coefficients [Ocho 95, Chan 09]. One way to derive the coupling conditions is to apply the volume-averaging technique [Gray 93, Whit 98]. The resulting conditions include excess surface terms to account for the transition between free-flow and porous-medium region [Ocho 95, Chan 09]. Based on these excess terms, the jump coefficients can be derived [Vald 09a]. However, the coupling conditions are often simplified by neglecting the contribution of these terms and assuming continuity, since the characteristics of theses surface excess terms at the interface are hard to determine [Vald 07]. The decision of continuity or discontinuity has to be made for mass and momentum respectively. One approach is to guarantee the continuity of normal forces and mass conservation across the interface [Layt 03]. Alternatively, [Ocho 95] proposed a stress-jump condition obtained by volume averaging. A two-step upscaling approach and the method of matched asymptotic expansions is used by [Chan 06, Chan 07] for the derivation of a velocity-jump and a stress-jump condition at the interface.

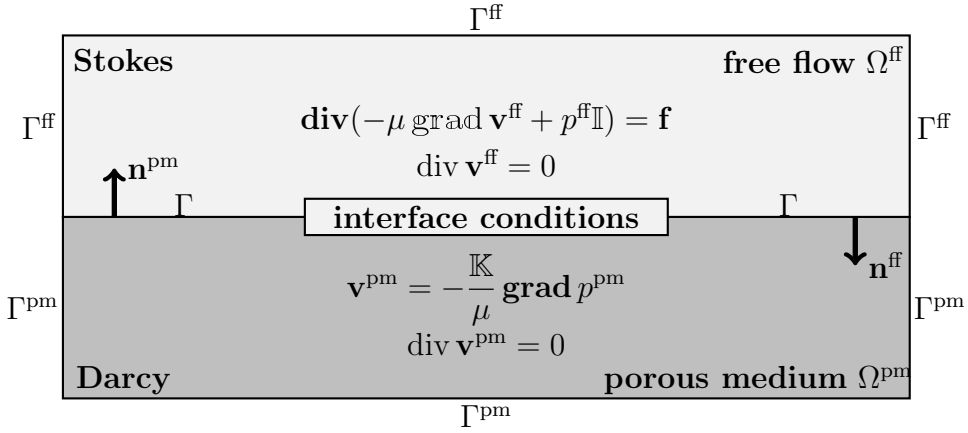

Figure 3.4: Two-domain coupling concept for a single-phase flow system.

Moreover, the Beavers-Joseph velocity-jump condition [Beav 67] is often used to provide a connection between the tangential free-flow velocity and the seepage velocity in the porous medium. It is required as an additional boundary condition for the Stokes domain, because the equations in the two domains are of different order. The relation between velocities and shear stress is given in terms of an additional parameter, the Beavers-Joseph coefficient. This parameter depends on the properties of the fluid and of the permeable material, such as the roughness of the interface, and can be determined experimentally or by numerical simulation. [Saff 71] showed that the filtration velocity (porous medium) in the Beavers-Joseph condition is negligible in comparison to the free-flow velocity. Hence, the Beaver-Joseph condition becomes a Cauchy boundary condition for the tangential free-flow velocity. The Beavers-Joseph-Saffman condition has been mathematically justified by [Jage 00, Jage 09] by means of homogenization. There exist several alternatives to the Beavers-Joseph condition, [Levy 75, Alaz 01, Goye 03].

Summing up, the challenge of the one-domain approach is the description of the spatial

variation of the parameters in the transition zone, whereas in case of the two-domain approach, the definition of coupling conditions that represent the transfer processes at the interface is the challenging task, especially, since a correct description should account for the surface excess terms. [Vald 07] analyzed the one- and the two-domain approach and pointed out that both can be derived by volume-averaging.

3.1.2 Extension to Non-Isothermal Compositional Flow

The concepts presented above have been developed for single-phase single-component systems describing the coupling for mass and momentum. However, in many applications compositional multi-phase flow occurs, and there is an urgent need for a more general model.

For an extension to a non-isothermal system, coupling approaches for the energy balance at the interface have to be found. [Prat 90] used the method of volume-averaging to analyze the one- and two-domain approach for conductive heat transfer between free-flow and porous medium. [Jame 09] showed the equivalence of the discontinuous one- and two-domain approach for a heat conduction problem, provided that the one-domain approach is mathematically interpreted in the sense of distributions. [Alaz 01] reviewed coupling conditions for conductive and convective heat transfer and found that both continuity and discontinuity of temperature and heat flux have been applied in various combinations, showing only minor differences.

For the description of transport processes in compositional single-phase flow, it is again possible to use either the one- or the two-domain approach. [Vald 06, Vald 07], for example, show the coupling of diffusive mass flux across the interface using both approaches. In [Vald 06], they describe diffusive mass transport between micro- and macro pores in packed-bed reactors and derive a jump condition for the two-domain approach from volume-averaging. Neglecting surface accumulation and surface transport excess, the jump in diffusive flux is determined by a jump coefficient that accounts for the reaction rate at the fluid-porous interface. This jump condition is supplemented by a continuity assumption for the concentrations at the interface. In case of a non-reactive medium, this leads to continuity of diffusive mass flux and concentration. [Vald 09b] extended the concept to convective transport, along with adsorption and reaction in the porous medium.

In summary, the concepts explained above allow the description of compositional non-isothermal systems and need to be extended in order to be applicable to multi-phase systems.

3.1.3 Objectives and Structure: Extension to a Two-Phase System Based on a Two-Domain Approach

The aim is to describe evaporation processes with a detailed model concept in order to be able to make well-founded assumptions, to gain a better understanding about the range of applicability of state-of-the-art models and to provide a tool for those cases where simplified model concepts fail. Therefore, it is necessary to have a flexible model that allows the modeling of separated compartments (free flow and porous media), characterized by different, arbitrarily complex flow and transport processes, and which uses clearly defined coupling conditions. In this context, our main contribution is the derivation of appropriate coupling conditions in section 3.3.

As stated above, a two-phase compositional flow model is applied in the porous medium and coupled to a laminar single-phase compositional free-flow region. The interface is assumed to be simple in the sense that it has no thickness and cannot store mass, momentum or energy. Coupling conditions for mass, momentum and energy are defined based on flux continuity and thermodynamic equilibrium. Moreover, the coupling concept employs the Beavers-Joseph concept in the knowledge of its limitations to parallel, single phase flow.

So far, the concept does not account for special interface processes like the formation of boundary layers, flow separation or radiation. These may be included in future development. Furthermore, the applied methodology is not restricted to two phases and two components, although all our systems are worked out in detail only for this special case. A generalization from two- to multi-component/multi-phase systems is straightforward. In addition, we note that all our illustrations are given for two dimensions, but the developed concept also holds for a three-dimensional case. The presented model may also be applied to applications similar to evaporation, for example, the design of industrial drying processes.

Clearly, the aim of this chapter is to obtain a general description on the REV scale and to develop a coupling concept that describes the processes at the transition of free flow and porous medium as simple as possible while still accounting for the underlying physics. The focus lies on developing coupling conditions that are based on consistent phenomenological explanations and existing model concepts. A rigorous derivation based on, for example, the thermodynamically constrained averaging theory [Jack 09] is not the objective of this article.

The chapter is structured as follows: first, the models applied in the two subdomains are explained in detail, stating the employed balance equations, constitutive relations and supplementary equations (see sections 3.2.1 and 3.2.2). Then, in section 3.3, the interface conditions for mass, momentum and energy, that allow a thermodynamically consistent coupling of the two subdomains, are explained. Finally, the fact that the coupled model derived here can be applied to evaporation processes is illustrated by a simple numerical test example.

3.2 Model Concepts in the Subdomains

In this section, we explain the two subdomain models. The respective coupling concept at the interface is presented in the next section. As illustrated in Figure 3.5, we consider two-phase flow (gas and liquid) in the porous medium, and a single phase (gas phase) in the free-flow domain. Each phase consists of two components (air, water). In the gas phase, water is present in the form of vapor. The liquid phase contains dissolved air. The following processes are to be described: transfer of heat and vapor across the interface, evaporation and condensation at the interface, vaporization/condensation and dissolution/degassing inside the porous medium.

To simplify the system in the free-flow region Ω^{ff}, we assume slow flow conditions, neglect the nonlinear inertia forces and consider a non-stationary Stokes flow. In the porous medium Ω^{pm} the multi-phase Darcy law in combination with a mass-balance equation for a component, the total mass balance and an energy balance are used, see for example [Clas 02]. Moreover, we assume local thermodynamic equilibrium to hold and all fluids to be Newtonian. The domains Ω^{ff} and Ω^{pm} are bounded and separated by the interface $\Gamma = \partial\Omega^{\mathrm{ff}} \cap \partial\Omega^{\mathrm{pm}}$ with the constant outward unit normal vectors $\mathbf{n}^{\mathrm{ff}}$ and $\mathbf{n}^{\mathrm{pm}}$ (Figure 3.4).

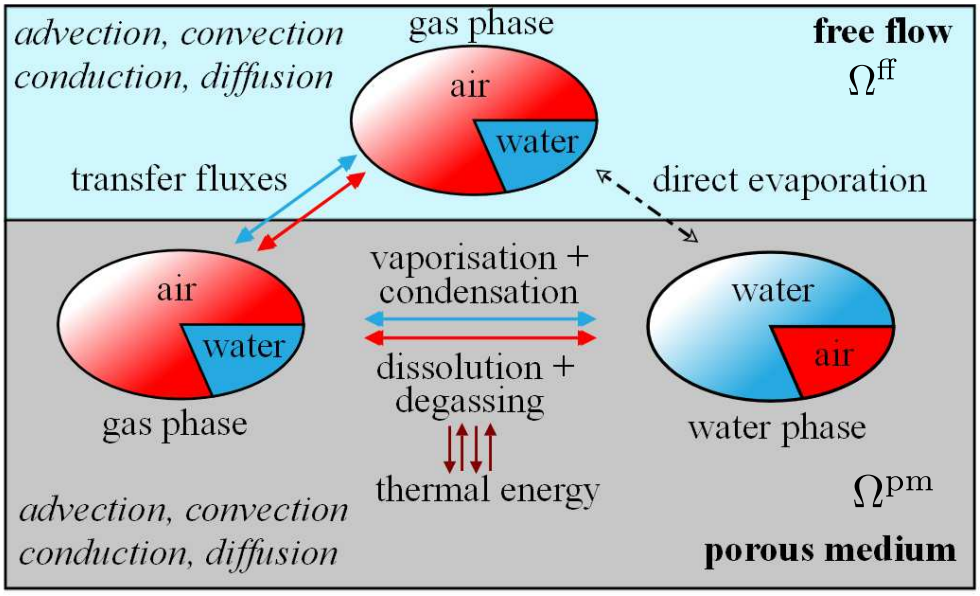

Figure 3.5: Model concept with a single phase in the free flow that interacts with two fluid phases in the porous medium.

For simplicity of notation, the superscripts (ff) and (pm) are only applied for the quantities at the interface, where (ff) refers to the values in the free-flow subdomain and (pm) stands for the porous-medium side.

3.2.1 Equations for the Porous Medium

For the porous medium, the following assumptions are considered:

1. local thermodynamic (mechanical, thermal and chemical) equilibrium,
2. a rigid solid phase (subscript s),
3. two-phase flow consisting of a liquid phase (subscript l) and a gas phase (subscript g),
4. two components being present in each phase: water (superscript w) and air (superscript a),
5. a compositional model which allows a transfer of components from one phase into the other,
6. a non-isothermal model that comprises two mass-balance equations (one for the water component and one for the total mass) and an energy balance,
7. slow flow velocities (Re $\ll 1$) allowing an application of the multi-phase Darcy law for the phase velocities,
8. negligible influence of dispersion.

Dispersion is linked to heterogeneities of flow velocities caused by differences in the pore sizes and the path lengths. It is neglected here, because of slow flow velocities and comparatively high diffusion coefficients in the gas phase.

The mass conservation in Ω^{pm} is expressed by two mass-balance equations, one for each component $\kappa \in \{\mathrm{w}, \mathrm{a}\}$,

$$\sum_{\alpha\in\{\mathrm{l,g}\}} \phi \frac{\partial \left(\varrho_\alpha X_\alpha^\kappa S_\alpha\right)}{\partial t} + \operatorname{div} \mathbf{F}^\kappa - \sum_{\alpha\in\{\mathrm{l,g}\}} q_\alpha^\kappa = 0, \tag{3.1}$$

where the mass fluxes of the components are given by

$$\mathbf{F}^\kappa = \sum_{\alpha\in\{\mathrm{l,g}\}} \left(\varrho_\alpha X_\alpha^\kappa \mathbf{v}_\alpha - \varrho_\alpha \mathbb{D}_{\alpha,\mathrm{pm}}^\kappa \mathbf{grad}\, X_\alpha^\kappa\right). \tag{3.2}$$

The porosity is denoted by ϕ, S_α is the saturation of the phase α, X_α^κ stands for the mass fraction of the component κ in the phase α, $\mathbf{v}_\alpha$ is the Darcy velocity, and q_α^κ are given source or sink terms. Since we consider compressible fluids, the phase densities ϱ_α depend on the pressure, temperature and fluid composition. The gas phase is assumed to be ideal and the formulations proposed in [IAPW 09] and [Reid 87] are used for the properties of the air-vapor mixture. The diffusion coefficients $\mathbb{D}_{\alpha,\mathrm{pm}}$ are functions of the soil properties (porosity, tortuosity) and of the fluid properties (saturation, binary diffusion coefficients). For the calculation of diffusion in the porous medium different concepts are conceivable. We employ the approach proposed in [Mill 60] for the definition of the diffusion coefficients in the porous medium $\mathbb{D}_{\alpha,\mathrm{pm}^\kappa}$ described in the following.

A binary system is considered, where the diffusion coefficients of both components within one phase are equal, $\mathbb{D}_\alpha^{\mathrm{w}} = \mathbb{D}_\alpha^{\mathrm{a}} = \mathbb{D}_\alpha$. Here, we approximate the diffusion coefficient for the phase α in the porous medium $\mathbb{D}_{\alpha,\mathrm{pm}}$ as

$$\mathbb{D}_{\alpha,\mathrm{pm}} = \tau\phi S_\alpha \mathbb{D}_\alpha.$$

The tortuosity τ can be estimated using the approach of [Mill 60]:

$$\tau = \frac{(\phi S_\alpha)^{7/3}}{\phi^2}.$$

Thus, we specify $\mathbb{D}_{\alpha,\mathrm{pm}}$ as a nonlinear function of the unknown saturation S_α.

By summing up the two mass-balance equations (3.1) for the two components, with $X_\alpha^{\mathrm{w}} + X_\alpha^{\mathrm{a}} = 1$, and assuming binary diffusion, we obtain the total mass-balance equation,

$$\sum_{\alpha\in\{\mathrm{l,g}\}} \phi \frac{\partial \left(\varrho_\alpha S_\alpha\right)}{\partial t} + \operatorname{div} \sum_{\alpha\in\{\mathrm{l,g}\}} \left(\varrho_\alpha \mathbf{v}_\alpha\right) - \sum_{\alpha\in\{\mathrm{l,g}\}} q_\alpha = 0, \tag{3.3}$$

where the source/sink term is given by $q_\alpha = q_\alpha^{\mathrm{w}} + q_\alpha^{\mathrm{a}}$. It is now possible to choose equivalently two of the three equations (3.1) for $\kappa \in \{\mathrm{w}, \mathrm{a}\}$ and (3.3) for a complete model description.

The phase velocities $\mathbf{v}_\alpha$ are prescribed by the multi-phase Darcy law, namely,

$$\mathbf{v}_\alpha = -\frac{k_{\mathrm{r}\alpha}}{\mu_\alpha} \mathbb{K} \left(\mathbf{grad}\, p_\alpha - \varrho_\alpha \mathbf{g}\right), \qquad \alpha \in \{\mathrm{l}, \mathrm{g}\}, \tag{3.4}$$

where μ_α and $k_{\mathrm{r}\alpha}$ are the phase dynamic viscosities and relative permeabilities, respectively, $\mathbf{g}$ is the gravity vector, $\mathbb{K}$ is the intrinsic permeability tensor of the porous medium, and p_α are the phase pressures. The relative permeability $k_{\mathrm{r}\alpha}$ of a phase α is described by a

function $k_{r\alpha}(S_\alpha)$ of the phase saturation S_α. We use the well-known Brooks-Corey model [Broo 64]:

$$k_{\mathrm{rw}} = S_{\mathrm{e}}^{\left(\frac{2+3\lambda}{\lambda}\right)},$$
$$k_{\mathrm{rn}} = (1 - S_{\mathrm{e}})^2 + \left(1 - S_{\mathrm{e}}^{\left(\frac{2+\lambda}{\lambda}\right)}\right),$$

where $S_{\mathrm{e}} = \frac{S_{\mathrm{w}} - S_{\mathrm{rw}}}{1 - S_{\mathrm{rw}}}$ is the effective saturation with the residual saturation S_{rw}, and λ is the Brooks-Corey parameter that has to be determined experimentally.

Related to the slow flow processes, local thermal equilibrium ($T_{\mathrm{l}} = T_{\mathrm{g}} = T_{\mathrm{s}} = T$) is assumed. Hence, we can use a single energy-balance equation that accounts for the convective and conductive heat fluxes, the heat sources q_T within the domain and the storage of heat in the fluid phases and the porous material. As shown in [Clas 02], we have

$$\sum_{\alpha \in \{\mathrm{l,g}\}} \phi \frac{\partial \left(\varrho_\alpha u_\alpha S_\alpha\right)}{\partial t} + (1 - \phi) \frac{\partial \left(\varrho_{\mathrm{s}} c_{\mathrm{s}} T\right)}{\partial t} + \operatorname{div} \mathbf{F}_T - q_T = 0, \tag{3.5}$$

with the internal energy $u_\alpha(p_\alpha, T) = h_\alpha(p_\alpha, T) - p_\alpha / \varrho_\alpha(p_\alpha, T)$, the soil density ϱ_{s}, the heat capacity c_{s} of the solid phase of the porous medium and the heat source/sink term q_T.

The heat flux is defined by

$$\mathbf{F}_T = \sum_{\alpha \in \{\mathrm{l,g}\}} \varrho_\alpha h_\alpha \mathbf{v}_\alpha - \lambda_{\mathrm{pm}} \mathbf{grad}\, T, \tag{3.6}$$

with the specific enthalpy h_α. The specific enthalpies are given as functions of the temperature T and phase pressure p_α. For the component air, we employ the simple relationship $h^{\mathrm{a}}(T) = 1005(T - 273.15\ \mathrm{K})$, while for the component water, we use [IAPW 09], which also accounts for the energy of vaporization in case of a phase change. For the gas phase, the resulting enthalpy h_{g} is evaluated as $h_{\mathrm{g}} = X_{\mathrm{g}}^{\mathrm{w}} h^{\mathrm{w}} + X_{\mathrm{g}}^{\mathrm{a}} h^{\mathrm{a}}$, while for the liquid phase, we simply take $h_{\mathrm{l}} = h^{\mathrm{w}}$. The effective heat conductivity $\lambda_{\mathrm{pm}}(S_{\mathrm{l}})$ accounts for the combined heat conduction in the fluids and the soil. It can be calculated as weighted sum of the effective heat conductivities of water-saturated soil $\lambda_{\mathrm{eff,l}}$ and air-saturated soil $\lambda_{\mathrm{eff,g}}$ according to [Some 74]:

$$\lambda_{\mathrm{pm}} = \lambda_{\mathrm{eff,g}} + \sqrt{S_{\mathrm{l}}}(\lambda_{\mathrm{eff,l}} - \lambda_{\mathrm{eff,g}}).$$

So far, the balance equations and the according equations of state for the porous-medium region have been presented. This system of equations contains more unknowns than equations. Hence, supplementary equations and constitutive relations have to be stated. Then, primary variables have to be chosen and the secondary variables have to be expressed in form of the primary variables.

To close the system, we need to take into account the following supplementary equations and constitutive relationships:

1. saturations: $S_{\mathrm{g}} = 1 - S_{\mathrm{l}}$,

2. capillary pressure: $p_{\mathrm{c}}(S_{\mathrm{l}}) = p_{\mathrm{g}} - p_{\mathrm{l}}$ with a given capillary pressure – saturation

relationship, where we use again [Broo 64]:

$$S_{\mathrm{e}}(p_{\mathrm{c}}) = S_{\mathrm{e}} = \frac{S_{\mathrm{w}} - S_{\mathrm{rw}}}{1 - S_{\mathrm{rw}}} = \left(\frac{p_{\mathrm{d}}}{p_{\mathrm{c}}}\right)^{\lambda},$$

where p_{d} is the entry pressure and λ the Brooks-Corey parameter,

3. mass and mole fractions: $X_\alpha^{\mathrm{w}} + X_\alpha^{\mathrm{a}} = x_\alpha^{\mathrm{w}} + x_\alpha^{\mathrm{a}} = 1$, where $\alpha \in \{\mathrm{l}, \mathrm{g}\}$,

4. mass and mole fractions can be converted with the help of the molar masses M^κ according to
$$X_\alpha^\kappa = x_\alpha^\kappa \mathrm{M}^\kappa / (x_\alpha^{\mathrm{w}} \mathrm{M}^{\mathrm{w}} + x_\alpha^{\mathrm{a}} \mathrm{M}^{\mathrm{a}}), \tag{3.7}$$
where $\alpha \in \{\mathrm{l}, \mathrm{g}\},\ \kappa \in \{\mathrm{w}, \mathrm{a}\}$,

5. Dalton's law: $p_{\mathrm{g}} = p_{\mathrm{g}}^{\mathrm{w}} + p_{\mathrm{g}}^{\mathrm{a}}$, introducing the partial pressures p_{g}^κ.

If both phases are present, one possible choice of primary variables are the pressure of the gas phase p_{g}, the saturation of the liquid phase S_{l} and the temperature T. We will assume this situation in the sequel.

In the case that one phase disappears and there is a pure gas phase, the saturations S_{l} and S_{g} are constant ($S_{\mathrm{l}} = 0$, $S_{\mathrm{g}} = 1$). Hence, the model (3.1)-(3.5) plus the constitutive equations can be considerably simplified. However, if only a single fluid phase is present, the saturation cannot be used as a primary variable anymore. Possible choices for the numerical algorithm are then a primary-variable switch [Clas 02] or the introduction of additional primary variables and additional constraints in the form of nonlinear complementarity functions, as proposed in [Laus 11].

If both phases are present and p_{g}, S_{l} and T are used as primary variables, the mass fractions can be calculated as secondary variables with the help of the following relations.

1. Due to the assumed small gas concentration in the water phase, Henry's law is used for the computation of the mole fraction of air in the liquid phase $x_{\mathrm{l}}^{\mathrm{a}}$, namely,
$$x_{\mathrm{l}}^{\mathrm{a}} = p_{\mathrm{g}}^{\mathrm{a}} / H_{\mathrm{gl}}^{\mathrm{a}}, \tag{3.8}$$
where $H_{\mathrm{gl}}^{\mathrm{a}}(T)$ is the Henry coefficient for the component air in the liquid-gas mixture.

2. The Kelvin equation accounts for the lowered saturated vapor pressure due to capillarity effects:
$$p_{\mathrm{sat,Kelvin}}^{\mathrm{w}} = p_{\mathrm{sat}}^{\mathrm{w}} \exp\left(-\frac{p_{\mathrm{c}}}{\varrho_{\mathrm{l}} R_{\mathrm{l}} T}\right), \tag{3.9}$$
where $p_{\mathrm{sat}}^{\mathrm{w}}(T)$ is the saturated vapor pressure and R_{l} the individual gas constant of water vapor. For the density $\varrho_{\mathrm{l}}(p_{\mathrm{l}}, T)$, a standard constitutive equation is employed, [IAPW 09].

3. The partial pressure $p_{\mathrm{g}}^{\mathrm{w}}$ is assumed to be equal to the vapor pressure $p_{\mathrm{sat,\ Kelvin}}^{\mathrm{w}}$ (consequence of the chemical equilibrium) which results in the relationship
$$x_{\mathrm{g}}^{\mathrm{w}} = p_{\mathrm{sat,Kelvin}}^{\mathrm{w}} / p_{\mathrm{g}}. \tag{3.10}$$

We note that in the case of a pure gas-phase system X_{l}^{κ} is undefined ($\kappa \in \{\mathrm{w}, \mathrm{g}\}$) and $S_{\mathrm{l}} = 0$.

The porous-medium model (3.1)-(3.5) has to be completed by appropriate interface and boundary conditions for the primary unknowns.

3.2.2 Equations for the Free-Flow Domain

The free-flow domain Ω^{ff}, where we assume laminar flow, is modeled by the non-stationary Stokes equations using the following setup:

1. single-phase flow (here a gas phase is considered: $\alpha = \mathrm{g}$),

2. the gas phase is composed of two components: water (w) and air (a),

3. four equations are solved in the domain: two scalar mass-balance equations (one for the water component and one for the total mass), one vector-valued momentum-balance equation and one scalar energy-balance equation.

We use the same notation as in the porous medium. With the mass fractions of the components in the gas phase X_{g}^{κ}, two mass balance equations, one for each component $\kappa \in \{\mathrm{w}, \mathrm{a}\}$, can be defined:

$$\frac{\partial \left(\varrho_{\mathrm{g}} X_{\mathrm{g}}^{\kappa}\right)}{\partial t} + \operatorname{div} \mathbf{F}^{\kappa} - q_{\mathrm{g}}^{\kappa} = 0, \tag{3.11}$$

where the mass flux is given by

$$\mathbf{F}^{\kappa} = \varrho_{\mathrm{g}} X_{\mathrm{g}}^{\kappa} \mathbf{v}_{\mathrm{g}} - \varrho_{\mathrm{g}} \mathbb{D}_{\mathrm{g}}^{\kappa} \mathbf{grad}\, X_{\mathrm{g}}^{\kappa}. \tag{3.12}$$

The source/sink term of a component is denoted as q_{g}^{κ}. As in the porous medium, a compressible gas phase is considered. The phase density ϱ_{g} depends on the pressure, temperature and the fluid composition, and the ideal gas law is used as equation of state. Moreover, we use Fick's law of diffusion and consider a binary system where the diffusion coefficients of both components are equal: $\mathbb{D}_{\mathrm{g}}^{\mathrm{w}} = \mathbb{D}_{\mathrm{g}}^{\mathrm{a}} = \mathbb{D}_{\mathrm{g}}$.

Based on the assumption of binary diffusion and $X_{\mathrm{g}}^{\mathrm{w}} + X_{\mathrm{g}}^{\mathrm{a}} = 1$, the sum of the two component balance equations (3.11) yields the mass-balance equation

$$\frac{\partial \varrho_{\mathrm{g}}}{\partial t} + \operatorname{div} \left(\varrho_{\mathrm{g}} \mathbf{v}_{\mathrm{g}}\right) - q_{\mathrm{g}} = 0, \tag{3.13}$$

where the source/sink term is given by $q_{\mathrm{g}} = q_{\mathrm{g}}^{\mathrm{w}} + q_{\mathrm{g}}^{\mathrm{a}}$. As in the porous medium, one can choose two of the three balances (3.11) for $\kappa \in \{\mathrm{w}, \mathrm{a}\}$ and (3.13) for a complete model description.

Furthermore, the momentum balance is described by the following equation introducing the gas-phase velocity $\mathbf{v}_{\mathrm{g}}$, neglecting the non-linear inertial term and considering gravity to be the only external force:

$$\frac{\partial \left(\varrho_{\mathrm{g}} \mathbf{v}_{\mathrm{g}}\right)}{\partial t} + \mathbf{div}\, \mathbb{F}_{\mathbf{v}} - \varrho_{\mathrm{g}} \mathbf{g} = \mathbf{0}. \tag{3.14}$$

The matrix-valued momentum flux is defined as

$$\mathbb{F}_{\mathbf{v}} = p_{\mathrm{g}}\mathbb{I} - \mathbb{T},$$

with the $d \times d$ identity tensor $\mathbb{I}$ and the shear stress tensor $\mathbb{T}$. By introducing the deformation tensor $\mathbb{E} = \frac{1}{2}\left(\mathbb{grad}\,\mathbf{v} + \mathbb{grad}\,\mathbf{v}^T\right)$ and employing Newton's law, the stress tensor $\mathbb{T}_{\mathrm{g}}$ can be written as

$$\mathbb{T}_{\mathrm{g}} = 2\mu_{\mathrm{g}}\mathbb{E}_{\mathrm{g}} - \left(\frac{2}{3}\mu_{\mathrm{g}}\,\mathrm{div}\,\mathbf{v}_{\mathrm{g}}\right)\mathbb{I}. \tag{3.15}$$

As explained in, for example, [Truc 96], $\lambda = -\frac{2}{3}\mu_{\mathrm{g}}$ is used as coefficient for dilatation. The combination of equations (3.14) and (3.15) leads to the instationary Stokes equation:

$$\frac{\partial\left(\varrho_{\mathrm{g}}\mathbf{v}_{\mathrm{g}}\right)}{\partial t} + \mathbf{div}\left(p_{\mathrm{g}}\mathbb{I} - \mu_{\mathrm{g}}\left(\mathbb{grad}\,\mathbf{v}_{\mathrm{g}} + \mathbb{grad}\,\mathbf{v}_{\mathrm{g}}^T\right)\right) - \mathbf{grad}\left(\frac{2}{3}\mu_{\mathrm{g}}\,\mathrm{div}\,\mathbf{v}_{\mathrm{g}}\right) - \varrho_{\mathrm{g}}\mathbf{g} = \mathbf{0}. \tag{3.16}$$

The energy-balance equation reads

$$\frac{\partial(\varrho_{\mathrm{g}}u_{\mathrm{g}})}{\partial t} + \mathrm{div}\,\mathbf{F}_T - q_T = 0, \tag{3.17}$$

with the internal energy of the gas phase u_{g} and the heat flux defined as

$$\mathbf{F}_T = \varrho_{\mathrm{g}}h_{\mathrm{g}}\mathbf{v}_{\mathrm{g}} - \lambda_{\mathrm{g}}\,\mathbf{grad}\,T, \tag{3.18}$$

where λ_{g} is the heat conductivity of the gas, h_{g} is the gas enthalpy and q_T are heat sources/sinks. The gas enthalpy and internal energy are calculated in the same way as in the porous domain, see section 3.2.1.

For the free-flow subdomain, the following supplementary relations are used:

1. mass and mole fractions: $X_{\mathrm{g}}^{\mathrm{w}} + X_{\mathrm{g}}^{\mathrm{a}} = x_{\mathrm{g}}^{\mathrm{w}} + x_{\mathrm{g}}^{\mathrm{a}} = 1$,
2. conversion between mass and mole fractions (3.7) for $\alpha = \mathrm{g}$.

As primary variables for the Stokes model (3.11)-(3.17), we choose the pressure of the gas phase p_{g}, the mass fraction of water in the gas phase $X_{\mathrm{g}}^{\mathrm{w}}$, the velocity of the gas phase $\mathbf{v}_{\mathrm{g}}$ and the temperature T. It has to be completed by appropriate boundary and initial conditions for these primary unknowns.

3.3 Interface Conditions

Suitable conditions at the interface need to be posed in order to couple the two domains properly. These conditions are based on the balance equations and primary variables of the subdomain models shown in Table 3.1. As stated before, we make assumptions based on phenomenological explanations to simplify the description of the interface and get as close as possible to a so-called simple interface [Hass 89]. Figure 3.6 illustrates the processes on the pore scale: mass, momentum and energy exchange between the three phases of the porous medium and the gas phase in the free-flow domain. Coupling conditions in form of volume-averaged quantities have to be found, which still account for the pore-scale processes. These conditions are integrated into the REV-scale models explained in sections 3.2.1 and 3.2.2.

Balance equations	**Primary variables**
Free-flow region:	
mass balance	p_g
component mass balance	X_g^w
momentum balances	v_x, v_y
energy balance	T
Porous medium region:	
mass balance	p_g
component mass balance	
two-phase system:	S_l
one-phase system:	X_g^w or X_l^a
energy balance	T

Table 3.1: Summary of the balance equations describing the different submodels and listing of the according primary variables.

The coupling of the single-phase two-component Stokes system and the two-phase two-component Darcy system is motivated by the assumption of thermodynamic equilibrium. However, due to the different model concepts applied in the two subdomains rigorous thermodynamic equilibrium, consisting of mechanical, thermal and chemical equilibrium, cannot be completely achieved. Based on phenomenological explications, assumptions are made that results in conditions that are physically meaningful and as close to thermodynamic equilibrium as possible. This leads to a solvable but still simple model that accounts for the physics at the interface.

The mechanical equilibrium (equilibrium of forces) is given by

1. the continuity of the normal stresses (3.21c) resulting in a possible jump in the gas-phase pressure,

2. the continuity of the normal mass fluxes (3.23),

3. a condition for the tangential component of the free-flow velocity. Here, the Beavers-Joseph-Saffman condition (3.22) is used, despite its limitations to single-phase parallel flow, its empirical character and the difficulty of determining the Beavers-Joseph coefficient.

The thermal equilibrium is given by

1. the continuity of the temperature (3.24),

2. the continuity of the normal heat fluxes (3.25).

The chemical equilibrium is defined through the continuity of the chemical potential in the gas phase. In the case of continuous pressure, this results in the continuity of the mole fractions at the interface. However, due to the pressure jump arising from the continuity of normal stresses, continuity of chemical potential cannot be presumed. Nevertheless, we assume continuity of mole fractions, see coupling condition (3.28), and note that this results

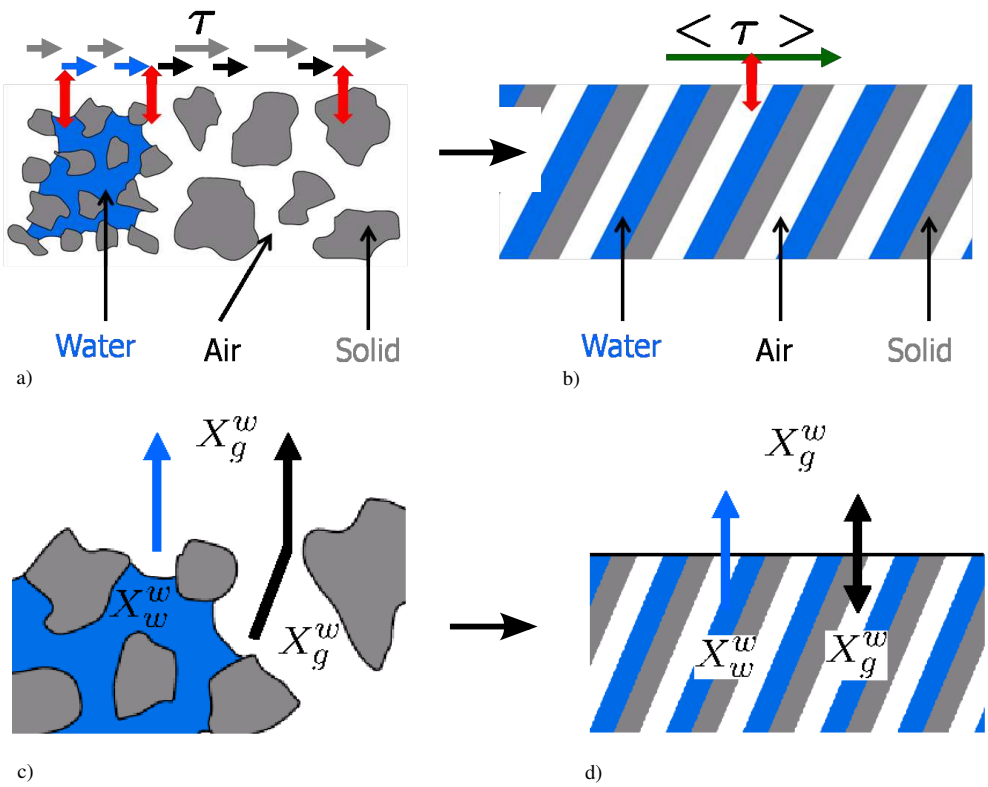

Figure 3.6: Transition from pore scale to a volume-averaged description: a) on the pore scale shear stresses occur due to interactions between the gas phase in the free-flow region and the gas, fluid and solid phases in the porous medium, b) a volume-averaged description has to account for all these contributions while the different phases of the porous medium are not locally resolved anymore, c) exchange processes also occur between the two mobile phases of the porous medium and the free gas phase (pore-scale description), d) on the REV scale coupling conditions account for these processes without resolving them locally.

in a possible discontinuity of the chemical potential. Furthermore, we require continuity of the component fluxes (3.29) across the interface.

Based on the physical equilibrium equations, we work out our mathematical and physical interface model in the following subsections. Figures 3.7 to 3.10 illustrate the conditions of thermodynamic equilibrium on the pore and REV scale. The pore-scale processes are simplified and shown for illustrative reasons only. Their purpose is to help to understand the phenomenological explanations for the presented coupling conditions.

3.3.1 Mechanical Equilibrium

On the pore scale, the mechanical equilibrium at the interface has to be formulated between the gas phase in the free-flow region and the gas, solid and water phase in the porous medium (see Figure 3.7). On the REV scale, one condition has to be found that accounts for the equilibrium between the gas phase in the free-flow region and all three phases in the porous medium, since the distribution of phases is not resolved on the macro scale anymore.

Therefore, the interface traction is decomposed into its normal and tangential contribution. The normal component of the traction tensor of a Newtonian fluid at the interface is

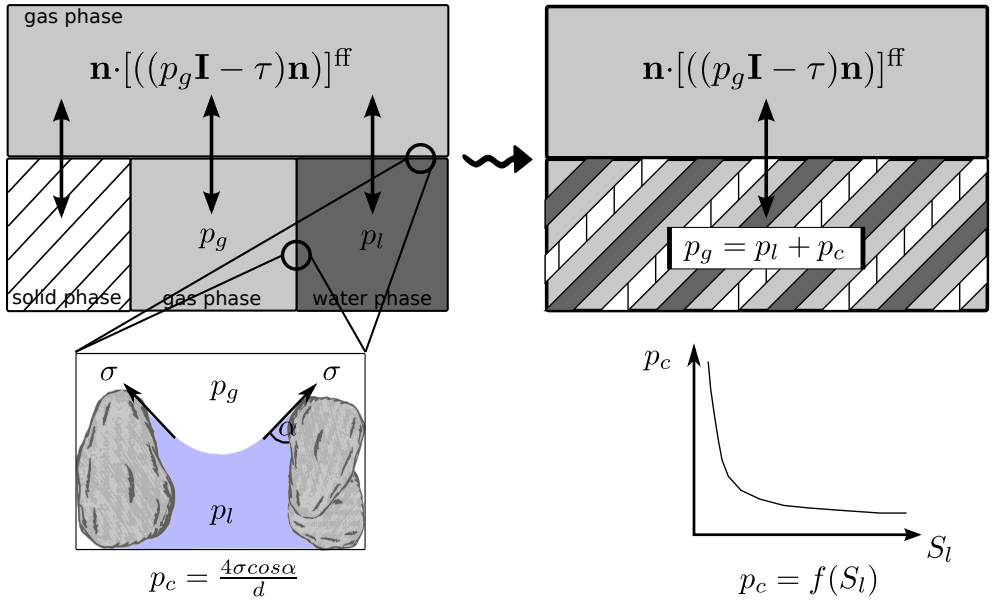

Figure 3.7: Mechanical equilibrium at the pore scale and at the REV scale (normal component). The coupling conditions on the REV scale have to account for the traction between the gas phase in the free-flow region and the gas, solid and water phase in the porous medium. Capillarity effects occur at the interface between the fluid phases in the porous medium as well as at the interface to the gaseous free-flow region. On the REV scale capillary pressure is a function of the water saturation.

given by

$$\mathbb{S}\mathbf{n} = (-p_{\mathrm{g}}\mathbb{I} + \mathbb{T})\,\mathbf{n} = \left(-p_{\mathrm{g}}\mathbb{I} + \mu_{\mathrm{g}}\left(\mathbb{grad}\,\mathbf{v}_{\mathrm{g}} + \mathbb{grad}\,\mathbf{v}_{\mathrm{g}}^{T}\right) - \left(\frac{2}{3}\mu_{\mathrm{g}}\,\mathrm{div}\,\mathbf{v}_{\mathrm{g}}\right)\mathbb{I}\right)\mathbf{n}. \tag{3.19}$$

It acts as a surface load on the fluid volume inside Ω^{ff}. Thus, the force on the interface Γ is equal to $-\mathbb{S}\mathbf{n}$. At the porous-medium side of the interface, slow flow velocities are assumed and Darcy's law is used. Hence, viscous stresses $\mathbb{T}$ have not to be treated explicitly since they are already accounted for in the permeability, see, for example, [Whit 98]. Consequently, only the pressure forces acting on Γ have to be taken into account in Ω^{pm}. Under the assumption of a rigid solid phase and no-slip at the solid-phase surface, no interface condition between gas phase and solid phase needs to be formulated. Mechanical equilibrium between the gas phases in the two domains is represented by the continuity of momentum fluxes shown in equation (3.21a). In order to identify the coupling conditions between the liquid and the gas phase across the interface, the pore scale processes must be considered. In the porous medium, capillarity effects occur at the gas-liquid interface (see Figure 3.7) due to interfacial tension. The result is a pressure discontinuity across the interface of the two fluids which is defined as capillary pressure (see equations 3.20 and, for example, [Helm 97]):

$$p_{\mathrm{c}} = \frac{4\sigma\cos\alpha}{d}, \tag{3.20a}$$

$$p_{\mathrm{c}} = p_{\mathrm{g}} - p_{\mathrm{l}} = p_{\mathrm{c}}(S_{\mathrm{l}}). \tag{3.20b}$$

The pore-scale equation (3.20a) is valid only for circular tubes and shows capillary pressure as a function of the surface tension σ, contact angle α and pore diameter d. The concept of pore-scale capillarity is transferred to the REV-scale by considering macroscopic capillarity through the capillary pressure – saturation relation (3.20b), $p_c(S_l) = p_g - p_l$, which has been introduced in section 3.2.1. Note that capillarity effects occur at the interface of the gas and liquid phase in the porous medium as well as at the interface of water filled pores and the gaseous free-flow region (see Figure 3.7). Following the same reasoning as inside the porous-medium region, the gas phase at the free-flow side of the interface has to balance the sum of the water pressure and the capillary pressure (see equations (3.20b) and (3.21b)). Hence, involving the normal traction (3.19), equation (3.21c) results as coupling condition representing the continuity of normal forces across the interface on the REV-scale.

$$\mathbf{n} \cdot [A_g((p_g \mathbb{I} - \mathbb{T})\mathbf{n})]^{\mathrm{ff}} = [p_g A_g]^{\mathrm{pm}} \tag{3.21a}$$

$$\mathbf{n} \cdot [A_l((p_g \mathbb{I} - \mathbb{T})\mathbf{n})]^{\mathrm{ff}} = [\underbrace{(p_l + p_c)}_{p_g} A_l]^{\mathrm{pm}} \tag{3.21b}$$

$$(3.21a) + (3.21b) \qquad \mathbf{n} \cdot [((p_g \mathbb{I} - \mathbb{T})\,\mathbf{n})]^{\mathrm{ff}} = [p_g]^{\mathrm{pm}} \tag{3.21c}$$

Relationship (3.21c) can be used as Neumann boundary condition for the normal component of the free-flow velocity (3.14), combined with the condition for the tangential component (3.22) as Cauchy boundary condition. Alternatively, (3.21c) can be used in (3.3) as Dirichlet boundary condition for the pressure in the porous medium.

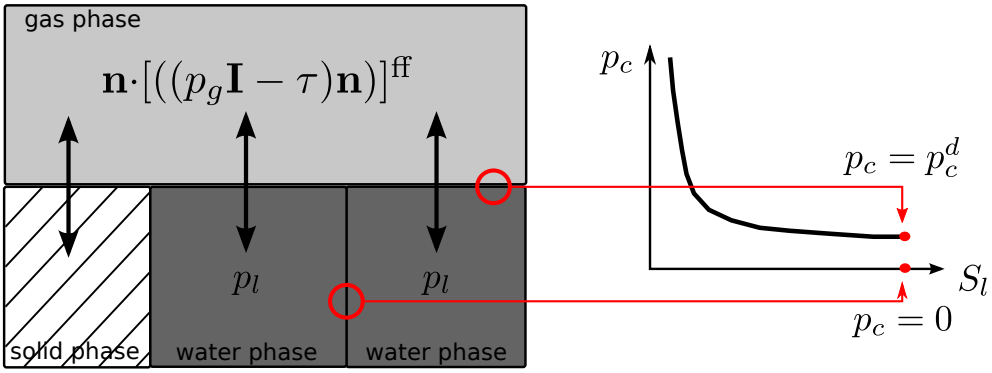

Figure 3.8: For a fully water-saturated porous medium ($S_l = 1$) the capillary pressure inside the porous medium is zero, while it equals the entry pressure at the interface to the gaseous free-flow region.

The capillary pressure at the interface in (3.21b) might be different from the capillary pressure inside the porous medium. This difference in the capillary pressure is assumed to be negligible and the same capillary pressure – saturation relation as inside the first layer of the porous medium is applied. However, note that in case of a fully water-saturated porous medium, the capillary pressure p_c at the interface to the gaseous free flow is equal to the entry pressure p_d, while the capillary pressure within the porous medium is not defined (see Figure 3.8) due to the absence of the gas phase. Hence, the gas-phase pressure in the porous medium in equation (3.21c) is equal to $p_g = p_w + p_d$. Due to condition (3.21c), the pressure is possibly discontinuous at the interface, and thus, a jump in the pressure-dependent variables, such as density and viscosity, can be expected. Pressure is usually a continuous thermodynamic property. The discontinuity arises from the use of different model concepts and causes a first perturbation of the thermodynamic equilibrium. We

note that (3.21c) is exactly the pressure drop in the artificial boundary condition derived in [Heyw 96].

Now, a condition for the tangential component of the velocity in the free-flow domain is required. Therefore, we follow the same lines as [Beav 67]. They state that the slip velocity along the interface is proportional to the shear stress at the interface. With the simplification of [Saff 71], i.e. neglecting the small tangential velocity in the porous medium at the interface, the Beavers-Joseph-Saffman condition can be written as, [Layt 03],

$$\left[\left(\mathbf{v}_\mathrm{g} + \frac{\sqrt{k_i}}{\alpha_\mathrm{BJ}\,\mu_\mathrm{g}}\mathbb{T}\,\mathbf{n}\right)\cdot\mathbf{t}_i\right]^\mathrm{ff} = 0, \quad i \in \{1,\ldots,d{-}1\} \tag{3.22}$$

where $\mathbf{t}_i$, $i \in \{1,\ldots,d{-}1\}$, denotes a basis of the tangent plane of the interface Γ. The parameter k is the corresponding component of the porous-medium permeability and equals $k_i = (\mathbb{K}\mathbf{t}_i)\cdot\mathbf{t}_i$. Equation (3.22) can be used as Neumann or Dirichlet condition for (3.14).

The Beavers-Joseph coefficient α_BJ has to be determined numerically or experimentally and has to be valid for a two-phase system. Figure 3.9 illustrates that the Beavers-Joseph coefficient should account for the traction between the gas phase in the free-flow region and the gas, solid and water phase in the porous medium. With a difference in viscosity between gas and water of three orders of magnitude, the no-slip condition is assumed to be valid not only for the solid phase but also for the liquid-phase surface. Thus, the Beavers-Joseph coefficient is also a function of the water saturation S_l. The determination of the

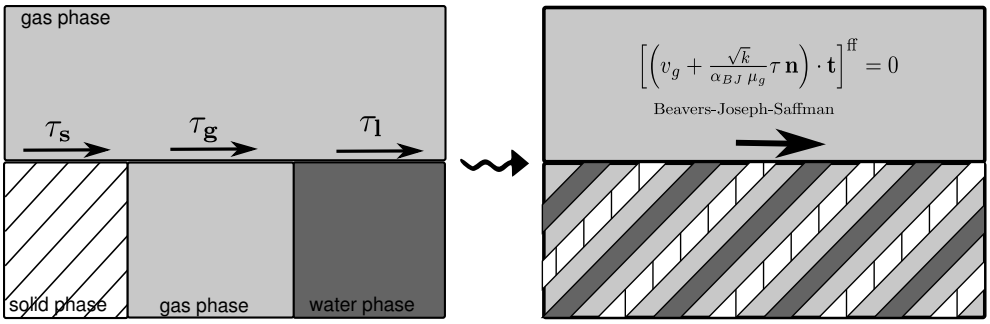

Figure 3.9: Mechanical equilibrium at the pore scale and at the REV scale (tangential component). The coupling conditions on the REV scale have to account for the traction between the gas phase in the free-flow region and the gas, solid and water phase in the porous medium.

Beavers-Joseph coefficient for two-phase systems will be a demanding task. However, it remains to be seen whether the tangential velocity at the free-flow side of the interface has a significant influence on the evaporation process. If numerical experiments will show a significant impact of this condition, (3.22) might be replaced by a more sophisticated condition, for example, derived from volume-averaging theory, in order to account more precisely for the influence of the multi-phase behavior, the surface roughness, the boundary layer and of the shear stresses at the interface.

Finally, to fulfill mechanical equilibrium the continuity of fluxes across the interface has to be guaranteed. The mass-balance requires the sum of the fluxes at the interface to be equal to zero. In the free-flow region, one phase is present, whereas in the porous medium we have to take both fluid phases into account. In general, the flux of the liquid phase does not vanish at the interface, but direct evaporation of the normal water flux is assumed.

Hence, the gas phase in the free-flow region takes up both the gas and liquid mass flux and the continuity equation for the normal phase fluxes reads

$$[\varrho_{\mathrm{g}}\mathbf{v}_{\mathrm{g}} \cdot \mathbf{n}]^{\mathrm{ff}} = -\left[(\varrho_{\mathrm{g}}\mathbf{v}_{\mathrm{g}} + \varrho_{\mathrm{l}}\mathbf{v}_{\mathrm{l}}) \cdot \mathbf{n}\right]^{\mathrm{pm}}. \tag{3.23}$$

This relationship can be used as Dirichlet boundary condition for the free-flow velocity in (3.14). Alternatively, if the total mass balance (3.3) is used in the porous medium, it may be used as boundary condition for p and S.

3.3.2 Thermal Equilibrium

The assumption of local thermal equilibrium at the interface provides two continuity conditions for the primary variable T and the associated heat flux,

$$[T]^{\mathrm{ff}} = [T]^{\mathrm{pm}}, \tag{3.24}$$

and

$$\left[(\varrho_{\mathrm{g}} h_{\mathrm{g}}\mathbf{v}_{\mathrm{g}} - \lambda_{\mathrm{g}}\,\mathbf{grad}\,T) \cdot \mathbf{n}\right]^{\mathrm{ff}} = -\left[(\varrho_{\mathrm{g}} h_{\mathrm{g}}\mathbf{v}_{\mathrm{g}} + \varrho_{\mathrm{l}}(h_{\mathrm{l}} + \Delta h_v)\mathbf{v}_{\mathrm{l}} - \lambda_{\mathrm{pm}}\,\mathbf{grad}\,T) \cdot \mathbf{n}\right]^{\mathrm{pm}}. \tag{3.25}$$

As we assume that the normal water flux from the porous medium evaporates totally and immediately at the interface (see equation (3.23)) the enthalpy of vaporization Δh_v is included in (3.25) to account for the phase change. Condition (3.24) can be used as Dirichlet boundary condition for the temperature T in one of the equations (3.5) or (3.17), while condition (3.25) can be applied as Cauchy boundary condition for T in one of the equations (3.5) or (3.17), with an additional nonlinear influence on the pressure via $\varrho_{\mathrm{g}}(p_{\mathrm{g}}, T)$ in the case of a compressible gas phase. For alternatives to the equilibrium condition we refer to [Alaz 01].

3.3.3 Chemical Equilibrium

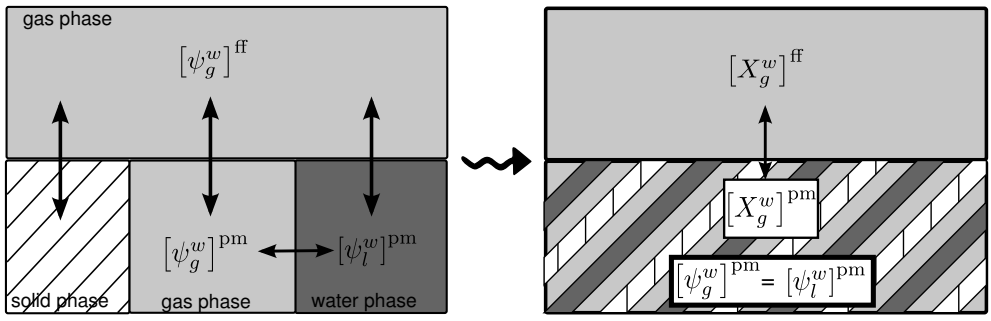

Figure 3.10: Chemical equilibrium at the pore scale and at the REV scale. On the micro scale, equilibrium conditions between the gas phase in the free-flow region and the two phases in the porous medium have to be formulated, consisting of continuity of chemical potential. On the REV scale, continuity of chemical potential between the phases inside the porous medium is assumed and continuity of mass fractions is applied as coupling condition between the gas phase in the free flow and porous medium.

The chemical equilibrium at the interface can be considered as an equilibrium between three compartments and two phases (see Figure 3.10). On the micro scale, the equilibrium for the chemical potentials of the component water ψ_α^{w}, $\alpha \in \{\mathrm{l}, \mathrm{g}\}$, can be stated from pair-wise considerations corresponding to Figure 3.10, under the assumption that the gas phase is separated by the interface,

$$\left[\psi_{\mathrm{g}}^{\mathrm{w}}\right]^{\mathrm{ff}} = [\psi_{\mathrm{l}}^{\mathrm{w}}]^{\mathrm{pm}}, \tag{3.26a}$$

$$\left[\psi_{\mathrm{g}}^{\mathrm{w}}\right]^{\mathrm{ff}} = \left[\psi_{\mathrm{g}}^{\mathrm{w}}\right]^{\mathrm{pm}}. \tag{3.26b}$$

In the subdomain model, the equilibrium between the gas and the liquid phase within the porous medium, $[\psi_{\mathrm{l}}^{\mathrm{w}}]^{\mathrm{pm}} = \left[\psi_{\mathrm{g}}^{\mathrm{w}}\right]^{\mathrm{pm}}$, is already satisfied (see section 3.2.1). As a consequence, only (3.26b) has to be imposed at the interface. On the REV scale however, continuity of the chemical potential cannot be postulated since the continuity of the normal forces (3.21c) leads to a jump in the gas-phase pressure. As already stated before, this pressure difference is due to differences in the model concepts applied in the subdomains. More precisely, it is due to the application of the potential theory in the porous-medium region where shear stresses are not explicitly resolved anymore. These small differences in pressure cause discontinuities in the chemical potentials and/or discontinuous mole fractions. Assuming all components to be ideal, the difference in the chemical potential [Atki 94] can be written as

$$\psi^{\mathrm{ff}}(p_{\mathrm{g}}^{\mathrm{ff}}) - \psi^{\mathrm{pm}}(p_{\mathrm{g}}^{\mathrm{pm}}) = \left[\mathrm{R}T \ln\left(x_{\mathrm{g}}^{\mathrm{w}} \frac{p_{\mathrm{g}}}{p_0}\right)\right]^{\mathrm{ff}} - \left[\mathrm{R}T \ln\left(x_{\mathrm{g}}^{\mathrm{w}} \frac{p_{\mathrm{g}}}{p_0}\right)\right]^{\mathrm{pm}} = \ln\left(\frac{\left[x_{\mathrm{g}}^{\mathrm{w}}\, p_{\mathrm{g}}\right]^{\mathrm{ff}}}{\left[x_{\mathrm{g}}^{\mathrm{w}}\, p_{\mathrm{g}}\right]^{\mathrm{pm}}}\right)^{\mathrm{R}T}, \tag{3.27}$$

where p_0 is the reference pressure and R is the universal gas constant. However, the magnitude of the difference in chemical potential is not known and a condition for the mole fractions cannot be deduced. We therefore assume the continuity of the mole fractions as coupling condition:

$$[x_{\mathrm{g}}^{\kappa}]^{\mathrm{ff}} = [x_{\mathrm{g}}^{\kappa}]^{\mathrm{pm}}, \quad \kappa \in \{\mathrm{a}, \mathrm{w}\}. \tag{3.28}$$

By taking into account the conversion between mass and mole fractions (3.7) for $\alpha = \mathrm{g}$, the coupling condition (3.28) can be employed as Dirichlet boundary condition for $X_{\mathrm{g}}^{\mathrm{w}}$ in (3.11). Alternatively, via the relationships (3.9),(3.10), it can be used as a nonlinear coupled boundary condition for p_{g}, S_{l} and T in (3.1).

Naturally, the continuity of the component fluxes across the interface is required for $\kappa \in \{\mathrm{w}, \mathrm{a}\}$:

$$\begin{aligned}\left[\left(\varrho_{\mathrm{g}} X_{\mathrm{g}}^{\kappa} \mathbf{v}_{\mathrm{g}} - \varrho_{\mathrm{g}} \mathbb{D}_{\mathrm{g}}\, \mathbf{grad}\, X_{\mathrm{g}}^{\kappa}\right) \cdot \mathbf{n}\right]^{\mathrm{ff}} = \\ - \left[\left(\varrho_{\mathrm{g}} X_{\mathrm{g}}^{\kappa} \mathbf{v}_{\mathrm{g}} - \varrho_{\mathrm{g}} \mathbb{D}_{\mathrm{g,pm}}\, \mathbf{grad}\, X_{\mathrm{g}}^{\kappa} + \varrho_{\mathrm{l}} X_{\mathrm{l}}^{\kappa} \mathbf{v}_{\mathrm{l}} - \varrho_{\mathrm{l}} \mathbb{D}_{\mathrm{l,pm}}\, \mathbf{grad}\, X_{\mathrm{l}}^{\kappa}\right) \cdot \mathbf{n}\right]^{\mathrm{pm}}.\end{aligned} \tag{3.29}$$

Based on the same reasoning as for the total mass fluxes, the component fluxes within both fluid phases of the porous medium that flow across the interface are added and balanced with the component fluxes in the gas phase of the free flow. Summing up equations (3.29) for $\kappa \in \{\mathrm{w}, \mathrm{a}\}$ results in the continuity of total mass flux (3.23). Two of the three conditions (3.23),(3.29) can be equivalently chosen according to the set of balance equations that is used in the submodels.

If applied to the free-flow domain, the conditions for the continuity of component fluxes

Equilibrium	Property	Porous medium	Free flow
Mechanical:	normal stress (3.21c)		Neumann for $\mathbf{v}_\mathrm{g} \cdot \mathbf{n}$
	tangential velocity (3.22)	–	Cauchy for $\mathbf{v}_\mathrm{g} \cdot \mathbf{t}$
Thermal:	temperature (3.24)		Dirichlet for T
	heat flux (3.25)	Cauchy for T	
Chemical:	mole fraction (3.28)		Dirichlet for X_g^w
	component flux w(3.29)	nonlinear coupled	
	mass flux (3.23)	conditions for	
		p, S, T	

Table 3.2: Interpretation of coupling conditions as boundary conditions.

are Cauchy conditions for X_g^κ in (3.11). For the porous-medium part, one can consider the constitutive relations (3.7),(3.8) for the liquid phase and (3.7),(3.9),(3.10) for the gas phase to arrive at two nonlinear coupled conditions for p, S and T in (3.1).

Note that the diffusion coefficients in both domains differ from each other. For the free-flow domain, the binary diffusion coefficient $\mathbb{D}_\mathrm{g}$ (dependent on temperature and pressure) is used, whereas for the porous medium, the diffusion coefficients $\mathbb{D}_{\alpha,\mathrm{pm}}$ are functions of the properties of the soil and the fluids.

Furthermore, if the liquid phase at the porous-medium side of the interface disappears, the previously mentioned primary-variable switch is triggered in the porous medium and the mass fraction X_g^w is used as a primary variable instead of the saturation. The coupling simplifies to a single-phase two-component system. Water can be transferred only by vapor diffusion and by advective transport in the gas phase over the soil-gas interface.

Summarized Interpretation as Boundary Conditions

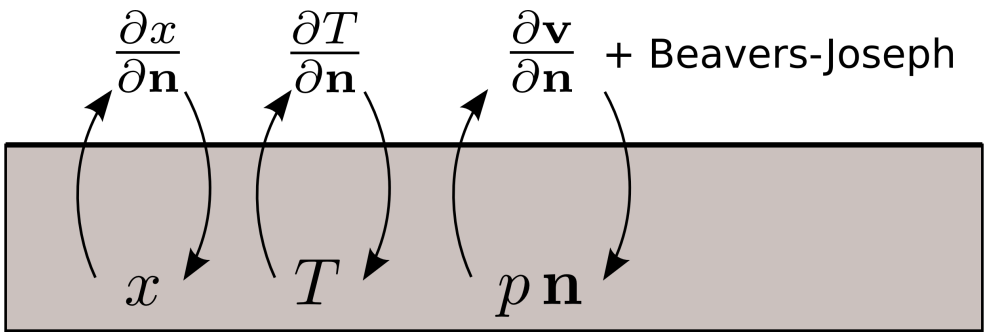

Figure 3.11: Schematic overview of the coupling conditions.

Table 3.2 summarizes one possible implementation of the coupling conditions combined with the models describing the free-flow and porous-medium compartments. The interface conditions play the role of internal boundary conditions for the coupled model, meaning that the information is handed over from the free-flow to the porous-medium side and vice versa. A consistent combination of Dirichlet and Neumann or Cauchy conditions is chosen (see Figure 3.11). We would like to mention that in the limit case of pure advective transport, the partial differential equations are changing in type and order and so do the coupling

conditions. Conditions (3.24) and (3.28) can be removed and the flux conditions (3.23), (3.25) and (3.29) have to be replaced by outflow/inflow conditions. We note that Table 3.2 only represents one of several possible combinations. If the solution is known within one subdomain, then the setting in Table 3.2 provides well-posed boundary conditions for the opposite subdomain.

3.4 Numerical Example

A two-dimensional numerical example is used to demonstrate the functionality of the developed coupling concept. The objective is to show the changes in the saturation in the porous medium due to evaporation, the evaporative cooling, the continuity of fluxes at the interface of the two domains and the transition from a two-phase to a single-phase system within the porous medium. We choose a setup with relatively dry air that blows horizontally over the surface of an unsaturated porous medium (0.25 m x 0.25 m) which is closed on all other sides. This may represent, for example, a sand-filled vessel in contact with the ambient air flow. The setup is illustrated in Figure 3.12.

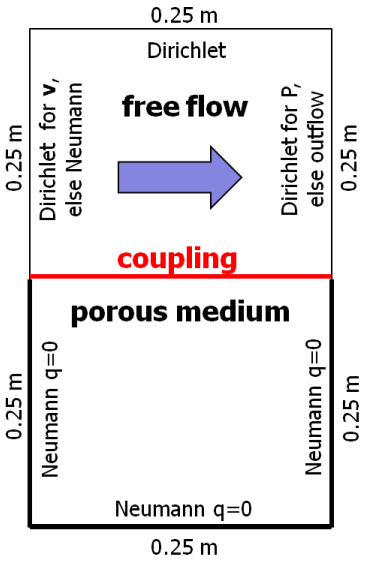

(a) Model setup.

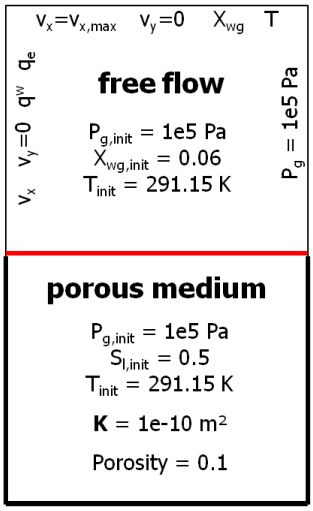

(b) Initial and boundary conditions.

Figure 3.12: General model setup with respective initial and boundary conditions.

The porous medium is initially 50 percent water-saturated and closed on all sides (homogeneous Neumann conditions) except at the top (see Figure 3.12b). It is coupled to a free-flow domain at the upper boundary, where the coupling conditions are set. As primary variables in the porous domain, the gas pressure p_g, the water saturation S_l and temperature T are selected. The initial gas pressure is 1e5 Pa and the initial temperature is set to 291.15 K. As explained in section 3.2.1, the mass fractions are calculated as secondary variables depending on pressure and temperature as long as two phases are present. As soil properties, we choose an isotropic permeability of $\mathbb{K} = 1\text{e-}10$ m^2 and a porosity of $\phi = 0.1$. We employ a Brooks-Corey parameterization for the capillary pressure – saturation and the relative permeability – saturation relationship with the parameters $p_d = 100$ Pa and

$\lambda = 2$. As effective heat conductivities, $\lambda_{\text{eff,g}} = 2.5$ W/(mK) for the air-saturated soil and $\lambda_{\text{eff,l}} = 2.65$ W/(mK) for the water-saturated soil are used.

In the free-flow domain, relatively dry air ($X_{\text{g}}^{\text{w}} = 0.006$) is blown horizontally over the surface of the porous medium. The initial and boundary conditions are depicted in the upper parts of Figure 3.12b. Initially, the pressure is set to 1e5 Pa and temperature to 291.15 K, which is conform with the initial temperature in the porous medium. We choose a linear velocity profile that is set as Dirichlet condition on the left and on the top boundary. The maximum horizontal velocity is set at the top boundary to $v_{x,max} = 1$ m/s and decreases to the Beavers-Joseph slip velocity at the coupling boundary. The horizontal inflow velocity is varied sinusoidally in the range of 1 ± 0.5 m/s over time with a period of one hour. Using a constant density and the described velocity field, the inflow of vapor and heat are specified via Neumann conditions on the left boundary as $\rho_{\text{g}} X_{\text{g}}^{\text{w}} \mathbf{v}_{\text{g}} \cdot \mathbf{n}$ and $\rho_{\text{g}} h_{\text{g}} \mathbf{v}_{\text{g}} \cdot \mathbf{n}$. Therefore, the mass fraction of vapor in the gas phase is fixed to $X_{\text{g}}^{\text{w}} = 0.006$, whereas temperature undergoes sinusoidal diurnal variations of 291.15 ± 5 K. For the mass balance equation outflow conditions are set everywhere except on the right boundary. The gas pressure is fixed as Dirichlet condition to 1e5 Pa on the right boundary with all other equations having outflow conditions.

The simulations are carried out within the modeling environment DuMu$^{\text{x}}$ [Flem 11], in combination with Dune-Multidomain and Dune-Multidomaingrid [Muth 12], which provide subdividable meta-grids and the handling of the respective stiffness matrices. The computational grid has 20 x 50 conforming elements and is chosen in a way that the elements become vertically finer (refined) towards the interface. The submodels in the two domains employ both a vertex-centered finite-volume (Box) scheme for the space [Hube 00] and an implicit Euler scheme for the time discretization. The coupling conditions are implemented according to the setting presented in Table 3.2. As Beavers-Joseph coefficient, we use $\alpha_{\text{BJ}} = 1.0$. Within both domains, the fluid viscosities and densities are set constant ($\mu_{\text{g}} = 1.71\text{e-}5$ Pa s, $\mu_{\text{l}} = 0.0013$ Pa s, $\rho_{\text{g}} = 1.189$ kg/m^3 and $\rho_{\text{l}} = 1000$ kg/m^3). Gravity is not considered in order to obtain a uniform initial saturation distribution. This facilitates the demonstration of the saturation changes and allows a simplified consideration of the complex system.

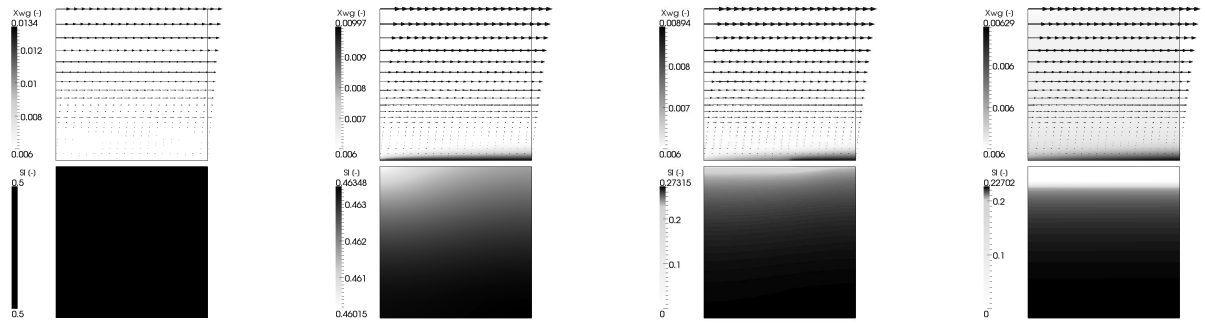

(a) t = 0 d (b) t = 1 d (c) t = 12.5 d (d) t = 33 d

Figure 3.13: Evolution of the saturation. The upper parts of the images show the mass fraction of vapor and the velocity vectors of the gas phase, the lower parts show the evolution of the saturation distribution in the porous medium. Different points in time are shown, starting with the initial conditions. After 12.5 days, half of the interface has already switched to a single-phase system. The last image is after 33 days showing a region that has already dried out completely.

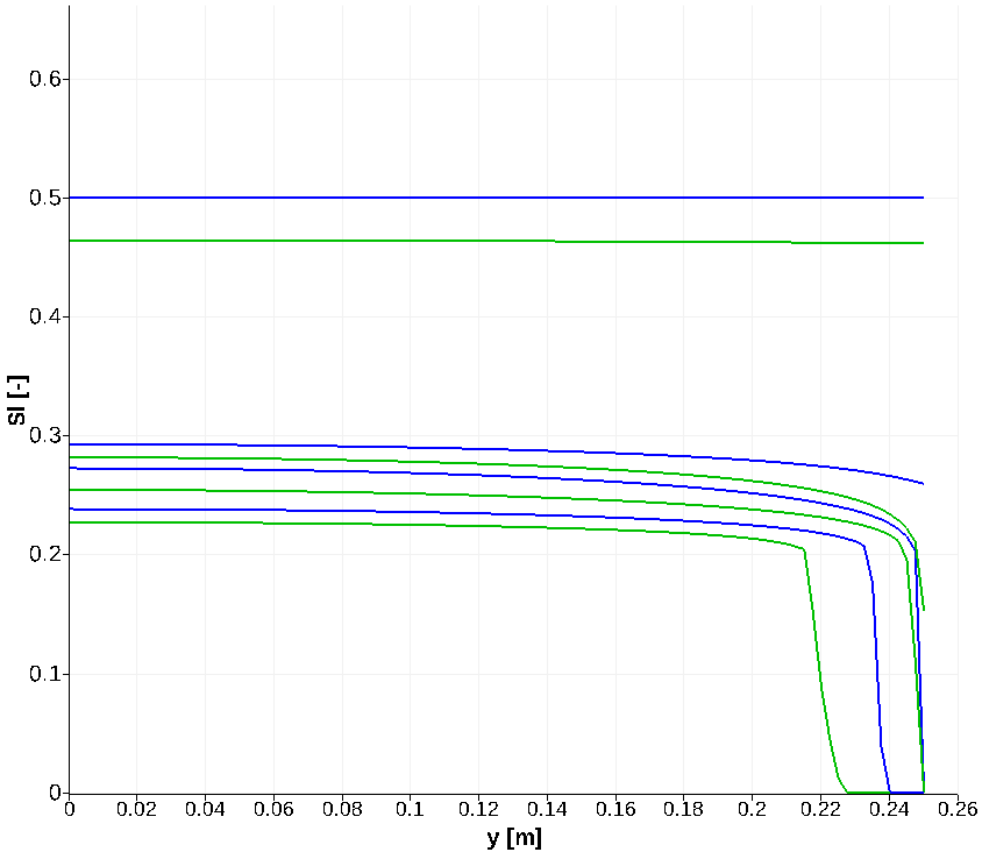

Figure 3.14: Saturation profiles at X = 0.01 m, corresponding to the following points in time (from top to bottom): 0 day, 1 day, 11 days, 12 days, 12.5 days, 15 days, 21 days and 33 days.

The vapor concentration in the gas phase increases along the interface of the two compartments as it flows over the evaporating porous surface (see Figure 3.13). Consequently, the water saturation in the porous medium decreases. Since the air that enters the domain at the inflow boundary is dryer, the evaporation rate and the resulting saturation and temperature distribution are non-symmetric as can be seen in Figures 3.13b and 3.15. As long as both fluid phases are present, the diffusive and capillary forces draw water from lower parts of the porous medium and sustain a relatively high evaporation rate.

After 12.5 days (Figures 3.13c and 3.15c), some cells in the porous domain have already dried out completely A variable switch is triggered towards a single-phase system using the mass fraction of vapor as primary variable at the vertices where the water phase has already disappeared. The resulting evaporative fluxes are much smaller, as can be seen in Figure 3.15c. Image 3.13d shows the state after 33 days, where a dry zone has formed in the upper part of the porous domain. Figure 3.14 supports this observation and depicts the water-saturation profiles over depth of the porous medium at different points in time. It can be seen, that the saturation decreases homogeneously over the depth until the upper parts of the porous medium dry out and the water saturation goes to zero. At that stage, water can be transported solely via the gas phase across the interface. The variable switch reflects the transition from the first stage evaporation, where capillary forces deliver water from the interior of the porous domain to the interface (capillary-dominated regime), and the second stage, where the transport occurs solely via the gas phase (diffusion-dominated regime).

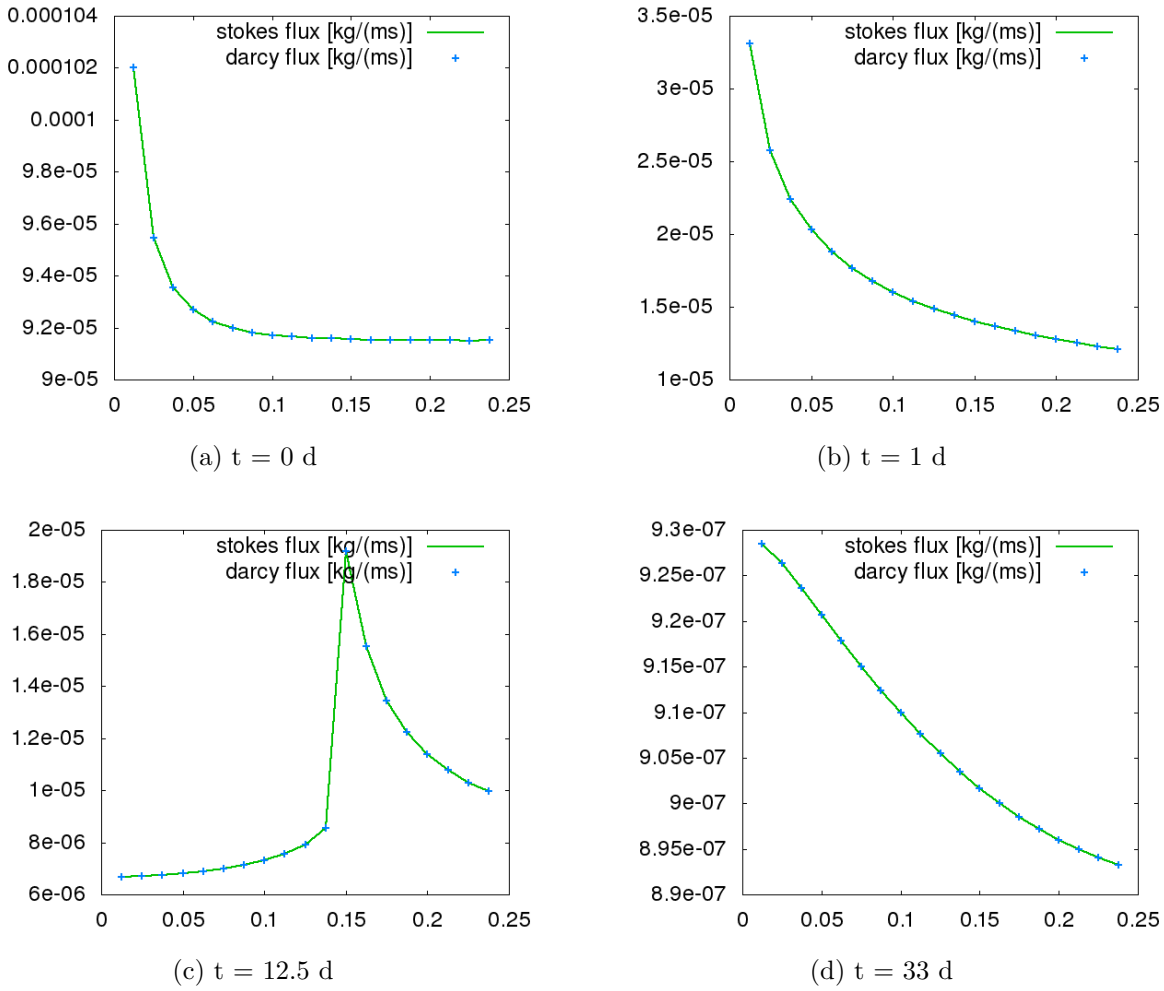

(a) t = 0 d

(b) t = 1 d

(c) t = 12.5 d

(d) t = 33 d

Figure 3.15: Mass fluxes of component water over the interface. After 12.5 days, the interface has partially dried out. The resulting water fluxes show a jump at the transition from a two-phase system including direct evaporation to a single-phase system, where water can only be transported as vapor in the gas phase across the interface.

The temporal evolution of the evaporation rate with the two distinct stages is depicted in Figure 3.16 and shows a similar behavior as measured evaporation rates [Lehm 08]. The oscillating behavior of the curve is due to the time-dependent inflow velocity and heat influxes.

The evolution of temperature reveals the expected behavior: It becomes cooler at the interface (see Figure 3.17) as long as water is directly evaporating from the water phase. It readjusts to the temperature of the free flow once the water phase has disappeared. Furthermore, the heat fluxes in the gas phase from both domains over the interface are depicted in Figure 3.18. In Figures 3.18a and 3.18b the two curves show a difference. This difference is the vaporization enthalpy for the water which is directly converted into vapor. As soon as the water phase disappears at a position on the interface, the vaporization enthalpy becomes zero and the two curves representing the heat fluxes at each side of the interface match exactly. This is illustrated in Figure 3.18c, where a certain part of the interface is already dry. In Figure 3.18d, only the gas phase is present and hence the heat

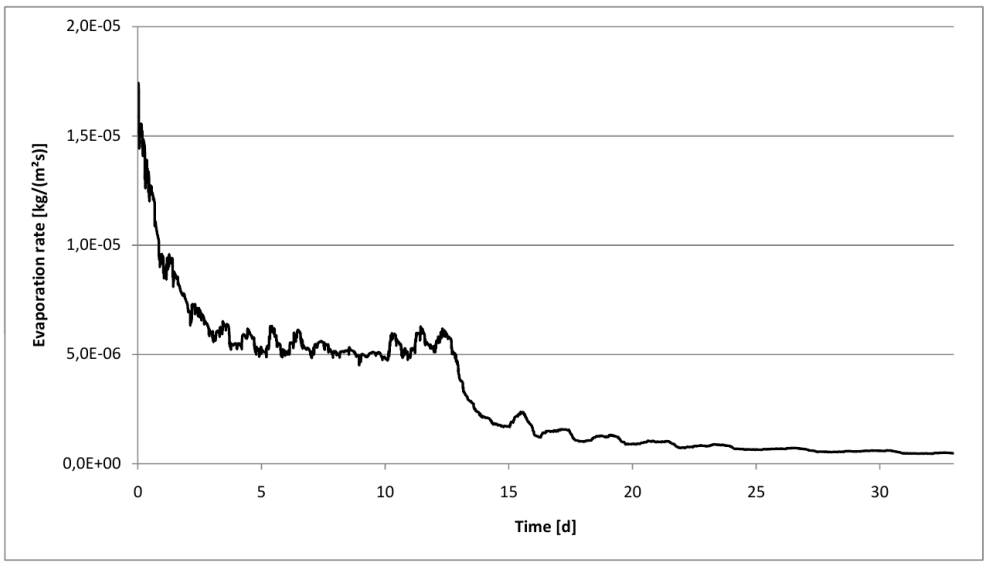

Figure 3.16: Temporal evolution of the evaporation rate. This reflects the time-dependent boundary conditions of the velocity and the heat fluxes.

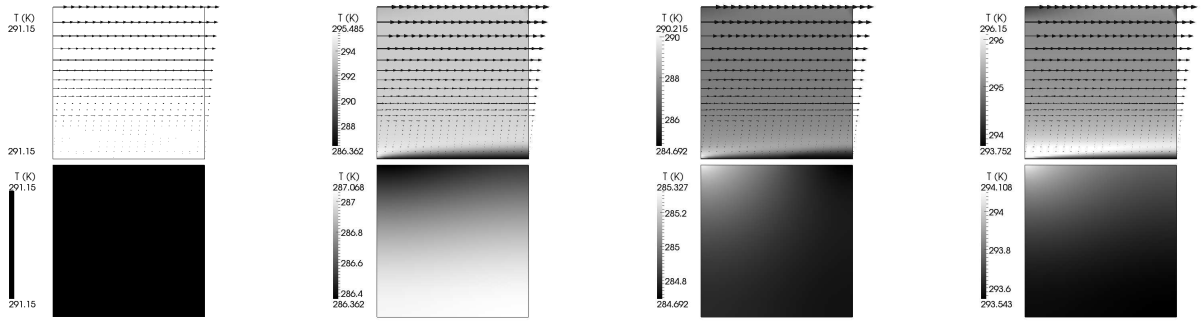

(a) t = 0 d (b) t = 1 d (c) t = 12.5 d (d) t = 33 d

Figure 3.17: Evolution of temperature. Due to the vaporization enthalpy the porous medium is cooled as long as two phases are present.

fluxes from both sides are identical.

3.5 Summary and Outlook

A coupling concept for free flow and flow in porous media is developed for the case of non-isothermal compositional one- and two-phase systems. It is valid on the REV scale and accounts for mass, momentum and energy transfer across the interface neglecting interface processes like the formation of boundary layers, flow separation and radiation.

The concept employs well-studied models in the subdomains which are then coupled by appropriate coupling conditions maintaining flexibility with respect to the subdomain models. Non-isothermal one-phase compositional free flow is described using the Stokes equations in combination with transport- and energy-balance equations. In the porous medium, these equations are combined with the extended Darcy law for two phases. Naturally, adaptations and extension of these models presented in sections 3.2.1 and 3.2.2 are possible. In the porous medium, for example, the Forchheimer or Brinkman equa-

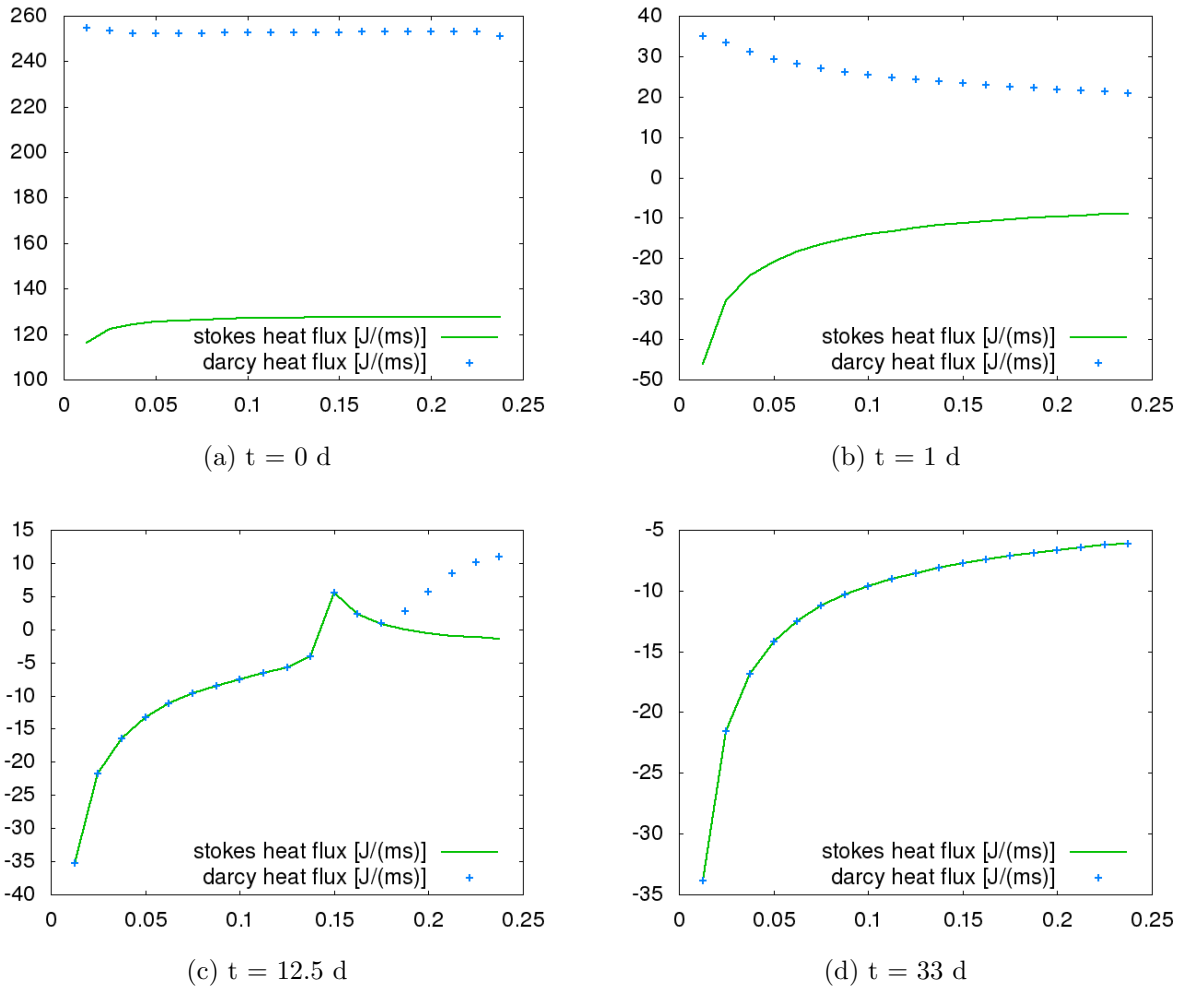

(a) t = 0 d

(b) t = 1 d

(c) t = 12.5 d

(d) t = 33 d

Figure 3.18: Heat fluxes in the gas phase across the interface. The heat fluxes from the porous medium do not contain the vaporization enthalpy from the water that directly evaporates. Hence, the fluxes from the two domains show a difference, as long as two phases are present at the interface. As soon as the water phase disappears, the vaporization enthalpy is zero and the two curves match.

tions can be applied. Alternative parameterizations may also be selected, for example, Van Genuchten for the capillary pressure – saturation relation instead of the Brooks-Corey parameterization. Moreover, the free-flow model can be extended using the Navier-Stokes equations and concepts that account for turbulent flow conditions.

For the coupling at the interface, we use a two-domain approach with a simple interface that cannot store mass, momentum or energy. The coupling conditions explained in section 3.3 are derived based on consistent phenomenological explanations considering micro-scale processes, local thermodynamic equilibrium and existing model concepts. Furthermore, they are based on the assumptions of slow, laminar flow in both compartments, Newtonian fluids and the applicability of the Beavers-Joseph-Saffman condition (3.22). This results in a simple and solvable model that accounts for the physics occurring at the interface. The presented coupling concept allows the detailed description of evaporation processes, where the gas phase of the atmosphere interacts with a gas-water system in the subsurface. Numerical examples show that transfer of heat and gas across the interface and evaporation of

water at the interface can be described as well as vaporization and condensation within the porous medium. The next step is to compare the developed model with existing concepts and with experimental results.

However, the presented concept has limitations and potential for enhancement. The Beavers-Joseph condition for the horizontal flow velocity at the interface should be replaced by a more suitable condition, which accounts for the porous material and the two phases present at the interface. So far, the condition is used despite the fact, that the assumption of purely parallel flow, for which is was originally developed, is not totally satisfied. Moreover, the determination of the Beavers-Joseph coefficient that accounts for the effects of two-phase flow in the porous medium has not yet been done. Additionally, the influence of turbulent gas flow (boundary layer and mixing of air) has to be investigated and integrated into the concept. Furthermore, radiation needs to be taken into account when evaporation is considered. In the future, some of the proposed conditions may be replaced or complemented by conditions that are more closely related to two-phase systems and, for example, derived by the thermodynamically constrained averaging theory [Jack 09].

The developed concept can be applied to other problems, for example, from industry, or in the field of biomechanics. Moreover, it can be extended to a multi-scale description, where the interface region and the occurring transfer processes are resolved on a smaller scale and coupled to the surrounding macro-models. Such a model can then, for instance, be used to describe transvascular exchange processes between vascular and interstitial compartments.

Part B

Locally Conservative Discretization Methods

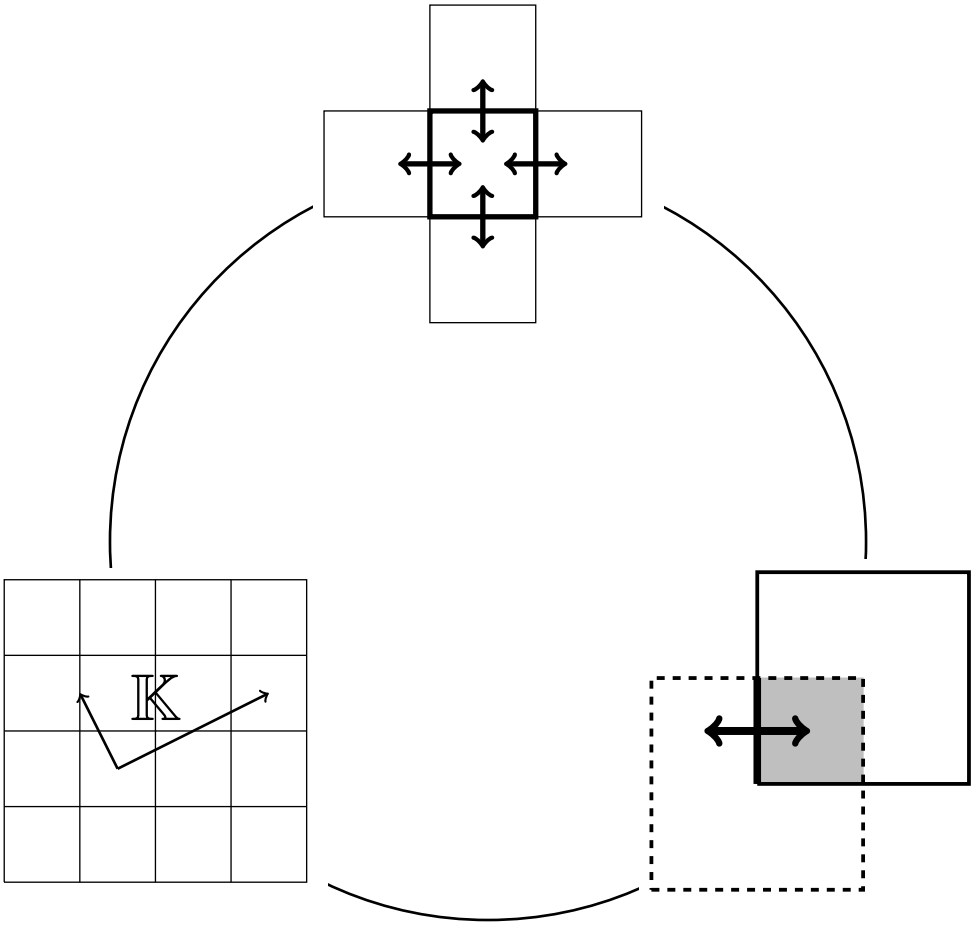

4 Review of Locally Conservative Discretization Methods

4.1 Introduction

Locally conservative methods (LCM) are indispensable for the simulation of transport processes in porous media. There exists a vast amount of literature on the topic and we will provide pointers to relevant articles in the beginning of each method presentation. However, articles discussing and comparing more than two LCM are rare, with the very good exceptions of [Klau 04, Nils 10b, Dron 10]. The special issue [Edwa 02] collects several excellent articles on individual LCM. No detailed numerical comparisons will be presented in this chapter. The benchmark sessions of the two symposia *Finite Volume Methods for Complex Applications V* and *VI* perform comparisons of several state-of-the-art LCM by means of two suites of benchmark problems, one in 2D, [Herb 08], and one in 3D, [Eyma 11].

This chapter is organized as follows. In the remainder of this section, we introduce the prototype model problem, the notion of locally conservative, and the discretization of the computational domain. In Sections 4.2-4.5, the individual LCM are introduced and reviewed by means of their traditional description. Section 4.6 provides interpretations of some of the LCM within the frameworks of mixed finite element and mimetic finite difference methods. Finally, a comparison of the discussed methods is given in Section 4.7.

Model Problem In this chapter, we face the model problem of an incompressible single-phase pressure equation,

$$\mathbf{u} = -\mathbb{K}\,\mathbf{grad}\,p, \tag{4.1a}$$

$$\operatorname{div}\mathbf{u} = q, \tag{4.1b}$$

in an open bounded domain $\Omega \subset \mathbb{R}^2$, subject to boundary conditions

$$p = p_{\mathrm{D}} \text{ on } \Gamma_{\mathrm{D}}, \tag{4.1c}$$

$$\mathbf{u}\cdot\mathbf{n} = q_{\mathrm{N}} \text{ on } \Gamma_{\mathrm{N}}, \tag{4.1d}$$

with $\partial\Omega = \overline{\Gamma_{\mathrm{D}} \cup \Gamma_{\mathrm{N}}}$ and $\Gamma_{\mathrm{D}} \cap \Gamma_{\mathrm{N}} = \emptyset$. The restriction to two dimensions has been made to avoid technical difficulties in the following exposition. Almost all of the presented methods can be extended to three dimensions. Although $\mathbb{K}$ and p stand for absolute permeability and pressure, everything can be easily adapted to the more general case of a mobility and a potential, respectively. Moreover, an additional storage term, appearing in (4.1b) in the case of a compressible fluid phase, usually does not pose any difficulties.

Locally Conservative Numerical Methods Like stated in [Klau 04], a *locally conservative* numerical method satisfies two properties which are of fundamental importance for transporting quantities by means of the velocity $\mathbf{u}$, namely,

1. The sum of the fluxes over the boundary of a control volume has to be equal to the source term.
2. The fluxes have to be continuous over all interfaces of neighboring control volumes.

In the following paragraph, a more precise characterization is provided.

Discretization of the Computational Domain The domain Ω is partitioned into n_{E} elements E_i, $i \in \{1, \dots, n_{\mathrm{E}}\}$. We also introduce a second partition of Ω into n_{CV} control volumes V_i, $i \in \{1, \dots, n_{\mathrm{CV}}\}$. For most of the following methods, the control volumes coincide with the elements, i.e., $V_i = E_i$. However, this may be different for the control-volume finite-element methods presented in Section 4.5. Each control volume V_i has a set of neighboring control volumes indexed by the set $\mathcal{N}_i$ such that for each $j \in \mathcal{N}_i$ there exists a non-trivial one-dimensional intersection $e_{ij} = V_i \cap V_j$ with unit outward normal $\mathbf{n}_{ij}$. The number of intersections for an element E_i is denoted by $n_{i,\mathrm{e}} = |\mathcal{N}_i|$. Each intersection e_{ij} is associated with an unknown flux f_{ij} approximating the value $\int_{e_{ij}} \mathbf{u} \cdot \mathbf{n}_{ij} \,\mathrm{d}\Gamma$. For control volumes at the boundary, i.e., $\partial V_i \cap \partial\Omega \neq \emptyset$, one has to additionally account for the boundary fluxes f_i^{B}. The defining properties of a LCM can now be stated more precisely as

$$\sum_{j \in \mathcal{N}_i} f_{ij} + f_i^{\mathrm{B}} = \int_{V_i} q \,\mathrm{d}V, \quad i = \{1, \dots, n_{\mathrm{CV}}\}, \tag{4.2a}$$

$$f_{ij} = -f_{ji}, \qquad i, j = \{1, \dots, n_{\mathrm{CV}}\}, \tag{4.2b}$$

with the obvious extensions $f_i^{\mathrm{B}} = 0$ for inner control volumes and $f_{ij} = 0$ if $j \notin \mathcal{N}_i$.

Whenever convenient, we drop the subscripts i and j and rather speak of an element E from the set of elements $\mathcal{T}_h$, a control volume V from the set of control volumes $\mathcal{V}_h$, or an intersection e from the set of all intersections $\mathcal{E}_h$. The set of intersections associated with an element E and a control volume V is denoted by $\mathcal{E}_E$ and $\mathcal{E}_V$, respectively. In order to associate a value v to an element, we either use v_i or v_E, if v is associated with an intersection, it is denoted either v_{ij} or v_e.

4.2 Control Volume Methods

Control volume methods (CVM) are locally conservative by nature. Starting from the mass balance (4.1b), the Gauß theorem is applied on every control volume V_i such that

$$\int_{\partial V_i} \mathbf{u} \cdot \mathbf{n} \,\mathrm{d}\Gamma = \int_{V_i} q \,\mathrm{d}V.$$

The surface integral is splitted into the contributions by intersections with other control volumes and possibly the domain boundary,

$$\int_{\partial V_i} \mathbf{u} \cdot \mathbf{n} \,\mathrm{d}\Gamma = \sum_{j \in \mathcal{N}_i} \int_{e_{ij}} \mathbf{u} \cdot \mathbf{n} \,\mathrm{d}\Gamma + \int_{\partial V_i \cap \partial\Omega} \mathbf{u} \cdot \mathbf{n} \,\mathrm{d}\Gamma.$$

Approximating $\int_{e_{ij}} \mathbf{u} \cdot \mathbf{n} \,\mathrm{d}\Gamma$ and $\int_{\partial V_i \cap \partial\Omega} \mathbf{u} \cdot \mathbf{n} \,\mathrm{d}\Gamma$ by numerical fluxes f_{ij} and f_i^{B}, respectively, the first requirement (4.2a) is taken as basis. It remains to find expressions for the fluxes f_{ij}

in terms of the unknown pressure. To this end, the pressure field is discretized by means of averaging over the control volumes, which yields one unknown value $p_i \approx |V_i|^{-1} \int_{V_i} p \, \mathrm{d}V$ per control volume. The defining feature of a control volume method then is the relationship

$$f_{ij} = f_{ij}(p_1, \ldots, p_{n_{\mathrm{CV}}}),$$

resulting via (4.2a) in a possibly nonlinear system of equations for the pressure values. In the following, we provide three particular examples of control volume methods: two-point flux approximation, multi-point flux approximation, and the discrete duality finite volume method.

4.2.1 Two-Point Flux Approximation (TPFA)

The easiest way to find an expression for the flux f_{ij} between two neighboring control volumes V_i and V_j is by only taking the two pressure values p_i and p_j into account. This is commonly referred to as *two-point flux approximation* and still the most employed method today in commercial porous media simulators, [Schl 09]. In particular, the flux f_{ij} is given in terms of a transmissibility t_{ij} and the pressure drop between the two control volumes, namely,

$$f_{ij} = t_{ij}(p_i - p_j). \tag{4.3}$$

The transmissibility t_{ij} of the interface e_{ij} depends on the permeability $\mathbb{K}$ and on the geometry of the neighboring control volumes V_i and V_j. The transmissibility is usually given as the harmonic average of transmissibilities t_i and t_j associated with V_i and V_j, i.e.,

$$t_{ij} = \frac{2t_i t_j}{t_i + t_j}.$$

In the case of an arbitrary geometry of the control volumes, they are given by, [Aava 01, Nils 10b],

$$t_i = \mathbf{d}_i \cdot \mathbb{K}_i \mathbf{n}_{ij} \frac{|e_{ij}|}{2|\mathbf{d}_i|^2}, \quad t_j = \mathbf{d}_j \cdot \mathbb{K}_j \mathbf{n}_{ji} \frac{|e_{ij}|}{2|\mathbf{d}_j|^2}, \tag{4.4}$$

where $\mathbf{d}_i$ is the vector pointing from the center of V_i to the center of the surface of V_i of which the interface e_{ij} is a part, see Figure 4.1.

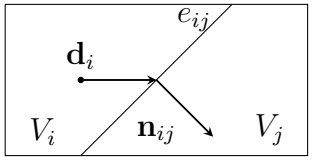

Figure 4.1: Two neighboring control volumes V_i, V_j sharing the intersection e_{ij}, distance vector $\mathbf{d}_i$ and unit outward normal vector $\mathbf{n}_{ij}$.

In the case of Cartesian grids and a diagonal permeability tensor or, more general, whenever the directions of the vectors $\mathbb{K}_i \mathbf{n}_{ij}$ and $-\mathbb{K}_j \mathbf{n}_{ji}$ coincide and are equal to the

directions of $\mathbf{d}_i$ and $-\mathbf{d}_j$, (4.4) simplifies to

$$t_i = k_i \frac{|e_{ij}|}{2|\mathbf{d}_i|}, \quad t_j = k_j \frac{|e_{ij}|}{2|\mathbf{d}_j|}, \tag{4.5}$$

with $k_i = \mathbf{n}_{ij} \cdot \mathbb{K}\mathbf{n}_{ij}$. Only if the permeability tensors are aligned with the control volumes and (4.4) can be simplified to (4.5), the two-point flux approximation works reasonably well. This requirement is referred to as *K-orthogonality*. One can provide another precise notion of *K-orthogonality* for the case of general quadrilaterals following the exposition in [Klau 06b]. In particular, we consider the bilinear mapping $\mathbf{f}_V : \widehat{V} \to V$ from the reference element $\widehat{V} = (0,1)^2$ to the actual control volume V. Denoting by $\mathbb{D}_\mathbf{f}$ the Jacobian matrix of $\mathbf{f}_V$, it is possible to define a reference permeability $\widehat{\mathbb{K}}$ by

$$\widehat{\mathbb{K}}^{-1} = (\det \mathbb{D}_\mathbf{f})^{-1} \mathbb{D}_\mathbf{f}^\mathrm{T} \mathbb{K}^{-1} \mathbb{D}_\mathbf{f}.$$

If the reference permeability $\widehat{\mathbb{K}}$ is a diagonal matrix for all control volumes, the grid is *K-orthogonal*.

4.2.2 Multi-Point Flux Approximation (MPFA)

In order to get over the very severe restriction of K-orthogonality, one possibility is to enhance the flux stencil, i.e., to extend the dependence of a flux f_{ij} to more than only two pressure values. This approach is referred to as *multi-point flux approximation* (MPFA). There exist various MPFA methods, labeled by Latin letters resembling the shape of their flux stencil: the G-method, [Agel 10b], the L-method, [Aava 08, Cao 11], the O-method, [Aava 02, Agel 10a], the U-method, [Aava 06a], and the Z-method, [Nord 05b]. Another noteworthy contribution is the enriched MPFA method, [Chen 08]. We only give a more detailed representation of the O-method for conforming quadrilateral grids, i.e., every intersection e_{ij} is an actual edge of the grid, and follow closely the description provided in [Aava 02].

We will drop the subscripts i and j. In MPFA, the relation (4.3) for calculating the flux f at an intersection e is extended towards

$$f = \sum_{k \in \mathcal{I}_e} t_k p_k, \tag{4.6}$$

with transmissibility coefficients t_k such that $\sum_{k \in \mathcal{I}_e} t_k = 0$. The index set $\mathcal{I}_e$ and the coefficients t_k depend on the particular MPFA-method. Here, $\mathcal{I}_e$ corresponds to the six cells surrounding the edge e, as depicted in Figure 4.2. In order to determine the transmissibility coefficients t_k, the dual grid is introduced which is obtained by connecting each cell center with all edge midpoints of this cell. The elements of the dual grid, each associated to a vertex of the computational grid, are referred to as *interaction regions*, see Figure 4.3. The interaction regions divide each edge e into two half-edges. Inside each interaction region, the transmissibility coefficients for each half-edge are determined. The contributions for the two half-edges are added to give the transmissibility coefficient for the whole edge.

The determination of the half-edge transmissibility coefficients inside an interaction region is based on three requirements: the pressure is assumed to be linear in each of the four sub-cells constituting the region, yielding twelve degrees of freedom. Moreover, the pressure has to be continuous at each edge center and should have the value of the cell

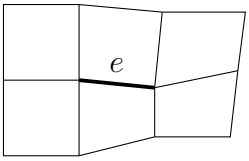

Figure 4.2: Multi-point flux approximation: the six cells corresponding to the index set $\mathcal{I}_e$ for the edge e.

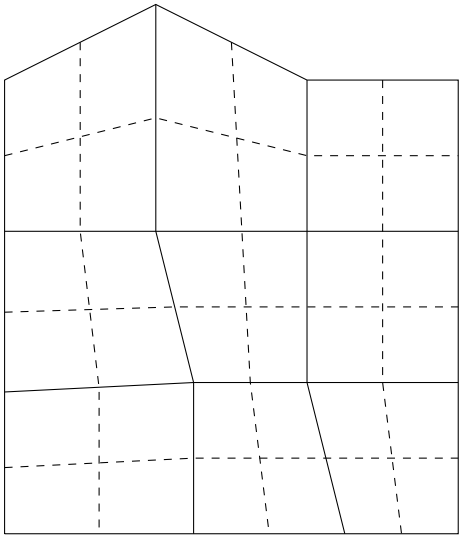

Figure 4.3: Multi-point flux approximation: primal grid (solid lines) and dual grid (dashed lines).

pressure at each cell center, summing up to eight constraints. Finally the fluxes from either side of a half-edge also have to be continuous, giving the four remaining constraints.

To make this more precise, let us consider the situation of a sub-cell i inside one interaction region depicted in Figure 4.4. Considering (4.1a), The flux over a half-edge $e/2$ is given as

$$f_{i,e/2} = -\mathbf{n}_{e/2} \cdot \mathbb{K}_i \, \mathbf{grad}\, p, \tag{4.7}$$

where the length of $\mathbf{n}_{e/2}$ is assumed to be equal to the length of $e/2$. Assuming the linearity of the pressure inside the sub-cell, one ends up with an expression for the constant sub-cell pressure gradient, namely,

$$\mathbf{grad}\, p = (\mathbf{x}_{10} \times \mathbf{x}_{20})^{-1} \sum_{\ell=1}^{2} (\bar{p}_\ell - p_0) \mathbb{R} \mathbf{x}_{\ell 0}, \tag{4.8}$$

where $\mathbf{x}_{\ell 0} = \bar{\mathbf{x}}_\ell - \mathbf{x}_0$ is the vector pointing from the cell center to the edge center, $\bar{p}_\ell$ is the pressure value at the edge center, and $\mathbb{R} = \begin{pmatrix} 0 & 1 \\ -1 & 0 \end{pmatrix}$ is the rotation by $\pi/2$ in clockwise

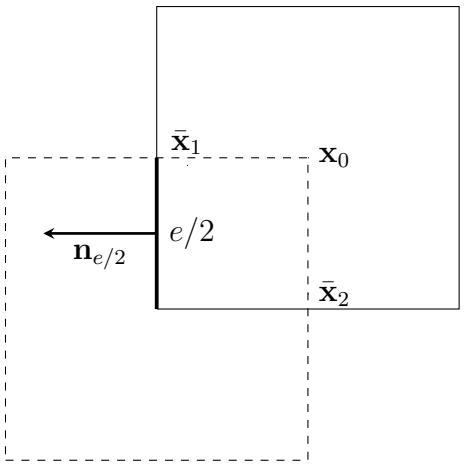

Figure 4.4: Multi-point flux approximation: primal cell (solid lines) and dual cell (dashed lines), calculation of the flux for the half-edge $e/2$.

direction. Combining (4.7) and (4.8) gives

$$f_{i,e/2} = \sum_{\ell=1}^{2} \omega_{e/2,i,\ell}(\bar{p}_\ell - p_0) \tag{4.9}$$

with coefficients $\omega_{e/2,i,\ell} = (\mathbf{x}_{10} \times \mathbf{x}_{20})^{-1}\mathbf{n}_{e/2} \cdot \mathbb{K}_i \mathbb{R}\mathbf{x}_{\ell 0}$.

The next step is to require the continuity of the half-edge fluxes $f_{i,e/2}$ and of the edge center pressures $\bar{p}_\ell$ for each half-edge of the interaction region. Inserting (4.9), this results in two local linear systems of equations, namely,

$$\mathbf{f} = \mathbb{C}\bar{\mathbf{p}} - \mathbb{D}\mathbf{p}, \qquad \mathbb{A}\bar{\mathbf{p}} = \mathbb{B}\mathbf{p},$$

for the half-edge fluxes $\mathbf{f}$, the edge pressures $\bar{\mathbf{p}}$, and the cell pressures $\mathbf{p}$. Eliminating the edge pressures $\bar{\mathbf{p}}$ yields an explicit expression of the half-edge fluxes in terms of the cell pressures,

$$\mathbf{f} = \mathbb{T}\mathbf{p} = (\mathbb{C}\mathbb{A}^{-1}\mathbb{B} - \mathbb{D})\mathbf{p}.$$

Adding up the contribution from two half-edges by considering the corresponding interaction regions leads to transmissibility coefficients for the full edge and to an expression of the form (4.6). Finally, (4.6) in combination with (4.2a) constitutes the global linear system for the cell pressure unknowns.

In terms of computational requirements, MPFA methods are considerably more costly than TPFA methods. For the determination of the transmissibility coefficients, a local linear system has to be inverted for each vertex of the grid. This can be done explicitly for simple situations, [Aava 02]. Moreover, for most transient multi-phase problems, the coefficients have only to be computed once. This changes for tensorial relative permeabilities, which is subject of Chapter 5. For the O-method described above, the flux stencil increases from two neighboring cells to six in 2D and to 18 in 3D, and the resulting cell stencil from five to nine in 2D and from seven to 27 in 3D. This results in higher costs for the linear

solver. The other MPFA-variants try to reduce the size of the stencil to increase efficiency.

4.2.3 Discrete Duality Finite Volume Method (DDFV)

The principle of the discrete-duality finite-volume method is to integrate the equations (4.1) over staggered meshes and to use as degrees of freedom the pressure values both at the centroids and at the vertices of the cells, [Herm 03]. The method relies on a dual grid, which in principle corresponds to the interaction regions encountered in the MPFA method, see Figure 4.3. The mass balance (4.1b) is integrated over each of the elements E_i of the primal grid and over each of the elements V_k of the dual grid, giving

$$\sum_{j\in\mathcal{N}_i^{\mathrm{p}}} \int_{e_{ij}^{\mathrm{p}}} \mathbf{u}\cdot\mathbf{n}\,\mathrm{d}\Gamma = \int_{E_i} q\,\mathrm{d}V, \qquad i=1,\ldots,n_{\mathrm{E}}, \tag{4.10a}$$

$$\sum_{\ell\in\mathcal{N}_k^{\mathrm{d}}} \int_{e_{k\ell}^{\mathrm{d}}} \mathbf{u}\cdot\mathbf{n}\,\mathrm{d}\Gamma = \int_{V_k} q\,\mathrm{d}V, \qquad k=1,\ldots,n_{\mathrm{CV}}, \tag{4.10b}$$

where the superscripts p and d indicate primal and dual quantities, respectively. Each primal edge e_{ij}^{p} corresponds to exactly one crossing dual edge $e_{k\ell}^{\mathrm{d}}$, see Figure 4.5. We note that one dual edge $e_{k\ell}^{\mathrm{d}}$ usually consists of two straight line segments.

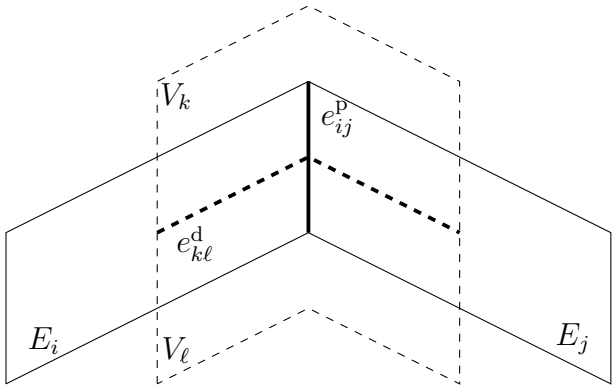

Figure 4.5: Discrete duality finite volume method: primal edge e_{ij}^{p} and corresponding dual edge $e_{k\ell}^{\mathrm{d}}$ with associated neighboring elements E_i, E_j and control volumes V_k, V_ℓ.

Specific approximations f_{ij}^{p} of the primal fluxes $\int_{e_{ij}^{\mathrm{p}}} \mathbf{u}\cdot\mathbf{n}\,\mathrm{d}\Gamma$ and $f_{k\ell}^{\mathrm{d}}$ of the dual fluxes $\int_{e_{k\ell}^{\mathrm{d}}} \mathbf{u}\cdot\mathbf{n}\,\mathrm{d}\Gamma$ are given by

$$\begin{pmatrix} f_{ij}^{\mathrm{p}} \\ f_{k\ell}^{\mathrm{d}} \end{pmatrix} = \begin{pmatrix} a_{\mathrm{pp}} & a_{\mathrm{pd}} \\ a_{\mathrm{dp}} & a_{\mathrm{dd}} \end{pmatrix} \begin{pmatrix} p_j^{\mathrm{p}} - p_i^{\mathrm{p}} \\ p_\ell^{\mathrm{d}} - p_k^{\mathrm{d}} \end{pmatrix}, \tag{4.11}$$

where the coefficients $a_{\mathrm{pp}}, a_{\mathrm{pd}}, a_{\mathrm{dp}}, a_{\mathrm{dd}}$ depend on the geometry of the grid and on the permeability $\mathbb{K}$. Enforcing local conservation (4.2) for both the primal and the dual fluxes

results in a linear system of the form

$$\begin{pmatrix} \mathbb{A}_{\mathrm{pp}} & \mathbb{A}_{\mathrm{pd}} \\ \mathbb{A}_{\mathrm{dp}} & \mathbb{A}_{\mathrm{dd}} \end{pmatrix} \begin{pmatrix} p_h^{\mathrm{p}} \\ p_h^{\mathrm{d}} \end{pmatrix} = \begin{pmatrix} q_{\mathrm{p}} \\ q_{\mathrm{d}} \end{pmatrix}, \tag{4.12}$$

where the system matrix is symmetric positive definite provided that the permeability $\mathbb{K}$ is symmetric positive definite. In contrast to the TPFA and MPFA method discussed above, both element pressures p_h^{p} and vertex pressures p_h^{d} appear as unknowns in (4.12). According to the examples provided in [Herm 03], the DDFV method handles distorted grids and full permeability tensors very well.

If both the primal and the dual grid are K-orthogonal, the system (4.12) decouples in the sense that $\mathbb{A}_{\mathrm{pd}}$ and $\mathbb{A}_{\mathrm{dp}}$ are both zero. In this case, the solutions p_h^{p} and p_h^{d} coincide with the solutions obtained by the TPFA method on the primal and dual grid, respectively.

4.2.4 Other Control Volume Methods

There exists a large variety of other control volume methods that try to overcome the restrictions of the TPFA method. Like the DDFV method presented above is based on the introduction of additional vertex pressure unknowns, one class of control volume methods is based on additional edge pressure unknowns. This includes the hybrid finite-volume scheme presented in [Eyma 07] and the SUSHI scheme, [Eyma 10]. While the former relies on one additional unknown for each edge, the latter allows to add unknowns only to a subset of edges. A rather different approach has been developed in form of nonlinear two-point flux approximation methods, [Lipn 09a]. There, the transmissibilities (4.4) depend on the unknown solution values. A great advantage of the scheme is monotonicity, coming at the expense of having to solve a nonlinear system of equations.

4.3 Finite Difference Methods

The defining feature of finite difference methods is the discretization of the differential operators appearing in the PDE to solve. In case of problem (4.1), this amounts to find discrete differential operators as approximations of div and **grad** or $\mathbb{K}\,$**grad**.

4.3.1 Mimetic Finite Difference Method (MFD)

Mimetic finite difference methods are discretization methods for partial differential equations which promise to be robust for general unstructured polygonal and polyhedral meshes, including adaptive local refinement, non-matching interfaces, and degenerate or non-convex elements. Moreover, in view of the considered problem (4.1), they qualify for dealing with strongly heterogeneous full tensorial permeabilities. Evolving from standard finite differences, the development of the methodology started originally in [Favo 81], where the name "support operator method" has been used. A good introduction is provided by [Shas 96], a framework for the mathematical analysis in terms of mixed formulations is developed in [Brez 05a], and a quite rich annotated bibliography can be found at [Robi 03]. Recent applications to porous media flow problems are presented in [Aarn 07, Aarn 08b, Nils 10b, Lipn 11].

As a representative example, we will present the family of mimetic finite difference methods developed in [Brez 05b]. After having obtained a triangulation of the computational

domain Ω, the first step is to choose approximation spaces for pressures and velocities. Here, just like for the control volume methods presented above, the space Q_h^{MFD} of element-wise constants is selected for the discretization of the pressures. The velocities are also approximated as before in a space X_h^{MFD} by associating a normal velocity u_e with every element E and intersection $e \in \mathcal{E}_E$, subject to the continuity condition $u_{ij} = -u_{ji}$ for two neighboring elements E_i and E_j. On Q_h^{MFD}, the usual L^2 scalar product is given and denoted by $(\cdot\,,\cdot)_{Q_h^{\mathrm{MFD}}}$, i.e.,

$$(p,q)_{Q_h^{\mathrm{MFD}}} = \int_\Omega pq \,\mathrm{d}V = \sum_{E\in\mathcal{T}_h} |E| p_E q_E. \tag{4.13}$$

The velocity space X_h^{MFD} is also assumed to be equipped with a scalar product $(\cdot\,,\cdot)_{X_h^{\mathrm{MFD}}}$, defined element-wise by

$$(\mathbf{u},\mathbf{v})_E = \mathbf{u}_E^{\mathrm{T}} \mathbb{M}_E \mathbf{v}_E, \tag{4.14}$$

where $\mathbf{u}_E$ denotes the vector with entries u_e, $e \in \mathcal{E}_E$, and $\mathbb{M}_E$ is a symmetric positive definite $n_{i,\mathrm{e}} \times n_{i,\mathrm{e}}$ matrix accounting for the element geometry and the element permeability $\mathbb{K}_i$. For more details on the construction of appropriate element matrices $\mathbb{M}_E$, we refer to [Brez 05b].

The fundamental idea is now to discretize the first order differential operators div and $-\mathbb{K}\,\mathbf{grad}$ to $\mathrm{div}_h : X_h^{\mathrm{MFD}} \to Q_h^{\mathrm{MFD}}$ and $\mathrm{G}_h : Q_h^{\mathrm{MFD}} \to X_h^{\mathrm{MFD}}$, respectively, in such a way that the discrete operators are adjoint to each other, i.e.,

$$(\mathbf{u}, \mathbf{G}_h p)_{X_h^{\mathrm{MFD}}} = (\mathrm{div}_h\,\mathbf{u}, p)_{Q_h^{\mathrm{MFD}}}, \quad \mathbf{u} \in X_h^{\mathrm{MFD}},\ p \in Q_h^{\mathrm{MFD}}. \tag{4.15}$$

Choosing div_h in the canonical way, i.e.,

$$(\mathrm{div}_h\,\mathbf{u})_E = |E|^{-1} \sum_{e\in\mathcal{E}_E} |e| u_e, \tag{4.16}$$

the crucial step is to select a suitable scalar product $(\cdot\,,\cdot)_{X_h^{\mathrm{MFD}}}$. The missing operator $\mathbf{G}_h$ is then uniquely determined by (4.15). Finally, the discrete problem is to find $(p_h, \mathbf{u}_h) \in Q_h^{\mathrm{MFD}} \times X_h^{\mathrm{MFD}}$ such that

$$\mathbf{u}_h = \mathbf{G}_h p_h, \tag{4.17a}$$

$$\mathrm{div}_h\,\mathbf{u}_h = q_h. \tag{4.17b}$$

From (4.17b) together with (4.16) and the observation that $f_e = |e| u_e$, it becomes obvious that the presented mimetic finite difference method is locally conservative.

In contrast to the control volume methods presented before, the fluxes are not explicitly given in terms of the pressure, but enter as degrees of freedom into the global system of linear equations. This global system exhibits a saddle-point structure. Just like for systems arising from a mixed finite element discretization, discussed below in Section 4.4.1, a hybridization can be performed which leads to a positive definite system for edge pressures. There also exists another variant of mimetic finite difference methods that allows to locally eliminate the fluxes without hybridization yielding a system for the cell pressures, [Lipn 09b].

4.4 Finite Element Methods

All finite element methods are based on weak formulations in the sense that the original strong form of the problem involving PDEs is transformed into an integral equation, thereby weakening the requirements on the smoothness of the solution components. The discretization is performed by discretizing the infinite-dimensional function spaces appearing in the weak formulation. In the following, we will examine four particular finite element methods for the solution of problem (4.1): the mixed finite element method, the discontinuous Galerkin method, the continuous Galerkin method, and the least-squares finite element method.

4.4.1 Mixed Finite Element Method (MFEM)

Mixed finite element methods constitute a rather universal tool for solving partial differential equations. An elaborated mathematical theory exists, which is the main reason, why many of the locally conservative methods discussed here have been interpreted in the mixed finite element framework, see Section 4.6. The monograph [Brez 91] provides a comprehensive description of the mathematical theory. There exist numerous applications of mixed finite element methods to porous media problems, including [Doug 83, Chou 91, Hube 99, Thom 11].

In the following, we develop the mixed weak formulation of (4.1). Darcy's law (4.1a) is first multiplied by $\mathbb{K}^{-1}$, then multiplied by a velocity test function $\mathbf{v}$ and integrated over the domain Ω, yielding

$$(\mathbb{K}^{-1}\mathbf{u}, \mathbf{v})_\Omega + (\mathbf{grad}\, p, \mathbf{v})_\Omega = 0,$$

where $(\,\cdot\,,\,\cdot\,)_\Omega$ indicates the L^2 scalar product on Ω. Partial integration of the second term, and incorporating the boundary conditions (4.1c), (4.1d) by assuming $\mathbf{v}\cdot\mathbf{n}|_{\Gamma_\mathrm{N}} = 0$ gives

$$(\mathbb{K}^{-1}\mathbf{u}, \mathbf{v})_\Omega - (\operatorname{div}\mathbf{v}, p)_\Omega = (p_\mathrm{D}, \mathbf{v}\cdot\mathbf{n})_{\Gamma_\mathrm{D}}. \tag{4.18}$$

Multiplying the mass balance (4.1b) by a pressure test function w and integrating over Ω results in

$$(\operatorname{div}\mathbf{u}, w)_\Omega = (q, w)_\Omega. \tag{4.19}$$

We observe that (4.18) and (4.19) hold for $p, w \in L^2(\Omega)$, $\mathbf{u} \in H^{\mathrm{div}}_\mathrm{N}(\Omega) = \{\mathbf{v} \in H^{\mathrm{div}}(\Omega) : \mathbf{v}\cdot\mathbf{n}|_{\Gamma_\mathrm{N}} = q_\mathrm{N}\}$ and $\mathbf{v} \in H^{\mathrm{div}}_0(\Omega) = \{\mathbf{v} \in H^{\mathrm{div}}(\Omega) : \mathbf{v}\cdot\mathbf{n}|_{\Gamma_\mathrm{N}} = 0\}$. Defining the bilinear forms

$$a(\mathbf{u}, \mathbf{v}) = (\mathbb{K}^{-1}\mathbf{u}, \mathbf{v})_\Omega, \quad b(\mathbf{v}, w) = -(\operatorname{div}\mathbf{v}, w)_\Omega,$$

we arrive at the mixed weak problem formulation: Find $(\mathbf{u}, p) \in H^{\mathrm{div}}_\mathrm{N}(\Omega) \times L^2(\Omega)$ such that

$$a(\mathbf{u}, \mathbf{v}) + b(\mathbf{v}, p) = (p_\mathrm{D}, \mathbf{v}\cdot\mathbf{n})_{\Gamma_\mathrm{D}}, \qquad \mathbf{v} \in H^{\mathrm{div}}_0(\Omega), \tag{4.20a}$$

$$b(\mathbf{u}, w) = -(q, w)_\Omega, \qquad w \in L^2(\Omega). \tag{4.20b}$$

The discretization is performed by a Galerkin method, where the infinite-dimensional spaces $H^{\mathrm{div}}(\Omega)$ and $L^2(\Omega)$ are approximated by finite-dimensional spaces X_h^{MFE} and Q_h^{MFE}, respectively, such that $Q_h^{\mathrm{MFE}} = \operatorname{div} X_h^{\mathrm{MFE}}$. The most popular choice are Raviart–Thomas finite elements for X_h^{MFE} and element-wise constants for Q_h^{MFE}, a great variety of other

choices is possible, [Brez 91]. The resulting discrete problem reads: Find $(\mathbf{u}_h, p_h) \in X_{h,\mathrm{N}} \times Q_h^{\mathrm{MFE}}$ such that

$$a(\mathbf{u}_h, \mathbf{v}) + b(\mathbf{v}, p_h) = (p_{\mathrm{D}}, \mathbf{v}\cdot\mathbf{n})_{\Gamma_{\mathrm{D}}}, \qquad \mathbf{v} \in X_{h,0}, \tag{4.21a}$$

$$b(\mathbf{u}_h, w) = -(q, w)_\Omega, \qquad w \in Q_h^{\mathrm{MFE}}. \tag{4.21b}$$

It is important that the discrete spaces X_h^{MFE} and Q_h^{MFE} form an *inf-sup* stable pairing, expressing the fact that the requirement (4.21b) does not pose too many or too few constraints. In mathematical terms, this is expressed as the requirement

$$\inf_{w\in Q_h^{\mathrm{MFE}}} \sup_{\mathbf{v}\in X_h^{\mathrm{MFE}}} \frac{b(\mathbf{v}, w)}{\|\mathbf{v}\|_{X_h^{\mathrm{MFE}}} \|w\|_{Q_h^{\mathrm{MFE}}}} \geq c > 0, \tag{4.22}$$

where the positive constant c is independent of the grid size, and $\|\cdot\|_{X_h^{\mathrm{MFE}}}$, $\|\cdot\|_{Q_h^{\mathrm{MFE}}}$ indicate appropriate norms.

As for mimetic finite differences, the discrete system (4.21) exhibits a saddle-point structure resulting in an indefinite system matrix in the linear system

$$\begin{pmatrix} \mathbb{A} & \mathbb{B} \\ \mathbb{B}^{\mathrm{T}} & 0 \end{pmatrix} \begin{pmatrix} \mathbf{u}_h \\ p_h \end{pmatrix} = \begin{pmatrix} p_{\mathrm{D},h} \\ q_h \end{pmatrix}. \tag{4.23}$$

This fact poses severe limitations on the choice of linear solvers. Moreover, unknowns are associated both with the velocity and the pressure such that the system size is considerably increased. A common way to circumvent both shortcomings is hybridization which in this case results in a positive definite linear system for new unknowns representing face pressures. To this end, the space X_h^{MFE} of discrete velocities is first enlarged by dropping the requirement on the continuity of the normal velocities over element faces, which gives the space $\widetilde{X}_h^{\mathrm{MFE}} = \prod_{E\in\mathcal{T}_h} X_{h,E}$, where $X_{h,E}$ denotes the space of velocities associated with the element E. The continuity of the fluxes is enforced explicitly by introducing Lagrange multipliers $\lambda \in M_h = \{\mu \in L^2(\mathcal{E}_h) : \lambda|_e \in P^k(e), e \in \mathcal{E}_h\}$, where $P^k(e)$ denotes the space of polynomials up to degree k on edge e. The choice of k relies on the choice of the discrete spaces for the velocity and the element pressures. For the combination of Raviart–Thomas and element-wise constants, $k = 0$ is chosen. Flux continuity is stated as

$$c_h(\mathbf{u}, \mu) = \sum_{e\in\mathcal{E}_h} ([\mathbf{u}\cdot\mathbf{n}]_e, \mu)_e = 0, \quad \mu \in M_h.$$

where $[\,\cdot\,]_e$ denotes the jump over the edge e. In addition, the weak form of (4.1) is derived by now integrating (4.1a) element-wise, and partial integration on each element results in the bilinear form $c_h(\,\cdot\,,\,\cdot\,)$ entering in a symmetric way. The hybrid version of the mixed discrete problem (4.21) reads: Find $(\mathbf{u}_h, p_h, \lambda_h) \in \widetilde{X}_{h,\mathrm{N}} \times Q_h^{\mathrm{MFE}} \times M_h$ such that

$$a(\mathbf{u}_h, \mathbf{v}) + b_h(\mathbf{v}, p_h) + c_h(\mathbf{v}, \lambda_h) = (p_{\mathrm{D}}, \mathbf{v}\cdot\mathbf{n})_{\Gamma_{\mathrm{D}}}, \qquad \mathbf{v} \in \widetilde{X}_{h,0}, \tag{4.24a}$$

$$b_h(\mathbf{u}_h, w) = -(q, w)_\Omega, \qquad w \in Q_h^{\mathrm{MFE}}, \tag{4.24b}$$

$$c_h(\mathbf{u}_h, \mu) = 0, \qquad \mu \in M_h, \tag{4.24c}$$

where $b_h(\,\cdot\,,\,\cdot\,)$ is an element-wise discretization of $b(\,\cdot\,,\,\cdot\,)$, namely,

$$b_h(\mathbf{v}, w) = -\sum_{E\in\mathcal{T}_h} (\operatorname{div}\mathbf{v}, w)_E.$$

The system of the hybridized discrete problem (4.24) is given by

$$\begin{pmatrix} \widetilde{\mathbb{A}} & \widetilde{\mathbb{B}} & \mathbb{C} \\ \widetilde{\mathbb{B}}^{\mathrm{T}} & 0 & 0 \\ \mathbb{C}^{\mathrm{T}} & 0 & 0 \end{pmatrix} \begin{pmatrix} \widetilde{\mathbf{u}}_h \\ p_h \\ \lambda_h \end{pmatrix} = \begin{pmatrix} p_{\mathrm{D},h} \\ q_h \\ 0 \end{pmatrix}. \tag{4.25}$$

The key difference to the original system (4.23) now is that the submatrix $\widetilde{\mathbb{A}}$ is block-diagonal with each block representing the element contributions of $a(\,\cdot\,,\,\cdot\,)$, thus, a local inversion is possible. In particular, the velocity $\mathbf{u}_h$ and the element pressures p_h can be locally eliminated by mans of a Schur complement reduction, yielding a positive definite system for the edge pressures λ_h,

$$(\mathbb{C}^{\mathrm{T}}\widetilde{\mathbb{A}}^{-1}\mathbb{C} - \mathbb{F}^{\mathrm{T}}\mathbb{D}^{-1}\mathbb{F})\lambda_h = \mathbb{F}^{\mathrm{T}}\mathbb{D}^{-1}q_h, \tag{4.26}$$

where $\mathbb{F} = \mathbb{B}^{\mathrm{T}}\widetilde{\mathbb{A}}^{-1}\mathbb{C}$ and $\mathbb{D} = \mathbb{B}^{\mathrm{T}}\widetilde{\mathbb{A}}^{-1}\mathbb{B}$, and where the Dirichlet boundary conditions p_{D} can be directly incorporated in a standard way. After determination of the edge pressures λ_h, the velocity $\mathbf{u}_h$ and the element pressures p_h can be reconstructed via a local post-process. It is remarkable that for lowest order spaces, the system (4.26) is equivalent to the system obtained directly from a non-conforming finite element discretization of (4.1) by means of Crouzeix–Raviart finite elements, [Chen 96].

4.4.2 Discontinuous Galerkin Method (DGFEM)

Discontinuous Galerkin (DG) methods are among the most popular PDE discretization methods today. This is mainly due to their ease of handling unstructured, and, in particular, nonconforming grids, local mesh adaptivity, higher order approximations, and parallelism. Recent textbooks are [Hest 08, Rivi 08]. Here, we present the DG method known as OBB-scheme, which has been introduced in [Oden 98], and applied to porous media flow in, for example, [Rivi 00, Bast 03].

Starting point is the strong formulation obtained after inserting Darcy's law (4.1a) into the mass balance (4.1b),

$$-\operatorname{div}\mathbb{K}\,\mathbf{grad}\,p = q. \tag{4.27}$$

The finite element space Q_h^{DG} for approximating the pressure p consists of element-wise polynomial, but globally discontinuous functions,

$$Q_h^{\mathrm{DG}} = \{w \in L^2(\Omega) : w|_E \in P^k(E),\ E \in \mathcal{T}_h\}. \tag{4.28}$$

Multiplying (4.27) with a test function $w \in Q_h^{\mathrm{DG}}$, integrating over an element E and applying integration by parts gives

$$(\mathbb{K}\,\mathbf{grad}\,p, \mathbf{grad}\,w)_E - \sum_{e\in\mathcal{E}_E} (\mathbf{n}\cdot\mathbb{K}\,\mathbf{grad}\,p, w)_e = (q, w)_E.$$

Introducing the average $\{\cdot\}_e$ over an edge e, summation over all elements E yields

$$\sum_{E\in\mathcal{T}_h}(\mathbb{K}\,\mathbf{grad}\,p,\mathbf{grad}\,w)_E-\sum_{e\in\mathcal{E}_h}((\{\mathbf{n}\cdot\mathbb{K}\,\mathbf{grad}\,p\},[w])_e+([\mathbf{n}\cdot\mathbb{K}\,\mathbf{grad}\,p],\{w\})_e)=(q,w)_\Omega.$$

The OBB-scheme drops the last term on the left hand side and introduces the additional term $(\{\mathbf{n}\cdot\mathbb{K}\,\mathbf{grad}\,w\},[p])_e$ on each edge. After insertion of the boundary conditions (4.1c), (4.1d), the final discrete problem reads: Find $p_h\in Q_h^{\mathrm{DG}}$ such that

$$a_h(p_h,w)=l_h(w),\qquad w\in Q_h^{\mathrm{DG}},\tag{4.29}$$

where

$$\begin{aligned}a_h(p,w)&=\sum_{E\in\mathcal{T}_h}(\mathbb{K}\,\mathbf{grad}\,p,\mathbf{grad}\,w)_E-\sum_{e\in\mathcal{E}_h}((\{\mathbf{n}\cdot\mathbb{K}\,\mathbf{grad}\,p\},[w])_e-(\{\mathbf{n}\cdot\mathbb{K}\,\mathbf{grad}\,w\},[p])_e)\,,\\ l_h(w)&=(q,w)_\Omega+\sum_{e\in\Gamma_{\mathrm{D}}}(\mathbf{n}\cdot\mathbb{K}\,\mathbf{grad}\,w,p_{\mathrm{D}})_e-\sum_{e\in\Gamma_{\mathrm{N}}}(w,q_{\mathrm{N}})_e.\end{aligned}$$

It is easy to see that the presented DG method is locally conservative on each element E by taking a test function w which is constant equal to one on E and zero everywhere else. Insertion in (4.29) gives

$$-\sum_{e\in\mathcal{E}_E}\int_e\{\mathbf{n}\cdot\mathbb{K}\,\mathbf{grad}\,p_h\}\,\mathrm{d}\Gamma=\int_E q\,\mathrm{d}V.$$

Therefore, the requirements (4.2) are achieved by setting $f_e=-\int_e\{\mathbf{n}\cdot\mathbb{K}\,\mathbf{grad}\,p_h\}\,\mathrm{d}\Gamma$. Still, the quantity $\mathbf{n}\cdot\mathbb{K}\,\mathbf{grad}\,p_h$ usually is point-wise discontinuous across element edges, which can lead to numerical problems for attached transport equations. One way to overcome these problems is to reconstruct point-wise continuous fluxes, as carried out in [Bast 03].

4.4.3 Continuous Galerkin Method with Flux Post-Processing (CGFEM)

The continuous Galerkin (CG) method is traditionally the most widely used finite element method in science and engineering, [Ciar 02, Hugh 87]. However, when it comes to the simulation of transport problems, the method suffers from the severe drawback that it is not locally conservative. Meanwhile, there exist some approaches to reconstruct locally conservative fluxes from the solution of the continuous Galerkin method, [Cock 07, Hugh 00]. In the following, we will present the approach introduced in [Cock 07].

Just like the other finite element methods presented above, the CG method also starts from a strong problem formulation given by a PDE and performs a transformation towards a weak formulation in variational form. In particular, multiplying (4.27) with a pressure test function w, an integration over the whole domain Ω is performed, partial integration is applied, and the boundary conditions (4.1c), (4.1d) are incorporated such that

$$(\mathbb{K}\,\mathbf{grad}\,p,\mathbf{grad}\,w)_\Omega=(q,w)_\Omega-(q_{\mathrm{N}},w)_{\Gamma_{\mathrm{N}}}.$$

The above integral equation has to hold for a pressure function $p\in H^1_{\mathrm{D},p}(\Omega)=\{w\in$

$H^1(\Omega) : w|_{\Gamma_\mathrm{D}} = p_\mathrm{D}\}$ and for all test functions w in $H^1_{\mathrm{D},0}(\Omega) = \{w \in H^1(\Omega) : w|_{\Gamma_\mathrm{D}} = 0\}$, with $H^1(\Omega)$ denoting the space of square-integrable functions with square-integrable first-order weak derivatives. This leads to the following variational problem: Find $p \in H^1_{\mathrm{D},p}(\Omega)$ such that

$$a(p, w) = l(w), \qquad w \in H^1_{\mathrm{D},0}(\Omega), \tag{4.30}$$

with the obvious definitions of the bilinear form $a(\,\cdot\,,\,\cdot\,)$ and of the linear form $l(\,\cdot\,)$. As before, the continuous variational problem (4.30) is discretized by discretizing the appearing infinite-dimensional function spaces, in this case $H^1(\Omega)$ and its subspaces with respect to the Dirichlet boundary condition on Γ_D. For the CG method, the discrete space of pressures is taken as

$$Q_h^\mathrm{CG} = \{w \in \mathcal{C}^0(\Omega) : w|_E \in P^k(E),\ E \in \mathcal{T}_h\}.$$

The major difference to the space Q_h^DG employed in DG methods (4.28) is the requirement that only globally continuous functions are allowed. The resulting discrete variational problem reads: Find $p_h \in Q_{h,\mathrm{D}}$ such that

$$a(p_h, w) = l(w), \qquad w \in Q_{h,0}, \tag{4.31}$$

where the subspaces $Q_{h,\mathrm{D}}$ and $Q_{h,0}$ are chosen according to the Dirichlet boundary condition (4.1c).

It is quite obvious that the CG finite element solution p_h of (4.31) is not locally conservative, at least not in a trivial way. The normal component of the gradient $-\mathbb{K}\,\mathbf{grad}\,p_h$ is discontinuous across element edges and defining an edge flux as an average of two element contributions would satisfy (4.2b), but in general violate (4.2a). Nevertheless, it is possible to reconstruct locally conservative fluxes, as is originally presented in [Cock 07]. We will present a brief summary of this work in the following. Having computed the finite element solution p_h of (4.31), a vectorial numerical flux $\mathbf{f}_h$ on the edges can be defined as

$$\mathbf{f}_h = \begin{cases} q_\mathrm{N}\mathbf{n}, & \text{on } \Gamma_\mathrm{N}, \\ -\mathbb{K}\,\mathbf{grad}\,p_h + \alpha\mathbf{j}_h, & \text{on } \Gamma_\mathrm{D}, \\ \{-\mathbb{K}\,\mathbf{grad}\,p_h\} - \boldsymbol{\beta}[\mathbf{n}\cdot\mathbb{K}\,\mathbf{grad}\,p_h] + \alpha\mathbf{j}_h, & \text{else}, \end{cases} \tag{4.32}$$

where α ($\boldsymbol{\beta}$) is an edge-wise constant positive single (vector) valued function, and $\mathbf{j}_h$ is an element of the space of jumps J_h which will be determined by a solution of an additional global problem. In particular, this space of jumps is defined in terms of the DG space Q_h^DG as

$$J_h = \{[w\mathbf{n}] : w \in Q_h^\mathrm{DG}\},$$

and the additional global problem reads: Find $\mathbf{j}_h \in J_h$ such that for all $[w\mathbf{n}] \in J_h$

$$\begin{aligned}(\alpha\mathbf{j}_h, [w\mathbf{n}])_{\mathcal{E}_h\setminus\Gamma_\mathrm{N}} =& (\{\mathbb{K}\,\mathbf{grad}\,p_h\} + \boldsymbol{\beta}[\mathbf{n}\cdot\mathbb{K}\,\mathbf{grad}\,p_h], [w\mathbf{n}])_{\mathcal{E}_h\setminus\partial\Omega} \\ &+ (\mathbb{K}\,\mathbf{grad}\,p_h, w\mathbf{n})_{\Gamma_\mathrm{D}} - \sum_{E\in\mathcal{T}_h} (\mathbb{K}\,\mathbf{grad}\,p_h, \mathbf{grad}\,w)_E + l(w).\end{aligned} \tag{4.33}$$

In [Cock 07], a basis of J_h is described which is suitable for the solution of the problem above. Moreover, it can be shown that the parameter α can be selected in such a way that the condition number of the matrix associated with $(\alpha\mathbf{j}_h, [w\mathbf{n}])$ is independent of the number of unknowns, and thus the additional costs for computing $\mathbf{j}_h$ are small compared

to the costs for the computation of p_h.

Local conservation for an element E can now be easily verified by setting $f_e = \int_e \mathbf{f}_h \cdot \mathbf{n}\,\mathrm{d}\Gamma$ and evaluating the expression $\sum_{e\in\mathcal{E}_E} \int_e \mathbf{f}_h \cdot \mathbf{n}\,\mathrm{d}\Gamma$. Inserting the definition (4.32) and testing (4.33) with the characteristic function associated with E shows (4.2a). As for discontinuous Galerkin methods, the numerical flux $\mathbf{f}_h$ can be processed to establish an H^{div}-conforming velocity field defined over the whole domain Ω.

4.4.4 Least-Squares Finite Element Method (LSFEM)

In least-squares finite-element methods, [Boch 09, Jian 98], the saddle-point variational problem is replaced by an unconstrained minimization of a quadratic least-squares functional defined by summing up the residuals in (4.1). Traditionally, the same approximations have been used for both the pressure and the velocity field, and no local conservation could be achieved. Recently, so-called *compatible* least-squares FEM have been investigated which are based on inf-sup stable pairings known from mixed finite element methods. In the following, the compatible LSFEM introduced in [Boch 08] is presented.

The least-squares method under consideration is defined in terms of the quadratic functional

$$J(p,\mathbf{u}) = \frac{1}{2}\left(\|\mathbb{K}^{-1/2}(\mathbf{u} + \mathbb{K}\,\mathbf{grad}\,p)\|_0^2 + \|\operatorname{div}\mathbf{u} - q\|_0^2\right).$$

It is immediately clear that a strong solution $(p,\mathbf{u})$ of (4.1) minimizes the functional J. After choosing finite element subspaces for pressure and velocity, the discrete problem reads: Find $(p_h,\mathbf{u}_h)$ in $Q_h^{\mathrm{LS}} \times X_h^{\mathrm{LS}}$ such that

$$J(p_h,\mathbf{u}_h) = \min_{w\in Q_h^{\mathrm{LS}},\,\mathbf{v}\in X_h^{\mathrm{LS}}} J(w,\mathbf{v}). \tag{4.34}$$

Presumably the most attractive feature of the proposed method is that the two spaces Q_h^{LS} and X_h^{LS} do not have to satisfy any compatibility condition. They even could be based on distinct triangulations of the domain Ω. Using standard variational calculus, it is easy to see that the minimization problem (4.34) is equivalent to solving the variational equation

$$(\mathbf{u}_h + \mathbb{K}\,\mathbf{grad}\,p_h,\ \mathbb{K}^{-1}\mathbf{v} + \mathbf{grad}\,w)_\Omega + (\operatorname{div}\mathbf{u}_h, \operatorname{div}\mathbf{v})_\Omega = (q, \operatorname{div}\mathbf{v})_\Omega, \quad (w,\mathbf{v}) \in Q_h^{\mathrm{LS}} \times X_h^{\mathrm{LS}}. \tag{4.35}$$

In terms of local conservation, the fluxes $f_e = \int_e \mathbf{u}_h \cdot \mathbf{n}\,\mathrm{d}\Gamma$ automatically satisfy (4.2b) provided that $X_h^{\mathrm{LS}} \subset H^{\mathrm{div}}(\Omega)$. However, the requirement (4.2a) is not necessarily satisfied. The authors of [Boch 08] suggest an easy local post-process which corrects the fluxes such that they satisfy both (4.2a) and (4.2b).

4.5 Control-Volume Finite-Element Methods

As the name indicates, control-volume finite-element methods (CVFEM) inherit features from both control volume methods and finite element methods. They have in common that the control volumes do not coincide with the elements of the computational grid. While conservation of quantities is formulated with respect to the control volumes, a finite element interpolation is used for evaluating the solution values at the quadrature nodes. This can be interpreted as choosing different sets of test functions compared to conventional finite

element methods. We will present two particular CVFEM: the box method in Section 4.5.1 and the control-volume mixed-finite-element method in Section 4.5.2.

4.5.1 Box Method

The box method is a mixture of a vertex-centered finite volume method and a continuous Galerkin finite element method. It has been theoretically analyzed in [Hack 89, Bank 87]. Applications to porous media flow can be found in [Cai 91, Schm 93, Durl 94, Clas 02].

The control volumes for the box method are the same as the interaction regions for the MPFA method, namely, the elements of the dual grid associated with the vertices, see Figure 4.3. On each such control volume V, the mass balance with incorporated Darcy's law (4.27) is integrated, and an application of the Gauß theorem gives

$$\sum_{e\in\mathcal{E}_V}\int_e -\mathbf{n}\cdot\mathbb{K}\,\mathbf{grad}\,p_h\,\mathrm{d}\Gamma = \int_V q\,\mathrm{d}V, \qquad V\in\mathcal{V}_h. \tag{4.36}$$

The discrete pressure p_h is assumed to be in Q_h^{CG}. We note that for general quadrilaterals, an edge e is usually not a straight line segment, but rather consists of two segments. The crucial observation now is that the boundary of a control volume V, i.e., the edges e, are in the interior of elements E, $E\cap V\neq\emptyset$. Therefore, the finite-element interpolation of the nodal pressure values can be chosen to approximate the value of the pressure gradient $\mathbf{grad}\,p$ on the control volume edges e. This would not be possible on the boundary of an element E, since the finite-element gradients are discontinuous there. Defining the fluxes in the usual way as $f_e=\int_e -\mathbf{n}\cdot\mathbb{K}\,\mathbf{grad}\,p_h\,\mathrm{d}\Gamma$ directly yields the local conservation requirements (4.2).

4.5.2 Control Volume Mixed Finite Element Method (CVMFEM)

The control volume mixed finite element method has been proposed in [Cai 97] with the aim to "provide a simple, systematic, easily implemented procedure for obtaining accurate velocity approximations on irregular (i.e., distorted logically rectangular) block-centered quadrilateral grids." In the following, we will summarize this original exposition.

Just like for the mixed method using lowest order Raviart–Thomas elements for the velocity and element-wise constants for the pressure, one degree of freedom for the flux f_{ij} is associated with each element edge e_{ij}. The control volumes for the pressure are the elements E_i, but different control volumes are associated with the edge fluxes. In particular, the control volume associated with the edge e_{ij} is the union of the two half elements obtained by taking the midpoints of the four edges adjacent to e_{ij}, and then joining the two pairs of midpoints by straight line segments, see Figure 4.6. The corresponding half of the element E_i is indicated by E_{ij}, the half of E_j by E_{ji}, such that the control volume associated with the edge e_{ij} can be written as $V_{ij}=E_{ij}\cup E_{ji}$.

The mass balance (4.1b) is now integrated on each element, and the usage of Gauß integration instantly yields the first requirement (4.2a) of local conservation. Darcy's law (4.1a) is integrated on each of the edge control volumes, after multiplying with $\mathbb{K}^{-1}$ and with a test function $\mathbf{v}_{e_{ij}}$, such that

$$(\mathbb{K}^{-1}\mathbf{u}_h,\mathbf{v}_{e_{ij}})_{V_{ij}}+(\mathbf{grad}\,p_h,\mathbf{v}_{e_{ij}})_{V_{ij}}=0. \tag{4.37}$$

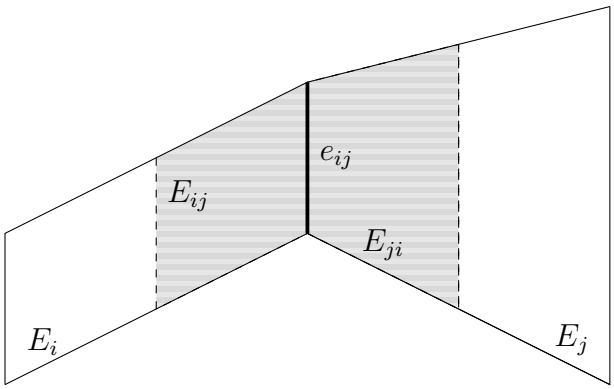

Figure 4.6: Control volume mixed finite element method: the shaded region depicts the control volume V_{ij} associated with the edge e_{ij}, composed of two sub-control volumes E_{ij} and E_{ji}.

The test function $\mathbf{v}_{e_{ij}}$ is constructed in the following way. Denote by $\mathbf{f}_{E_i} : \widehat{E} \to E_i$ the bilinear mapping from the reference element $\widehat{E} = (0,1)^2$ to the actual element E_i, and by $\mathbb{D}_i = (\mathbf{x}_i, \mathbf{y}_i)$ the Jacobian of $\mathbf{f}_{E_i}$ with columns $\mathbf{x}_i$ and $\mathbf{y}_i$. The determinant of $\mathbb{D}_i$ is indicated by J_i. The test function $\mathbf{v}_{e_{ij}}$ is chosen as

$$\mathbf{v}_{e_{ij}} = \begin{cases} \mathbf{z}_i / J_i(\hat{\mathbf{x}}_{ij}), & \text{on } E_{ij}, \\ \mathbf{z}_j / J_j(\hat{\mathbf{x}}_{ji}), & \text{on } E_{ji}, \\ 0, & \text{else.} \end{cases}$$

For a half element E_{ij}, the vector function $\mathbf{z}_i$ and the local coordinate $\hat{\mathbf{x}}_{ij}$ are chosen according to the image $\hat{e}_{ij} = \mathbf{f}_{E_i}^{-1}(e_{ij})$ on the reference element:

$$(\mathbf{z}_i, \hat{\mathbf{x}}_{ij}) = \begin{cases} (\mathbf{x}_i,\, (3/4, 1/2)), & \hat{e}_{ij} = \{1\} \times (0,1), \\ (\mathbf{x}_i,\, (1/4, 1/2)), & \hat{e}_{ij} = \{0\} \times (0,1), \\ (\mathbf{y}_i,\, (1/2, 3/4)), & \hat{e}_{ij} = (0,1) \times \{1\}, \\ (\mathbf{y}_i,\, (1/2, 1/4)), & \hat{e}_{ij} = (0,1) \times \{0\}. \end{cases}$$

Having chosen the test function $\mathbf{v}_{e_{ij}}$ as described above, the two integrals in (4.37) have to be evaluated. In this step, the finite element part comes into play. Starting with the second integral $(\mathbf{grad}\, p_h, \mathbf{v}_{e_{ij}})_{V_{ij}}$, the pressure p_h is assumed to be linear on each half element E_{ij} and E_{ji}, similar to the assumption made in the MPFA method for the interaction volumes. Being carried out in detail in [Cai 97], this assumption and the choice of $\mathbf{v}_{e_{ij}}$ results in the simple expression

$$(\mathbf{grad}\, p_h, \mathbf{v}_{e_{ij}})_{V_{ij}} = p_j - p_i.$$

It remains to evaluate the second integral $(\mathbb{K}^{-1}\mathbf{u}_h, \mathbf{v}_{e_{ij}})_{V_{ij}}$. Here, the discrete velocity function $\mathbf{u}_h$ is taken to be the Raviart–Thomas interpolant of the four edge fluxes on each half element E_{ij}. The resulting linear system is of the same structure (4.23) as the one for MFEM or MFD.

4.6 Interpretations within other Frameworks

It is often very useful to interprete one method as a specific variant of another method. We will briefly summarize the efforts in interpreting locally conservative methods within the framework of mixed finite element methods in Section 4.6.1, and as mimetic finite difference methods in Section 4.6.2.

4.6.1 Interpretations within Mixed FEM

Since mixed finite element methods can build upon an elaborated and well-understood mathematical theory, it is especially attractive to analyze other methods within this framework. We will have a brief look at how to interprete TPFA (Section 4.2.1), MPFA (Section 4.2.2), MFD (Section 4.3.1), CGFE (Section 4.4.3)), and CVMFE (Section 4.5.2 methods as mixed finite element methods. All the interpretations essentially boil down to using a specific quadrature formula or specific test functions in the general mixed finite element formulation.

TPFA is a Mixed FEM

In [Chav 91], the authors show that the control volume method using two-point flux approximation, see Section 4.2.1, can be interpreted as a lowest-order Raviart–Thomas mixed finite element method, provided that the permeability $\mathbb{K}$ is scalar and that the grid is K-orthogonal. The main step consists of approximating the bilinear forms $a(\,\cdot\,,\,\cdot\,)$ and $b_h(\,\cdot\,,\,\cdot\,)$ in the hybridized problem (4.24) by means of the element-wise quadrature formula summing up the four nodal values, i.e.,

$$\int_E g \,\mathrm{d}V \approx \mathcal{Q}_E(g) = \frac{|E|}{4} \sum_{k=1}^{4} g(\mathbf{x}_{E,k}), \tag{4.38}$$

where $\mathbf{x}_{E,k}$ is the coordinate of the vertex k of element E. This choice leads to a complete decoupling of the Raviart–Thomas edge degrees of freedom such that the matrix $\widetilde{\mathbb{A}}$ becomes diagonal. This allows to explicitly eliminate the flux as well as the edge pressure degrees of freedom, resulting in the standard two-point flux approximation (4.3) with K-orthogonal transmissibilities (4.5). A positive side-effect of the interpretation as mixed method is a more natural treatment of boundary conditions as well as an expression for the velocities inside each control volume by means of the Raviart–Thomas functions.

MPFA is a Mixed FEM

The equivalence of the MPFA-O method on quadrilaterals introduced in Section 4.2.2 with a specific mixed finite element method is shown in [Klau 04] and analyzed in [Klau 06a, Klau 06b]. We only present the two central ingredients here, namely the definition of the velocity finite element space $X_h \subset H^{\mathrm{div}}(\Omega)$ and of the numerical quadrature rule to discretize the bilinear form $a(\,\cdot\,,\,\cdot\,)$ in (4.21).

On the reference element $\widehat{E} = (0,1)^2$, a broken Raviart–Thomas space $RT^{1/2}$ is intro-

duced as the space of all vector fields of the form

$$\begin{pmatrix} a(\hat{y}) + b(\hat{y})\hat{x} \\ c(\hat{x}) + d(\hat{x})\hat{y} \end{pmatrix},$$

with piecewise constant coefficients a, b, c, d allowing a discontinuity at $1/2$. The corresponding global finite element space is defined as

$$RT_h^{1/2} = \{\mathbf{v} \in H^{\mathrm{div}}(\Omega) : \mathbf{v}|_E \in \mathcal{P}_E(RT^{1/2}),\ E \in \mathcal{T}_h\},$$

where $\mathcal{P}_E$ denotes the Piola transformation from the reference element $\widehat{E}$ to E, i.e.,

$$\mathcal{P}_E\hat{\mathbf{v}} = J_E^{-1}\mathbb{D}_E\hat{\mathbf{v}} \circ \mathbf{f}_E^{-1},$$

with the notations for the element transformation adopted from Section 4.5.2. The degrees of freedom for $RT_h^{1/2}$ can be chosen as normal velocities at the centers of the half edges of the MPFA interaction volumes.

The second ingredient is a numerical quadrature rule for approximating the bilinear form $a(\,\cdot\,,\,\cdot\,)$ in (4.21), which turns out to be again the trapezoidal rule (4.38). The element contribution of the discretized bilinear form $a_h(\,\cdot\,,\,\cdot\,) = \sum_{E\in\mathcal{T}_h} a_E(\,\cdot\,,\,\cdot\,)$ is defined as

$$a_E(\mathbf{u}, \mathbf{v}) = \mathcal{Q}_{\widehat{E}}(J_E^{-1}\mathbb{D}_{E,\mathrm{c}}^{\mathrm{T}}\mathbb{K}^{-1}\mathbb{D}_E\hat{\mathbf{u}} \cdot \hat{\mathbf{v}}),$$

where $\mathbb{D}_{E,\mathrm{c}}$ is the Jacobian of the element transformation evaluated at the center of the reference element. Setting $X_h = RT_h^{1/2}$ and replacing $a(\,\cdot\,,\,\cdot\,)$ by $a_h(\,\cdot\,,\,\cdot\,)$ in (4.21) states the discrete problem. In, for example, [Klau 04], it is shown that the resulting matrix $\mathbb{A}$ in the linear system (4.23) is block-diagonal, and, thus, the velocity degrees of freedom can be locally eliminated to yield a linear system for the element pressures, which is equivalent to the system obtained by the original MPFA-O approach.

In [Vohr 06], the author shows an equivalence between lowest order mixed finite elements and a particular MPFA method for simplicial triangulations in two and three dimensions, without the need for a numerical quadrature formula. This again admits to locally eliminate the velocity unknowns and to derive a system for the element pressures only.

MFD is a Mixed FEM

The equivalence of mimetic finite differences and mixed finite element methods has been described in, for example, [Bern 01, Bern 05, Klau 04], and mainly utilized for establishing a convergence theory. Meanwhile, a convergence theory for MFD methods has been established on its own, with far less restrictive assumptions than used in the MFE method, [Brez 05a]. We nevertheless provide a brief exposition of the equivalence.

Starting from the discrete mimetic problem formulation (4.17), we multiply the discrete Darcy law (4.17a) with a velocity test function $\mathbf{v} \in X_h^{\mathrm{MFD}}$ by means of the scalar product $(\,\cdot\,,\,\cdot\,)_{X_h^{\mathrm{MFD}}}$ and apply the fundamental identity (4.15), such that

$$(\mathbf{u}_h, \mathbf{v})_{X_h^{\mathrm{MFD}}} - (\mathrm{div}_h\,\mathbf{v}, p)_{Q_h^{\mathrm{MFD}}} = 0, \quad \mathbf{v} \in X_h^{\mathrm{MFD}}. \tag{4.39}$$

The discrete mass balance (4.17b) is multiplied by a pressure test function $w \in Q_h^{\mathrm{MFD}}$ by

means of the scalar product $(\cdot\,,\cdot\,)_{Q_h^{\mathrm{MFD}}}$, yielding

$$(\operatorname{div}_h \mathbf{u}_h, w)_{Q_h^{\mathrm{MFD}}} = (q, w)_{Q_h^{\mathrm{MFD}}}. \tag{4.40}$$

Provided that one chooses lowest order Raviart–Thomas elements for X_h^{MFE} and elementwise constants for Q_h^{MFE}, i.e., $Q_h^{\mathrm{MFE}} = Q_h^{\mathrm{MFD}}$, it is easy to observe that

$$b(\mathbf{v}, w) = (\operatorname{div}_h \mathbf{v}, w)_{Q_h^{\mathrm{MFD}}},$$

where $b(\cdot\,,\cdot\,)$ is the bilinear form from the mixed problem (4.21), and where $\mathbf{v}$ is once interpreted as mixed velocity in X_h^{MFE} and once as mimetic fluxes in X_h^{MFD}. Therefore, on admissible grids, the MFD problem (4.17) can be equivalently written as mixed problem (4.21) with $a(\cdot\,,\cdot\,)$ approximated by the scalar product $(\cdot\,,\cdot\,)_{X_h^{\mathrm{MFD}}}$. From that perspective, the MFD method can be interpreted as MFE method allowing more general grids, needing less geometrical information, and no finite element basis functions. On the other hand, the MFE method offers instant access to higher order discretizations.

CVMFEM is a Mixed FEM

The interpretation of the control-volume mixed-finite-element method as a mixed-finite-element method already becomes obvious in the presentation of the method in Section 4.5.2. We summarize it here for convenience. In analogy to the discrete mixed problem (4.21), we can formulate the CVMFE method as: Find $(\mathbf{u}_h, p_h) \in X_h^{\mathrm{MFE}} \times Q_h^{\mathrm{MFE}}$ such that

$$a_V(\mathbf{u}_h, \mathbf{v}) + b_V(\mathbf{v}, p_h) = (p_{\mathrm{D}}, \mathbf{v}\cdot\mathbf{n})_{\Gamma_{\mathrm{D}}}, \qquad \mathbf{v} \in X_h^V, \tag{4.41a}$$

$$b_E(\mathbf{u}_h, w) \qquad\qquad = -(q, w)_\Omega, \qquad w \in Q_h^{\mathrm{MFE}}. \tag{4.41b}$$

where

$$a_V(\mathbf{u}, \mathbf{v}) = \sum_{e\in\mathcal{E}_h} (\mathbb{K}^{-1}\mathbf{u}, \mathbf{v})_{V_e},$$

$$b_V(\mathbf{v}, w) = \sum_{e\in\mathcal{E}_h} (\mathbf{grad}\, w, \mathbf{v})_{V_e},$$

and $b_E(\cdot\,,\cdot\,) = b(\cdot\,,\cdot\,)$ from (4.21). The space X_h^V collects all the edge test functions $\mathbf{v}_e$ introduced in Section 4.5.2.

4.6.2 Interpretations within MFD

In [Brez 05a], a convergence theory for MFD methods has been established with far less restrictive assumptions than used in the MFE method. Therefore, interpreting a method in the framework of MFD method enables the usage of this analysis for the method in question. We present two locally conservative control volume methods interpreted as MFD method: the multi-point flux approximation method from Section 4.2.2 and the discrete-duality finite-volume method from Section 4.2.3.

MPFA is a MFD method

In [Klau 08], the MPFA O-method is interpreted as a mimetic finite difference method. The approach is similar to the interpretations of MPFA and MFD as mixed finite element methods above, casting the the MPFA method into a form similar to the weak problem formulation (4.39), (4.40) of the MFD method. The velocity space for the MPFA method is chosen as the set of degrees of freedom of the space $RT_h^{1/2}$ introduced above, i.e. the normal velocities at the centers of the half edges of the MPFA interaction volumes. It will be indicated by $X_{h/2}^{\mathrm{MFD}}$. In contrast to the interpretation as MFE method, no explicit interpolation of the values to the element interiors is required. The divergence operator $\mathrm{div}_{h/2}$ is defined element-wise, similar to the one for the original MFD method (4.16),

$$(\mathrm{div}_{h/2}\,\mathbf{u})_E = |E|^{-1} \sum_{e\in\mathcal{E}_E} \sum_{k=1,2} |e^k| u_e^k, \tag{4.42}$$

where e^k, $k = 1, 2$ indicate the two half-edges of the edge e and u_e^k the corresponding normal velocity values. In analogy to the mimetic scalar product $(\,\cdot\,,\,\cdot\,)_{X_h^{\mathrm{MFD}}}$ defined element-wise in (4.14), the discretization of $(\mathbb{K}^{-1}\mathbf{u}, \mathbf{v})_\Omega$ by means of the MPFA O-method can be written as $(\mathbf{u}, \mathbf{v})_{X_{h/2}^{\mathrm{MFD}}}$, defined element-wise as

$$(\mathbf{u}, \mathbf{v})_E = \mathbf{u}_E^{\mathrm{T}} \mathbb{\Lambda}_E \mathbf{v}_E, \tag{4.43}$$

with a block-diagonal matrix $\mathbb{\Lambda}_E$, where each 2×2-block corresponds to a vertex of the element E with its attached two half-edges. This allows for an explicit flux representation in contrast to the standard mimetic finite difference method. The values of $\mathbb{\Lambda}_E$ depend on the element geometry and on the permeability $\mathbb{K}$.

However, the matrix $\mathbb{\Lambda}_E$ is in general neither symmetric nor positive definite, unlike $\mathbb{M}_E$ in (4.14) appearing in the mimetic method. Therefore, $(\,\cdot\,,\,\cdot\,)_{X_{h/2}^{\mathrm{MFD}}}$ is not a scalar product. Under a certain coercivity assumption on the symmetric part $\mathbb{\Lambda}_{E,\mathrm{S}} = \frac{1}{2}(\mathbb{\Lambda}_E + \mathbb{\Lambda}_E^{\mathrm{T}})$, optimal order convergence can still be shown, [Klau 08]. Since $\mathbb{\Lambda}_{E,\mathrm{S}}$ incorporates both the element shape and the permeability, this assumption poses restrictions on these parameters. Although these restrictions are already violated for rather mildly distorted meshes and relatively low anisotropy ratios of the permeability, an optimal order convergence can be numerically observed on much rougher meshes and for larger anisotropies.

DDFV is a MFD method

An interpretation of the discrete duality finite volume method introduced in Section 4.2.3 as a mimetic finite difference method is carried out in [Coud 10]. The space of discrete pressures is given by the scalar values associated with the primal elements E and dual elements V, i.e.

$$Q_h^{\mathrm{DD}} = \{\{p_E, E \in \mathcal{T}_h\}, \{p_V, V \in \mathcal{V}_h\}\}\,.$$

In addition to the primal and the dual mesh, a third triangulation termed *diamond mesh* of the domain is needed to properly describe the space of velocities. It is constructed by connecting the endpoints of the pairs of crossing primal and dual edges, see Figure 4.7. Thus, each element D_e of the diamond mesh is associated with such a pair $(e^{\mathrm{p}}, e^{\mathrm{d}})$, $e \in \mathcal{E}_h$. The space of discrete velocities is given by the vector values associated with the elements

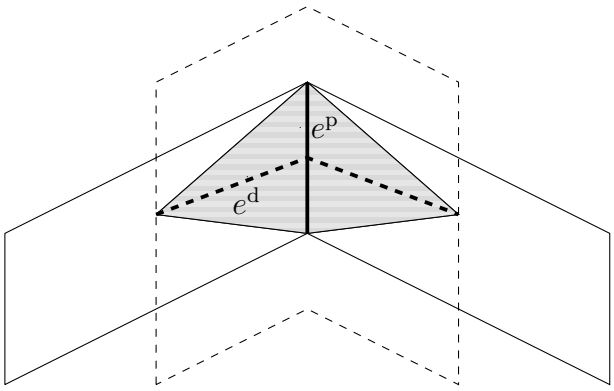

Figure 4.7: Discrete duality finite volume method: the shaded region depicts an element D_e of the diamond mesh associated with the primal edge e^{p} and its dual e^{d}.

D_e, namely

$$X_h^{\mathrm{DD}} = \{\mathbf{u}_e, e \in \mathcal{E}_h\}.$$

The spaces Q_h^{DD} and X_h^{DD} are equipped with the scalar products

$$(p,q)_{Q_h^{\mathrm{DD}}} = \frac{1}{2}\left(\sum_{E\in\mathcal{T}_h} |E| p_E q_E + \sum_{V\in\mathcal{V}_h} |V| p_V q_V\right),$$
$$(\mathbf{u},\mathbf{v})_{X_h^{\mathrm{DD}}} = \sum_{e\in\mathcal{E}_h} |D_e| \mathbf{u}_e \mathbf{v}_e.$$

The discrete gradient operator $\mathbf{grad}_h : Q_h^{\mathrm{DD}} \to X_h^{\mathrm{DD}}$ is defined on each diamond element D_e as

$$\mathbf{grad}_e\, p = \frac{1}{2|D_e|}\left((p^{\mathrm{d}}_{e,2} - p^{\mathrm{d}}_{e,1})|e^{\mathrm{d}}|\mathbf{n}^{\mathrm{d}}_e + (p^{\mathrm{p}}_{e,2} - p^{\mathrm{p}}_{e,1})|e^{\mathrm{p}}|\mathbf{n}^{\mathrm{p}}_e\right),$$

where $p^{\mathrm{d}}_{e,\ell}$ is the value associated with the vertex $\mathbf{x}^{\mathrm{d}}_{e,\ell}$ adjacent to the primal edge e^{p}, while $p^{\mathrm{p}}_{e,\ell}$ is the value associated with the element center $\mathbf{x}^{\mathrm{p}}_{e,\ell}$ adjacent to the dual edge e^{d}, see Figure 4.8. The normal vector $\mathbf{n}^{\mathrm{d}}_e$ is pointing from $\mathbf{x}^{\mathrm{d}}_{e,1}$ to $\mathbf{x}^{\mathrm{d}}_{e,2}$, while $\mathbf{n}^{\mathrm{p}}_e$ is directed from $\mathbf{x}^{\mathrm{p}}_{e,1}$ to $\mathbf{x}^{\mathrm{p}}_{e,2}$. The discrete divergence operator $\mathrm{div}_h : X_h^{\mathrm{DD}} \to Q_h^{\mathrm{DD}}$ is given on each primal element E and on each dual element V as

$$\mathrm{div}_E\, \mathbf{u} = |E|^{-1} \sum_{e^{\mathrm{p}}\subset\partial E} |e^{\mathrm{p}}| \mathbf{n}^{\mathrm{p}}_e \cdot \mathbf{u}_e,$$
$$\mathrm{div}_V\, \mathbf{u} = |V|^{-1} \sum_{e^{\mathrm{d}}\subset\partial V} |e^{\mathrm{d}}| \mathbf{n}^{\mathrm{d}}_e \cdot \mathbf{u}_e.$$

In analogy to (4.15), it can be shown that the following discrete integration-by-parts formula holds,

$$(\mathrm{div}_h\, \mathbf{u}, p)_{Q_h^{\mathrm{DD}}} + (\mathbf{u}, \mathbf{grad}_h\, p)_{X_h^{\mathrm{DD}}} = \langle \mathbf{u}, p\mathbf{n}\rangle_{h,\Gamma}, \quad \mathbf{u} \in X_h^{\mathrm{DD}},\ p \in Q_h^{\mathrm{DD}}, \tag{4.44}$$

where $\langle\,\cdot\,,\,\cdot\,\rangle_{h,\Gamma}$ is a bilinear form taking into account boundary values. The DDFV formu-

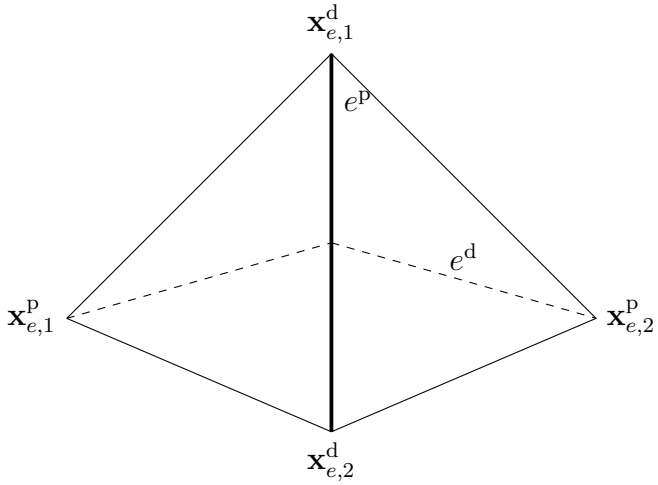

Figure 4.8: Discrete duality finite volume method: dual nodes $\mathbf{x}^{\mathrm{d}}_{e,1}$, $\mathbf{x}^{\mathrm{d}}_{e,2}$ and primal nodes $\mathbf{x}^{\mathrm{p}}_{e,1}$, $\mathbf{x}^{\mathrm{p}}_{e,2}$ associated with the primal edge e^{p} and the dual edge e^{d}, respectively.

lation can now be cast into the mimetic form (4.17), i.e.

$$\mathbf{u}_h = \mathbf{G}_h p_h, \qquad \operatorname{div}_h \mathbf{u}_h = q_h,$$

by setting $\mathbf{G}_h = -\mathbb{K}_h \, \mathbf{grad}_h$, where $\mathbb{K}_h$ is obtained by projecting the permeability $\mathbb{K}$ onto the diamond elements D_e, and where the discrete source term q_h is determined from averaging q over the primal and dual elements.

4.7 Comparison

In the following, we try to summarize the expositions above by comparing the presented locally conservative methods. We thereby foremost deal with the characteristics of the standard representatives of each method. Obviously, several variants of each method exist with possibly different features.

In Table 4.1, the discrete pressure and velocity spaces used for the different locally conservative methods are compared. The more control-volume oriented methods TPFA, MPFA, DDFV, MFD, and CVMFEM all employ spaces consisting of values associated with mesh entities like control volumes and intersections. The finite-element oriented methods MFEM, DGFEM, CGFEM, LSFEM, and Box rather use spaces of element-wise polynomial functions. In terms of geometrical data, the TPFA and MFD methods need nothing more than positions and areas of control volumes and intersections, as well as a normal vector for each intersection. The MPFA, DDFV and Box methods additionally require the construction of a dual mesh which can be quite involved for general grids. The necessary construction of the control volumes associated with the intersections in the CVMFEM method appears considerably simpler. All finite-element-type methods need a polynomial interpolation of the seeked quantities on the elements and intersections. If continuity requirements over the interfaces have to fulfilled, this can be a difficult task, like for pressure spaces $Q_h \subset \mathcal{C}^0(\Omega)$ or

LCM	$\boldsymbol{Q_h}$	$\boldsymbol{X_h}$
TPFA	$\{p_E : E \in \mathcal{T}_h\}$	$\{f_e : e \in \mathcal{E}_h\}$
MPFA	$\{p_E : E \in \mathcal{T}_h\}$	$\{f_e : e \in \mathcal{E}_h\}$
DDFV	$\{\{p_E : E \in \mathcal{T}_h\}, \{p_V : V \in \mathcal{V}_h\}\}$	$\{f_e^{\mathrm{p}}, f_e^{\mathrm{d}} : e \in \mathcal{E}_h\}$
MFD	$\{p_E : E \in \mathcal{T}_h\}$	$\{f_e : e \in \mathcal{E}_h\}$
MFEM	$Q_h = \operatorname{div} X_h$	$\{\mathbf{u} \in H^{\mathrm{div}}(\Omega) : \mathbf{u}\|_E \in P^k(E)\}$
DGFEM	$\{p \in L^2(\Omega) : p\|_E \in P^k(E)\}$	$\{\{\mathbf{n} \cdot \mathbb{K}\,\mathbf{grad}\, p\}_e : p \in Q_h, e \in \mathcal{E}_h\}$
CGFEM	$\{p \in \mathcal{C}^0(\Omega) : p\|_E \in P^k(E)\}$	(4.32), (4.33)
LSFEM	$\{p \in \mathcal{C}^0(\Omega) : p\|_E \in P^k(E)\}$	$\{\mathbf{u} \in H^{\mathrm{div}}(\Omega) : \mathbf{u}\|_E \in P^k(E)\}$
Box	$\{p \in \mathcal{C}^0(\Omega) : p\|_E \in P^k(E)\}$	$\{-\mathbb{K}\,\mathbf{grad}\, p\|_E : p \in Q_h, E \in \mathcal{T}_h\}$
CVMFEM	$\{p_E : E \in \mathcal{T}_h\}$	$\{f_e : e \in \mathcal{E}_h\}$

Table 4.1: Comparison of locally conservative methods: discrete pressure and velocity/flux spaces.

velocity spaces $X_h \subset H^{\mathrm{div}}(\Omega)$. Therefore, the application of the finite-element-type methods MFEM, CGFEM, LSFEM and Box is usually restricted to non-degenerated or even conforming meshes. Once the restrictions are met, these methods can make use of higher-order polynomials to significantly improve the approximation quality. The only method that is by default capable of handling both general meshes and higher order approximations, is the discontinuous Galerkin method. However, this usually comes at the expense of a large number of degrees of freedom.

LCM	**mesh requirements**	**higher order**	**number of dof**
TPFA	1	no	$\|\mathcal{T}_h\|$
MPFA	3	no	$\|\mathcal{T}_h\|$
DDFV	3	no	$\|\mathcal{T}_h\| + \|\mathcal{V}_h\|$
MFD	1	no	$\|\mathcal{E}_h\|$ $(+\|\mathcal{T}_h\|)$
MFEM	4	yes	$\|\mathcal{E}_h\|$ $(+\|\mathcal{T}_h\|)$
DGFEM	2	yes	$\|P^k\| \cdot \|\mathcal{T}_h\|$
CGFEM	4	yes	$\|\mathcal{V}_h\|$
LSFEM	4	yes	$\|Q_h^{\mathrm{LS}}\| + \|X_h^{\mathrm{LS}}\|$
Box	4	yes	$\|\mathcal{V}_h\|$
CVMFEM	2	no	$\|\mathcal{E}_h\|$ $(+\|\mathcal{T}_h\|)$

Table 4.2: Comparison of locally conservative methods: mesh requirements, number of degrees of freedom.

5 An MPFA Method for the Treatment of Tensorial Relative Permeabilities

Bibliographic Note: The content of this chapter is based on the following original article [Wolf 12]: M. Wolff, B. Flemisch, R. Helmig, I. Aavatsmark (2012): Treatment of tensorial relative permeabilities with multipoint flux approximation. *International Journal of Numerical Analysis & Modeling* **9**(3), pp. 725–744.

Summary Multi-phase flow in porous media is most commonly modeled by adding a saturation-dependent, scalar relative permeability into the Darcy equation. However, in the general case anisotropically structured heterogeneities result in anisotropy of upscaled parameters, which not only depends on the solid structure but also on fluid-fluid or fluid-fluid-solid interaction. We present a method for modeling of incompressible, isothermal, immiscible two-phase flow, which accounts for anisotropic absolute as well as relative permeabilities. It combines multipoint flux approximation (MPFA) with an appropriate upwinding strategy in the framework of a sequential solution algorithm. Different tests demonstrate the capabilities of the method and motivate the relevance of anisotropic relative permeabilities. Therefore, a porous medium is chosen, which is heterogeneous but isotropic on a fine scale and for which averaged homogeneous but anisotropic parameters are known. Comparison shows that the anisotropy in the large-scale parameters is well accounted for by the method and agrees with the anisotropic distribution behavior of the fine-scale solution. This is demonstrated for both the advection dominated as well as the diffusion dominated case. Further, it is shown that off-diagonal entries in the relative permeability tensor can have a significant influence on the fluid distribution.

5.1 Introduction

Multi-phase flow and transport phenomena in porous media are the governing processes in many relevant systems. An example for a natural system is the subsurface, considering for example the remediation of non-aqueous phase liquids or modeling of CO_2 storage scenarios (for example, [Clas 09]). Biological systems can for example be found in the human body, where flow through the brain or in the lung can be modeled as flow through porous media (for example, [Seri 91, Smit 07, Erbe 12]), and there also exist many technical applications in which multi-phase flow through porous media is important (for example, [Barb 05, Acos 06]).

Flow and transport processes in permeable media occur on different spatial scales and are in general highly affected by heterogeneities. Usually, averaged equations applying an REV (Representative Elementary Volume) concept are used, where the most common model is the so-called Darcy equation.This model can be used for single phase flow as well as for multi-phase flow. Parameters of averaged equations usually directly (analytical methods, averaging methods, etc.) or indirectly (for example, experiments, measurements, etc.) imply an upscaling of processes which occur on smaller scales. If upscaling methods are applied

to flow in porous media with distinctive anisotropically structured block heterogeneities, a direction dependence of the upscaled large-scale parameters results. It is fairly common to assume and determine anisotropic absolute permeabilities on various scales. Anisotropic phase-dependent behavior is often neglected in the upscaling process. However, it has been observed at different scales that upscaling can also lead to phase-dependent anisotropic full-tensor effects (for example, [Saad 95, Brau 05, Eich 05]). These can either be treated in a classical sense by deriving anisotropic phase-dependent parameters like phase and relative permeabilities respectively [Pick 96] or by upscaling strategies which are more closely linked to a certain discretization method and account for full-tensor effects by incorporating global effects into isotropic upscaled parameters (for example, [Chen 06b, Chen 09]). We will further focus on the former. If the principal directions of an upscaled total permeability coincide with the directions of a Cartesian computational grid, the extension of a basic finite volume scheme is quite obvious. In that case, it just has to be distinguished between the different grid directions. In all other cases, new numerical techniques have to be developed which are able to account for anisotropies which are represented by full tensor relative permeability functions, and which are largely independent of the choice of the grid (structured, unstructured). Moreover, upwinding strategies have to be revisited to account properly for the advection dominated behavior of multiphase flows.

In the following sections a mathematical model including the general case of anisotropic phase permeabilities is introduced and some mathematical as well as physical issues of the tensor properties of this parameters are discussed. It is important to choose a mathematical formulation which allows a numerical treatment which meets the challenges presented by the tensor properties. A numerical scheme is developed that accounts for anisotropic behavior due to tensorial parameters in both the advective or gravity driven case as well as in the capillary dominated case. The scheme is based on multipoint flux approximation (MPFA) which has been derived for second order elliptic equations like Darcy's law [Aava 96, Edwa 98, Aava 02]. There exist various types of MPFA methods where the most common one is the MPFA O-method. MPFA can be applied to unstructured grids [Aava 98] and in general shows good convergence properties for single-phase flow on quadrilateral grids [Aava 06b, Pal 06, Klau 06a, Cao 11]. However, different kinds of MPFA methods differ with regard to convergence rates and monotonicity of the solution. Monotonicity of MPFA methods has been studied for example in [Nord 05a, Nord 07, Pal 11]. The application of MPFA to multi-phase flow (extended Darcy) is straight forward as long as the relative permeabilities are described by scalar functions [Aava 96, Aava 02]. In that case, the problem of evaluating the fluxes by MPFA is the same as for single-phase flow. However, if the relative permeabilities are tensors, the MPFA has to be extended to correctly account for the properties of this specific multi-phase flow regime. This applies to the simplified case neglecting capillary pressure and gravity, and becomes even more important for situations in which capillary pressure and gravity cannot be neglected. In particular, special attention is payed to a consistent upwinding strategy. The numerical method is tested on various examples, which are physically motivated and demonstrate the effects of anisotropic phase permeabilities as well as the capability to account for this effects.

5.2 Mathematical Model for Two-Phase Flow

In the following, we describe our mathematical model for two-phase flow assuming immiscible and incompressible fluids. It is based on two conservation equations for mass, one for

each of the fluid phases:

$$\phi \frac{\partial S_{\mathrm{w}}}{\partial t} + \operatorname{div} \mathbf{v}_{\mathrm{w}} - q_{\mathrm{w}} = 0, \tag{5.1}$$

$$\phi \frac{\partial S_{\mathrm{n}}}{\partial t} + \operatorname{div} \mathbf{v}_{\mathrm{n}} - q_{\mathrm{n}} = 0. \tag{5.2}$$

The wetting phase fluid is indicated by subscript w and the non-wetting phase fluid by subscript n, S is the saturation, ϕ is the porosity of the porous medium and q a source/sink term. The momentum equations to get the phase velocities $\mathbf{v}_{\mathrm{w}}$ and $\mathbf{v}_{\mathrm{n}}$ can be simplified, applying several reasonable assumptions, to Darcy's law (for example, [Whit 98]). It was originally derived from experimental studies for one-phase flow and extended to multi-phase flow (for example, [Sche 74, Helm 97])

$$\mathbf{v}_{\mathrm{w}} = -\frac{\mathbb{K}_{\mathrm{tot,w}}}{\mu_{\mathrm{w}}} (\mathbf{grad}\, p_{\mathrm{w}} + \varrho_{\mathrm{w}} g\, \mathbf{grad}\, z), \tag{5.3}$$

$$\mathbf{v}_{\mathrm{n}} = -\frac{\mathbb{K}_{\mathrm{tot,n}}}{\mu_{\mathrm{n}}} (\mathbf{grad}\, p_{\mathrm{n}} + \varrho_{\mathrm{n}} g\, \mathbf{grad}\, z). \tag{5.4}$$

In Equations (5.3) and (5.4) $\mathbb{K}_{\mathrm{tot}}$ is the total phase permeability that is usually split up into relative permeability of a phase times absolute permeability of the porous medium, μ the dynamic fluid viscosity, p the pressure and ϱ the density of the phases, and g is the gravity constant acting in z-direction. To close the system given by Equations (5.1) to (5.4) further statements are needed: The pores are entirely filled with both phases

$$S_{\mathrm{w}} + S_{\mathrm{n}} = 1, \tag{5.5}$$

the phase pressures are not independent but related by the capillary pressure

$$p_{\mathrm{c}} = p_{\mathrm{n}} - p_{\mathrm{w}}, \tag{5.6}$$

and the capillary pressure as well as the total phase permeabilities are modeled as functions of the saturation, which are given in terms of nonlinear constitutive relations

$$p_{\mathrm{c}} := p_{\mathrm{c}}\left(S_{\mathrm{w}}\right), \tag{5.7}$$

$$\mathbb{K}_{\mathrm{tot},\alpha} := \mathbb{K}_{\mathrm{tot},\alpha}\left(S_{\mathrm{w}}\right), \quad \alpha \in \{\mathrm{w}, \mathrm{n}\}. \tag{5.8}$$

Considering Darcy's law, it is obvious that the total permeability is acting like a diffusion coefficient for pressure. Thus, in the general case, it should be a symmetric tensor (real eigenvalues which are the permeabilities acting in the direction of the associated eigenvectors) and it should be positive semi-definite (which means that the eigenvalues are non-negative so that flow always takes place in the direction of decreasing potential). Further, in the fully saturated case, the total phase permeability should be the absolute permeability

$$\mathbb{K}_{\mathrm{tot,w}}(1) = \mathbb{K}_{\mathrm{tot,n}}(1) \stackrel{!}{=} \mathbb{K}, \tag{5.9}$$

while in the unsaturated case the medium is effectively impermeable for the corresponding phase

$$\mathbb{K}_{\mathrm{tot,w}}(0) = \mathbb{K}_{\mathrm{tot,n}}(0) \stackrel{!}{=} \mathbb{O}. \tag{5.10}$$

As stated before, the total phase permeability is usually split up into relative permeability of a phase and absolute permeability of the porous medium

$$\mathbb{K}_{\mathrm{tot},\alpha} = k_{\mathrm{r}\alpha}\mathbb{K}. \tag{5.11}$$

In the general case the absolute or intrinsic permeability depends on the geometric structure of the porous medium, which means it can be different in different spatial directions, and thus has to appear as a full tensor in the Darcy equations. Usually, it is assumed that the anisotropic character of flow is independent of the actual flow process and solely controlled by the porous medium and thus by the absolute permeability. Therefore, relative permeability, which includes fluid-fluid as well as fluid-fluid-solid interactions, is a scalar coefficient. However, starting from the statements on total permeability given before, under the assumption that it consists of a relative permeability times absolute permeability, a general expression for relative permeability is given by

$$\mathbb{K}_{\mathrm{r}\alpha}\left(S_\alpha\right) = \mathbb{K}_{\mathrm{tot},\alpha}\left(S_\alpha\right)\mathbb{K}^{-1}, \tag{5.12}$$

which leads to

$$\mathbb{K}_{\mathrm{tot},\alpha} = \mathbb{K}_{\mathrm{r}\alpha}\mathbb{K}. \tag{5.13}$$

Examples and physical motivation for the need for both full tensor absolute as well as relative permeability have already been given before (Sec. 5.1) and are further extended in Section 5.4.

The tensorial coefficients, especially the tensorial relative permeabilities, lead to new challenges for the numerical method. These will be discussed in detail in the next section which deals with the discretization of the mathematical model. However, meeting these challenges also influences the choice of the mathematical formulation and thus some points are already mentioned here: If the direction of flow is saturation dependent via saturation dependent tensorial coefficients, the upwind direction cannot necessarily be estimated directly from the solution of the old time step. Thus, we reformulate Equations (5.1) to (5.4) into a system of equations which can be solved sequentially. It is a common assumption that the resulting pressure equation (Eq. (5.16)) can be treated without upwinding, because it balances total flow instead of phase flow. Further, we choose a formulation which introduces phase potentials instead of phase pressures [Hote 08]. By solving for the potentials, the gravity term is not completely moved to the right-hand side of the system of equations that has to be solved. We have observed that this can lead to a better solution behavior in the context of a sequential solution strategy where the solution for the velocity field and for the transport of the phases are decoupled. Finally, for reasons of efficiency, the formulation should ensure that the number of different transmissibilities which have to be calculated by the MPFA method is as small as possible.

With definitions of the phase mobilities $\lambda_{\mathrm{w}} = \mathbb{K}_{\mathrm{rw}}/\mu_{\mathrm{w}}$ and $\lambda_{\mathrm{n}} = \mathbb{K}_{\mathrm{rn}}/\mu_{\mathrm{n}}$, the total mobility $\lambda_{\mathrm{t}} = \lambda_{\mathrm{w}} + \lambda_{\mathrm{n}}$, and the potentials

$$\begin{aligned}
\Phi_{\mathrm{w}} &= p_{\mathrm{w}} + \varrho_{\mathrm{w}} g z \\
\Phi_{\mathrm{n}} &= p_{\mathrm{n}} + \varrho_{\mathrm{n}} g z \\
\Phi_{\mathrm{c}} &= \Phi_{\mathrm{n}} - \Phi_{\mathrm{w}} = p_{\mathrm{c}} + (\varrho_{\mathrm{n}} - \varrho_{\mathrm{w}}) g z
\end{aligned} \tag{5.14}$$

a total velocity can be formulated as sum of the phase velocities as

$$\begin{aligned}\mathbf{v}_\mathrm{t} =& \mathbf{v}_\mathrm{w} + \mathbf{v}_\mathrm{n} = -\mathbb{\lambda}_\mathrm{w}\mathbb{K}\,\mathbf{grad}\,\Phi_\mathrm{w} - \mathbb{\lambda}_\mathrm{n}\mathbb{K}\,\mathbf{grad}\,\Phi_\mathrm{n} \\ =& -\mathbb{\lambda}_\mathrm{w}\mathbb{K}\,\mathbf{grad}\,\Phi_\mathrm{w} + \mathbb{\lambda}_\mathrm{n}\mathbb{K}\,\mathbf{grad}\,\Phi_\mathrm{w} - \mathbb{\lambda}_\mathrm{n}\mathbb{K}\,\mathbf{grad}\,\Phi_\mathrm{w} - \mathbb{\lambda}_\mathrm{n}\mathbb{K}\,\mathbf{grad}\,\Phi_\mathrm{n} \\ =& -\mathbb{\lambda}_\mathrm{t}\mathbb{K}\,\mathbf{grad}\,\Phi_\mathrm{w} - \mathbb{\lambda}_\mathrm{n}\mathbb{\lambda}_\mathrm{t}^{-1}\mathbb{\lambda}_\mathrm{t}\mathbb{K}\,\mathbf{grad}(\Phi_\mathrm{n} - \Phi_\mathrm{w}) \\ =& \underbrace{-\mathbb{\lambda}_\mathrm{t}\mathbb{K}\,\mathbf{grad}\,\Phi_\mathrm{w}}_{\mathbf{v}_{\mathrm{a,w}}} \underbrace{-\mathbb{F}_\mathrm{n}\mathbb{\lambda}_\mathrm{t}\mathbb{K}\,\mathbf{grad}(\Phi_\mathrm{c})}_{\mathbf{v}_\mathrm{c}}\end{aligned} \tag{5.15}$$

where $\mathbf{v}_{\mathrm{a},\alpha}$ is called advective velocity of the phase α, $\mathbf{v}_\mathrm{c}$ can be called capillary velocity, although it also includes gravity effects, and $\mathbb{F}_\alpha = \mathbb{\lambda}_\alpha\mathbb{\lambda}_\mathrm{t}^{-1}$ is a tensorial definition of the fractional flow function of the phase α. By adding equations (5.1) and (5.2), we get a total mass balance equation. In the case of immiscible and incompressible flow this equation, which is also called pressure equation, simplifies to

$$\operatorname{div}\mathbf{v}_\mathrm{t} = \operatorname{div}(\mathbf{v}_{\mathrm{a,w}} + \mathbf{v}_\mathrm{c}) = q_\mathrm{t}. \tag{5.16}$$

One additional equation is needed for transport of the phase and the phase mass, respectively. In case of immiscible flow we simply use one of the conservation equations for mass (Eq. (5.1) and (5.2)), which is then called saturation equation and insert phase velocities which now can be expressed in terms of $\mathbf{v}_\mathrm{a}$ and $\mathbf{v}_\mathrm{c}$:

$$\phi\frac{\partial S_\mathrm{w}}{\partial t} + \operatorname{div}(\mathbb{F}_\mathrm{w}\mathbf{v}_{\mathrm{a,w}}) = q_\mathrm{w}, \tag{5.17}$$

$$\phi\frac{\partial S_\mathrm{n}}{\partial t} + \operatorname{div}(\mathbb{F}_\mathrm{n}\mathbf{v}_{\mathrm{a,w}} + \mathbf{v}_\mathrm{c}) = q_\mathrm{n}. \tag{5.18}$$

5.3 Numerical Method and Multi-Point Flux Approximations

We apply a cell-centered finite-volume method (CCFV) to Equations (5.16) and (5.17) leading to the system of equations

$$\int_{\partial V}\mathbf{v}_\mathrm{t}\cdot\mathbf{n}\,\mathrm{d}\Gamma = \int_V q_\mathrm{t}\,\mathrm{d}V, \tag{5.19}$$

$$\int_V \phi\frac{\partial S_\mathrm{w}}{\partial t}\,\mathrm{d}V + \int_{\partial V}\mathbf{v}_\mathrm{w}\cdot\mathbf{n}\,\mathrm{d}\Gamma = \int_V q_\mathrm{w}\,\mathrm{d}V, \tag{5.20}$$

where $\mathbf{n}$ is the normal vector pointing outward of volume V at the volume boundary ∂V. Equations (5.19) and (5.20) can now be written in discrete form

$$\sum_{i=1}^{n} f_{\mathrm{tot},i} = q_\mathrm{t}|V| \tag{5.21}$$

$$\phi\frac{\partial S_\mathrm{w}}{\partial t}|V| + \sum_{i=1}^{n} f_{\mathrm{w},i} = q_\mathrm{w}|V|, \tag{5.22}$$

where $f_{\mathrm{tot},i}$ is the total flux and $f_{\mathrm{w},i}$ the wetting phase flux at a cell face i. According to the mathematical formulation introduced before we further split the total flux into its two

components:

$$\sum_{i=1}^{n} f_{\mathrm{tot},i} = \sum_{i=1}^{n} \left(f_{\mathrm{a,w},i} + f_{\mathrm{c},i}\right) = q_{\mathrm{t}}|V| \tag{5.23}$$

The main challenge using the CCFV scheme now is the calculation of the numerical flux, which has to be capable of managing a tensorial relative permeability. Further, this flux should by its design be able to deal with the special challenges of advection-dominated problems. This means that the need for an upwinding concept has to be considered.

5.3.1 Existing Numerical Flux Functions

The method most commonly used in finite-volume codes for groundwater or reservoir simulation is two-point flux approximation (TPFA) and descendants as numerical flux functions. However, during the last decade, the technique of multi-point flux approximations (MPFA) has been developed, supplementing the former.

Both classes of numerical flux functions are related to each other, as MPFA can be interpreted as a conceptual upgrade of TPFA. They were originally designed for flow laws like

$$\mathbf{v} = -\mathbb{K}\,\mathbf{grad}\,p \tag{5.24}$$

which describes one-phase Darcy flow (for the sake of simplicity, gravity and viscosity are neglected here).

TPFA are motivated by classical finite-difference methods. Thus the flux at face i is approximated as

$$f_i \approx T_i(p_2 - p_1), \tag{5.25}$$

where subscript 1 and 2 denote the two finite-volume grid cells which share interface i and T_i is the transmissibility at face i. In case of one-phase flow (Eq. (5.24)) it includes the absolute permeability and some geometric information. A common approach in standard finite volume simulators is to apply a harmonic average to calculate absolute permeabilities at a face i from the cell permeabilities. Compared to a arithmetic average the harmonic average naturally accounts for impermeable layers or structures. It should be mentioned that TPFA corresponds to an one-dimensional approximation of the flux leading to an important assumption for TPFA methods which is the assumption on the grid property known as K-orthogonality (see [Aava 96, Aava 02]). If the grid is not K-orthogonal, TPFA yields an inconsistent approximation of the flux. This leads to an error in the solution which does not vanish if the grid is refined [Aava 07].

One approach to solving this problem is MPFA. There exists a variety of MPFA methods like the MPFA-O(η) method [Aava 96, Edwa 98, Pal 06], the MPFA-U method [Aava 06a], the MPFA-Z method [Nord 05b], the MPFA- L method [Aava 08, Cao 09], etc. The main aspect of MPFA methods is to increase accuracy compared to TPFA, especially in case of general non-orthogonal grids or anisotropic coefficients, by increasing the flux stencil. The various methods differ in the size of the flux stencil due to differently shaped control volumes for flux approximation. This leads to different convergence behavior and monotonicity of the methods, although it seems that there is no method, which is superior for all kinds of grids or applications. The most popular method, which is also further used in this work, is the MPFA-O method (MPFA-O(0), for example, [Aava 02]). However, the ideas that are developed later to treat phase-dependent anisotropic parameters can be transferred to any MPFA method.

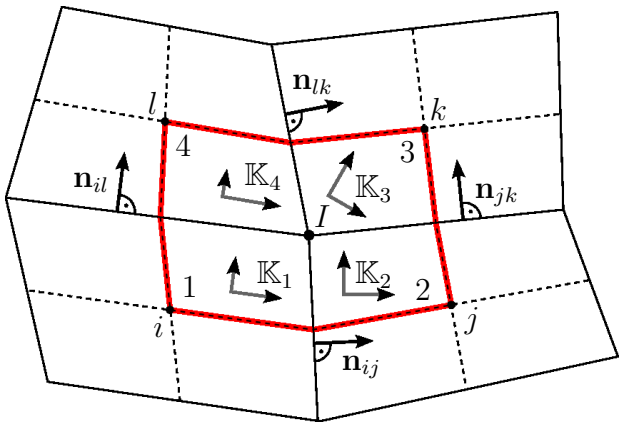

Figure 5.1: Example interaction volume for motivation of MPFA

The fundamental concept of MPFA is simple: Instead of the one-dimensional approximation used by TPFA, a multi-dimensional approximation is applied:

$$f_i \approx \sum_{j \in J} t_{ij}(p_j), \tag{5.26}$$

where the set J includes all cells j which surround face i (for example, 6 cells (2-d), or 18 cells (3-d) for a quadrilateral grid), and t_{ij} are called transmissibility coefficients.

For reasons of simplicity only the two-dimensional case will be further considered, although everything can be easily transferred to three dimensions. A finite-volume grid is sketched in Figure 5.1 (solid lines). A dual grid (dashed lines) is constructed by drawing lines from each cell center (i, j, k, l, ...) to the midpoints of the cell faces. Every grid cell of the dual mesh now includes one vertex of the finite-volume mesh and divides its cell faces in two parts. Further, the dual grid cells, called interaction volumes, can be divided into four sub-volumes, one corresponding to every cell of the finite-volume grid that is part of the interaction volume. In analogy to the TPFA procedure, the idea is to use a linear approximation for the pressure in every sub-volume of an interaction volume. Like the TPFA, these approximations have to interpolate the nodal value of pressure at the cell centers. Furthermore, the approximation of pressure at an edge midpoint has to be the same from both sides. To preserve local conservation of fluxes it is requested that the flux leaving one control volume is equal to that entering the next one (for example, $f_{ij} \stackrel{!}{=} f_{ji}$). We exemplarily write the equation describing conservation of flux along the edge from i to j

$$\begin{aligned} f_{ij} &\approx -\mathbf{n}_{ij}^{\mathrm{T}} \mathbb{K}_i \frac{\Gamma_{ij}}{2F_i} \left[(p_{ij} - p_i)\, \boldsymbol{\nu}_{ij}^{(i)} + (p_{il} - p_i)\, \boldsymbol{\nu}_{il}^{(i)} \right] \\ &= \mathbf{n}_{ij}^{\mathrm{T}} \mathbb{K}_j \frac{\Gamma_{ij}}{2F_j} \left[(p_{ij} - p_j)\, \boldsymbol{\nu}_{ij}^{(j)} - (p_{jk} - p_j)\, \boldsymbol{\nu}_{jk}^{(j)} \right]. \end{aligned} \tag{5.27}$$

The definition of the quantities F_i, p_{ij}, $\boldsymbol{\nu}_{ij}^{(i)}$, Γ_{ij} as well as the details on the approximation of the pressure gradient are not further given here, but can be found for example in [Aava 02]. Finally, using these expressions for equality of fluxes, a system of 4 equations can be formulated for every interaction volume. This can be solved for the transmissibility matrix

$\mathbb{T}$, such that

$$\mathbb{T}\mathbf{p} = \mathbf{f}, \tag{5.28}$$

where $\mathbf{p}$ is the vector of cell pressures of the four adjacent finite-volume cells sharing one interaction volume, and $\mathbf{f}$ is the vector of fluxes over the corresponding half edges. For detailed introduction and derivation of a MPFA-O method we exemplarily refer to [Aava 02, Aava 06a, Eige 05].

In case of one-phase flow, the whole procedure of calculating the global transmissibility matrix can be accomplished in a single preprocessing step as the transmissibilities do not change during the simulation. For K-orthogonal grids, the described MPFA method reduces to TPFA with harmonic averages. However, the former can also be consistently applied to any full-tensor permeability fields on arbitrary grids. In case of multi-phase flow, the approximation of the fluxes by MPFA reduces to the form described before for one-phase flow as long as the relative permeabilities are scalars and assumed to be constant along the cell faces [Aava 96, Aava 02].

5.3.2 Extension of Multi-Point Flux Approximations for Multi-Phase Flow and Tensorial Relative Permeabilities

The next step is the transfer of the concepts introduced before for one-phase flow (Eq. (5.24)) to multiphase flow (Eq. (5.3) and (5.4)) in the general case in which relative permeabilities are tensors. This means that saturation dependent quantities appear in the MPFA approximation. Thus, a fundamental difference is that the MPFA operators are saturation dependent and change with time. The transmissibilities $\mathbb{T}_\mathrm{t}$ (advective wetting phase flux $f_\mathrm{a,w}$), $\mathbb{T}_\mathrm{n}$ (capillary flux f_c) and $\mathbb{T}_\mathrm{w}$ (wetting phase flux f_w) are either related to total flow ($\mathbb{T}_\mathrm{t}$) or to phase flow ($\mathbb{T}_\mathrm{n}$, $\mathbb{T}_\mathrm{w}$). Especially the latter involves a careful treatment. One reason is the requirement that phase dependent quantities require an upwinding for advection-dominated problems. Another reason is that phase dependent properties like $\mathbb{F}_\alpha$ become zero if the phase is not present. Thus, the equations for conservation of fluxes (for example, Eq. (5.29)) can degenerate to the trivial statement $0 = 0$, and the system of equations that has to be solved for the transmissibility matrix would be under-determined. Further, MPFA by construction acts like a harmonic average, which means that a fluid α could never enter a cell if $S_\alpha = 0$ and therefore $\mathbb{F}_\alpha = 0$. This once more points out that an appropriate upwind scheme is important. In the case of scalar relative permeability functions, upwinding is straight forward because the direction of flow can be directly determined from the single phase transmissibilities. However, in the case of tensorial relative permeabilities, the determination of an upwind direction is challenging. Following, the multi-point flux approximations of the different flux terms ($f_\mathrm{a,w}$, f_c and f_w) are derived, while special emphasis is given to upwinding in case of tensorial phase-dependent coefficients.

Advective Flux

Comparing Equation (5.24)) and Equation (5.15) it is obvious that the advective flux can be approximated similar to the case of one-phase flow simply by adding the total permeability into the approximation. Again, we write the equation for conservation of flux at the half

edge from i to j:

$$\begin{aligned} f_{ij} &\approx -\mathbf{n}_{ij}^{\mathrm{T}} \mathbb{\Lambda}_{\mathrm{t},i} \mathbb{K}_i \frac{\Gamma_{ij}}{2F_i} \left[(\Phi_{ij} - \Phi_i) \boldsymbol{\nu}_{ij}^{(i)} + (\Phi_{il} - \Phi_i) \boldsymbol{\nu}_{il}^{(i)} \right] \\ &= \mathbf{n}_{ij}^{\mathrm{T}} \mathbb{\Lambda}_{\mathrm{t},j} \mathbb{K}_j \frac{\Gamma_{ij}}{2F_j} \left[(\Phi_{ij} - \Phi_j) \boldsymbol{\nu}_{ij}^{(j)} - (\Phi_{jk} - \Phi_j) \boldsymbol{\nu}_{jk}^{(j)} \right]. \end{aligned} \tag{5.29}$$

The total mobility $\mathbb{\Lambda}_{\mathrm{t}}$, which is a property of the total flux, can be easily included into the concept. It is not necessary to apply any upwinding and it can never become zero, because it is the sum of the phase mobilities. The advective flux term can thus be approximated as

$$\mathbf{f}_{\mathrm{a,w}} = \mathbb{T}_{\mathrm{t}} \boldsymbol{\Phi}_{\mathrm{w}}, \tag{5.30}$$

where $\mathbb{T}_{\mathrm{t}}$ is called total transmissibility and is an operator for the approximation of $\Gamma \mathbf{n}^{\mathrm{T}} \mathbb{\Lambda}_{\mathrm{t}} \mathbb{K} \, \mathbf{grad}$, with Γ being the area of an half cell face. The vector $\mathbf{f}_{\mathrm{a,w}}$ contains the advective fluxes of the wetting phase corresponding to the sub-faces, while $\boldsymbol{\Phi}_{\mathrm{w}}$ holds wetting-phase potentials associated with sub-volumes (Fig. 5.1).

Capillary Flux

The second flux term, which has to be approximated is the term f_{c}, which includes not only the total mobility tensor (Eq. (5.29)) but the product $\mathbb{F}_{\mathrm{n}} \mathbb{\Lambda}_{\mathrm{t}}$. Thus, instead of the total transmissibility a phase transmissibility is required giving the capillary flux at the half face between cell i and j as

$$\mathbf{f}_{\mathrm{c}} = \mathbb{T}_{\mathrm{n}} \boldsymbol{\Phi}_{\mathrm{c}}. \tag{5.31}$$

However, there exist two main problems for the calculation of the phase transmissibility $\mathbb{T}_{\mathrm{n}}$. First, the fractional flow function tensor has to be approximated at the cell face. Since the capillary flux term in this formulation includes both capillary and gravity effects, where the flux driven by gravity has advective character, an upwinding scheme is necessary ($\mathbb{F}_{\mathrm{n}} = \mathbb{F}_{\mathrm{n}}^{\mathrm{upw}}$). Second, in contrast to the total mobility, the phase mobility can become zero if the phase is at or below residual saturation. Like discussed before, this would lead to a degeneration of the system of equations which has to be solved to get the transmissibility matrix.

As mentioned upwinding can cause problems in the context of tensorial coefficients: by adding $\mathbb{F}_{\mathrm{n}}^{\mathrm{upw}}$ into Equation (5.29) we multiply $\mathbb{\Lambda}_{\mathrm{n}}$ and $\mathbb{K}$ and thus the relative permeability with the absolute permeability. So, depending on upw $= i$ or upw $= j$, one of the products of relative and absolute permeability (from cell i or j) is a product where both permeabilities come from the same cell whereas the other product is a mixed product. For the latter case it is not guaranteed that the total permeability satisfies the criteria discussed before (sec. 5.2). Even if both, the absolute permeability as well as the relative permeability are symmetric and positive definite, the total permeability resulting from the mixed product does not have to satisfy this properties, because the principal directions could be completely different. An entirely unphysical behavior could be the result, for example a flow in the direction of increasing potential. Furthermore, we multiply $\mathbb{\Lambda}_{\mathrm{t}}^{\mathrm{T}}$ and $\mathbb{\Lambda}_{\mathrm{t}}$, which could result in similar problems although the total mobility is supposed to be quite smooth and numerically easy to handle.

The solutions to these problems are quite simple. Instead of upwinding the whole mobilities only the quantity that shows hyperbolic character, namely the saturation, is used

in the upwinding procedure. Accordingly, we write

$$\mathbb{F}_{\mathrm{n},ij} = \mathbb{F}_{\mathrm{n},ij}^{\mathrm{upw}} = \mathbb{F}_{\mathrm{n},ij}\left(S^{\mathrm{upw}}\right). \tag{5.32}$$

We assumed before that we do not need to apply an upwinding scheme on the total mobility $\mathbb{\lambda}_{\mathrm{t}}$ to calculate the advective flux. To be consistent we also use this assumption for the other flux terms. For the capillary flux this means that only the fractional flow function is calculated from an upwind saturation S^{upw}. The determination of an upwind direction which is quite simple for scalar fractional flow functions however is nontrivial for tensor functions. The reason is that a tensor coefficient like $\mathbb{F}$ can lead to phase normal flux in opposite direction than the total flux as well as the phase potential difference of two neighboring cells. We therefore suggest the following procedure:

1. Calculate the phase transmissibilities without upwinding.
2. Calculate phase fluxes using the pressure field of the old time step (this is reasonable as in the sequential solution strategy the capillary flux term is also assumed to be known from the old time step and thus completely moved to the right hand side).
3. Calculate upwind fractional flow functions, where the directions of the previously calculated phase fluxes determine the upwind direction.

To address the second problem of possibly ill-posed linear systems during the calculation of the phase transmissibilities, we suggest the following: the coefficients $f_{\mathrm{c},ij}$ of the vector $\mathbf{f}_{\mathrm{c}}$ are given by

$$f_{\mathrm{c},ij} = \Gamma_{ij}\mathbf{n}_{ij}^{\mathrm{T}}\mathbb{F}_{\mathrm{n},\varepsilon,ij}\mathbf{n}_{ij}f_{\mathrm{c,mpfa},ij}, \tag{5.33}$$

where $f_{\mathrm{c,mpfa},ij}$ are the coefficients of a flux vector $\mathbf{f}_{\mathrm{c,mpfa}}$,

$$\mathbf{f}_{\mathrm{c,mpfa}} = \mathbb{T}_{\mathrm{n}}\mathbf{\Phi}_{\mathrm{c}}, \tag{5.34}$$

with the transmissibility $\mathbb{T}_{\mathrm{n}}$ calculated from flux balances like

$$\begin{aligned} f_{\mathrm{c,mpfa},ij} &\approx -\mathbf{n}_{ij}^{\mathrm{T}}\mathbb{F}_{\mathrm{n,mpfa},ij}\mathbb{\lambda}_{\mathrm{t},i}\mathbb{K}_i\frac{\Gamma_{ij}}{2F_i}\left[\left(\Phi_{ij}-\Phi_i\right)\boldsymbol{\nu}_{ij}^{(i)} + \left(\Phi_{il}-\Phi_i\right)\boldsymbol{\nu}_{il}^{(i)}\right] \\ &= \mathbf{n}_{ij}^{\mathrm{T}}\mathbb{F}_{\mathrm{n,mpfa},ij}\mathbb{\lambda}_{\mathrm{t},j}\mathbb{K}_j\frac{\Gamma_{ij}}{2F_j}\left[\left(\Phi_{ij}-\Phi_j\right)\boldsymbol{\nu}_{ij}^{(j)} - \left(\Phi_{jk}-\Phi_j\right)\boldsymbol{\nu}_{jk}^{(j)}\right]. \end{aligned} \tag{5.35}$$

To ensure that the system of flux balances can always be solved for a transmissibility matrix we now add the condition

$$\mathbb{F}_{\mathrm{n,mpfa}} = \begin{cases} \mathbb{I}, & \text{if } \lambda\left(\mathbb{F}_{\mathrm{n,mpfa}}\right) < \varepsilon \\ \mathbb{F}_{\mathrm{n}}, & \text{else} \end{cases}, \qquad \mathbb{F}_{\mathrm{n},\varepsilon} = \begin{cases} \mathbb{I}, & \text{if } \lambda\left(\mathbb{F}_{\mathrm{n},\varepsilon}\right) \geq \varepsilon \\ \mathbb{F}_{\mathrm{n}}, & \text{else} \end{cases}. \tag{5.36}$$

which ensures that the fractional flow function tensor is removed from the transmissibility calculation if one of its eigenvalues $\lambda\left(\mathbb{F}_{\mathrm{n}}\right)$ is smaller than a certain threshold ε.

Wetting-Phase Flux

From Equation (5.17) we see that the wetting phase flux has the same structure than the capillary flux. Thus, the MPFA approximation can be written by substituting the

capillary potential in Equation (5.34) by the wetting phase potential, the non-wetting phase fractional flow functions of Equations (5.33) and (5.35) by the wetting phase fractional flow function, and the capillary flux by the advective flux:

$$f_{\mathrm{w},ij} = \Gamma_{ij}\mathbf{n}_{ij}^{\mathrm{T}}\mathbb{F}_{\mathrm{w},\varepsilon,ij}\mathbf{n}_{ij}f_{\mathrm{w,mpfa},ij}, \tag{5.37}$$

$$\mathbf{f}_{\mathrm{w,mpfa}} = \mathbb{T}_{\mathrm{w}}\boldsymbol{\Phi}_{\mathrm{w}}. \tag{5.38}$$

The crucial points concerning phase quantities in the MPFA method have already been discussed for the approximation of the capillary flux. It is obvious that the same problems occur for the approximation of the phase flux. Thus, we approximate the wetting phase fractional flow function tensor at a face ij as

$$\mathbb{F}_{\mathrm{w},ij} = \mathbb{F}_{\mathrm{w},ij}^{\mathrm{upw}} = \mathbb{F}_{\mathrm{w},ij}\left(S^{\mathrm{upw}}\right). \tag{5.39}$$

Compared to the capillary flux, which has to be determined for the solution of the pressure equation, the wetting phase flux is needed to solve the saturation transport equation. This means, that in a sequential solution strategy the pressure field of the new time step is already known. Thus, the scheme to determine the upwind directions given for the capillary flux is also applied for the phase flux, but substituting the pressure of the old time step in step (2) by the pressure of the new time step.

As stated before, in the original MPFA method for single-phase flow the transmissibilities have to be calculated only once in a preprocessing step and do not change during a simulation. Of course, this is different if a saturation dependent quantity like mobility is included into the transmissibility. Additionally, different terms like advective term, gravity or capillary pressure term need different treatment leading to different MPFA operators or transmissibilities, respectively. In the proposed method we need to calculate three different transmissibilities to calculate the different fluxes (advective flux, capillary flux, wetting/non-wetting phase flux). Further, four additional transmissibilities are needed to determine the upwind directions (wetting and non-wetting phase direction for each potential and saturation transport calculation) leading to seven transmissibility calculations for each grid vertex and each time step. Depending on the flow problem, it can be reasonable to determine the upwind direction only once each time step (for both equations). This would reduce the transmissibility calculations to five, but could also reduce accuracy. To make further statements about efficiency different methods have to be investigated. One alternative can be found in [Keil 12], where the authors approximate the phase fluxes using an approximate Riemann solver.

Some Remarks on Upwinding

There exists one crucial difficulty for upwinding in presence of tensor coefficients like relative permeability, which are saturation dependent and therefore change in time. Except for the case where it can be assumed that the direction of the total permeability does not change with saturation but only the absolute values, it is not possible to base the upwinding decision on the solution of the old time step. However, in the general case the direction of tensorial total permeabilities is saturation dependent. Thus, the direction of flow can

change from one time step to another as saturation changes.

The challenge of an MPFA concept for multi-phase flow is to avoid upwinding whenever this is possible and if it can not be avoided to find a solution that is sufficiently accurate and computationally efficient. If Equations (5.1) and (5.2) are solved simultaneously applying a fully implicit scheme the only way out of the upwinding dilemma seems to be the following: First, calculate transmissibility matrices for every possible upwind combination for every interaction volume ($2e4 = 16$ combinations $= 16$ transmissibility matrices for each interaction volume (2-d)). Second, find and apply kind of heuristic criteria to decide which is the most likely combination. It is obvious, that on the one hand formulation of reasonable criteria can be difficult and on the other hand recalculation of the transmissibilities is very costly (already in 2-d). This consideration is the motivation to use a different model formulation. The reformulation into one equation for potentials and one equation for transport of saturation accompanied with a sequential solution strategy allows for decoupling of some steps. Thus, upwinding decisions described before are not based on the old solution, but always on information of the new time step that is already available. Of course, this concept also includes some necessary assumptions:

- It is common to use the total mobility without any upwinding because it is a property of the total flow which uses to behave quite smooth within the model domain. We assume that this still holds for tensorial total mobilities. This allows to calculate the advective flux (Eq. (5.29) without any upwinding.

- The capillary as well as the gravity part are assumed to be known from the old time step, and put to the right hand side of the system of equations. This is common if a pressure (or potential) equation and a transport equation (for example, for saturation) are solved sequentially. Thus, it is assumed that it is sufficient to base the upwind decision for this flux term also on the solution of the old time step.

- In the procedure to determine the upwind directions, cell values of the phase quantities are used for transmissibility calculation. Thus, it is assumed that the upwinding has no influence on the direction of flow but only on the amount of fluid that crosses a cell face.

- We apply saturation upwinding instead of direct upwinding of the relative permeability. In the homogeneous case this results in the same relative permeability than relative permeability upwinding. However, saturation upwinding also ensures that heterogeneous anisotropy is accounted for in the flux approximation and that unphysical fluxes (for example, in opposite direction to the potential gradient) are avoided.

5.4 Numerical Examples

In this section different numerical experiments are performed and the results are shown to demonstrate and test the capabilities of the proposed numerical method. In a first part, we use a diagonal relative permeability tensor derived for a horizontally layered system. It has been shown for example in [Brau 05, Eich 05] that in such systems layers of different entry pressures can lead to anisotropic relative permeabilities at a larger scale. In the second part, we consider full tensor relative permeabilities. If we still think of a layered system a full tensor could result from an upscaling if the layers are not horizontal but rotated.

Of course there are also other effects that might cause anisotropy of large scale relative permeability functions. Although the example we present is not the result of an upscaling, but artificially generated, it demonstrates the effects of a full relative permeability tensor as well as it provides a meaningful test for our numerical method. We do not compare MPFA and TPFA as it has already been shown for simpler cases that TPFA leads to inaccuracy if it is used on unstructured grids or with anisotropic parameters (for example, [Cao 09]). We further remark that all numerical test examples discussed in the following use symmetric tensors for the total phase permeability. However, the presented algorithm does not require this symmetry.

5.4.1 Diagonal Relative Permeability Tensor from Upscaling

The first test example is taken from [Eich 05], where flow experiments and numerical simulations of a horizontally layered system are compared. The layers consist of three different soil types (permeability $\mathbb{K}_{\text{fine}} = 6.38 \times 10^{-11}$, $\mathbb{K}_{\text{medium}} = 1.22 \times 10^{-10}$, $\mathbb{K}_{\text{coarse}} = 2.55 \times 10^{-10}$, porosity $\Phi = 0.38$). The setup is shown in Figure 5.2. A DNAPL (Denser Non-Aqueous-

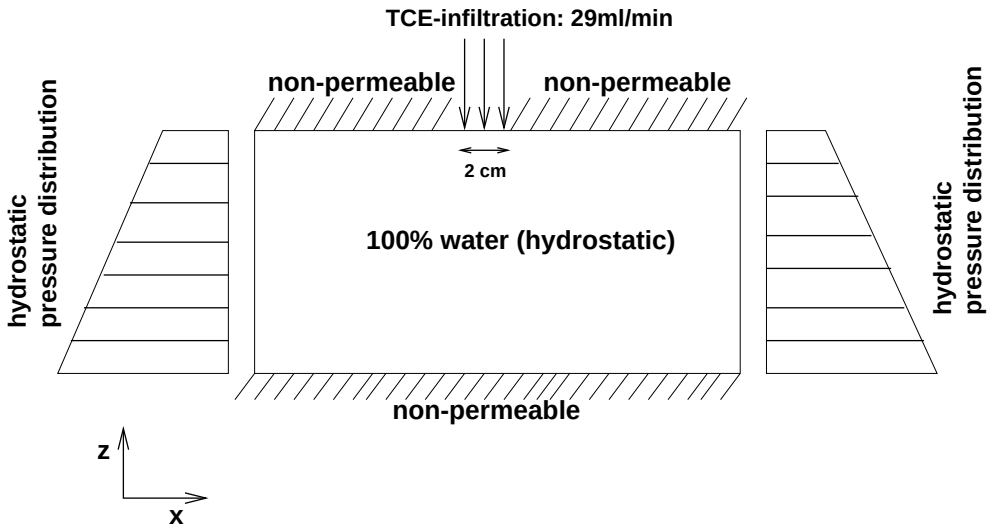

Figure 5.2: Setup of the infiltration experiment.

Phase Liquid, here TCE) is injected from the top into a domain of 1.2 m length and 0.5 m height. The upper and lower boundaries are closed for flow, except for the injection area. On the right as well as on the left boundary a hydrostatic pressure profile is assumed. The domain is initially fully water saturated. The location of the layers as well as the entry pressures of the differently permeable layers (entry pressure $p_{\text{d}_{\text{fine}}} = 882.9$, $p_{\text{d}_{\text{medium}}} = 539.55$, $p_{\text{d}_{\text{coarse}}} = 353.16$) are shown in Figure 5.3. On this scale (fine scale) Brooks-Corey type functions are used for capillary pressure-saturation and relative-permeability-saturation relations [Broo 64]. The capillary pressure-saturation curves of the different layers are correlated to the permeabilities according to a Leverett J-function [Leve 41]. The upscaled capillary pressure function for this system is plotted in Figure 5.4a, the effective relative permeability functions for the two fluids in different coordinate directions are shown in Figure 5.4b. Both kinds of effective coarse scale functions are derived from capillary equilibrium conditions. The steady state fluid distributions (each representing one point on each graph shown in Figure 5.4) are obtained from a static site-percolation model (see, for example, [Stau 85]) and used to calculate a coarse scale saturation for a given equilibrium

capillary pressure. The relative permeability functions are calculated from the steady state saturation distributions applying an upscaling concept for single-phase flow [Durl 91]. The simulated time is 1 hour while the injection is stopped after $\sim$ 50 minutes. For a more detailed description of the problem setting and the upscaling method we refer to [Eich 05].

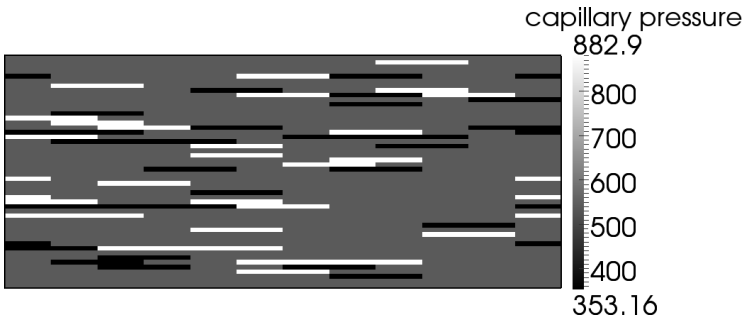

Figure 5.3: Model domain with the discrete lenses showing the different entry pressures.

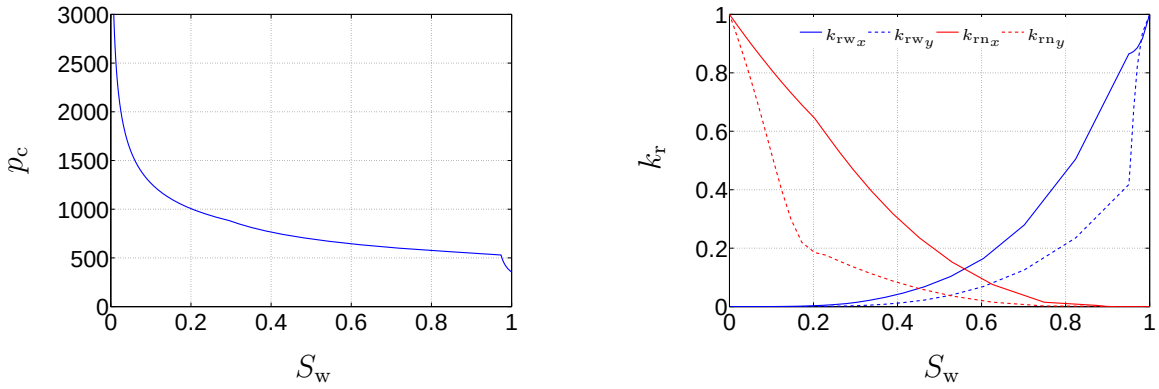

(a) capillary pressure

(b) relative permeability

Figure 5.4: Coarse scale constitutive relations from upscaling (see [Eich 05]).

First, we compare the results using the upscaled, diagonal relative permeability tensor function with the results modeling the discrete lenses (no anisotropy on the scale of the single layers). For better comparability we use the same numerical methods (Cell Centered Finite Volumes with MPFA), but for scalar relative permeability functions in the discrete case. The grid consists of 60×50 elements which allows the resolution of the lenses. The saturation distribution resulting from the simulation of the discrete system shown in Figure 5.5 is in good agreement with the results presented in [Eich 05] for the real experiment as well as for the numerical simulation. The simulations using the upscaled tensor functions are carried out on different grid types which are shown in Figures 5.6a to 5.6d. The unstructured grids (B-D) are chosen to be no longer K-orthogonal, which means that the normal vectors of the cell faces do not have to be in alignment with the directions of the anisotropy. Like for the discrete calculations grids consisting of 60×50 elements (grids A-C) and approximately 60×50 elements (grid D, 3082 elements) respectively are used. In particular, the same amount of TCE is injected. The results are shown in Figure 5.7a (structured), and Figures 5.7b to 5.7d (unstructured). For better comparison, the following

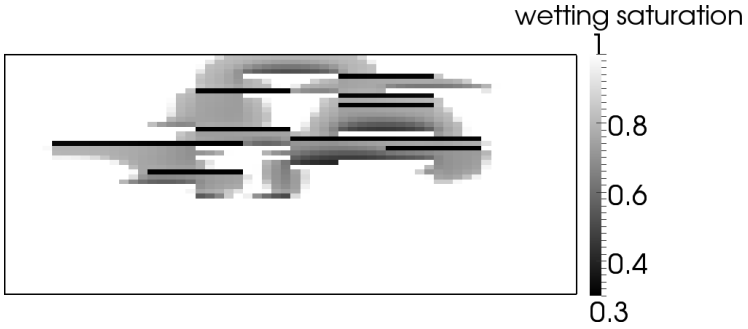

Figure 5.5: Saturation distributions of example 1 calculated with resolved lenses.

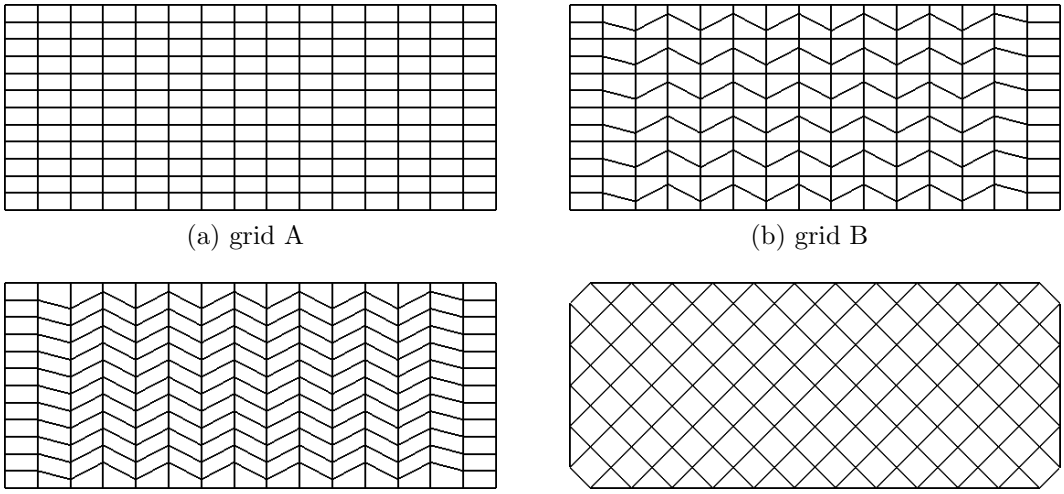

(a) grid A (b) grid B

(c) grid C (d) grid D

Figure 5.6: Different structured and unstructured grids used to test the MPFA method.

spatial moments are calculated:

$$m_0 = \int_V \phi S_\mathrm{n} \,\mathrm{d}V, \tag{5.40}$$

$$\mathbf{m}_1 = \frac{1}{m_0} \int_V \phi S_\mathrm{n} \mathbf{x} \,\mathrm{d}V, \tag{5.41}$$

$$\mathbb{M}_2 = \frac{1}{m_0} \int_V \phi S_\mathrm{n} (\mathbf{x} - \mathbf{m}_1)(\mathbf{x} - \mathbf{m}_1)^\mathrm{T} \,\mathrm{d}V, \tag{5.42}$$

where m_0 is the non-wetting phase volume in the system, $\mathbf{m}_1$ is the center of gravity of the non-wetting phase plume, and $\mathbb{M}_2$ is the matrix of variances and covariances of the plume related to its center of gravity. The transformation of $\mathbb{M}_2$ into a diagonal matrix gives the variances along the main axis of the plume (assuming an elliptical approximation). Accordingly, the spatial extent of the plume can in average be approximated by the square root of the diagonalized variance matrix. For the horizontally layered system, the main axis are in horizontal and vertical direction. The results of the spatial moments analysis are plotted in Figure 5.8. Qualitatively, the main features of the discrete model are captured well. This demonstrates that the proposed numerical model accounts for the anisotropic parameters. However, quantitatively the horizontal spreading of the infiltrating non-wetting phase is underestimated (Fig. 5.8a), whereas the vertical spreading is overestimated (Fig. 5.8b). This might be due to gravity effects, but is not further investigated

here as the upscaling itself is not part of this work. Further, only negligible differences can be observed in the moment analysis using the different grids. The total mass which is injected is not plotted in Figure 5.8 but is equal for the compared simulations. Differences between Figure 5.7a to 5.7c and Figure 5.7d are mainly caused by a different propagation along the upper boundary, where triangles instead of quadrilaterals are used for grid D. The use of isotropic effective relative permeability functions has been tested, but the results are not shown here. It can be observed that the anisotropic distribution behavior of the discrete system is mainly caused by the different entry pressures of the lenses and can not be covered just by a tensorial absolute permeability. This is in accordance with the results of [Eich 05].

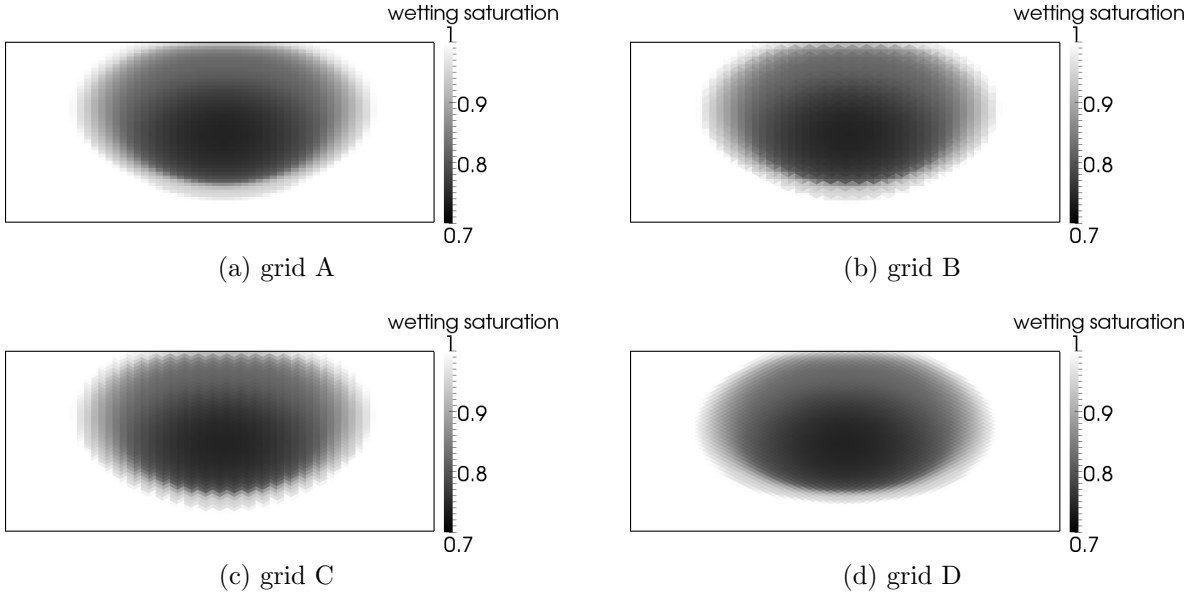

(a) grid A (b) grid B

(c) grid C (d) grid D

Figure 5.7: Saturation distributions of example 1 using the upscaled coarse scale functions on the different grids shown in Figures 5.6a-5.6d.

In a next test, we keep the domain of the previous example, but neglect gravity ($g = 0$) and apply a diagonal pressure gradient comparable to a classical five-spot problem. The grid is a Cartesian grid consisting of 120×50 elements. We place an injection well at the lower left corner and a production well at the upper right corner and close all boundaries for flow. The shape of the domain has to remain rectangular instead of quadratical, what is usually the case for a five-spot problem, because the upscaled functions are derived for the whole rectangular domain. Still the effect is a diagonal gradient which is not aligned with the grid axis. In a second test we again close all boundaries and place injection wells at the lower left as well as at the upper right corner and production wells at the lower right and upper left corner. The sources are chosen in such a way that the pressure gradient is small and capillary forces are not negligible. This should eliminate effects which may not be captured by the upscaling method used in [Eich 05]. The results are shown in Figures 5.9a and 5.9b. In both cases the results using the upscaled relative permeability tensor functions are in good agreement with the fine scale simulations. Further, there is no difference between the non-wetting phase distributions of the two cases on the lower left part of the domain. This shows that the gradient is approximated well independent of the direction of the gradient in relation to the orientation of the grid axis (structured grid).

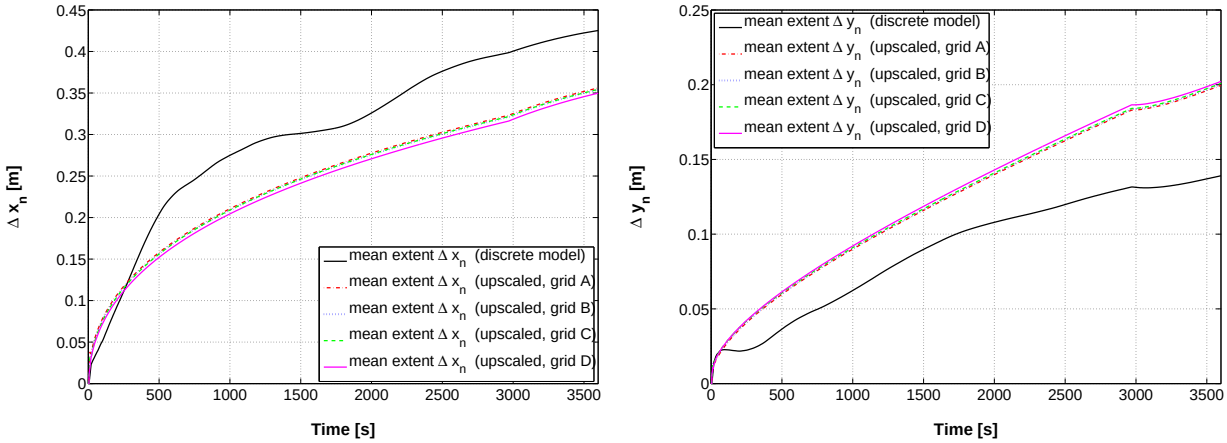

(a) averaged extent of the non-wetting fluid distribution in horizontal direction (standard deviation × 2 - from 2nd spatial moment)

(b) averaged extent of the non-wetting fluid distribution in vertical direction (standard deviation × 2 - from 2nd spatial moment)

Figure 5.8: Comparison of the results shown in Figures 5.5, 5.7a-5.7d using spatial moment analysis.

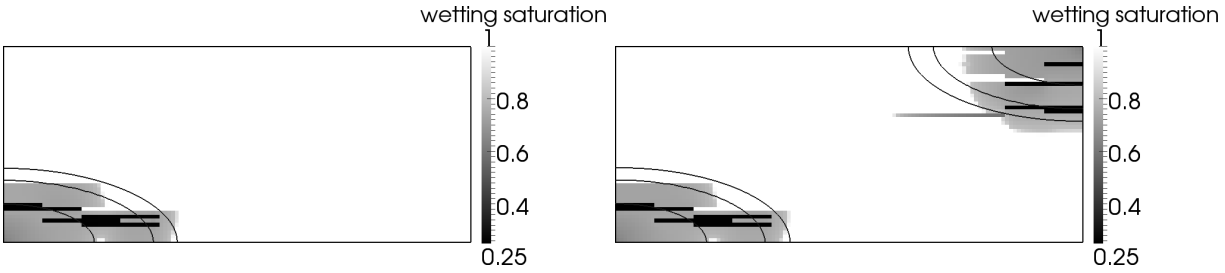

(a) Source in the lower left corner

(b) Sources in the lower left and upper right corner

Figure 5.9: Saturation distributions of the discrete lens model applying a diagonal pressure gradient. The solid lines are the contours of the saturation distributions resulting from the upscaled tensor functions.

5.4.2 Full Relative Permeability Tensor

So far, all numerical test examples use a diagonal tensor relative permeability derived from upscaling. Rotation of the orientation of the lenses (Fig. 5.3) would result in non-diagonal, full tensor relative permeability functions. However, upscaling of two-phase flow parameters is not part of this work. Thus, we use the same experimental setup than for the diagonal tensor relative permeability functions (Fig. 5.2) but replace the relative permeability function by the function derived in [Keil 12] which results from the consideration of vertically segregated upscaling:

$$\mathbb{K}_{r\alpha}(S_\alpha) = S_\alpha \begin{pmatrix} 1 & \frac{0.9}{2\pi S_\alpha}(1-\cos(2\pi S_\alpha)) \\ \frac{0.9}{2\pi S_\alpha}(1-\cos(2\pi S_\alpha)) & S_\alpha^{\frac{1}{2}} \end{pmatrix}, \qquad \alpha \in \{\mathrm{w},\mathrm{n}\}\,. \tag{5.43}$$

Although this function is physically motivated, it has no physical meaning in the sense it is used here. It can be seen as any artificially generated full tensor relative permeability function to test the capabilities of the numerical model as well as to show that there can be

a notable influence of off-diagonal effects. Additionally, compared to the previous examples where only the anisotropy ratio is saturation dependent, the direction of the eigenvectors of the matrices resulting from Equation (5.43) is saturation dependent. The simulations are carried out on two different grids, grid A (Fig. 5.6a, structured) and grid B (5.6b, unstructured) which again consist of 60×50 elements. The results are plotted in Figures 5.10a and 5.10b. Comparing these results with the results of the diagonal tensor case (Fig. 5.7a-5.7d) it is obvious that there can be a huge influence of the off-diagonal effects. The infiltrating non-wetting phase only spreads into the left side of the domain, whereas the spreading in the diagonal case is symmetric. The results are further independent of the two different kinds of grids chosen for these calculations.

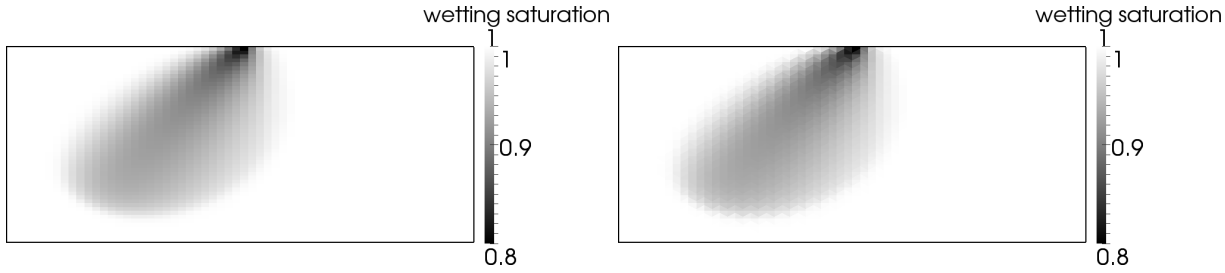

(a) grid A (b) grid B

Figure 5.10: Saturation distributions of example 3 on grid A (Fig. 5.6a) and B (Fig. 5.6b).

5.5 Summary/Conclusions

Upscaling of two-phase flow in anisotropically structured porous media can result in anisotropic large scale properties. It is common to use absolute permeability tensors, but it has been shown that there exists also an anisotropy in the multi-phase flow behavior. Thus, it is obvious that upscaling should also result in anisotropic multi-phase properties, namely anisotropic relative permeabilities.

In this work we have considered the general case of an anisotropic, full tensor phase permeability and have discussed the consequences for a splitting into the product of absolute and relative phase permeability. The case of the product of two full tensors (instead of a scalar and a tensor, what is usually assumed) requires new concepts to solve the model equations numerically. We have introduced a new numerical method using a cell centered finite volume technique with multipoint flux approximation, which includes a special upwinding strategy to properly account for the effects of the full tensor relative permeability functions.

For validation, different numerical experiments have been carried out and it has been shown that the proposed method properly accounts for the anisotropy, also in the case of a full (rotated) tensor. Further, the examples show that different physical effects of two-phase flow, which means also capillary pressure and gravity effects, are accounted for in a meaningful way and independent of the choice of the (quadrilateral) numerical grid. The performance of the method is still sufficient, although not as good as in the case of scalar relative permeabilities. The reason is the more expensive upwinding procedure. However, the costs to determine the upwind direction do not increase if the dimension

is increased, which means the costs of the upwinding become less important for three-dimensional problem settings.

If we think about a coarse scale model as a combination of an upscaling method and a suitable numerical scheme, it is obvious that a wrong coarse-scale solution compared to a given (averaged) fine-scale solution can either be introduced by the upscaling or by the numerical scheme or by both of them. So far, upscaling methods resulting in tensorial phase-dependent parameters could not be treated numerically in a proper way. This makes it difficult to validate the quality of the upscaling part alone because comparable results are those of the combined coarse scale model. However, the development of a suitable numerical method can only be the first step. The next step must be to use the method for a closer investigation of different upscaling concepts, in order to obtain a better understanding of the effects of anisotropic structures on different scales.

6 Numerical Investigation of a Mimetic Finite Difference Method

Bibliographic Note: The content of this chapter is based on the following original article [Flem 08]: B. Flemisch, R. Helmig (2008): Numerical investigation of a mimetic finite difference method. *Finite volumes for complex applications V*, ISTE, London, pp. 815–824.

Summary This benchmark study investigates the behavior of a mimetic finite difference method. It solves the majority of the proposed problems with convincing accuracy and robustness. It appears to be most promising for tackling real applications, which is also due to the ease of implementation.

6.1 Presentation of the Scheme

Mimetic finite difference methods are discretization methods for partial differential equations which promise to be robust for general unstructured polygonal and polyhedral meshes, including adaptive local refinement, non-matching interfaces, and degenerate or non-convex elements. Moreover, in view of the considered diffusion problem, they qualify for dealing with strongly heterogeneous full tensorial permeabilities. Evolving from standard finite differences, the development of the methodology started originally in [Favo 81], where the name "support operator method" has been used. A good introduction is provided by [Shas 96], a framework for the mathematical analysis in terms of mixed formulations is developed in [Brez 05a], and a quite rich annotated bibliography can be found at [Robi 03]. For this benchmark study, we aim to investigate the behavior of the mimetic finite difference method developed and presented in [Brez 05b]. Since we did not develop the method ourselves, we only provide a brief and rough overview in the following. For more details, we would like to refer to the original work [Brez 05b] and the references therein.

The starting point is the continuous problem formulation of seeking a scalar pressure function p and a velocity vector field $\mathbf{u}$ such that

$$\operatorname{div} \mathbf{u} = f, \quad \mathbf{u} = -\mathbb{K} \operatorname{grad} p$$

inside a domain Ω, completed by appropriate boundary conditions. After obtaining a triangulation of Ω, the space Q_h of element-wise constants is selected for the discretization of the pressures. The velocities are approximated in a space X_h by associating for every element E a normal velocity u_E^f with each face f of E, subject to the continuity condition $u_{E_1}^f = -u_{E_2}^f$ for two neighboring elements E_1 and E_2. On Q_h, the usual L^2 scalar product is given and denoted by $(\,\cdot\,,\,\cdot\,)_{Q_h}$. The velocity space X_h is also assumed to be equipped with a scalar product $(\,\cdot\,,\,\cdot\,)_{X_h}$, defined element-wise by $(\mathbf{u}, \mathbf{v})_E = \mathbf{u}_E^{\mathrm{T}} \mathbb{M}_E \mathbf{v}_E$, where $\mathbf{u}_E$ denotes the vector with entries $u_E^{f_1}, \ldots, u_E^{f_{k_E}}$, and $\mathbb{M}_E$ is a symmetric positive definite $k_E \times k_E$ matrix. The fundamental idea is now to discretize the first order differential operators div and

$-\mathbb{K}\,\mathrm{grad}$ to $\mathrm{div}_h : X_h \to Q_h$ and $\mathbf{G}_h : Q_h \to X_h$, respectively, in such a way that the discrete operators are adjoint to each other, i.e.,

$$(\mathbf{u}, \mathbf{G}_h p)_{X_h} = (\mathrm{div}_h \mathbf{u}, p)_{Q_h}, \quad \mathbf{u} \in X_h,\ p \in Q_h. \tag{6.1}$$

Choosing div_h in the canonical way, i.e., $(\mathrm{div}_h \mathbf{u})_E = |E|^{-1} \sum u_E^f |f|$, the crucial step is to select a suitable scalar product $(\,\cdot\,,\,\cdot\,)_{X_h}$. The missing operator $\mathbf{G}_h$ is then uniquely determined by (6.1). Finally, the discrete problem is to find $(p_h, \mathbf{u}_h) \in Q_h \times X_h$ such that

$$\mathrm{div}_h \mathbf{u}_h = f_h, \quad \mathbf{u}_h = \mathbf{G}_h p_h. \tag{6.2}$$

6.2 Numerical Results

In order to keep the exposition as part of this thesis more self-contained, we first repeat here the description that originally appeared in [Herb 08]. In particular, as test results, the following numbers had to be computed, if applicable for the corresponding test. More detailed explanations on the computation of these numbers in the context of the investigated mimetic finite difference method are provided after the list.

- `nunkw`: the number of unknowns in the linear system to be solved.
- `nnmat`: the number of nonzero terms in the matrix of the linear system.
- `sumflux`: the discrete flux balance, namely

  $$\texttt{sumflux} = \texttt{flux0} + \texttt{flux1} + \texttt{fluy0} + \texttt{fluy1} - \texttt{sumf},$$

  where `flux0`, `flux1`, `fluy0` and `fluy1` are the outward fluxes at the domain boundaries $x = 0$, $x = 1$, $y = 0$ and $y = 1$, respectively, and $\texttt{sumf} = \sum_{E \in \mathcal{T}_h} |E| f(\mathbf{x}_E)$.
- `pmin`, `pmax`: minimum and maximum value of the numerical solution.
- `erl2`: relative discrete L^2 norm of the error, namely,

  $$\texttt{erl2} = \left(\frac{\sum_{E \in \mathcal{T}_h} |E| (p(\mathbf{x}_E) - p_E)^2}{\sum_{E \in \mathcal{T}_h} |E| p(\mathbf{x}_E)^2} \right)^{\frac{1}{2}}.$$

- `ergrad`: relative L^2 norm of the error in the gradient.
- `ratiol2`, `ratiograd`: if a test is performed on a series of meshes indexed by $i \in \{1, \ldots, i_{\max}\}$, these numbers indicate the numerical order of convergence with respect to the number of unknowns, for example

  $$\texttt{ratiol2}(i) = -2 \frac{\log(\texttt{erl2}(i)) - \log(\texttt{erl2}(i-1))}{\log(\texttt{nunkw}(i)) - \log(\texttt{nunkw}(i-1))}.$$

- `erflx0`, `erflx1`, `erfly0`, `erfly1`: relative error between, for example, `flux0` and the

corresponding flux of the exact solution:

$$\texttt{erflx0} = \left| \frac{\texttt{flux0} + \int_{x=0} \mathbb{K}\,\mathbf{grad}\,\mathbf{u}\cdot\mathbf{n}}{\int_{x=0} \mathbb{K}\,\mathbf{grad}\,\mathbf{u}\cdot\mathbf{n}} \right|$$

- `erflm`: L^∞ norm of the error in the fluxes through the mesh edges, namely,

$$\texttt{erflm} = \max\left\{ \left| \frac{1}{|e|} \int_e (\mathbb{K}\,\mathbf{grad}\,p\cdot\mathbf{n} - f_E) \right|,\ e \in \mathcal{E}_h \right\}.$$

- `ocvl2`, `ocvgradl2`: order of convergence of the method in the L^2 norm with respect to the mesh size h, for example,

$$\texttt{ocvl2} = \frac{\log(\texttt{erl2}(i_{\max})) - \log(\texttt{erl2}(i_{\max}-1))}{\log(h(i_{\max})) - \log(h(i_{\max}-1))}.$$

- `ener1`, `ener2`: For tests with $f = 0$, `ener1` and `ener2` should be the diiscrete approximations of the energies $\int_\Omega \mathbb{K}\,\mathbf{grad}\,p\cdot\,\mathbf{grad}\,p\,\mathrm{d}V$ and $\int_{\partial\Omega} p\mathbb{K}\,\mathbf{grad}\,p\cdot\mathbf{n}\,\mathrm{d}\Gamma$, respectively.

- `eren`: relative error between `ener1` and `ener2`,

$$\texttt{eren} = \frac{|\texttt{ener1} - \texttt{ener2}|}{\max(\texttt{ener1}, \texttt{ener2})}.$$

The main contribution of [Brez 05b] is to present a whole family of suitable scalar products guaranteeing the stability and convergence of the mimetic discretization scheme. Further narrowing down this choice by considering computational efficiency, we are still able and responsible to choose an element-wise constant $\tilde{u}_E$. A very robust choice turned out to be $\tilde{u}_E = c|E|^{-1}\mathrm{trace}\,\mathbb{K}_E$ with $c \in [2, 80]$, see page 1547 in [Brez 05b]. For all tests except test 8, we simply chose $c = 2$. The exact algorithm for calculating the inverse $\mathbb{W}_E = \mathbb{M}_E^{-1}$ is given by Algorithm 1 in [Brez 05b].

By usual hybridization known from mixed finite elements, system (6.2) can be transformed to a sparse system for unknown pressure traces at the element faces with a symmetric positive definite system matrix. After solving this system, the original variables p_h and $\mathbf{u}_h$ can be efficiently calculated by a local postprocess. Thus, the number of degrees of freedom `nunkw` is given by the total number of element faces. For the evaluation points $\mathbf{x}_E$ in the formulas for `sumf` and `erl2`, the barycenter of E is selected. Moreover, the discrete numerical flux needed for `flux0`, ..., `erflm`, is simply given by $u_E^f|f|$ on the face f. The integrals involving the exact solution appearing in `erflx0`, ..., `erflm`, have been computed by using lowest order Gauß quadrature.

Although originally not available, discrete element-wise gradients can be obtained by a postprocess from the fluxes $u_E^f|f|$. For quadrilaterals, we first define a reference velocity $\widehat{\boldsymbol{v}}$ on the unit square $\widehat{E}$ by setting

$$\widehat{u}_x = 0.5(u_E^{f_\mathrm{r}}|f_\mathrm{r}| - u_E^{f_\mathrm{l}}|f_\mathrm{l}|), \quad \widehat{u}_y = 0.5(u_E^{f_\mathrm{t}}|f_\mathrm{t}| - u_E^{f_\mathrm{b}}|f_\mathrm{b}|),$$

where f_r, f_l, f_t, and f_b indicate the right, left, top, and bottom face of $\widehat{E}$. Using the Piola transformation yields an element velocity $\mathbf{u}_E = (\det\mathbb{D})^{-1}\mathbb{D}\widehat{\boldsymbol{v}}$, with the Jacobian $\mathbb{D}$ of the

usual element mapping $\widehat{E} \to E$, [Haeg 07]. For triangles, the element velocity $\mathbf{u}_E$ is defined as being the interpolant in terms of Raviart–Thomas finite elements. Having calculated $\mathbf{u}_E$, the discrete gradient $\mathrm{grad}_h p_h$ is given by $(\mathrm{grad}_h p_h)_E = -\mathbb{K}_E^{-1}\mathbf{u}_E$. The relative L^2 norm of the error in the gradient `ergrad` is chosen analogously to `erl2`.

The implementation has been performed within the multi-scale multi-physics toolbox DuMu^x, [Flem 07], which is based on the recently released DUNE framework, [Bast 08b]. The arising systems of linear equations have been solved by employing the sparse direct solver PARDISO, [Sche 04]. We note that mimetic finite difference methods are very well suited for non-conforming grids. We can simply consider each hanging node of an element as being a vertex of this element, admitting an angle of 180 which does not pose any theoretical or numerical difficulties for the approach. Before listing the actual results for each test, we provide a summary of its description that was originally given in [Herb 08]. The results for each test are merely listed, clustered comments on the results are provided in Section 6.3. For all tests except Test 8, the computational domain is the unit square $\Omega = (0,1)^2$.

Test 1: Mild anisotropy

This test considers the homogeneous anisotropic tensor

$$\mathbb{K} = \begin{pmatrix} 1.5 & 0.5 \\ 0.5 & 1.5 \end{pmatrix}.$$

Test 1.1 The exact solution is given by $p(x,y) = 16x(1-x)y(1-y)$ with extreme values $p_{\min} = 0$ and $p_{\max} = 1$. As boundary condition, the Dirichlet values are prescribed on the whole domain boundary. First this is tested on a series of regular triangular meshes indicated by `mesh1`. The corresponding mesh for $i = 1$ is illustrated in the left picture of Figure 6.1.

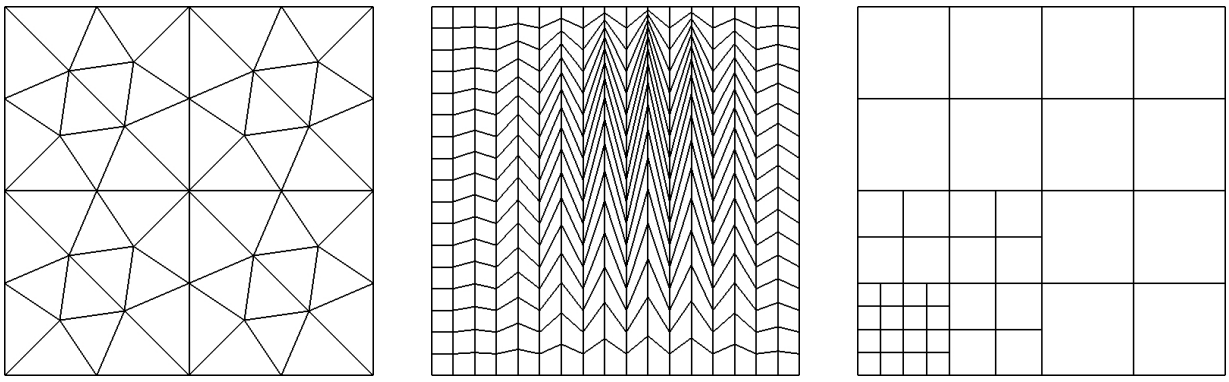

Figure 6.1: Test meshes `mesh1_1` (left), `mesh4_1` (middle), `mesh3_1` (right).

i	nunkw	nnmat	sumflux	erl2	ergrad	ratiol2	ratiograd
1	9.20E+01	4.28E+02	1.78E-14	2.03E-02	1.72E-01	–	–
2	3.52E+02	1.70E+03	-3.91E-14	4.61E-03	8.55E-02	2.21E+00	1.04E+00
3	1.38E+03	6.75E+03	3.91E-14	1.11E-03	4.26E-02	2.08E+00	1.02E+00
4	5.44E+03	2.69E+04	3.84E-13	2.75E-04	2.13E-02	2.03E+00	1.01E+00
5	2.16E+04	1.08E+05	2.31E-12	6.85E-05	1.06E-02	2.01E+00	1.01E+00
6	8.63E+04	4.30E+05	-9.96E-12	1.71E-05	5.32E-03	2.00E+00	1.00E+00
7	3.45E+05	1.72E+06	-3.18E-11	4.28E-06	2.66E-03	2.00E+00	1.00E+00

ocvl2 = 2.01E+00, **ocvgradl2** = 1.00E+00.

i	erflx0	erflx1	erfly0	erfly1	erflm	pmin	pmax
1	2.00E-02	2.00E-02	2.00E-02	2.00E-02	2.87E-01	7.33E-02	9.21E-01
2	5.12E-03	5.12E-03	5.12E-03	5.12E-03	1.69E-01	1.92E-02	9.81E-01
3	1.29E-03	1.29E-03	1.29E-03	1.29E-03	9.17E-02	4.90E-03	9.95E-01
4	3.22E-04	3.22E-04	3.22E-04	3.22E-04	4.77E-02	1.23E-03	9.99E-01
5	8.06E-05	8.06E-05	8.06E-05	8.06E-05	2.43E-02	3.10E-04	1.00E-00
6	2.02E-05	2.02E-05	2.02E-05	2.02E-05	1.23E-02	7.75E-05	1.00E-00
7	1.03E-05	1.03E-05	1.03E-05	1.03E-05	6.17E-03	1.94E-05	1.00E-00

A second test is carried out on a coarse (C) and a fine (F) distorted quadrangular mesh, `mesh4_1` and `mesh4_2`, respectively, where the former is depicted in the middle picture of Figure 6.1.

grid	nunkw	nnmat	sumflux	erl2	ergrad
C	612	4080	9.24E-14	3.84E-02	4.02E-02
F	2244	15312	1.10E-13	1.08E-02	1.11E-02

grid	erflx0	erflx1	erfly0	erfly1	erflm	pmin	pmax
C	1.39E-03	2.75E-04	2.24E-04	1.23E-03	1.85E-01	9.73E-03	9.45E-01
F	1.40E-04	1.85E-04	8.71E-05	6.66E-05	5.11E-02	2.90E-03	9.83E-01

Test 1.2 The exact solution is now given as $p(x, y) = \sin((1-x)(1-y)) + (1-x)^3(1-y)^2$ with extreme values $p_{\min} = 0$, $p_{\max} = 1 + \sin 1$, and a sharp increase towards the origin of the domain. Like before, this is first tested on the series of regular triangular meshes `mesh1`.

i	nunkw	nnmat	sumflux	erl2	ergrad	ratiol2	ratiograd
1	9.20E+01	4.28E+02	-2.22E-15	6.63E-03	1.26E-01	–	–
2	3.52E+02	1.70E+03	-9.77E-15	1.64E-03	6.17E-02	2.08E+00	1.06E+00
3	1.38E+03	6.75E+03	2.49E-14	4.10E-04	3.07E-02	2.03E+00	1.02E+00
4	5.44E+03	2.69E+04	2.04E-13	1.03E-04	1.53E-02	2.01E+00	1.02E+00
5	2.16E+04	1.08E+05	1.43E-12	2.56E-05	7.66E-03	2.02E+00	1.00E+00
6	8.63E+04	4.30E+05	5.04E-13	6.41E-06	3.83E-03	2.00E+00	1.00E+00
7	3.45E+05	1.72E+06	2.18E-12	1.61E-06	1.91E-03	2.00E+00	1.00E+00

ocvl2 = 2.01E+00, **ocvgradl2** = 1.01E+00.

i	erflx0	erflx1	erfly0	erfly1	erflm	pmin	pmax
1	1.96E-03	4.28E-04	1.20E-02	8.42E-03	1.23E-01	4.92E-03	1.37E+00
2	4.36E-04	2.73E-04	3.17E-03	2.64E-03	8.26E-02	1.24E-03	1.59E+00
3	9.51E-05	8.62E-05	8.60E-04	8.26E-04	4.75E-02	3.10E-04	1.72E+00
4	2.02E-05	2.35E-05	2.34E-04	2.53E-04	2.54E-02	7.76E-05	1.78E+00
5	4.15E-06	6.09E-06	6.38E-05	7.53E-05	1.31E-02	1.94E-05	1.81E+00
6	8.09E-07	1.55E-06	1.73E-05	2.19E-05	6.67E-03	4.85E-06	1.83E+00
7	1.64E-07	3.87E-07	4.34E-06	6.30E-06	3.34E-03	1.21E-06	1.83E+00

A second test on locally refined non-conforming rectangular meshes indicated by `mesh3` is carried out, where `mesh3_1` is illustrated in the right picture of Figure 6.1.

i	nunkw	nnmat	sumflux	erl2	ergrad	ratiol2	ratiograd
1	9.60E+01	6.40E+02	-1.18E-12	1.42E-02	1.41E-02	–	–
2	3.52E+02	2.40E+03	-2.11E-12	3.38E-03	5.44E-03	2.21E+00	1.47E+00
3	1.34E+03	9.28E+03	1.84E-12	8.05E-04	2.01E-03	2.14E+00	1.49E+00
4	5.25E+03	3.65E+04	-1.32E-10	1.94E-04	7.29E-04	2.08E+00	1.49E+00
5	2.07E+04	1.45E+05	-2.53E-10	4.73E-05	2.61E-04	2.06E+00	1.50E+00

ocvl2 = 2.04E+00, **ocvgradl2** = 1.48E+00.

i	erflx0	erflx1	erfly0	erfly1	erflm	pmin	pmax
1	6.67E-03	3.19E-02	2.17E-03	2.63E-02	9.22E-02	1.20E-02	1.66E+00
2	1.78E-03	8.26E-03	6.19E-04	6.98E-03	4.22E-02	3.19E-03	1.75E+00
3	4.50E-04	2.09E-03	1.62E-04	1.76E-03	2.02E-02	8.09E-04	1.79E+00
4	1.13E-04	5.27E-04	4.13E-05	4.40E-04	1.00E-02	2.03E-04	1.82E+00
5	2.82E-05	1.32E-04	1.04E-05	1.10E-04	4.97E-03	5.08E-05	1.83E+00

Test 2: Numerical locking

This test considers the homogeneous, but highly anisotropic tensor

$$\mathbb{K} = \begin{pmatrix} 1 & 0 \\ 0 & \delta \end{pmatrix}.$$

with $\delta \in \{10^5, 10^6\}$. The exact solution is chosen as $p(x,y) = \sin(2\pi x)e^{-2\pi\sqrt{\frac{1}{\delta}}y}$ with extreme values $p_{\min} = -1$, $p_{\max} = 1$. As boundary condition, the Neumann values are prescribed on the whole domain boundary, completed by the normalizing condition $\int_\Omega p \, \mathrm{d}V = 0$. Since the extreme solution values are located on the domain boundary, theymight be difficult to obtain with the pure Neumann boundary conditions. The tests are performed on the series of regular triangular meshes `mesh1`.

First, the results for $\delta = 10^5$ are listed.

i	nunkw	nnmat	sumflux	erl2	ergrad	ratiol2	ratiograd
1	9.20E+01	4.28E+02	4.49E-10	2.61E-01	3.54E-01	–	–
2	3.52E+02	1.70E+03	1.86E-09	3.57E+00	1.61E+01	-3.90E+00	-5.69E+00
3	1.38E+03	6.75E+03	-1.72E-09	6.51E-01	5.75E+00	2.49E+00	1.51E+00
4	5.44E+03	2.69E+04	1.33E-09	1.00E-01	1.97E+00	2.73E+00	1.56E+00
5	2.16E+04	1.08E+05	1.31E-09	1.62E-02	6.83E-01	2.64E+00	1.54E+00
6	8.62E+04	4.30E+05	-2.25E-09	2.75E-03	2.40E-01	2.56E+00	1.51E+00
7	3.45E+05	1.72E+06	3.02E-09	4.76E-04	8.44E-02	2.53E+00	1.51E+00

ocvl2 = 2.54E+00, **ocvgradl2** = 1.51E+00.

i	erflx0	erflx1	erfly0	erfly1	erflm	pmin	pmax
1	1.81E-11	7.66E-12	1.29E-10	1.60E-10	5.69E+02	-1.06E+00	1.07E+00
2	2.55E-11	2.27E-10	5.66E-10	4.00E-11	5.06E+02	-6.50E+00	5.75E+00
3	5.68E-11	1.72E-11	-4.95E-10	-7.63E-10	4.27E+02	-2.46E+00	2.29E+00
4	1.02E-10	7.27E-12	3.03E-11	7.09E-10	2.73E+02	-1.10E+00	1.09E+00
5	4.57E-11	5.18E-10	1.14E-09	-2.76E-09	4.78E+01	-1.01E+00	1.01E+00
6	7.97E-11	5.30E-11	6.18E-10	-2.70E-09	7.16E+01	-1.00E+00	1.00E+00
7	2.05E-10	3.46E-09	-6.62E-09	-1.06E-08	3.59E+01	-1.00E+00	1.00E+00

Second, the results for $\delta = 10^6$ are provided.

i	nunkw	nnmat	sumflux	erl2	ergrad	ratiol2	ratiograd
1	9.20E+01	4.28E+02	2.01E-09	2.61E-01	3.54E-01	–	–
2	3.52E+02	1.70E+03	1.31E-09	1.13E+01	5.10E+01	-5.62E+00	-7.41E+00
3	1.38E+03	6.75E+03	1.73E-07	2.06E+00	1.82E+01	2.49E+00	1.51E+00
4	5.44E+03	2.69E+04	1.69E-08	3.16E-01	6.21E+00	2.73E+00	1.57E+00
5	2.16E+04	1.08E+05	2.91E-08	5.12E-02	2.16E+00	2.64E+00	1.53E+00
6	8.62E+04	4.30E+05	1.07E-08	8.66E-03	7.57E-01	2.57E+00	1.52E+00
7	3.45E+05	1.72E+06	2.68E-08	1.50E-03	2.67E-01	2.53E+00	1.50E+00

ocvl2 = 2.53E+00, **ocvgradl2** = 1.51E+00.

i	erflx0	erflx1	fluy0	fluy1	erflm	pmin	pmax
1	2.94E-11	2.99E-10	1.25E-09	-9.31E-10	1.80E+03	-1.07E+00	1.07E+00
2	7.60E-10	9.69E-10	2.85E-08	-2.85E-08	1.61E+03	-1.86E+01	1.63E+01
3	3.84E-09	1.09E-08	1.09E-07	-2.85E-08	1.36E+03	-6.59E+00	6.08E+00
4	7.37E-10	1.89E-11	1.15E-08	8.86E-10	8.70E+02	-1.84E+00	1.75E+00
5	2.03E-09	2.78E-10	1.87E-08	-5.83E-10	4.51E+02	-1.06E+00	1.06E+00
6	6.89E-10	4.56E-10	8.24E-09	-4.75E-09	2.27E+02	-1.00E+00	1.00E+00
7	4.63E-09	3.94E-09	-1.87E-08	4.13E-08	1.14E+02	-1.00E+00	1.00E+00

Test 3: Oblique flow

For this test, the permeability tensor is chosen as

$$\mathbb{K} = \mathbb{R}_\theta \begin{pmatrix} 1 & 0 \\ 0 & \delta \end{pmatrix} \mathbb{R}_\theta^{-1}, \tag{6.3}$$

with $\delta = 10^{-3}$, and where $\mathbb{R}_\theta$ describes the rotation by an angle of $\theta = 40$ degrees. No exact solution is given, and the boundary conditions are pure Dirichlet, namely,

$$p_{\mathrm{D}} = \begin{cases} 1 & \text{on } ((0, 0.2) \times \{0\}) \cup (\{0\} \times (0, 0.2)), \\ 0 & \text{on } ((0.8, 1) \times \{1\}) \cup (\{1\} \times (0.8, 1)), \\ 0.5 & \text{else.} \end{cases}$$

The source term is set to $f = 0$. Therefore, the boundary conditions try to appoint a flow from the lower left to the upper right corner. However, this is impeded by the permeability tensor which prescribes a high permeability in the direction at 40 degrees

Figure 6.2: Solutions for the oblique flow on `mesh2_`i for $i = 2$ (left), $i = 3$ (center), $i = 4$ (right).

from the horizontal and low permeability in the orthogonal direction. The tests are carried out on a series of rectangular grids indicated by `mesh2`. Three solution snapshots are provided in Figure 6.2.

To evaluate the quality of the solution, the discrete energies `ener1` and `ener2` are calculated as described above. As reference mesh, mesh2_7 with mesh size 5.52E-03 has been chosen.

i	`nunkw`	`nnmat`	`sumflux`	`pmin`	`pmax`
1	4.00E+01	2.32E+02	-1.33E-15	7.06E-02	7.06E-02
2	1.44E+02	9.12E+02	-6.63E-15	3.14E-02	9.69E-01
3	5.44E+02	3.62E+03	-2.98E-14	1.63E-02	9.84E-01
4	2.11E+03	1.44E+04	-1.55E-13	8.25E-03	9.92E-01
5	8.32E+03	5.75E+04	-5.93E-13	4.10E-03	9.96E-01
ref	1.32E+05	9.18E+05	-8.66E-12	1.00E-03	9.99E-01

i	flux0	flux1	fluy0	fluy1	`ener1`	`ener2`	`eren`
1	-1.93E-01	1.93E-01	-9.57E-02	9.57E-02	2.19E-01	2.77E-01	2.09E-01
2	-1.90E-01	1.90E-01	-1.00E-01	1.00E-01	2.41E-01	2.72E-01	1.15E-01
3	-1.92E-01	1.92E-01	-9.99E-02	9.99E-02	2.38E-01	2.43E-01	1.88E-02
4	-1.93E-01	1.93E-01	-9.89E-02	9.89E-02	2.42E-01	2.43E-01	4.49E-03
5	-1.93E-01	1.93E-01	-9.88E-02	9.88E-02	2.42E-01	2.42E-01	1.28E-03
ref	-1.93E-01	1.93E-01	-9.87E-02	9.87E-02	2.42E-01	2.42E-01	1.05E-04

Test 4: Vertical fault

The medium is chosen to be layered with a vertical fault at $x = 0.5$. The distribution of the layers is shown in the left picture of Figure 6.3. The permeability values are given by

$$\mathbb{K} = \begin{pmatrix} \alpha & 0 \\ 0 & \beta \end{pmatrix},$$

with $\alpha = 10^2$, $\beta = 10$ for the more permeable black region, and $\alpha = 10^{-2}$, $\beta = 10^{-3}$ for the less permeable white region. No exact solution is given, and a Dirichlet boundary condition $p_{\mathrm{D}}(x, y) = 1 - x$ is applied on the whole domain boundary. A non-conforming rectangular

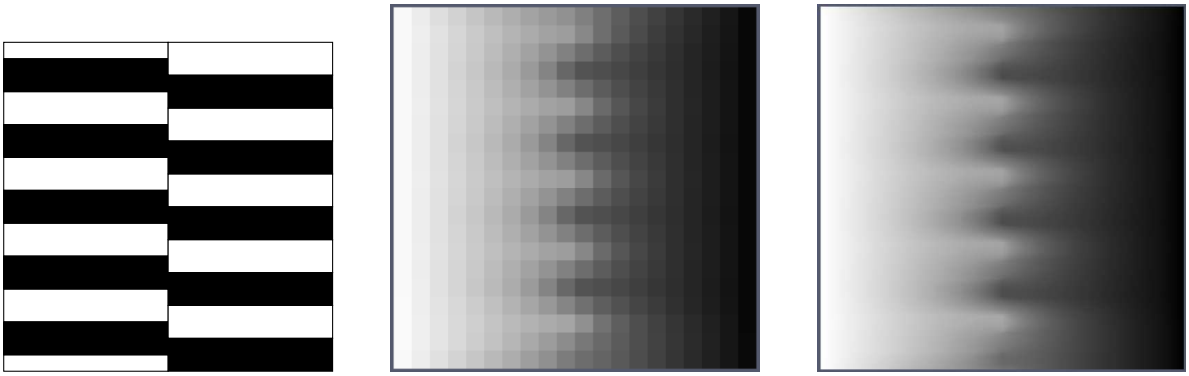

Figure 6.3: Test 4: the permeability distribution for the vertical fault, where black indicates the high values and white the low values (left). Solution on a regular 20x20 mesh (middle), and a reference 256x256 mesh (right).

grid `mesh5` has been proposed, such that each geological layer is meshed with one layer of discretization cells only. However, none of the available 2d DUNE grid managers allows for a corresponding non-conforming macro triangulation, so this test could not be carried out. Two other tests are performed, one for the additionally proposed regular grid `mesh5_reg`, and one for a reference mesh, for which `mesh2_7` with mesh size 5.52E-03 has been chosen. The solution values for these two meshes are visualized in the middle and right picture of Figure 6.3. The calculated values correspond to the one from Test 3.

i	`nunkw`	`nnmat`	`sumflux`	`pmin`	`pmax`
1	–	–	–	–	–
reg	8.40E+02	5.64E+03	-4.14E-12	2.12E-02	9.81E-01
ref	1.32E+05	9.18E+05	-3.74E-11	1.63E-03	9.98E-01

i	flux0	flux1	fluy0	fluy1	`ener1`	`ener2`	`eren`
1	–	–	–	–	–	–	–
reg	-4.19E+01	4.43E+01	-2.34E+00	8.14E-04	4.26E+01	4.31E+01	1.17E-02
ref	-4.21E+01	4.45E+01	-2.47E+00	7.98E-04	4.32E+01	4.32E+01	3.53E-04

Test 5: Heterogeneous rotating anisotropy

For this test, a heterogeneous rotating anisotropic permeability tensor is given by

$$\mathbb{K} = \frac{1}{x^2+y^2}\begin{pmatrix} 10^{-3}x^2+y^2 & (10^{-3}-1)xy \\ (10^{-3}-1)xy & x^2+10^{-3}y^2 \end{pmatrix}.$$

The exact solution is $p(x,y) = \sin\pi x \sin\pi y$, and the corresponding Dirichlet values are prescribed on the domain boundary. The series `mesh2` of uniform rectangular grids is chosen.

i	`nunkw`	`nnmat`	`sumflux`	`erl2`	`ergrad`	`ratiol2`	`ratiograd`
1	4.00E+01	2.32E+02	0.00E+00	1.94E-01	5.69E-01	–	–
2	1.44E+02	9.12E+02	-1.78E-15	3.16E-02	2.25E-01	2.91E+00	1.45E+00
3	5.44E+02	3.62E+03	-2.66E-15	5.92E-03	7.41E-02	2.59E+00	1.67E+00
4	2.11E+03	1.44E+04	-7.11E-15	1.31E-03	2.02E-02	2.26E+00	1.92E+00
5	8.32E+03	5.75E+04	6.22E-15	3.17E-04	5.09E-03	2.08E+00	2.01E+00

ocvl2 = 2.06E+00, **ocvgradl2** = 1.99E+00.

i	erflx0	erflx1	erfly0	erfly1	erflm	pmin	pmax
1	2.70E-01	2.14E-01	2.70E-01	2.14E-01	1.20E+00	1.74E-01	9.04E-01
2	8.33E-02	8.91E-02	8.33E-02	8.91E-02	6.53E-01	4.10E-02	9.71E-01
3	2.55E-02	4.29E-02	2.55E-02	4.29E-02	3.34E-01	9.78E-03	9.92E-01
4	7.68E-03	2.17E-02	7.68E-03	2.17E-02	1.68E-01	2.39E-03	9.98E-01
5	2.26E-03	1.10E-02	2.26E-03	1.10E-02	8.45E-02	5.99E-04	9.99E-01

Test 6 Oblique drain

In this test, flow is mostly concentrated in an oblique drain that consists of a very permeable layer. The permeability distribution is illustrated in the left picture of Figure 6.4, with

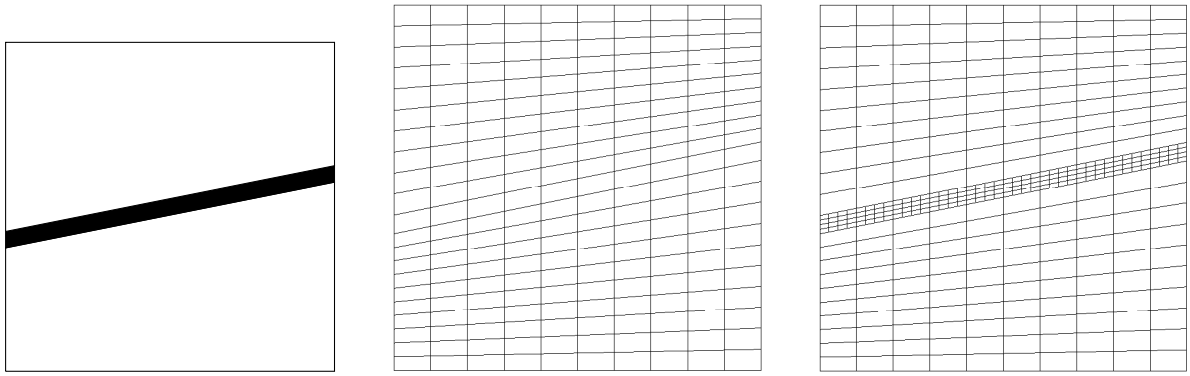

Figure 6.4: Left: the permeability distribution for the oblique drain of Test 6, where black indicates the high values and white the low values. The computational grids `mesh6` (middle) and `mesh6_ref` (right).

values given by

$$\mathbb{K} = \mathbb{R}_\theta \begin{pmatrix} \alpha & 0 \\ 0 & \beta \end{pmatrix} \mathbb{R}_\theta^{-1},$$

where $\theta = \arctan \delta$ corresponds to the slope $\delta = 0.2$ of the drain, and $\alpha = 10^2$, $\beta = 10$ for the drain region, while $\alpha = 1$, $\beta = 10^{-1}$ are set for the surroundings. A linear exact solution $p(x, y) = -x - \delta y$ is chosen and also imposed as a Dirichlet boundary condition. The goal of this test is to check whether the in- and outward fluxes can be reproduced by the numerical method, The employed computational grids are shown in the middle and right picture of Figure 6.4. The fine mesh is a bit different from the one proposed in [Herb 08]. Since the macro grid has to be conform and only a regular red refinement rule could be used, the cells in the drain are also refined in vertical direction.

grid	nunkw	nnmat	sumflux	erl2	ergrad
C	4.51E+02	2.97E+03	-2.17E-13	4.99E-15	4.38E-14
F	7.84E+02	5.70E+03	-7.45E-11	5.56E-12	3.01E-11

grid	erflx0	erflx1	erfly0	erfly1	erflm	pmin	pmax
C	1.22E-14	2.60E-14	1.53E-15	5.05E-14	3.06E-12	-1.15E+00	-5.38E-02
F	3.74E-12	7.81E-12	5.40E-12	2.37E-11	6.05E-10	-1.15E+00	-5.38E-02

Test 7: Oblique barrier

The setting for this test is similar to the one for Test 6, except that the black subdomain now represents a barrier. A scalar permeability field is chosen, with constant value 10^{-2} in the barrier and 1 in the surrounding region. An exact solution is considered that is piecewise linear with respect to the subdomains. The test should be only run on the conforming grid `mesh6`.

nunkw	nnmat	sumflux	erl2	ergrad
4.51E+02	2.97E+03	-4.45E-13	3.25E-15	4.73E-15

erflx0	erflx1	erfly0	erfly1	erflm	pmin	pmax
8.42E-13	1.39E-13	9.99E-16	2.50E-13	4.24E-13	-5.54E+00	5.37E-01

Test 8: Perturbed parallelograms

This test has been designed to check a numerical scheme for the violation of the discrete maximum principle. It is the only test where the computational domain is not the unit square. Both the domain and the proposed grid `mesh8` are depicted in Figure 6.5. The

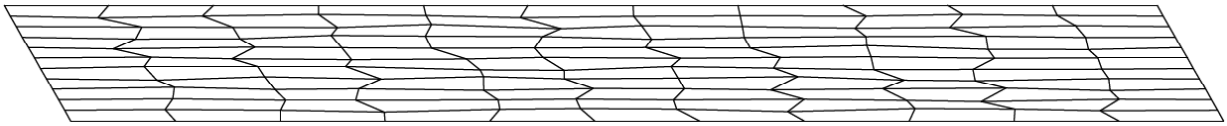

Figure 6.5: The perturbed parallelogram grid `mesh8`, where the extension in y-direction is magnified by a factor of 3.

elements are perturbed parallelograms of a very flat shape with a ratio of width to length equal to 1/30. The permeability is scalar and homogeneous with a value of 1. Zero Dirichlet conditions are applied onn the whole boundary. A source with $\int_E^q f \, \mathrm{d}V = 1$ is prescribed, where E^q is the element indexed by $i = j = 6$ in lexicographical ordering. Accoring to the maximum principle, the solution should have a maximum in E^q and decrease smoothly to zero towards the boundary. If the numerical solution shows oscillations, Hopf's first lemma is violated, [Hell 60].

As mentioned above, there is one parameter $\tilde{u}_E$ for tuning the scheme. In all tests before, this parameter was set element-wise to $\tilde{u}_E = c|E|^{-1} \operatorname{trace}(K_E)$ with $c = 2$. For this test, it seems necessary to choose the constant c larger in order to stabilize the scheme and reduce the unfortunately appearing oscillations. For the following table, c was set to 32. The definition of flux0, flux1, and fluy1 was changed in the obvious way to meet the requirements of the domain shape.

nunkw	nnmat	sumflux	pmin	pmax
2.64E+02	1.72E+03	5.51E-14	-2.04E-02	8.44E-02

flux0	flux1	fluy0	fluy1
-2.29E-02	3.43E-03	5.10E-01	5.09E-01

The following table shows the numerical solution values for each grid cell according to its lexicographical ordering. The first and last column have been omitted for sake of exposition.

i\j	2	3	4	5	6	7	8	9	10
1	-4.02E-04	1.10E-03	-3.74E-03	3.99E-03	1.19E-02	-2.68E-03	9.09E-04	1.76E-03	-9.25E-04
2	-7.02E-04	1.94E-03	-6.77E-03	1.06E-02	2.86E-02	-4.25E-03	2.55E-03	7.72E-03	-3.29E-03
3	-1.42E-03	2.06E-03	-7.15E-03	1.58E-02	4.46E-02	2.41E-03	-9.51E-03	1.12E-02	-3.29E-03
4	-1.91E-03	5.53E-03	-1.51E-02	1.28E-02	6.51E-02	1.47E-03	-1.23E-02	1.07E-02	-2.21E-03
5	-2.00E-03	8.65E-03	-1.89E-02	1.08E-02	8.01E-02	2.40E-03	-1.29E-02	1.46E-02	-3.09E-03
6	-2.75E-03	8.31E-03	-1.63E-02	6.35E-03	**8.46E-02**	-2.57E-03	-1.68E-02	1.41E-02	-2.02E-03
7	-3.33E-03	9.55E-03	-1.07E-02	-8.65E-03	7.25E-02	8.50E-03	-1.65E-02	9.92E-03	-7.34E-04
8	-4.47E-03	8.11E-03	-2.39E-03	-1.35E-02	5.86E-02	2.59E-02	**-2.04E-02**	9.54E-03	-1.29E-03
9	-5.07E-03	5.09E-03	-2.39E-03	-9.27E-03	5.22E-02	1.68E-02	-1.73E-02	1.15E-02	-1.76E-03
10	-2.47E-03	2.65E-03	-2.69E-03	-3.53E-03	3.09E-02	1.07E-02	-1.12E-02	9.74E-03	-2.08E-03
11	-6.82E-05	5.68E-05	-3.12E-04	1.28E-05	6.21E-03	3.90E-03	-2.99E-03	2.86E-03	-1.06E-03

Test 9: Anisotropy with wells

Again considering the unit square, the permeability now is of the form (6.3) with $\theta = 67.5$ degrees and $\delta = 10^{-3}$. The source term f is equal to zero and homogeneous Neumann boundary conditions are prescribed on the outer boundary. The pressure should be fixed in two cells, namely, $p = p_{\min} = 0$ in cell $(4, 6)$ and $p = p_{\max} = 1$ in cell $(8, 6)$. The computational mesh is a square uniform grid consisting of 11×11 cells. If the numerical solution has extrema on the no-flow boundary with values less than $p_{\min}$ or greater than $p_{\max}$, the second Hopf lemma is violated, [Hell 60].

The implementational effort necessary to incorporate the required boundary conditions was considered too high. Therefore, the problem setting has been slightly changed. In particular, elements (4,6) and (8,6) have been omitted, resulting in two holes inside the domain. On the boundary of the two holes, the corresponding Dirichlet conditions have been set.

nunkw	nnmat	sumflux	pmin	pmax
2.64E+02	1.69E+03	-7.03E-15	-4.21E-02	1.04E+00

The following table shows again the discrete solution values for each cell. This time, columns 5 and 7 are omitted.

i\j	1	2	3	4	6	8	9	10	11
1	-4.18E-02	1.01E-02	2.18E-01	5.56E-01	9.74E-01	1.02E+00	1.02E+00	1.02E+00	1.02E+00
2	-3.61E-02	-2.28E-02	1.10E-01	4.03E-01	9.38E-01	1.02E+00	1.02E+00	1.02E+00	1.02E+00
3	-8.86E-03	**-4.21E-02**	3.95E-02	2.60E-01	8.78E-01	1.01E+00	1.02E+00	1.02E+00	1.02E+00
4	-7.69E-03	-2.32E-02	-1.68E-02	1.53E-01	7.82E-01	1.01E+00	1.02E+00	1.02E+00	1.02E+00
5	-2.19E-02	-7.90E-03	-2.74E-02	5.68E-02	6.39E-01	1.00E+00	1.02E+00	1.02E+00	1.02E+00
6	-1.66E-02	-1.84E-02	-1.14E-02	**0.00E+00**	5.00E-01	**1.00E+00**	1.01E+00	1.02E+00	1.02E+00
7	-1.75E-02	-1.69E-02	-1.61E-02	-4.59E-03	3.61E-01	9.43E-01	1.03E+00	1.01E+00	1.02E+00
8	-1.74E-02	-1.73E-02	-1.64E-02	-1.11E-02	2.18E-01	8.47E-01	1.02E+00	1.02E+00	1.01E+00
9	-1.74E-02	-1.73E-02	-1.69E-02	-1.40E-02	1.22E-01	7.40E-01	9.60E-01	1.04E+00	1.01E+00
10	-1.74E-02	-1.74E-02	-1.71E-02	-1.56E-02	6.18E-02	5.97E-01	8.90E-01	1.02E+00	**1.04E+00**
11	-1.74E-02	-1.74E-02	-1.73E-02	-1.64E-02	2.64E-02	4.44E-01	7.82E-01	9.90E-01	**1.04E+00**

6.3 Comments on the Results

Some more technical comments have already been made in section 2. Concerning the quality of the results, the mimetic finite difference method proves to be very robust and accurate in most tests. In particular, for tests 1, 2, 5, 6, and 7 with available exact solution, we observe the following:

- The error decay for the pressures always exhibits the typical quadratic convergence behavior.
- Concerning the error in the solution gradients, a standard linear decay can be observed for the simplicial meshes in tests 1 and 2, while for the conforming quadrilateral grids, super-convergence results in a quadratic decay in tests 1 and 5. We point out that this super-convergence cannot only be observed for the uniform grids `mesh2`, but also for the distorted meshes `mesh4`. For the series `mesh3` of non-conforming quadrilateral grids with hanging nodes, the observed order of convergence in the gradients is 1.5.

- Concerning the fluxes, the errors `erflx0`, ..., `erflm` show at least the expected linear decay. Here, we like to add that, evaluated in the norm associated with the scalar product $(\cdot, \cdot)_{X_h}$, we usually also observe a super-convergent behavior for the error in the fluxes.

- Especially remarkable are the tests 6 and 7 where all calculated errors are practically zero since the piecewise linear exact solution, its gradient, and its fluxes are exactly reproduced at the barycenter of the elements and faces, respectively.

- Unfortunately, test 2 produces quite unsatisfactory results. After an already reasonable solution with respect to the mesh size is produced at the coarsest level, the solution as well as the errors blow up at the second one. Over the following levels, it becomes obvious that some higher order terms take effect, since the convergence is accelerated by half an order. It would be very interesting to obtain an explanation for this behavior.

For the other tests 3, 4, 8, and 9, the following observations are made:

- The sum of the fluxes over the boundary is always practically zero, which nicely illustrates the total mass conservation of the scheme.

- For test 3, the minimum and maximum pressure values, as well as the boundary fluxes and the discrete energies; converge fast towards the values of the reference solution. Already for quite coarse meshes, reasonable solutions are calculated.

- Test 4 shows that the solution on the regular 20×20 mesh is already very close to the reference solution.

- Tests 8 and 9 unfortunately show that the Hopf lemmas are violated. While test 9 still produces a good result and the violation is within an acceptable range, the oscillations in test 8 heavily reduce the quality of the solution. In order to improve the method, we could set up a suggestion of the developers made in [Brez 05b]. In particular, by making use of the freedom in selecting members of the proposed family of mimetic methods, we could try to enforce a discrete maximum principle. However, it is not yet clear how to explicitly tune the parameters of the method to achieve this.

Overall, the implemented mimetic finite difference method solves the majority of the proposed problems with convincing accuracy and robustness. It appears to be most promising for tackling real applications, and has already proved to be able to do so, [Aarn 08b]. This is not only due to accuracy and robustness, but also due to the remarkable ease of implementation.

Part C

Open-Source Porous-Media Simulation

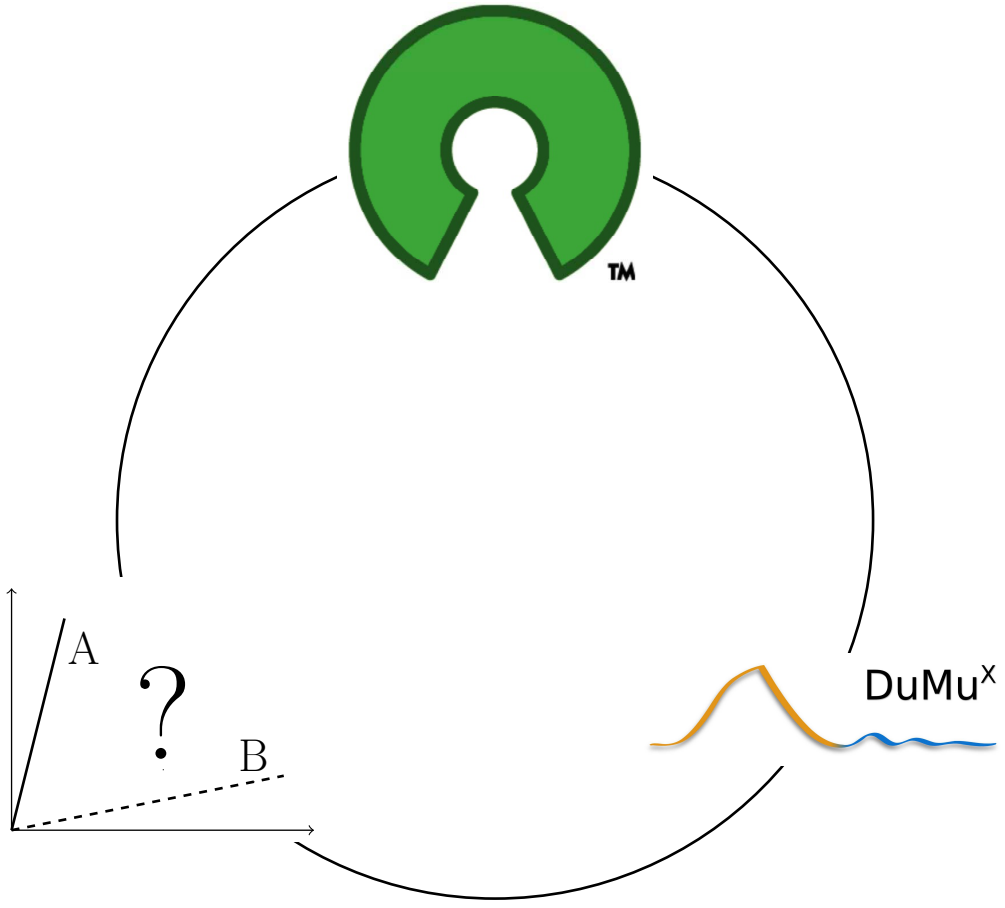

7 Open Source in Computational Science and Engineering

Free and Open-Source Software (FOSS) is ubiquitous in many people's lives. Operating systems and other important software components for stationary and mobile devices like desktop PCs and computer clusters, smartphones, satellite or cable receivers, may all be based on FOSS. Especially in computational science and engineering, the use of FOSS components has become standard. However, it is still uncommon for most academic individuals and groups to develop and release their in-house code in an open-source manner. In Section 7.1 of this chapter, we first provide a motivation for developing open-source code in academia. The background and definitions of FOSS are presented in Section 7.2. A list of porous media simulators currently being developed is given in Section 7.3, while the final Section 7.4 introduces necessary and useful infrastructure components for open-source projects.

7.1 Why Develop Open Source in Academia?

In the following, we provide three basic arguments for developing open-source research code as an individual scientist or academic group. The first states that providing access to source code is mandatory as reproducibility is fundamental to the scientific method. The second argument is the expected increase in code quality and applicability. Finally, the potential for collaboration with industrial or academic partners is greatly facilitated and simplified by using open-source development principles.

In their "Proposals for safeguarding good scientific practice" [Deut 98], the German Research Foundation DFG rephrases one of the main ingredients of the scientific method: "The primary test of a scientific discovery is its reproducibility." The increasing complexity of scientific results renders their reproducibility a highly challenging task. This especially holds if the scientific result in question has been achieved by a numerical experiment. While a few decades ago, one still could describe a computational algorithm in detail in a journal paper such that an interested researcher could reprogram it on his own and reproduce the proposed results, this is impossible for today's complex numerical models. The only viable way of enabling the scientific community to reproduce the results gained by computer code is to grant access to this code. To put it in more provoking words [Ince 10]: "..., if you are publishing research articles that use computer programs, if you want to claim that you are engaging in science, the programs are in your possession and you will not release them then I would not regard you as a scientist; I would also regard any papers based on the software as null and void." Granting code access constitutes the first main principle of free and open-source software.

Another motivation for developing academic research software by means of open-source principles is that code quality will increase and the period of vocational adjustment for new users and developers will be decreased. The usual software development in many academic groups is based on fragmented and individual research. While the resulting

computer programs may demonstrate the excellence of a given special-purpose model or method, they are rarely applicable to modified problem settings. In fact, they usually are inaccessible to outsiders and incapable of handling real application data like industry-standard geological models. The typical life-span of the code is approximately the duration of employment of the PhD candidate or PostDoc that programmed it, its reusability is minimal. Allowing the community to look at the code and to use it for any purpose will increase the number of opportunities for detecting programming errors and limits of the proposed numerical model or algorithm. This of course requires that the community provides feedback to the code developers regarding their experiences in using the code. This feedback will also help to improve the quality of the code, including the coding style or the number and comprehensibility of code comments. If an active user community emerges, it can also be expected that "programmers who report problems with an open-source project often not only provide a problem description but also contribute a software patch which solves the problem" [Pude 00]. Overall, an open-source development model can improve code quality, readability, applicability and robustness. This in turn is highly beneficial for the academic group developing the software and will allow a sustainable and long-lasting program development.

open-source code development can also attract industrial partners. The partners will profit from an accelerated technology transfer from academia, since new research results will be immediately available as free software. The development and testing of new models and computational methods will be enhanced and simplified. Moreover, commercial simulators may fail to give answers in many cases, requiring alternative solution strategies. Especially in safety-critical applications like the use and protection of the subsurface, the answer of only one simulator is not enough to build confidence in the computed results. Open-source code offers the opportunity to calculate and compare the results from different simulators, helping to increase the confidence of modelers and decision makers. These are also positive arguments that open source will foster collaboration in joint research projects between academic institutions. The participating researchers have full control over, for example, discretizations and solvers. Joint benchmarking and the exchange of new methods is facilitated. Moreover, once a set of basic building blocks is available, one can go right to the interesting problems.

It is debatable whether the aforementioned benefits can only be achieved by following the open-source idea, and, even more, whether these benefits can really be achieved and are not only wishful thinking. In [Fugg 03], the author dissociates himself from the belief that only open source can provide the desired advantages and is *the* solution to many problems. However, he makes a crucial exception for research codes: "Nevertheless, there are particular market situations where open source is probably the only viable solution to support successful and effective software development. Typical examples are research communities that need specific software products to support their research work."

7.2 The Definitions of Free and Open-Source Software

Free and open-source software (FOSS) has a history that is as long as software itself, see [Gonz 13] and the references therein. There are currently two main organizations behind the FOSS idea: the Free Software Foundation (FSF), `fsf.org`, and the Open Source Initiative (OSI), `opensource.org`. Both define FOSS in a similar way, but they have fundamentally different motivational backgrounds, according to the FSF: "Open source is a development

methodology; free software is a social movement ... [and] an ethical imperative," [Stal 13]. In the following, the two organizations are introduced briefly and their FOSS definitions are provided and discussed.

Free Software Foundation The FSF was founded in October 1985 by Richard Stallman, who has been acting as the foundation's president ever since. The FSF describes itself as a nonprofit organization "with a worldwide mission to promote computer user freedom and to defend the rights of all free software users," `fsf.org/about/`. Its main activities are sponsoring the GNU project, `gnu.org`, and campaigning for promoting the philosophy of free software and "against threats to computer user freedom." The FSF maintains the *Free Software Definition*, `gnu.org/philosophy/free-sw.html`:

> "A program is free software if the program's users have the four essential freedoms:
>
> - The freedom to run the program, for any purpose (freedom 0).
> - The freedom to study how the program works, and change it so it does your computing as you wish (freedom 1). Access to the source code is a precondition for this.
> - The freedom to redistribute copies so you can help your neighbor (freedom 2).
> - The freedom to distribute copies of your modified versions to others (freedom 3). By doing this you can give the whole community a chance to benefit from your changes. Access to the source code is a precondition for this."

From the definition, it is obvious that the term "free" in "free software" is not supposed to indicate "free of charge" but rather tries to stress the user's freedom. Nevertheless, one of the main reasons for the large success of free and open-source software surely is the fact that the software actually is free of charge in many cases.

Open Source Initiative Influenced by the release of the Netscape browser's source code and by the increasing popularity of Linux operating systems, the Open Source Initiative was founded in 1998. The label "open source" was preferred to the label "free," both to avoid its ambiguity and to establish a more pragmatic view in contrast to the missionary attitude of the FSF. The OSI describes itself as "a non-profit corporation with global scope formed to educate about and advocate for the benefits of open source and to build bridges among different constituencies in the open-source community," `opensource.org/about/`. Its main activity is maintaining the *Open Source Definition*, `opensource.org/docs/osd/`:

> "Open source doesn't just mean access to the source code. The distribution terms of open-source software must comply with the following criteria:
>
> 1. The license shall not restrict any party from selling or giving away the software ...
> 2. The program must include source code, and must allow distribution in source code as well as compiled form. ...

3. The license must allow modifications and derived works, and must allow them to be distributed under the same terms as the license of the original software.

...

6. The license must not restrict anyone from making use of the program in a specific field of endeavor. ...

... "

The very first sentence of the definition reveals the shortcoming of the label "open source:" providing access to the source code is not enough. So neither "free" nor "open source" are satisfying descriptions of their intended meanings.

Although the definition provided by the OSI is more detailed than the FSF one, both "lead to the same result in practice," and "in general, the terms *free software* and *open-source software* can be used interchangeably," `opensource.org/faq#free-software`. In the following, it will not be distinguished between the two terms, and usually the term "open source" is used.

For the developers of open-source software, choosing the right license can be a crucially important step. This step is especially complicated due to the availability of currently more than 70 OSI- and FSF-compliant licenses, many of which only differ in small but possibly important legal details. A good overview of the main possibilities is provided in [Mori 12]. In general, one should use one of the licenses which are approved both by the FSF and the OSI. It is also advisable to choose a license from the most common ones that are used for many other open-source projects. If the developed code is based on another project, the best choice usually is to stick with the license from that particular project. The two most fundamental differences that an open-source license can make in practice are the following:

- Allowing that the code can be linked with code/programs distributed under another license. This can be important for the further utilization of the code as part of an otherwise proprietary program.

- Requiring that changes to the code have to be released under the same license. Such licenses are referred to as "copyleft" type licenses [Wiki 13b].

A change of the license can be a very difficult step. Theoretically, everyone that owns copyright on a piece of the code involved has to agree to such a change. This might be complicated, if such persons already left the development team or if someone disagrees with the proposed change.

7.3 Porous Media Simulators

Various porous media simulators are under ongoing development, some examples are listed below in alphabetical order. A simulator is only considered if it primarily targets simulations on the Darcy scale. The distribution and licensing policies for the simulators listed vary from proprietary commercial to open source and free of charge.

DuMu^x DUNE for multi-{phase, component, scale, physics, ...} flow and transport in porous media (DuMu^x), `dumux.org`, is a free and open-source simulator for flow and transport processes in porous media, [Flem 11]. It is based on the Distributed and Unified Numerics Environment DUNE, `dune-project.org`, [Bast 08a]. Its main intention is to provide a sustainable and consistent framework for the implementation and application of model concepts, constitutive relations, discretizations, and solvers. It has been successfully applied to CO_2 storage scenarios, environmental remediation problems, transport of therapeutic agents through biological tissue, and subsurface-atmosphere coupling. DuMu^x is part of the OPM (Open Porous Media) initiative, `opm-project.org`. The development of DuMu^x started in 2007 at the University of Stuttgart's Department of Hydromechanics and Modelling of Hydrosystems. The first release was in July 2009, the current release is 2.3 under the GNU GPL. DuMu^x is presented and discussed in greater detail in Chapter 8.

ECLIPSE ECLIPSE, `slb.com/eclipse/`, is a proprietary reservoir simulator that has been the standard and reference in industrial reservoir simulation for over two decades, [Schl 09]. It offers a broad range of capabilities, ranging from standard black-oil models with sophisticated well controls to chemical reactions, combustion, biodegradation, decay of radioactive tracers, and non-equilibrium reactions. One of the defining features that sets ECLIPSE apart from many other porous media simulators is its capability of handling corner-point grids. While being logically Cartesian, such grids allow for arbitrary degeneracies of cell faces and edges and admit geometrically non-conforming cells. The standard spatial discretization method employed is cell-centered finite volumes with two-point flux approximation. ECLIPSE offers fully implicit and IMPES approaches. It is mostly written in Fortran. The current release is named ECLIPSE 2012.

FEHM Finite Element Heat and Mass Transfer Simulator (FEHM), `fehm.lanl.gov`, is a porous media fluid flow simulator developed by the Los Alamos National Laboratory almost forty years ago, [Zyvo 07]. It is written in Fortran 77 and Fortran 90. Modelling capabilities range from isothermal single phase to non-isothermal three-phase flow. Available components are air, water, CO_2, oil and several chemically reactive and sorbing tracers. By default, a control-volume finite-element method is used for the spatial discretization. A fully implicit approach is employed, where the derivatives for the Jacobian matrix are calculated analytically. FEHM also can simulate geomechanical processes coupled to the flow processes. For research purposes, an executable can be obtained free of charge after signing an end-user software license agreement from the LANL. The version currently available is 3.00.

IMEX/GEM/STARS Another set of commercial tools is developed by the Computer Modelling Group (CMG), `cmgl.ca`: the three-phase black-oil reservoir simulator IMEX, the compositional and unconventional reservoir simulator GEM, and the advanced processes and thermal reservoir simulator STARS. Like ECLIPSE, CMG's simulators are capable of simulating geological models based on corner-point grids. They all use an adaptive implicit formulation. The current releases are called IMEX/GEM/STARS 2012.

GPRS General Purpose Research Simulator (GPRS) is developed by the Reservoir Simulation Research Program (SUPRI-B) at the School of Earth Sciences at Stanford University,

[Cao 02, Jian 07]. It is written in C++ and the first release to SUPRI-B members took place in 2002. GPRS is capable of modeling flow in porous media for mixtures with an arbitrary number of phases, including chemical reactions. It provides a variety of formulations like fully implicit, IMPES and adaptive implicit. The default spatial discretization is a cell-centered finite-volume method. The calculation of the necessary derivatives is based on automated differentiation. Large efforts are put into programming robust and efficient preconditioners.

IPARS Integrated Parallel Accurate Reservoir Simulator (IPARS), `csm.ices.utexas.edu/software-ipars.php`, developed at the Center for Subsurface Modeling at the University of Texas, is a framework for parallel models of subsurface flow and transport through porous media, [Whee 01]. Apart from standard models for tackling reservoir engineering problems, IPARS focuses on multi-model formulations that allow the incorporation of multi-numerics and multi-physics approaches. While cell-centered differences are used by default for spatial discretization, several state-of-the-art methods have been additionally implemented, including mixed finite-element and discontinuous Galerkin methods. IPARS also offers the possibility of handling multi-block nonmatching grids by means of the mortar method. Moreover, it has been used for coupled geomechanical deformation and reservoir simulation. One of the main strengths is also that it is capable of running "mega-size" problems on modern high performance computing architectures. It is programmed mostly in Fortran, uses an individual license and provides access to the source code.

MODFLOW MODFLOW, `water.usgs.gov/nrp/gwsoftware/modflow.html`, is a finite-difference groundwater flow model from the U.S. Geological Survey. It can be considered as a standard for modeling groundwater flow in aquifers. Its original development started in the 1980s, [McDo 03]. The current version MODFLOW-2005 1.9.01 is written primarily in Fortran 90 and C and distributed as public domain free software. Several proprietary and open-source graphical user interfaces are in active development, [Wiki 13c]. Many other groundwater flow simulators exist, like the proprietary packages FEFLOW, `feflow.com`, [Tref 07], and HYDRUS, `pc-progress.com/en/Default.aspx?hydrus-3d`, [Yu 10].

MRST The MATLAB Reservoir Simulation Toolbox (MRST), `sintef.no/Projectweb/MRST/`, is developed by SINTEF Applied Mathematics and is a result of their research on the development of new (multiscale) computational methodologies, [Lie 12]. It is "mainly intended as a toolbox for rapid prototyping and demonstration of new simulation methods and modeling concepts on unstructured grids." MRST is able to handle corner-point grids and ECLIPSE input files. The current release 2012b contains solvers for single-phase and immiscible two-phase flow, as well as for black-oil and discrete fracture-matrix formulations. It is available under the GNU GPL.

OpenGeoSys OpenGeoSys, `opengeosys.org`, "is a free, multi-platform, scientific modeling package that enables numerical simulations of individual or coupled thermo-hydro-mechanical-chemical (THMC) processes in porous and fractured media." A finite-element method is used for spatial discretization. The project incorporates more than 150 benchmark tests which are described in [Kold 12]. OpenGeoSys is programmed in C++ and the

currently available release is 5.3.6. It is distributed under an individual license based on the BSD 3-Clause license. Special emphasis is put on making "the project an open dialog with the user & developer community."

PANDAS Porous Media Adaptive Nonlinear finite element solver based on Differential Algebraic Systems (PANDAS), `mechbau.uni-stuttgart.de/pandas/`, is a finite element package developed at the Institute of Applied Mechanics of the University of Stuttgart for the solution of porous media problems. Special emphasis is placed on a correct description of the geomechanical aspects in coupled porous-media fluid-solid interaction problems. In particular, it allows geometrically linear or finite deformations, as well as combinations of elastic, viscoelastic, plastic and viscoplastic behavior of the solid material. PANDAS is written in C/C++ and distributed under an individual license. The version currently available is 5.01.

ParFlow ParFlow, `computation.llnl.gov/casc/parflow/`, is a collaborative effort of Colorado School of Mines, Lawrence Livermore National Laboratory, University of Bonn and UC Berkeley. It "simulates the three-dimensional saturated and variably saturated subsurface flow in heterogeneous porous media in three spatial dimensions using a multigrid-preconditioned conjugate gradient solver and a Newton-Krylov nonlinear solver," [Maxw 10]. Parflow has been used for regional-scale hydrologic simulations on massively parallel computing architectures, [Koll 10]. It has been coupled to solvers for atmospheric flow, [Will 11]. Parflow is primarily written in C and released under the GNU LPGL, the latest release being Version 3.605.

PFloTran PFloTran, `ees.lanl.gov/source/orgs/ees/pflotran/`, is an open source, state-of-the-art massively parallel subsurface flow and reactive transport code, mainly developed at Los Alamos National Laboratory. It mainly focuses on CO_2 storage and contaminant migration as applications. PETSc, `mcs.anl.gov/petsc/`, is the basis for its parallel framework, which is a suite of data structures and routines for the scalable parallel solution of partial differential equations, [Bala 12]. PFloTran is capable of handling both unstructured grids and adaptive mesh refinement on structured grids. Finite volume discretizations are used by default. The primary programming language is Fortran 2003, and it is developed under the GNU LGPL.

STOMP Subsurface Transport Over Multiple Phases (STOMP), `stomp.pnnl.gov`, is developed at Pacific Northwest National Laboratory. It models subsurface flow and transport over three distinct phases (aqueous, gas, and NAPL) and offers the possibility of adding an additional conservation equation to simulate salt concentration or surfactants, [Whit 00]. STOMP uses a fully implicit formulation with local variable switching, based on integrated finite differences. It is programmed in Fortran 77 and 90 and follows a proprietary licensing strategy. The current release is termed Version 4.

TOUGH Transport Of Unsaturated Groundwater and Heat (TOUGH), `esd.lbl.gov/research/projects/tough/`, is a suite of software codes for non-isothermal multi-phase flow and transport in fractured porous media. It is developed by researchers from Lawrence Berkeley National Laboratory, and has been in use since the early 1980s. The core module TOUGH2, [Prue 04], can be enhanced by other dedicated modules,

like TOUGHREACT which enables advanced geochemical transport modeling capabilities. The spatial discretization is based on integrated finite differences, and first-order fully-implicit time differencing is applied to the governing equations. It is possible to buy proprietary licenses for executables only or for the full source code. The current version of the core module TOUGH2 is 2.1. The modules of TOUGH are mostly programmed in Fortran 77 and 95.

ASCEM/Amanzi Advanced Simulation Capabilities for Environmental Management (ASCEM) is a project headed by the US Department of Energy's Office of Environmental Management (DOE-EM), with the participation of several US National Laboratories. According to their homepage at `esd.lbl.gov/research/projects/ascem/`, ASCEM "is a software project that aims at developing next-generation, science-based reactive flow and transport simulation capabilities and supporting modeling toolsets within a high-performance computing framework to address DOE-EMs waste storage and environmental cleanup challenges." The project is thus driven by environmental applications, in particular atomic waste disposal. The "multi-process HPC Simulator" Amanzi constitutes one of the three ASCEM technical thrust areas. The majority of the code is supposed to be developed in C++ with the aim of achieving modularity and extensibility. Apparently, the project follows an open-source release strategy, but no explicit licensing information has been made available yet. For the initial release, development focuses on single-phase and Richards flow models. Though planned for January 2013, a release was not available in March 2013.

7.4 Infrastructure for Open-Source Projects

In the following, several important parts of the infrastructure of an open-source project are reviewed. All of these parts can be realized by open-source solutions themselves. In particular, code hosting, revision control, website, bug tracking, automated testing, mailing list, and analysis tools are discussed. Each part is annotated by an example on how it has been realized for the simulator DuMu^{x}.

7.4.1 Revision Control

Revision (or version) control is the management of changes to the program code and accompanying files like documentation, build system etc. Corresponding tools are indispensable for joint code development (and at least very helpful for individual development). They can be classified in two categories: centralized and distributed.

Centralized Revision Control The classical approach in revision control systems is *centralized*, indicating a *client-server model*. In particular, one single data store is declared to be the central *repository*, and all access and changes to the data are undertaken with respect to this repository. The most prominent centralized version control system is Subversion, `subversion.apache.org`.

Distributed Revision Control In distributed revision control, there is technically no single authoritative repository. All individual working copies themselves are repositories, and

data access/changes can be done referring to each one of those. In recent years, Git, `git-scm.com`, has emerged as the most widely used distributed revision control system.

DuMu^x uses the centralized revision control system Subversion. The first commit took place in March 2007. Roughly six years later, the commit count has reached more than 10,000. The repository structure follows the one which is most commonly used for Subversion projects: besides the `trunk` containing the main line of development, it contains a subfolder `branches` for managing developments off the main line, including the releases. Moreover, it contains a subfolder `tags` where each release is identified by means of a particular revision number.

7.4.2 Code Hosting

By default, code developed under centralized revision control needs a place to store the central repository. Such a place is also desirable for code that is developed with the help of distributed version control systems, both as an access point for developers and users, and as a reference location for releases. In academic environments, such a place may be provided on the servers that are administrated by the academic institution itself. Nevertheless, it can be beneficial to make use of one of the available code hosting services like SourceForge, `sourceforge.net`, or GitHub, `github.com`. They do not only offer to host the code, but also several of the additionally needed infrastructure components like website, bug trackers and discussion boards.

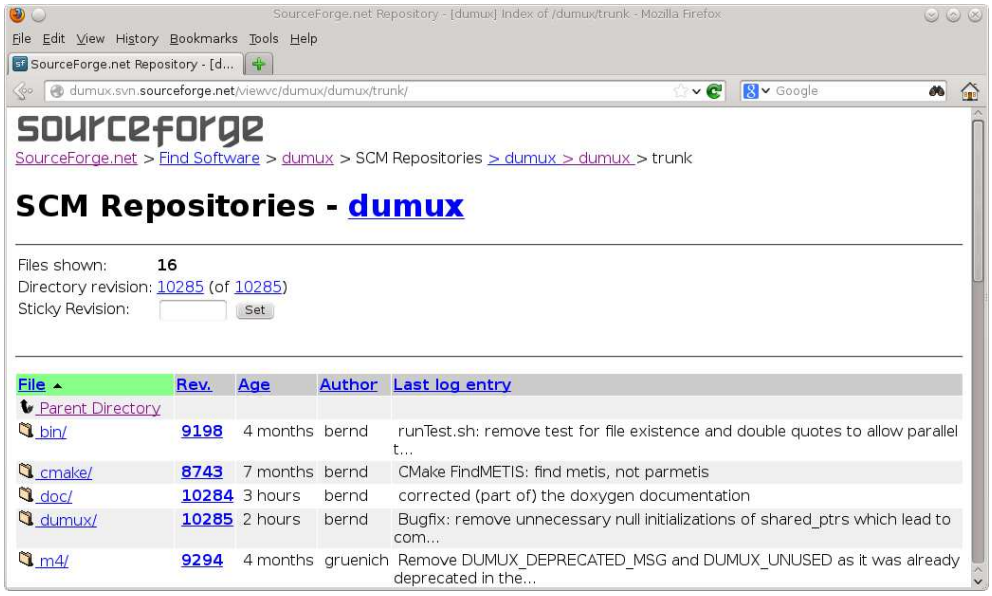

Figure 7.1: The SourceForge mirror of the DuMu^x Subversion repository.

The Subversion repository of DuMu^x is hosted at the Institute for Modelling Hydraulic and Environmental Systems of the University of Stuttgart. Additionally, a mirror repository has been set up at SourceForge, `dumux.svn.sourceforge.net`, see Figure 7.1. This mirror repository is synchronized with the original one at several fixed times during each working day.

7.4.3 Website

A dedicated website is the showcase of the developed simulator for the outside world. It should be easy to find and attract potential users to download and test the code. It should provide access to the source code and, if available, to binaries or packages for different platforms. It should also contain basic installation instructions and pointers to the detailed code documentation and additional documents like a handbook or a tutorial. To illustrate the capabilities of the simulator, a gallery with screen shots from selected applications and a list of achieved publications are helpful.

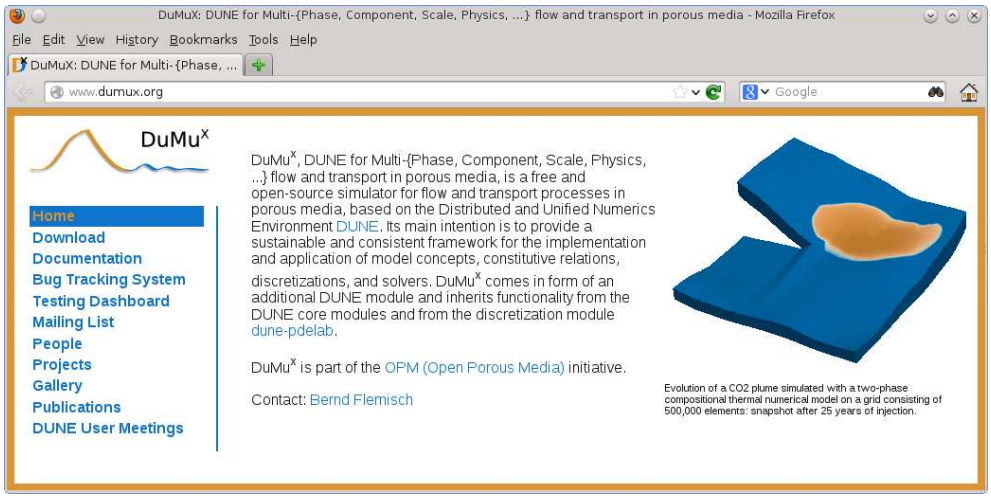

Figure 7.2: The DuMu^x home page at `dumux.org`.

The homepage of the simulator DuMu^x can be accessed at `dumux.org`, see Figure 7.2. It is maintained by the DuMu^x developer group and hosted at the Computer Center of the University of Stuttgart (RUS), `www.rus.uni-stuttgart.de`.

7.4.4 Mailing List

A mailing list can help to interact with the user community of a software project. Anybody interested can sign up for the list and post and receive emails dedicated to the project. From the developers' side, the list can be employed to make important announcements like the release of a new version or the detection of a severe issue. The users should be encouraged to post questions related to the code that can be answered by the developers or also by other users. Archiving the mails helps to keep track of the topics discussed.

For DuMu^x, the mailing-list server of the RUS is used and the list can be reached at `dumux@listserv.uni-stuttgart.de`. It is possible to sign up for the list via the DuMu^x home page. The list also forwards the emails generated by the issue tracker, whenever a new issue is reported or an existing issue changes, see the next section.

7.4.5 Issue Tracking

When developing software, it is crucially important to keep track of software bugs and other issues like feature requests formally. An issue tracking system is a tool that helps to achieve this bookkeeping by means of a database. A large variety of such tools exist,

[Wiki 13a], many of them free of charge and with an easy-to-use web interface that can be customized to the project at hand. If the issue at hand is a software bug, then, according to [Spol 00], "a minimal useful bug database must include the following data for every bug: complete steps to reproduce the bug, expected behavior, observed (buggy) behavior, who it's assigned to, whether it has been fixed or not." Issue tracking systems help to administer and to keep track of this information and to resolve the issues.

While having such a tool is helpful for any kind of software and development team, the open-source approach enables the users to file high-quality bug reports and to assist the developers in improving the code quality. The users themselves can find out the precise location of the bug and thus perform the first important step towards its removal. It is also possible that a user resolves the issue himself and provides a patch for the developers that can be directly applied to the code base. Other users can instantly profit from the improved software.

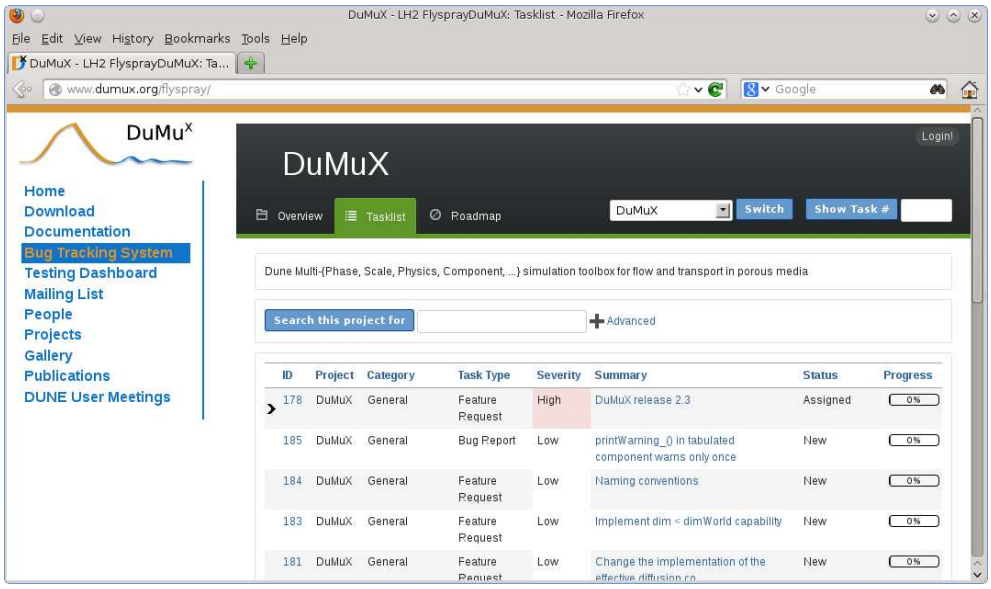

Figure 7.3: The Flyspray bug tracker of DuMu^x at `dumux.org/flyspray/`.

DuMu^x uses the bug tracking system Flyspray, `flyspray.org`, a web-based bug tracking system written in PHP and released under the GNU LGPL, [Anon 12]. The corresponding database is publicly accessible at `dumux.org/flyspray/`, see Figure 7.3. After registration, every user is able to open new issues and to contribute to existing ones. Most of the issues listed are not bug reports, but feature requests. A particularly useful possibility of the system is that each issue can be associated with an upcoming release, and a roadmap that lists the open issues for a release is created automatically.

7.4.6 Automated Testing and Dashboards

Writing and performing tests is another indispensable ingredient of sustainable software development. It is good practice to perform regression tests that seek "to uncover new software bugs, or regressions, in existing ... areas of a system after changes ... have been made to them," [Wiki 13d]. Since performing such tests manually can be a time-consuming, cumbersome and error-prone task, it is desirable to use tools for test automation. Also here,

a large variety of such tools is available, [Wiki 13e]. They facilitate the definition, building and execution of a test suite. The tests can then be performed automatically, for example at fixed time intervals or whenever a change to the code has occurred. Depending on the individual outcome, each test can then be marked as passed or failed. Since the amount of data created by building and execution of the test suite can be very large, it is highly desirable that the automation tool also provides the possibility of a suitable visualization of the test results.

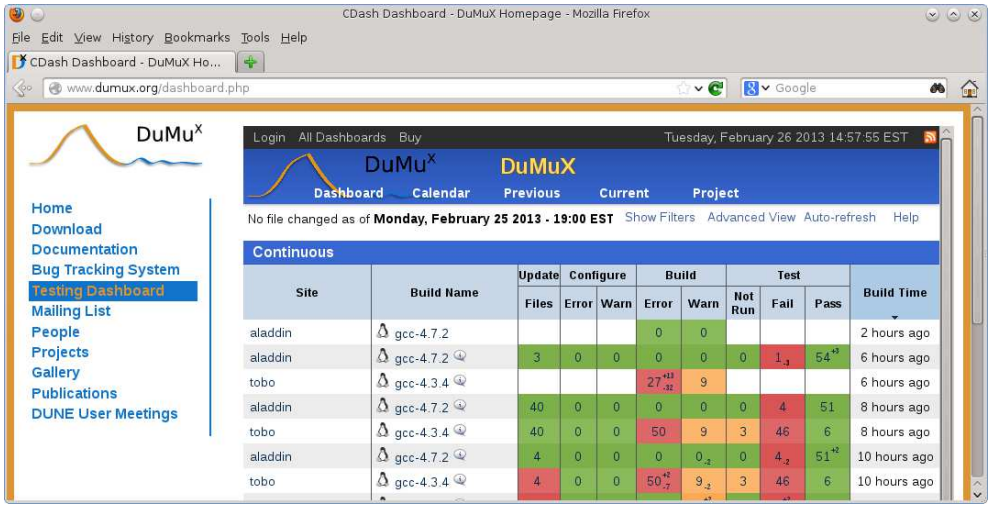

Figure 7.4: The dashboard of DuMu^x at `dumux.org/dashboard.php`.

For DuMu^x, the tests are defined with the help of the open-source build system CMake and the testing tool CTest it includes, `cmake.org`. In February 2013, the test suite contained 55 tests that covered common components like the material system and each numerical model for a selection of benchmark cases. If a numerical model is tested, a reference solution is given in the form of an output file for the visualization software Paraview, containing the values of primary and secondary model variables at each geometric position. The output file produced by a test is compared with the corresponding reference solution. If a solution value deviates from the reference value by more than a defined relative measure, the test is marked as failed. CTest takes care of updating a working copy of the Subversion repository, compiling, linking and execution of each test. It additionally can perform a code coverage analysis. The results are displayed on a public dashboard at `dumux.org/dashboard.php`, by employing the web-based software testing server CDash, `cdash.org`, see Figure 7.4. This dashboard enables each user to examine the results interactively, like displaying compilation errors or investigating the coverage of each individual source code file.

7.4.7 Project Analysis

It is a challenging task to measure the quality of an open-source project, apart from subjective user opinions. Some websites like Ohloh, `ohloh.net`, "a free, public directory of free and open-source software" offer this service. If a project is registered that offers anonymous read access to its source code repository, the code's history and ongoing updates are analyzed. It provides measures like the number of commits and committers to the project,

what programming languages are used and how the code lines are distributed among actual code, comments and blanks. Based on this and the evolution of these numbers, labels are given that provide information about, for example, the size and activity of the development team, as well as the stability of the development activity. Moreover, it provides an estimate for the cost of the project based on the Constructive Cost Model, [Boeh 81].

In February 2013, the analysis of the DuMu^x project received the labels "Very well-commented source code," "Large, active development team," "Young, but established codebase," and "Stable year-over-year development activity." The estimated programming effort amounted to 20 person years, leading to a project cost of roughly one million USD.

8 DuMu^x: an Open-Source Porous-Media Simulator

Bibliographic Note: The content of this chapter is based on the following original article [Flem 11]: B. Flemisch, M. Darcis, K. Erbertseder, B. Faigle, A. Lauser, K. Mosthaf, S. Müthing, P. Nuske, A. Tatomir, M. Wolff, R. Helmig (2011): DuMu^x: DUNE for Multi-{Phase, Component, Scale, Physics, ...} Flow and Transport in Porous Media. *Advances in Water Resources* **34**(9), pp. 1102–1112.

Summary DuMu^x is a free and open-source simulator for flow and transport processes in porous media, based on the Distributed and Unified Numerics Environment DUNE. Its main intention is to provide a sustainable and consistent framework for the implementation and application of model concepts, constitutive relations, discretizations, and solvers. This chapter provides an overview of DuMu^x with the focus on software-related aspects. Selected examples highlight the multi-scale and the parallel capabilities.

8.1 Introduction

The quality of any type of computational modeling crucially depends on the quality of the employed software framework. Research codes very often fail to be developed and maintained in a continuous manner. On the contrary, software development at academic institutions usually is highly fragmented and driven by individual short-term needs. Furthermore, work is often done redundantly, diverting resources from the original focus of research projects by a need for reinventing the wheel. We are therefore convinced that the free and open-source (FOSS) idea provides a chance for sustainable high quality software development also in academia.

DuMu^x is a simulator for flow and transport processes in porous media. It is built on top of DUNE, the Distributed and Unified Numerics Environment, a modular toolbox for solving partial differential equations with grid-based methods, [Bast 08b, Bast 08a]. DuMu^x is licensed under the terms and conditions of the GNU General Public License (GPL) version 2 or later, [GNU 91]. Stable releases are available for download, [DuMu 13], and anonymous read-access to the Subversion repository is granted.

DuMu^x includes several standard models of varying complexity, ranging from stationary isothermal single-phase single-component flow to transient non-isothermal multi-phase compositional flow. Active research is currently undertaken to include multi-scale and multi-physics concepts, as well as non-standard formulations like multiple continua approaches or models involving interfacial area as primary state variable. All models employ efficient nonlinear solvers in close combination with a sophisticated time step management. The capabilities of DUNE are heavily exploited to offer various spatial discretization schemes as well as the possibility of parallel computations. The applications currently targeted by DuMu^x include fuel cells, groundwater remediation, evaporation from partially saturated soils, CO_2 storage, and drug delivery into human tissue. Several scientists from

diverse areas of expertise (computer science, engineering, mathematics) are involved in the code development.

Various porous media simulators are under ongoing development, we list some examples in the following. Most prominently, ECLIPSE is a simulation tool used extensively in the oil and gas industry, [Schl 09]. Another commercial tool is the Generalized Equation-of-state Model compositional reservoir simulator (GEM), [Comp 06]. Finite Element Heat and Mass Transfer Simulator (FEHM) is a porous media fluid flow simulator developed by the Los Alamos National Laboratory, [Robi 00]. Stanford's General Purpose Research Simulator (GPRS) serves as a research platform for reservoir simulation, [Cao 02, Jian 07]. Integrated Parallel Accurate Reservoir Simulators (IPARS), developed at the University of Texas, is a framework for parallel models of subsurface flow and transport through porous media, [Whee 01]. OpenGeoSys is a project for the development of numerical methods for the simulation of thermo-hydro-mechanical-chemical processes in porous and fractured media, [Open 13b]. MUFTE-UG, the predecessor of DuMu^x, is capable of solving isothermal and non-isothermal multi-phase flow problems including compositional effects, [Asst 05]. The simulation code TOUGH2 was developed by researchers from Lawrence Berkeley National Laboratory, [Prue 04]. The MATLAB Reservoir Simulation Toolbox (MRST) is developed by SINTEF Applied Mathematics and is a result of their research on the development of new (multiscale) computational methodologies, [Lie 10]. The distribution and licensing policies for the listed simulators vary from proprietary commercial to open source and free of charge. From the list, only MRST is released under a GPL license from the Free Software Foundation.

This chapter is structured as follows: in the remaining part of this introduction, the vision, concept and design ideas behind DuMu^x are presented. In Section 8.2, the common base of all DuMu^x models is outlined. Section 8.3 describes the available models in DuMu^x. In Section 8.4 some examples highlighting the capabilites of DuMu^x are given. We summarize and give an outlook in Section 8.5. Concerning the notation it should be mentioned that quantities that have a direct representation within the code base of DuMu^x — be it a class name or the name of a folder containing a model — are set in `typewriter`.

8.1.1 Vision

Up to now, DuMu^x is an academic research code and thus primarily targeted towards researchers and particularly PhD students to code, test and apply new mathematical and numerical modeling approaches. Thanks to the abstraction principles employed in the DUNE framework, this can be achieved without any knowledge of the underlying detailed implementations. Still, a profound knowledge of advanced C++ programming techniques is required from the current users and developers. In the future, the capabilities of DuMu^x are expected to attract end-users, who are mainly interested in applying existing numerical models to their concrete problem at hand. For this group of users, which includes prospective bachelor and master students as well as partners from industry, it will be important to offer a framework allowing general problem descriptions and a model selection without requiring in-depth programming knowledge.

It is evident that only one research group cannot cover all aspects of the computational modeling of porous media flow and transport processes. Therefore, it is important to combine the expertise from different groups, and free and open-source software development is the most natural way to achieve a sufficiently flawless integration of individual solution components. For this purpose, DuMu^x is part of the recently funded Open Porous Media

(OPM) initiative, [Open 13a], which is dedicated to develop a simulation suite that is capable of modeling industrially and scientifically relevant flow and transport processes in porous media and to bridge the gap between the different application areas of porous media modeling.

8.1.2 Concepts and Design Ideas

Modularity is the leitmotif to design the code. DuMu^x provides shelves of modularized objects, enabling the user to choose the appropriate parts according to the problem at hand. This can be compared to somebody, who can easily grab a different shirt out of a shelf without changing the trousers and without ending up with a combination of clothes that do not match. Following that design idea, DuMu^x is meant to provide a collection of shelves each holding interchangeable alternatives, that are still fully interactive to other shelves by using common interfaces. The user is able to select each part of the implementation at each shelve through an efficient compile-time `property system` (Section 8.2.4). Part of this modular setup (see Figure 8.1) are the shelves from which to choose

- model concepts (Section 8.3),
- numerical schemes,
- control strategies for the simulation (Section 8.2.3),
- multitude of substances, material laws (Section 8.2.2),
- small and large-scale examples and applications.

A clear separation, for example, of model concepts and problem definitions, is also beneficial to maintain the software, as the repeated code is kept to a limit. When solution approaches or discretization schemes differ substantially, as for example fully-implicit and and decoupled semi-implicit solution schemes, reimplementations in the code are not yet completely avoided, which increases the workload in case of a change in program interfaces.

Furthermore, the following design principles are of high importance:

1. Like DUNE, DuMu^x is coded in C++ and employs high-level generic programming techniques. The design principles guiding the DUNE development, see Section 8.2.1, are also closely followed within DuMu^x.

2. The whole project is free and open source, and fully available to the public. By this, the project is open to all kinds of participation from different areas of expertise, which attracts new streams of ideas to improve DuMu^x.

3. A framework of this size (several 100,000 lines of code) has to be in good maintenance requiring a sound infrastructure: a common repository with a version control system through Subversion (SVN), [Apac 13], an online bugtracking and feature request system, [Anon 12], and the regular submission of build and test results to a dashboard, [CDas 13].

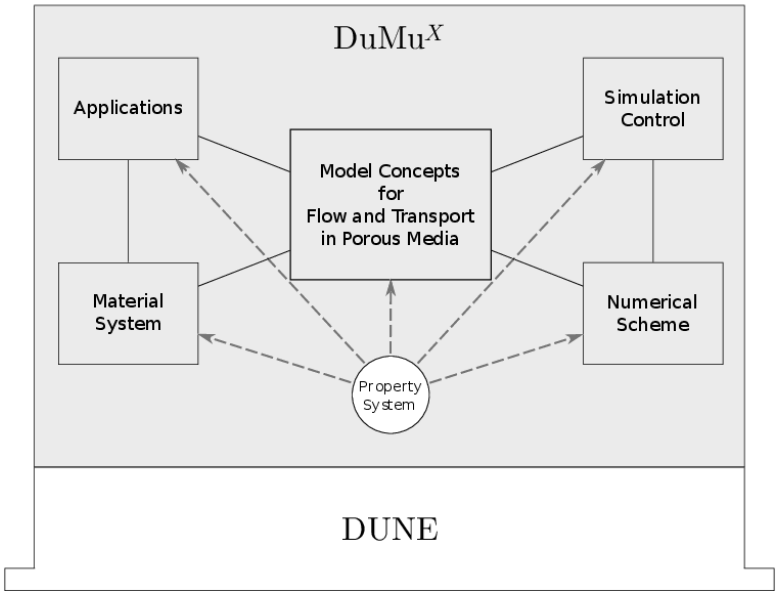

Figure 8.1: Modular design of DuMu^x.

8.2 The Backbone of DuMu^x

This section deals with the common structures employed by most DuMu^x models. Most prominently, these are the grid, solver and discretization interfaces provided by the DUNE framework described in Subsection 8.2.1. Of crucial importance for the ability to solve real life porous media flow problems is a flexible and extendable material system, introduced in Subsection 8.2.2, as well as a sophisticated simulation control, which is outlined in Subsection 8.2.3. Finally, we propose a convenient alternative to traits classes in Subsection 8.2.4.

8.2.1 DUNE

DUNE, the Distributed and Unified Numerics Environment, is a modular toolbox for solving partial differential equations with grid-based methods, [Bast 08b, Bast 08a]. To quote from [DUNE 13]:

> The underlying idea of DUNE is to create slim interfaces allowing an efficient use of legacy and/or new libraries. Modern C++ programming techniques enable very different implementations of the same concept (i.e. grids, solvers, ...) using a common interface at a very low overhead. Thus DUNE ensures efficiency in scientific computations and supports high-performance computing applications. DUNE is based on the following main principles:
>
> - Separation of data structures and algorithms by abstract interfaces.
> - Efficient implementation of these interfaces using generic programming techniques.
> - Reuse of existing finite element packages with a large body of functionality.

DUNE is organized as a modular system. The current release 2.0 includes the core modules dune-common (basic classes), dune-grid (grid interface and implementations), dune-

istl (iterative solver template library), and dune-localfunctions (interface for finite element shape functions). In addition to these, DuMu^x also uses the DUNE external module dune-pdelab, which provides a large variety of finite element function spaces, global assembly of residuals and operators, linear and nonlinear solvers as well as explicit and implicit time discretizations based on the method of lines approach, [Bast 10]. Moreover, for the multi-scale and multi-physics approaches, the external module dune-multidomaingrid is employed, which supplies a meta grid allowing the division of a given grid into separate sub-domains, [Muth 12].

The use of DUNE as basis on which DuMu^x is built on (Figure 8.1) offers several advantages. The most important one is the ability to use a wide range of different grid implementations and several linear solvers without having to care about the underlying data structures of the individual implementations. This particularly includes capabilities like parallelism and adaptivity, which comes at minimal additional programming cost for the user. Thus, the main part of the development of DuMu^x can concentrate on the implementation of physical and mathematical models. The key modules of DuMu^x (Figure 8.1) are introduced in the following subsections.

8.2.2 Material System

The biggest challenges in porous media simulation are the possibly highly heterogeneous distribution of parameters and the complex nonlinear material laws. The DuMu^x material system constitutes a framework that allows a convenient definition and usage of parameters and material laws. Due to the strong interconnection of these properties, it proves difficult to achieve modularity. Nevertheless, it is possible to achieve a modular structure by a separation into the following parts.

`Components` The term component stands for constituents of the phases, which can be associated with a unique chemical species, or, more generally, with a group of species exploiting similar physical behavior. Each component is implemented as a class consisting primarily of static member functions describing the physical properties of the component. This ranges from simple constants like the molar mass to possibly very complex functional relationships like the density depending on pressure and temperature.

`FluidSystems` A `FluidSystem` describes the properties of the participating fluid phases. This includes phase densities and viscosities as well as fugacities and diffusion coefficients of components inside phases, where each phase may consist of one or more components. The properties of the fluid phases usually depend on their current composition, which is described in a separate object of type `FluidState` containing the saturation and mole fraction values. A `FluidSystem` is implemented in the same way as a `Component`.

`FluidMatrixInteractions` This part collects the material laws, which are necessary for the description of the interaction of the fluid phases with the porous medium, i.e. capillarity and relative permeability. A collection of standard laws is provided, including, for example, van Genuchten and Brooks–Corey. For our extended model concepts, elaborate interfacial area - capillary pressure - saturation – relationships are included as well as standard hysteresis models. Through modular adapters, regularization schemes can be imposed

for extreme values. Each material law uses a set of appropriately definable parameters of type `MaterialLawParams`, which may depend on the location inside the domain.

`SpatialParameters` This part collects all parameters that may vary depending on the location within the porous medium. It admits a local assignment of purely intrinsic properties like porosity, permeability, or heat capacity as well as of the aforementioned parameters for the material law.

8.2.3 Simulation Control

Two standard approaches for the solution of porous media problems exist: a coupled fully-implicit approach and a decoupled semi-implicit approach. The fully-implicit approach discretizes the original coupled balance equations by an appropriate method in space and by an implicit method in time. The decoupled approach manipulates the balance equations towards one equation for the pressure and one or more equations for transport (of phases, components, energy, etc.), where the pressure equation is solved implicitly while the transport equations are solved explicitly. Other approaches like, for example, iterated fully implicit, are currently not available.

In DuMu^x, both the coupled fully-implicit and the decoupled semi-implicit models use the same code for the time-step control: The temporal domain is first divided into episodes, defined as time periods where boundary conditions, source terms and material parameters are differentiable with respect to time. Simulation time is then advanced by the minimum of the time-step size suggested by the underlying numerical model or the time span until the end of an episode. For the coupled fully-implicit models, the time-step size is controlled based on the number of iterations required by the Newton method to achieve convergence for the last time integration: The time-step size is reduced, if the number of iterations exceeds a specified threshold, whereas it is increased, if the method converges within less iterations. This ability to cut the time step is crucial to overcome convergence problems and guarantee robustness. The main influential parameters are the threshold value for the Newton convergence and how it is determined, and the factors for increasing and decreasing the time-step size. While a default implementation for each numerical model is available, these parameters can be changed to be problem-specific. For the decoupled models, the time-step size is calculated by CFL-like criteria.

8.2.4 Property System

On the one hand, DuMu^x modules can be freely combined, on the other hand, dynamic polymorphism is avoided for reasons of performance. Thus, a consistent set of parameters has to be provided throughout the module hierarchy at compile time. Examples for such parameters are the classes including the problem description, where initial and boundary conditions are typically defined on the highest level of the class hierarchy but are required by the code of the low-level spatial discretization.

Many such parameters are typically necessary and providing all of them as C++ template parameters would be very cumbersome and error-prone. One option is to use traits classes. In this approach a class hierarchy is created where each level stores the parameters required by the corresponding level of abstraction. A fundamental problem with this approach is the inability to change parameters of low levels at higher levels. This is because the

parameters may be defined only using those of lower levels in the traits hierarchy. This problem is illustrated by the following simple example:

```
struct MyBaseTraits {
  typedef int Scalar;
  typedef std::vector<Scalar> Vector;
};
struct MyDoubleTraits : public MyBaseTraits {
  typedef double Scalar;
};
int main() {
  MyDoubleTraits::Vector v{1.41421, 1.73205};
}
```

Contrary to what is intended, `v` is a vector of integers. This problem can also not be solved using static polymorphism, since it would lead to a cyclic dependency between `MyBaseTraits` and `MyDoubleTraits`.

To remedy this, the DuMu^x property system has been developed based on the C++ template specialization mechanism. In this system, a hierarchy of nodes – called type tags – is defined. Then all parameters are labeled and attached to the appropriate nodes in this acyclic graph. The labels are called property tags, whereas the parameters actually attached are called properties. The definition of properties may depend on arbitrary other properties, which may be overwritten at any higher node of the acyclic graph. The only requirement for properties is that they may not exhibit cyclic dependencies. The above example transforms as follows:

```
NEW_TYPE_TAG(BaseTag);
SET_TYPE_PROP(BaseTag, Scalar, int);
SET_TYPE_PROP(BaseTag, Vector,
    std::vector<GET_PROP_TYPE(BaseTag, Scalar)>);

NEW_TYPE_TAG(DoubleTag, INHERITS_FROM(BaseTag));
SET_TYPE_PROP(DoubleTag, Scalar, double);

int main() {
  typedef GET_PROP_TYPE(DoubleTag, Vector) Vector;
  Vector v{1.41421, 1.73205};
}
```

Now `v` is a vector of doubles as intended.

8.3 Models

This section describes the models currently implemented in DuMu^x. In Table 8.1, an overview of the available models is given. They can be chosen – largely independent from the problem description – according to the task at hand. The individual models will be described in further detail here. As outlined above, we distinguish between decoupled semi-implicit and coupled fully-implicit approaches. Furthermore, a brief sketch of the multi-scale and multi-physics capabilities is given. The following nomenclature will be

Table 8.1: Currently available models within DuMu^x. With `p` standing for phase, `c` for component, `ni` for non-isothermal and `ia` for interfacial area.

	coupled fully-implicit	**decoupled semi-implicit**
Standard	`1p, 1p2c, 2p, 2pni, 2p2c, 2p2cni, Richards`	`1p, 2p, 2p2c, 2p2cni, 3p3c`
Extended	`2pia, 2p2cia, 2pNc, linear-elasticity 2pDFM, 2pMINC, 1DPipe3DPorousFlow, 1p2cDoubleContinuum`	
	`multiscale, multiphysics`	

used from this point on: `p` stands for phase, `c` for component, `ni` for non-isothermal and `ia` for interfacial area.

We note that the fully-implicit models are modularized with as little code replication as possible. A model can be given in terms of physical quantities like storage, flux and source terms. Non-isothermal models inherit from isothermal ones and basically only add the energy equation. For the decoupled models, this strong modularization has not been achieved yet and is subject of future work.

8.3.1 Decoupled Semi-Implicit Numerical Models

As already described above, decoupled models solve a system of equations in which the single equations are only weakly coupled with each other. Thus, a sequential solution strategy can be applied where the standard scheme for multi-phase flow in porous media is an IMPES/IMPEC algorithm (IMplicit Pressure Explicit Saturation/Concentration). IMPES/IMPEC schemes first implicitly solve a pressure equation to get the flow field. Afterwards, the transport equations can be solved explicitly in the simplest case by using an explicit Euler scheme.

`1p` This model solves an elliptic pressure equation in a fully-saturated porous medium. Available discretization methods are: Cell-centered finite volumes with TPFA (Two-Point-Flux-Approximation), or with MPFA (Multi-Point-Flux-Approximation, [Aava 02]), and mimetic finite differences, [Flem 08].

`2p` Formulations for immiscible isothermal two-phase flow are implemented as classical fractional flow formulation (incompressible, for example, [Binn 99]) or decoupled phase pressure formulation (slightly compressible/incompressible, see for example, [Chen 06c]). Transport equations for saturation are discretized by cell-centered finite volumes, for the solution of the pressure equations various discretization methods (see `1p` model) are available. An IMPES strategy is applied.

`2p2c/ni` Miscible compressible two-phase flow can be modeled isothermally (`2p2c`) as well as non-isothermally (`2p2cni`). Capillary pressure is at the stage of this publication

neglected. Instead of saturation equations, transport equations for concentrations of the components (`2c` - two components) are solved and flash calculations are performed afterwards to determine the phase composition. Details on the formulation can be found in [Frit 12]. Both pressure and transport equations for concentrations are discretized by cell-centered finite volumes, and an IMPEC scheme is used for the solution of the system.

`3p3c` This model for three-phase three-component flow and transport is similar to the `2p2c` model.

8.3.2 Coupled Fully-Implicit Numerical Models

We provide brief descriptions of standard and extended models treated in a coupled fully-implicit manner.

Standard models The standard coupled models can be subdivided into several groups. It can be distinguished between the phase-based formulations (`1p`, `2p` and `2pni`) and the component-based models (`1p2c`, `2p2c`, `2p2cni`). Further, thermal effects can be taken into account (non-isothermal models: `2pni`, `2p2cni`). In general, a modular structure is used and the models with a higher complexity inherit the functionality from the simpler ones and extend it accordingly. As spatial discretization, a vertex-centered finite volume scheme (box method, [Hube 00]) is used. So far, the implicit Euler scheme is applied for the temporal discretization.

`interfacial area` Usually, flow and transport in the bulk phases is modeled using the assumption of local thermodynamic equilibrium. The interfacial area models (abbreviated `2pia` and `2p2cia`) extend this approach by incorporating flow and evolution of the area separating the fluid phases [Nies 09]. This enables the description of kinetic mass and energy transfer between the fluid phases (thermal and chemical non-equilibrium). A natural description of hysteresis in the capillary pressure – saturation relationship is envisaged.

`linear-elasticity` In the case of large pressure gradients the assumption of a rigid porous medium might be violated. The linear-elasticity models account for the deformation of the solid matrix and its interaction with a single- or two-phase flow system based on the theory of [Biot 55]. A first application of the DuMu^x single-phase linear-elasticity model is described in [Stov 12].

`2pNc` In general it is desirable not to write a new model whenever an additional component is to be modeled. This, as well as the general prevention of switches in the primary variables – in the case of one phase disappearing – are the distinctions of the 2Nc model, with `Nc` standing for N-number of components .

`2pDFM` The model simulates the two-phase flow in fractured porous systems using a discrete fracture model (DFM) approach [Berk 02], with a lower dimensional representation for the fractures [Reic 06]. The representative fracture network of the DFM is reconstructed with a geostatistic fracture generator [Asst 08].

`2pMINC` In contrast to the `2pDFM`, this model does not discretize the fractures but simulates the two-phase flow in fractured porous media using the MINC method [Prue 85], [Prue 92].The fractures are treated as an equivalent homogeneous porous medium, which requires the determination of appropriate effective parameters and transfer functions between continua, but reduces considerably the geometrical complexity of the problem, see Figure 8.2a.

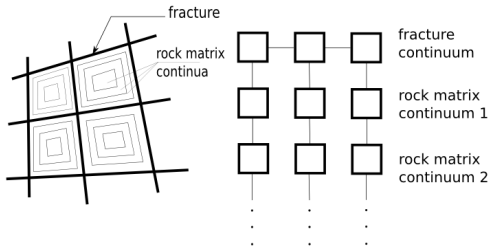

(a) MINC discretization of a fractured porous system

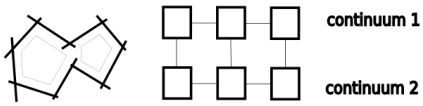

	2pDFM	1p2cDouble Continuum	1DPipe3D PorousFlow
cont. 1	Discrete Fracture System	Capillary blood vessels	Pipe System
cont. 2	Rock Matrix Continuum	Biological Tissue	Rock Matrix Continuum

(b) Example of a double-continuum discretization for various applications

Figure 8.2: Sketch of the relation between model concepts and the continuum representation. Schematic diagrams of connectivity for the continuum models

`1p2cDoubleContinuum` It models the flow, transport and reaction processes through the terminal vascular bed (capillary vessels) and the surrounding biological tissues as an application to pulmonary cancer therapy. This is done by using the 1p2c model concept, where both the capillary vessels and the surrounding tissue are described as two interacting porous media.

`1DPipe3DPorousFlow` It simulates a coupled flow and transport system composed of quasi one-dimensional hollow structures embedded into a 3D porous medium [Doga 09]. The hollow structures are expressed with the cross-sectionally averaged one-dimensional pipe flow equation, like Hagen-Poiseuille, whereas for the flow within the porous medium the Darcy law is used.

The `2pDFM`, `1p2cDoubleContinuum`, and `1DPipe3DPorousFlow` models use the coupling strategy of a standard double-continuum approach, that is, the exchange terms between the two continua are implemented by additional source/sink terms, see Figure 8.2b.

8.3.3 Multi-Scale and Multi-Physics Models

The modular concept of DuMu^x allows the combination of the single models described before in multi-scale and/or multi-physics concepts. Multi-scale methods combine simulations on different length or time scales dependent on the processes that are to be modeled and on the information available. In DuMu^x, this can be done in the context of classical numerical upscaling (or downscaling) methods (for example, permeability upscaling) or in combination with multi-physics strategies. In space, multi-physics can be volume coupling (see for example, multi-continuum models) or surface coupling of different model domains depending on the occurring processes that dominate in a sub-domain. In time, it could

be a sequential solution strategy, where the model type is switched if the dominating processes change. The idea of both multi-scale and multi-physics methods is to be able to model complex processes occurring in large model domains. Examples on the capabilities of DuMu^x concerning multi-scale and multi-physics ideas can be found in Section 8.4.

8.4 Selected Examples

We present two examples that demonstrate the capabilities of DuMu^x for applications, relevant for the simulation of multi-phase flow in porous media. The multi-scale example presents an approach allowing the coarse-scale description of flow and transport in a fine-scale heterogeneous domain. This is accomplished by exploiting the capabilities of DUNE and DuMu^x for handling grids on multiple scales and solving small flow problems in order to incorporate the influence of sub-scale heterogeneities on the coarse scale.

Many real life applications require large modeling domains on the one hand and high model complexity on the other hand. Typically, this results in computationally demanding tasks. Therefore, the second example focuses mainly on the parallelization of code, which comes at little additional effort to the programmer. Furthermore, it is shown that the single models (described in Section 8.3) can be applied sequentially.

8.4.1 Multi-Scale

The multi-scale framework of DuMu^x is a general framework for implementation of local(-global) upscaling (downscaling) methods. The term local(-global) method is not used in the context of a special implementation, but in a more general sense. It means that local flow simulations are carried out in subdomains much smaller than the global domain and on any scale. These can be decoupled from the global solution (local method) or coupled to the global solution (local-global method). The local fine-scale simulations are numerical experiments to estimate effective parameters, which can be used in global coarse-scale simulations (for example, grid block permeability upscaling methods [Durl 91, Wen 03], etc.). Alternatively, the local solutions can be directly used to adjust the coarse scale fluxes (for example, interblock transmissibility upscaling methods [Chen 03a, Chen 06a], etc.). In the following, two scales are considered. The term fine-scale is used for the scale of the finest heterogeneities that are accounted for (*Darcy*-scale on which the previously described models (Section 8.3) are valid), whereas the term coarse-scale indicates the scale to which an upscaling is applied.

One basic idea of the general framework is that any of the fine-scale models, which are available in DuMu^x, can be chosen for the local calculations without any changes in these model implementations. A second idea is that different kinds of post-processing routines, which calculate the effective parameters, are implemented once, and can be easily reused as well as combined in different kinds of local(-global) upscaling methods. Thirdly, depending on the upscaling approach one of the fine-scale model implementations could also be used on the coarse scale (with different parameters) or new coarse-scale models can be implemented, which again might be combined respectively with the different fine-scale and post-processing methods. Figure 8.3 shows the general flow of a local(-global) multi-scale simulation in DuMu^x. In the following paragraphs, we describe the conceptual and the mathematical model for one exemplary implementation of a local upscaling method and show some results.

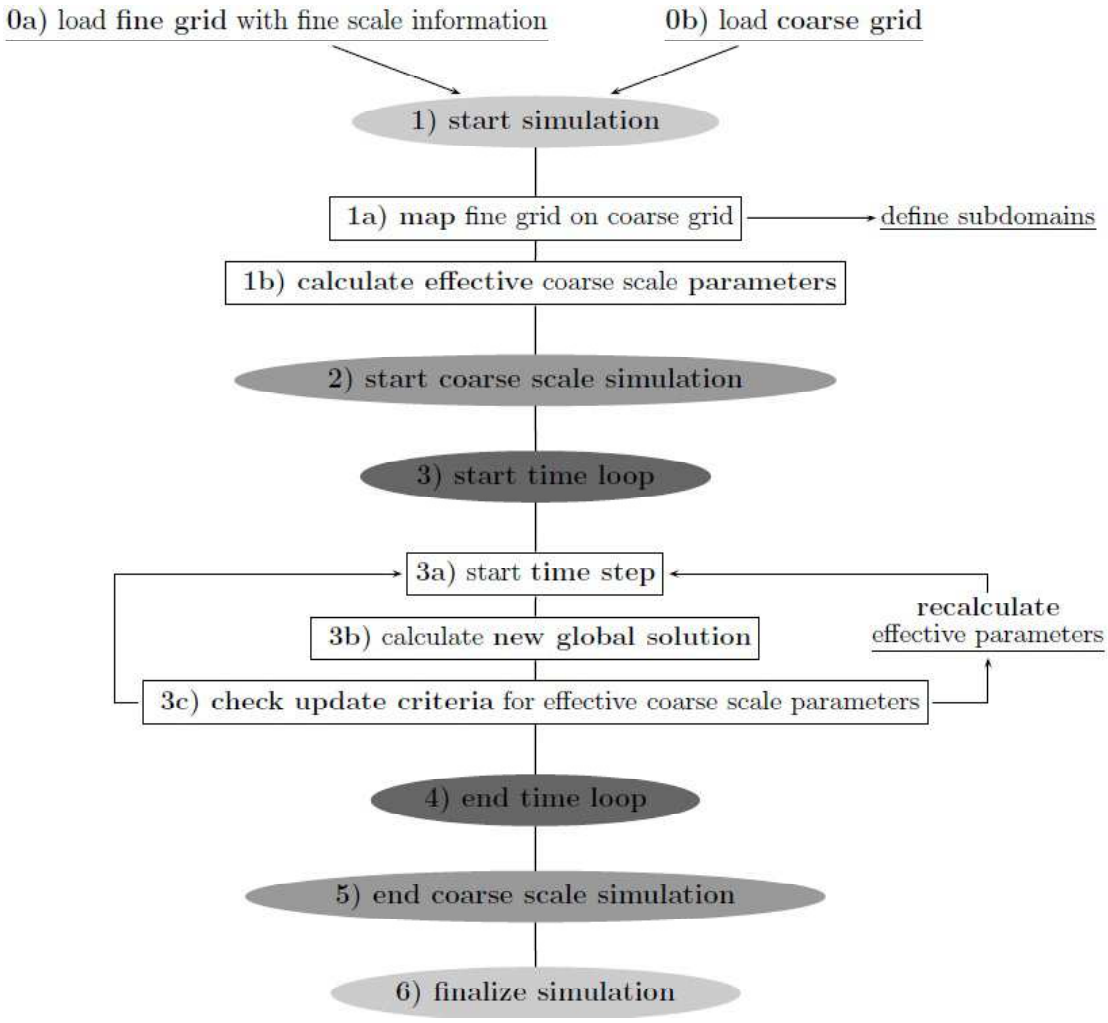

Figure 8.3: Flow of a multi-scale simulation in DuMu^x.

Conceptual Model The example shown here is a local intrinsic permeability upscaling method (see for example, [Durl 91, Wen 03]), where a heterogeneous fine-scale permeability field is assumed to be known. It divides the global model domain into sub-domains assigned to coarse grid blocks (Figure 8.3, 1a)). The grids for the single sub-domains are managed using the DUNE module `dune-multidomaingrid` [Muth 12]. Effective coarse-scale intrinsic permeabilities are calculated for every coarse grid block using the results of local fine-scale simulations. As the fine-scale intrinsic permeability field is not dependent on saturation or pressure if the porous matrix is rigid, it is possible to calculate effective permeabilities that are also independent of the coarse-scale pressure and saturation field. This can be done in a preprocessing step (Figure 8.3, 1b)). After the preprocessing the global coarse-scale simulation can be directly started using the newly calculated effective intrinsic permeabilities (Figure 8.3, 2)). If an adaptive local-global approach is used in which effective permeabilities are updated depending on the flow field, a criterion which triggers the recalculation has to be checked at the end of every time step (Figure 8.3, 2c)). In the example below, a full tensor effective intrinsic permeability is calculated only once in a preprocessing step.

Mathematical Model An isothermal incompressible two-phase flow model is used in a decoupled formulation (decoupled - 2p) and in the simplest form, neglecting capillary pressure as well as gravity. The following equations have to be solved:

$$\operatorname{div}\left(-\lambda_{\mathrm{t}}\mathbb{K}\,\mathbf{grad}\,p_{\mathrm{w}}\right) = \sum_{\alpha} q_{\alpha}, \quad \alpha \in \{\mathrm{w}, \mathrm{n}\}, \tag{8.1}$$

$$\phi\frac{\partial S_{\mathrm{w}}}{\partial t} + \operatorname{div}\left(-\lambda_{\mathrm{w}}\mathbb{K}\,\mathbf{grad}\,p_{\mathrm{w}}\right) = q_{\mathrm{w}}, \tag{8.2}$$

where $\mathbb{K}$ is the intrinsic permeability, ϕ is the porosity, λ_{α} is the mobility of phase α and $\lambda_{\mathrm{t}} = \sum_{\alpha} \lambda_{\alpha}$ is the total mobility, p_{w} is the pressure of the wetting phase, S_{w} is the saturation of the wetting phase, and q_{α} is the source or sink term of phase α. Equation 8.1 is called pressure equation and Equation 8.2 is called saturation equation. The same set of equations is used for both, fine scale and coarse scale, while effective (upscaled) coefficients are used on the coarse scale (e. g. $\mathbb{K} = \mathbb{K}_{\mathrm{eff}}$, see [Wen 03]).

Upscaling Results The models of this example are discretized by a cell-centered finite volume method. To account for the full tensor permeabilities a MPFA o-method is used (see [Aava 02], [Eige 05]) for discretization of the pressure equation. The setup of the simple test-example (2-D) is shown in Figure 8.4a. The computational domain is the

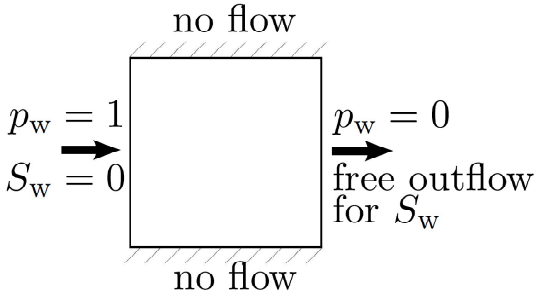

(a) boundary conditions

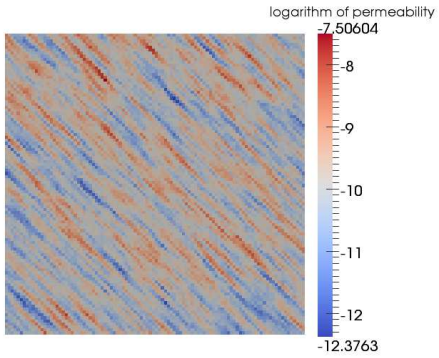

(b) logarithmic intrinsic permeability distribution

Figure 8.4: Setup of the multi-scale simulation example.

unit square. The heterogeneous permeability field (Figure 8.4b) is randomly generated by the open-source tool GSTAT [Pebe 98], which can be used for geostatistical modeling. A uniform fine grid of 100×100 elements is used, while the coarse grid consists of 10×10 elements. Quantities other than intrinsic permeabilities are assumed to be homogeneous over the entire model domain and not included in the upscaling procedure. The relative permeabilities are linear functions of saturation and we assume a constant porosity of 0.2. Initially, the domain is fully water-saturated, and replaced by oil from the left. The result of the coarse-scale simulation is shown in Figure 8.5b and shows good agreement with the fine-scale reference solution depicted in Figure 8.5a. Even for the quite simple and small test problem a significant speed-up of the multi-scale model ($>$ factor 40) can be achieved. Since the emphasis of this example is not to discuss the quality of existing and well established upscaling methods, but to show that they can be easily implemented and used within the DuMu$^{\mathrm{x}}$ multi-scale framework, we refer to [Wolf 13b] for details.

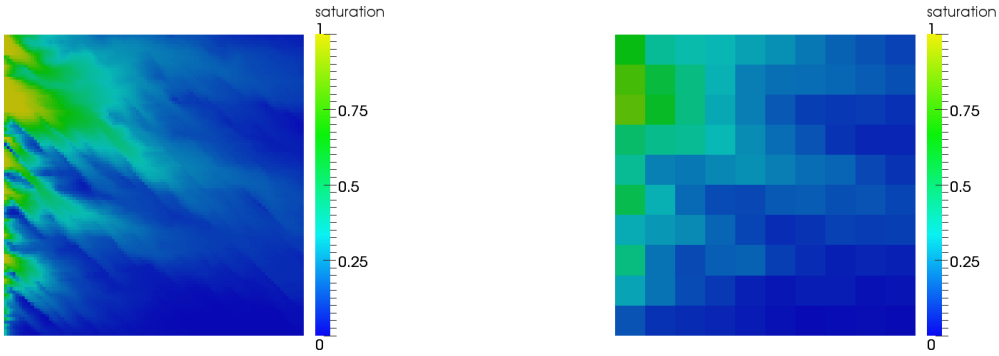

(a) fine-scale reference

(b) coarse-scale solution (permeability upscaling method)

Figure 8.5: Saturation distribution at $t = t_{end}$.

8.4.2 CO_2 Storage – A Large Scale Example

As a large scale application example, the injection of CO_2 into a heterogeneous saline aquifer is modeled with DuMu^x. The geometry and the hydraulic parameters are chosen according to the Benchmark Problem 3.1 given in [Clas 09]. The model domain and the position of the injection well are shown in Figure 8.6. The domain has lateral dimensions of 9,600 m × 8,900 m and a varying thickness of 90 m to 140 m. The fault within the aquifer is assumed to be an infinitely permeable fault and is included as a Dirichlet boundary with hydrostatic pressure and geothermal temperature distribution. The same holds for the remaining lateral boundaries. On top and on the bottom Neumann no-flow boundary conditions are assigned. The heterogeneous permeability and porosity fields applied here

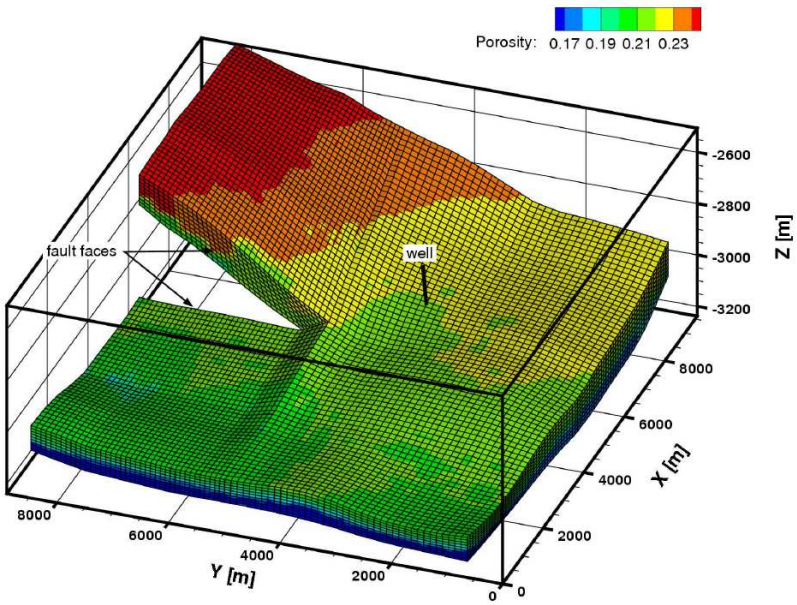

Figure 8.6: Aquifer geometry and porosity distribution of the Benchmark Problem 3.1 given in [Clas 09]. The aquifer lies in a depth between 2,500 m and 3,200 m, the position of the injection is x = 5,440 m and y = 3,300 m.

are given in the benchmark study for a mesh with a resolution of approximately 100 m

in lateral direction and 15 m in vertical direction leading to 62,800 vertices in total. The remaining aquifer properties are listed in Table 8.2.

CO_2 is injected for 25 years with a rate of 15 kg/s over the bottom 50 m of the vertical injection well (Fig. 8.6). The temperature of the injected CO_2 is 80°C. After the injection stop, the migration of the CO_2 plume is modeled for another 25 years. We present the conceptual and the mathematical model as well as some results in the following paragraphs.

Table 8.2: Aquifer properties given in the Benchmark Problem 3.1 [Clas 09].

property	**value**
residual brine saturation S_{rw}	0.2
residual CO_2 saturation S_{rn}	0.05
relative permeability	Brooks and Corey [Broo 64]
capillary pressure	Brooks and Corey [Broo 64]
entry pressure	10^4 Pa
Brooks-Corey parameter λ	2.0
initial temperature at 3000 m depth	100°C
geothermal temperature gradient	0.03
brine salinity	0.1 kg/kg

Conceptual Model In order to reduce the computational effort, the simulation of the injection and post-injection period is performed with a sequentially coupled model. Sequential model coupling can be applied if the dominating physical processes change over time. With respect to CO_2 storage it is possible to distinguish such different time periods. The injection period is governed by viscous and buoyancy driven multi-phase flow processes, which are hardly influenced by compositional processes such as CO_2 dissolution, diffusion and density-driven convection. After injection stop, the compositional effects become increasingly important and finally dominate the flow processes.

The sequential model applied here consists of two standard coupled fully-implicit models (Section 8.3.2). The injection period is simulated with a two-phase model (`2pni`) and the post-injection period is simulated with a more complex two-phase, two-component model (`2p2cni`). Both models include an energy balance equation to take into account non-isothermal effects such as the cooling caused by the CO_2 injection temperature, which has an influence on the fluid properties and in the post-injection period also on the compositional processes.

Due to the modular structure of DuMu$^{\mathrm{x}}$ the setup of a sequential model only requires the implementation of a suitable interface, which allows a reasonable transfer of the primary variables between the coupled models. For more details on sequential model coupling in general, its application for the simulation of CO_2 storage and the obtained speed-up factor, the reader is referred to [Darc 11].

Mathematical Model In the model of the first time period (`2pni`), the following mass balance equation is solved for both the wetting brine phase w and the non-wetting CO_2

phase n,

$$\phi \frac{\partial(\varrho_\alpha S_\alpha)}{\partial t} - \operatorname{div}\left(\varrho_\alpha \lambda_\alpha \mathbb{K}(\mathbf{grad}\, p_\alpha - \varrho_\alpha \mathbf{g})\right) = q_\alpha, \quad \alpha \in \{\mathrm{w}, \mathrm{n}\}. \tag{8.3}$$

Here, ϱ_α represents the phase densities. Additionally, the energy balance equation of the fluid-solid mixture is solved to describe the non-isothermal processes. Assuming local thermal equilibrium, the energy balance equation can be written as

$$\begin{aligned} &\phi \frac{\partial\left(\sum_\alpha \varrho_\alpha u_\alpha S_\alpha\right)}{\partial t} + (1-\phi)\frac{\partial(\varrho_\mathrm{s} c_\mathrm{s} T)}{\partial t} \\ - &\sum_\alpha \operatorname{div}\left(\varrho_\alpha h_\alpha \lambda_\alpha \mathbb{K}\left(\mathbf{grad}\, p_\alpha - \varrho_\alpha \mathbf{g}\right)\right) - \operatorname{div}\left(\lambda_\mathrm{pm}\, \mathbf{grad}\, T\right) = q_h, \end{aligned} \tag{8.4}$$

including a summation over the phases $\alpha \in \{\mathrm{w}, \mathrm{n}\}$. T is the temperature, u_α and h_α stand for the internal energy and the enthalpy of the fluid phases. The density ϱ_s and the heat capacity c_s are properties of the rock matrix and λ_pm is the saturation-dependent thermal conductivity of the porous medium. To close this system of equations, the following auxiliary conditions are applied:

$$\sum_\alpha S_\alpha = 1 \quad \text{and} \quad p_\mathrm{w} = p_\mathrm{n} - p_\mathrm{c}(S_w), \tag{8.5}$$

with the primary drainage capillary pressure p_c.

The model of the second time period (`2p2cni` model) solves compositional mass balances for the components CO_2 and brine. Brine is a pseudo-component and represents water with a certain salinity. The component mass balances are described by

$$\begin{aligned} &\phi \frac{\partial(\sum_\alpha \varrho_\alpha X_\alpha^\kappa S_\alpha)}{\partial t} - \sum_\alpha \operatorname{div}\left(\varrho_\alpha X_\alpha^\kappa \lambda_\alpha \mathbb{K}(\mathbf{grad}\, p_\alpha - \varrho_\alpha \mathbf{g})\right) \\ - &\sum_\alpha \operatorname{div}\left(\mathbb{D}^\kappa_{\alpha,\mathrm{pm}} \varrho_\alpha\, \mathbf{grad}\, X_\alpha^\kappa\right) = \sum_\alpha q_\alpha^\kappa, \qquad \kappa \in \{\text{brine}, \mathrm{CO_2}\}. \end{aligned} \tag{8.6}$$

Here, X_α^κ is the mass fraction of the component κ, $\mathbb{D}^\kappa_{\alpha,\mathrm{pm}}$ is the porous medium diffusion coefficient and q_α^κ is the source or sink term of the component κ in the phase α. The energy equation of the `2p2cni` model is similar to Equation (8.5), but the phase enthalpies and internal energies are functions of the dissolved components in addition to pressure and temperature. Besides the equations given in (8.5), a further auxiliary condition needs to be fulfilled for each phase in the `2p2cni` model:

$$\sum_\kappa X_\alpha^\kappa = 1. \tag{8.7}$$

The fluid properties of CO_2 are calculated as functions of pressure and temperature. The properties of brine additionally depend on the salinity, and in the compositional model, on the CO_2 mass fraction. The mutual solubilities of water and CO_2 are calculated according to [Spyc 05]. For further information on the fluid property functions, the reader is referred to [Biel 06].

Results The large scale simulation is performed on a grid with 469,813 vertices leading to 1,409,439 degrees of freedom. The permeability and porosity values, which are only given for the coarse grid (62,800 vertices) in the benchmark study, are transferred to the fine grid by linear interpolation. For the parallelization of the DuMu^x models, almost no additional implementation work is required, since DUNE provides arbitrary data decomposition in a generic way and the employed assembly operator from dune-pdelab and linear solvers from dune-istl are designed correspondingly. To test the parallel scaling a simulation on one core is required representing the reference value. Since this is not feasible with the fine grid due to time constraints, the parallel scaling tests are carried out for the coarse grid.

Figure 8.7 shows the resulting CO_2 saturation distribution for the fine grid after 25 years (injection period) and after 50 years. The simulation results fit into the range of the results given in the benchmark study [Clas 09]. In Table 8.3, the computation time, the average

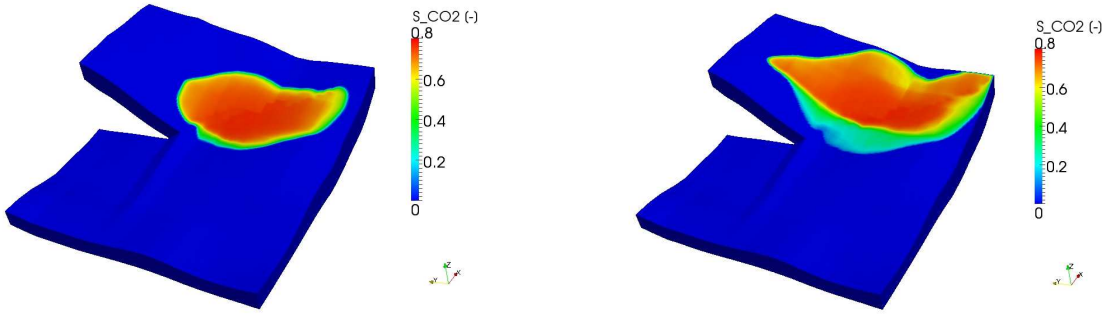

(a) CO_2 plume after 25 years (b) CO_2 plume after 50 years

Figure 8.7: CO_2 saturation distribution after 25 years (end of the injection period) and after 50 years.

time required for assembling per time step and the average time required by the linear solver per time step are given for simulations on 32 and 64 cores. The ratios indicate the

Table 8.3: Computation time, average time required for assembling per time step and average time required by the linear solver per time step for the fine grid simulations on 32 and 64 cores.

cores	**time [s]**	**ratio**	**assembly [s]**	**ratio**	**solver [s]**	**ratio**
32	492,509	-	57.60	-	579.84	-
64	323,760	1.52	28.55	2.02	393.35	1.47

time needed for 32 cores divided by the time needed for 64 cores, thus, a value of 2 would correspond to perfect linear scaling. While this can be achieved for the assembly part, the overall performance is dominated by the one of the linear solver which does not scale very well. Nevertheless, the overall gain in computation time still justifies the usage of more processes.

A more detailed description of the parallel performance is based on the coarse grid and given in the Figures 8.8 - 8.10. In Figure 8.8a, the computation time for the simulation of the benchmark problem is plotted against the number of cores applied in each simulation. The

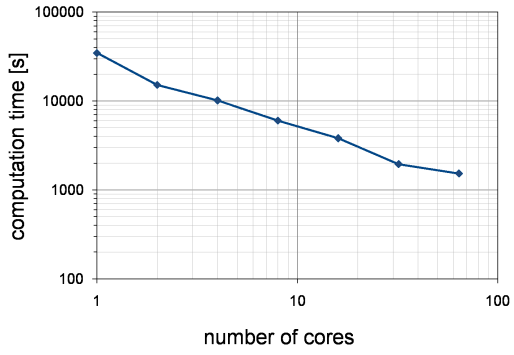

(a) Computation time

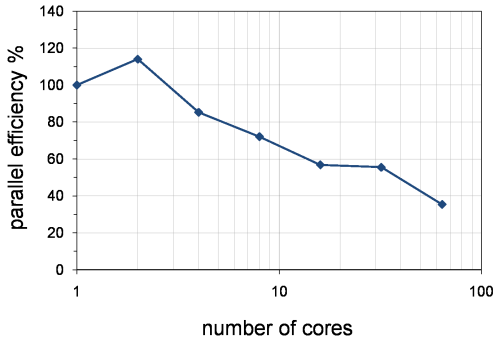

(b) Parallel efficiency – computation time

Figure 8.8: Computation time for the simulation of the Benchmark Problem 3.1 versus number of cores (a) and parallel efficiency (b).

computation time is decreasing for an increasing number of cores. The parallel efficiency, which is shown in Figure 8.8b, is the product of the computation time and the number of cores divided by the computation time of the simulation on one core. For two cores the parallel efficiency increases above 100%. One reason for this behavior could be the fact that the performance of the applied scheme is very sensitive to the amount of available cache. For the simulation on two cores, the available cache is doubled and thus the parallel efficiency increases. However, for more than two processes, we observe that the parallel efficiency decreases for an increasing number of cores.

In order to investigate this further, the two main parts, namely matrix assembly and linear solver, are examined separately. Figure 8.9a illustrates the average time required per time step for assembling the global stiffness matrix with respect to the number of cores applied in each simulation. For an increasing number of cores the assembling time contin-

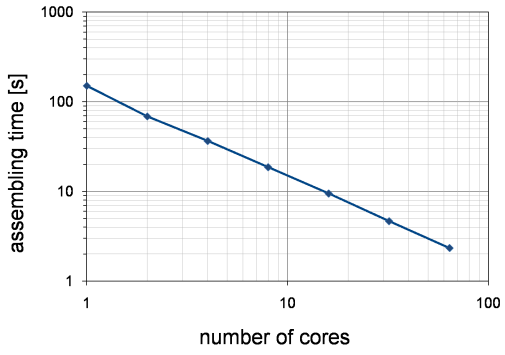

(a) Assembling time

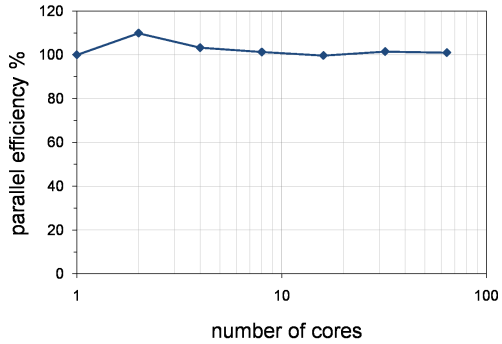

(b) Parallel efficiency – assembling time

Figure 8.9: Average assembling time per time step versus number of cores (a) and parallel efficiency (b).

uously decreases. The parallel efficiency with respect to assembling time is approximately constant around 100% for all simulations (Figure 8.9b), thus, with respect to assembling, linear scaling is observed. This behavior can be expected, due to the facts that no communication is needed during the assembly process and that the grid is partitioned in a

non-overlapping manner. Moreover, due to the computation-intensive constitutive relations, it can be assumed that comparatively few accesses to slow memory are necessary.

As already observed for the fine scale runs, the average time required per time step for the solution of the global linear system by the iterative solver is not scaling linearly with the number of cores (Figure 8.10). This is due to at least two reasons. The first

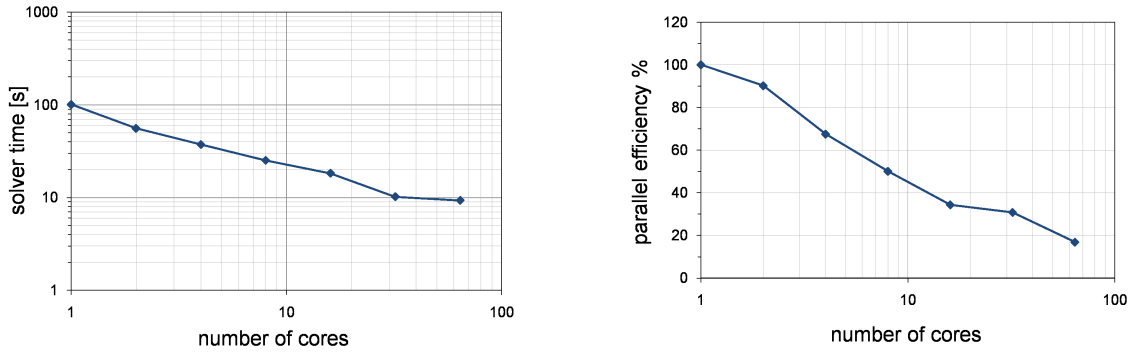

(a) Linear solver time

(b) Parallel efficiency – solver time

Figure 8.10: Average time required by the linear solver per time step versus number of cores (a) and parallel efficiency (b).

reason is that the ratio of communication time over calculation time increases with an increasing number of processes, since the global problem size is kept constant. The second reason is that a sub-optimal linear solver is applied in the current implementation. In particular, a BiCGSTAB solver is used, preconditioned by an additive Schwarz method consisting of ILU applications locally on each process. No coarse grid correction is used and a linear parallel speed-up is not possible. In order to overcome this deficiency, an algebraic multigrid solver for non-overlapping grids is currently developed within DUNE and will be available for parallel simulations with DuMu^x in the future. Trying to identify the influence of the two reasons, the average iteration count can be considered. While this number was almost constant at around 80 between 2 and 32 processes, it increased by 25% to 101 for 64 processes. This suggests that the first reason is controlling the behavior for up to 32 processes while afterwards the importance of the second reason increases. We moreover emphasize that on today's architectures, an optimal efficiency is only achievable for algorithms tuned to optimal cache reusage, which is not the case for the presented scheme.

8.5 Summary and Outlook

This chapter has been devoted to introduce DuMu^x, a free and open-source simulator for flow and transport processes in porous media. The vision, concept and design ideas have been presented. The common base of all DuMu^x models has been outlined, most importantly, the employed framework provided by DUNE, the Distributed and Unified Numerics Environment, as well as the flexible and extendable material system, the advanced simulation control, and the alternative to traits classes. The available models have been described, distinguishing between decoupled and fully coupled implicit approaches and briefly sketching the multi-scale and multi-physics capabilities. Two examples have been

presented, one discussing the multi-scale framework in more detail and one focusing on a large scale application.

In the future, the modeling capabilities will be further extended. Increased emphasis will be devoted to the efficiency and robustness of the implemented numerical models. An enhanced user-friendliness will attract more users from outside of the developers group. Within the Open Porous Media (OPM) initiative, DuMu^x will become part of a simulation suite integrating the expertise of several academic and industrial partners.

9 Uncertainties in the Practical Simulation of CO_2 Storage

Bibliographic Note: The content of this chapter is based on the following original article [Nord 12]: J.M. Nordbotten, B. Flemisch, S.E. Gasda, H.M. Nilsen, Y. Fan, G.E. Pickup, B. Wiese, M.A. Celia, H.K. Dahle, G.T. Eigestad, K. Pruess (2012): Uncertainties in practical simulation of CO2 storage. *International Journal of Greenhouse Gas Control* **9**, pp. 234–242.

Summary Practical simulation of CO_2 storage in geological formations inherently involves decisions concerning relevant physics, upscaling, and numerical modeling. These decisions are unavoidable, since the full problem cannot be resolved by existing numerical approaches. Here, we report on the impact of three distinct approaches to make the problem computationally tractable: Reduced physics, upscaling, and non-converged discretizations. Compounding these different strategies, we have used a benchmark study to try to assess the impact of an expert group on the results of the numerical simulations. In order to restrict the scope of the investigation, the geometric and geological description of the storage aquifer was simplified to the greatest extent possible.

The different strategies applied to simplify the problem, lead to significantly deviating answers when addressing relevant storage questions. Furthermore, there is room for interpretation when complex simulation results are simplified to the type of higher-level information sought in decision making processes. Our experience leads us to conclude that, important questions relating to CO_2 storage cannot be predicted convincingly to satisfactory accuracy with numerical simulation tools, even for highly idealized problems. This emphasizes the need for real-time monitoring and history matching during injection operations.

9.1 Introduction and Problem Statement

Geological storage of CO_2 remains one of the most promising options for mitigating anthropogenic release of greenhouse gases. Key aspects favoring this technology include experience from more than 150 years of subsurface oil and gas production; vast storage capacity; and small impact on natural and environmental resources [IPCC 05]. Large volumes of CO_2 will need to be injected to meet global emissions criteria, and the longevity of CO_2 in the subsurface is paramount to the success of this technology. To this end, quantifying the long-term fate of CO_2 using practical and reliable modeling tools will be important for site evaluation and risk management of CO_2 storage projects.

While there is a large amount of experience in modeling multi-phase flow in porous media from the petroleum community, few models can claim significant predictive capability (see, for example, Carter et al for an interesting discussion [Cart 10]). Well-established commercial reservoir simulators are used to obtain quantitative estimates largely through history matching and detailed geological models. The continuous nature of production data allows

for frequent updating and improvement of these predictive measures. In contrast, due to less favorable economics, CO_2 storage projects will likely be plagued with sparse geological data and little or no production data (no existing aquifer storage projects have production wells). Another source of experience comes from the nuclear waste disposal community, where increasing confidence in the predictive capabilities of ensemble modeling has been built over the last few decades (see, for example, the evaluation of the Yucca Mountain project [US D 02]). However, it is unclear to what extent those modeling approaches are applicable for multi-phase flow at the length and time scales involved in modeling carbon storage. Additionally, the disposal problem is very localized for a few systems, whereas the carbon community is looking at many thousands of locations around the world, further compounding a difficult modeling problem. With these modeling challenges, we will depend even more on the inherent capabilities of the model and, to some extent, the modeler. This requires a comprehensive evaluation of CO_2 storage models with regard to long-term effects of CO_2 migration and immobilization.

Recently, studies have examined the fate of CO_2 after injection ceases, when CO_2 can potentially migrate hundreds of kilometers over thousands of years before becoming immobilized (see, for example, [Hess 08]). The extent of migration depends greatly on the geology, rock and fluid properties. Capturing the relevant flow and trapping mechanism using traditional modeling approaches across these exceptionally large spatial and temporal scales is a difficult modeling problem. As a result, the carbon modeling community is faced with a new challenge in terms of model simplifications [Celi 09, Nord 09b]. In particular, it is clear that traditional computational science methods based on the standard Darcy equations in 3D, where the governing equations are discretized on successively finer grids until a converged solution is obtained, will likely not be computationally feasible for this problem [Clas 09]. This has been largely acknowledged, and several simplified modeling approaches have been proposed [Hess 08, Nord 09b, Pers 08].

In this chapter, we discuss two important aspects of the modeling uncertainty resulting from inherent simplifications. Here, uncertainty is defined as the variability in model predictions obtained by independent researchers solving the same benchmark problem. The first aspect we address is the issue of the relative impact on model predictions from sources of variability related to differences in modeling approach, interpretation and other numerical effects. Secondly, we discuss what properties of the solution are quantifiable. Our scope is limited to simulation of long-term migration of CO_2. In particular, we will consider the relationship between point measures such as plume tip migration and integral measures such as center of mass and variance of CO_2 distribution. We are thus not considering short-term measures associated with the injection process, as simulation of this process is already well studied through the analogy to oil and gas production. Within these two general questions, we address secondary issues related to upscaling, model simplification, convergent simulations, and post-processing of data. As such, this work forms part of our broader efforts to understand the fundamental issues related to predictability and uncertainty within CO_2 storage.

9.2 Methodology

An important goal of this comparison study is to examine the variability in model predictions obtained by different participants in response to the benchmark problem definition. We define a participant as an individual or group who have applied a model that has

either been developed within their institution or is readily available for their use. We are interested in comparing different estimates obtained across the participating groups (inter-group), and in some cases we will compare different responses obtained by the same participant (intra-group). Our objective in this study is to achieve a collection of responses from the participants, all representing research groups with extensive experience from simulating CO_2 sequestration, that were obtained independently from one another. Thus, in the inter-group comparison, we are interested in the variability that is due to the different ways in which participants interpret and approach the problem working alone, rather than attempting to converge on identical model predictions, as is the case in many benchmark studies. To be fair, some inter-group communication is necessary, both for clarity and understanding, yet the goal is to limit the communication so that our end results are not conditioned on each other. The correct balance in this respect is difficult, but we believe our approach is within reason.

Initially, a core group devised and described a benchmark problem [Dahl 08]. This problem is conceptually simple, yet retains some of the intrinsic challenges related to interacting scales that are typical for CO_2 storage. In our experience, the benchmark problem cannot be solved exactly with available computational technology and resources, and simplifications must be introduced.

The benchmark was circulated to three parties, and a mini-symposium organized at the June 2009 Society of Industrial and Applied Mathematics Geosciences conference. At this minisymposium, initial results were presented from the three participating groups and discussed. After the mini-symposium, the benchmark was circulated to a wider group of researchers for discussion at the Svalbard workshop on Numerical Modeling of CO_2 Storage (Longyearbyen, August 2009).

Following the first two stages of discussions, the core group revised the benchmark to increase clarity. The response criteria were also expanded to include integral measures, and a minimum complexity in terms of physical processes was prescribed.

This report is based on the responses to the revised benchmark. During this stage, inter-group communication has been kept to a minimum. We hope that this level of communication can be seen as reflective of the process where independent groups are studying the same problem, following initial briefing sessions.

9.3 Benchmark Description

The full benchmark description is given elsewhere [Dahl 08], and we will only give the main aspects herein.

The benchmark describes injection from a 1-km long horizontal well at the bottom of a homogeneous formation with a constant tilt (perpendicular to the injection well) of 1%, as shown in Figure 9.1 . The formation is relatively large, extending 50 km downslope and 150 km upslope from the injection well, and with a width of 100 km. Boundary conditions are impermeable at the top and bottom surfaces of the formation, while the outer boundary conditions are all hydrostatic. Injection is considered for a period of 20 years, after which the post injection period continues until all fluid movement is ceased. The modeling of fluid properties and physical processes is left open to the participants. Critical questions to be answered (as detailed in the results section) include phase partitioning, together with physical measures of extent such as furthest updip plume extent, and mean and variance of the location of the CO_2 phase.

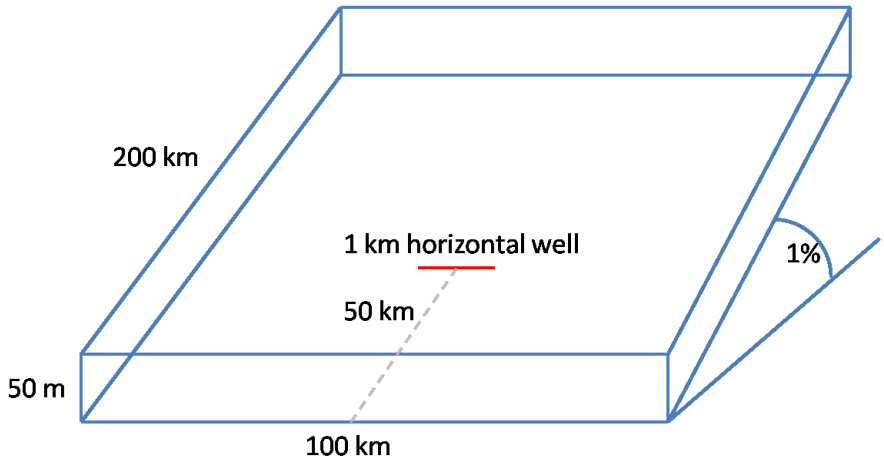

Figure 9.1: Domain for benchmark problem.

9.4 Benchmark Participants

Six research groups reported simulations regarding the benchmark problem. Of these, four groups used a traditional approach, consisting of coupled physical models discretized on a 3D numerical grid with low-order methods in space and time with generalized solvers. Another group reported results using vertically upscaled models, while the last group used simplified physics to simplify the problem so that the resulting equations could be approximated using dedicated solvers with reasonable numerical accuracy. Notably, several groups also conducted an intra-group sensitivity study regarding different simplifications. We briefly outline these contributions below, a summary is also provided in Table 1. The first three groups presented were the core groups which discussed the benchmark at the SIAM GS mini-symposium.

9.4.1 Stuttgart

The Department of Hydromechanics and Modeling of Hydrosystems, Universität Stuttgart, reported four sets of results, emphasizing the inclusion of different levels of physical complexity. Their simulations used their in-house simulator DuMu^x [Flem 11], using a variable-resolution grid with a total of 45,760 elements. Linearization and time-stepping is based on an IMplicit Pressure, Explicit Concentrations (IMPEC) approach.

The suite of results from Stuttgart considers compressible fluids, however they simplify the modeling by neglecting capillary pressure and molecular diffusion. The sensitivity analysis explores A) the importance of including hysteresis and B) the effect of including solubility between the fluids.

We refer to the data from Stuttgart as Stu-X-Y, where X = { hys, non} depending on whether the run includes hysteresis, and Y = { sol, imm} depending on whether the run includes solubility. The Stuttgart data is colored red in the results.

9.4.2 SINTEF ICT

The Department of Applied Mathematics, SINTEF ICT (Oslo), reported one set of results that aim at providing a converged numerical approximation. To this aim, they neglect

capillary forces, solubility and compressibility, while focusing their attention on the basic two-phase flow equations. Hysteresis (residual saturation) is approximated by using the imbibition relative permeability curve.

The governing equations are resolved by a series of grids, where the finest non-uniform grid consists of 0.6M cells, while the finest uniform grid consists of 1.2M cells. The reported results are an extrapolation from the two finest grid resolutions. To achieve a fast numerical method capable of calculating on the finest grid, the time-stepping is resolved by operator splitting, where the structures that appear as advection, convection, and segregation in the governing equations are time-stepped separately [Nils 10a].

We refer to the data from SINTEF ICT as Sintef, and the data are colored blue in the results.

9.4.3 UNC

The Department of Environmental Sciences and Engineering, University of North Carolina (UNC) reported results using vertically upscaled equations.

The upscaled model is derived through vertical integration of the three-dimensional governing equations for two-phase flow under the assumptions of vertical equilibrium, complete gravity segregation, and a sharp-interface between the CO_2 and brine. The resulting model is a two-dimensional model for flow in the lateral directions only (vertical flow is zero). The sharp-interface assumption implies that capillary forces at the CO_2-brine interface are negligible. The vertically upscaled equations account for fluid and matrix compressibility as well as hysteresis in the relative permeability function. In the vertically upscaled equations only the end-point relative permeabilities enter, which were calculated using Land's scaling of the primary drainage curve. Solubility of CO_2 in brine is also considered in the upscaled model, which is comprised of two components: 1) equilibrium partitioning into the regions containing residual brine and residual CO_2; and 2) convectively-driven dissolution below the CO_2 front.

The two-dimensional upscaled equations were discretized on a 200 x 200 horizontal grid using a standard finite difference approximation. The grid employed non-constant spacing, as small as 250 x 250 m near the injection well and increasing geometrically towards the boundaries. The system equations is solved using an IMplicit Pressure, Explicit Saturation (IMPES) type of approach. For this system, fluid properties are assumed to be incompressible and constant in space and time. The density ρ and viscosity μ of CO_2 c and brine b are as follows: $\rho_c = 733$ kg/m^3, $\rho_b = 1099$ kg/m^3, $\mu_c = 0.0611$ mPa-s, and $\mu_b = 0.511$ mPa-s.

Results both with [Gasd 09], and without [Gasd 11a], upscaling of convective mixing were reported. We refer to the data from UNC as Unc-X, where X = { sol, imm} depending on whether solubility and upscaled convective mixing is included in the run. The data from UNC is colored black in the results.

9.4.4 Potsdam

The German Research Centre for Geosciences, Potsdam, reported results obtained using the commercial simulator Eclipse 100 [Schl 09]. They include four runs, with varying complexity and grid resolution. Since the problem is symmetric only a half model was calculated. The coarse model has a regular grid with 1000x1000x1 m which corresponds to 1,000,000 cells. The rectilinear grid of the fine model has a resolution of 200*200 m in the area of the CO_2 plume. The top layer has a thickness of 20 cm, gradually increasing to 7

m for the bottom layer, corresponding to 372,300 cells. Both discretizations are calculated with high and low complexity. The different processes are the dissolution of CO_2 in brine and capillary pressure. PVT properties of brine and CO_2 are adapted from TOUGH2.

We refer to the data from Potsdam as Pot-X in the results, where X = { sol, imm} depending on whether solubility is included in the run. Data from Potsdam is colored green in the results.

9.4.5 Heriot-Watt

The Institute of Petroleum Engineering at Heriot-Watt University, Edinburgh (HWU) used the commercial compositional simulator Eclipse 300, along with the CO2STORE module which was developed for CO_2 storage in saline aquifers [Schl 09]. This module accounts for the mutual solubility of CO_2 and can simulate hysteresis in relative permeability and capillary pressure. An adaptive implicit method was used for solving the equations (AIM). Full details of this work are described in [Enwo 10]. A global grid of 40 x 50 x 5 cells was used, with local grid refinement in the vicinity of the plume, and grid coarsening at the edges of the model. The minimum cell size was 100 m in the horizontal and 5 m in the vertical and there was a total of 190,000 cells. HWU were aware that the resolution was not high enough, especially in the vertical direction, to resolve the migrating CO_2 plume. (See, for example, [Pick 10]). Therefore, a simulation with 175,000 with a minimum cell size of 200 m in the horizontal and 1 m in the vertical was also carried out.

Some additional simulations using the CMG compositional simulator, GEM [Comp 06] were performed. A similar grid was used for these simulations, but without the grid coarsening at the edges. This model had 210,000 cells. Due to long simulation times, the GEM simulation was only run for 100 years post injection, so the results are not presented here. A comparison of results showed that there were significant differences between the two simulators: in GEM the plume traveled 10% less, and there was approximately 10% less mobile CO_2 after 100 years [Enwo 10].

We refer to the data from Heriot-Watt University as HWU, and the data are colored orange in the results.

9.4.6 Stanford

The SUPRI-B research group in Department of Energy Resources Engineering, Stanford University, reported results using their in-house code General Purpose Research Simulator (GPRS) [Cao 02, Jian 07]. Their initial tests showed that the injected CO_2 is confined in the central area far from the boundaries after running the model for 20,000 years. Therefore, a section of the aquifer is considered, which is 15 km in the dip direction and 10 km in the direction perpendicular to the dip. Constant pressure was assumed for the horizontal boundaries of the considered section. The results reported herein are all from the sectional aquifer model.

Because of symmetry, half of the section was modeled, which was discretized into 300,000 (150×50×40) uniform structured grid blocks. The size of each grid block is $100\times100\times1.25m^3$. Finite difference approximation was applied, and fully implicit method (FIM) was used. Fluid properties and phase equilibrium were modeled with Peng-Robinson Equation of State (PR-EOS), which captured the solubility of CO_2 in the water phase and the vaporization effect of water into the gas phase. Compressibilities of both phases were inherently included in the EOS, and the volume shift parameters (used for correcting phase

densities) and interaction coefficients (used for correcting solubility) were tuned to the reservoir temperature. In addition, hysteresis is included in the relative permeability to the gas phase to determine the amount of residually trapped CO_2. The primary drainage capillary pressure was also modeled, but the hysteresis of capillary pressure is not included. Dynamic thermal effects were not accounted for in the simulation, though the presence of a geothermal gradient was modeled. Geomechanical effects were also excluded by assuming constant porosity and permeability throughout the whole simulation.

We refer to the data from Stanford as Stanford, and the data are colored magenta in the results.

9.5 Reported Data

Results were reported in two forms. Both as time series, and in table form for selected comparison times. For the presentation herein, we choose to present all data in figures based on the time series. Where data was reported only for comparison times, we report these by symbols in the figures. Not all groups reported data for all runs and all metrics (depending in part on included physics). However, all metrics were reported on by a meaningful number of participants.

9.5.1 Plume Extent

The most basic metric is the furthest upslope extent of the plume, both as a function of time (speed) and its ultimate distance until immobilization. All groups reported on this measure, as shown in Figure 9.2.

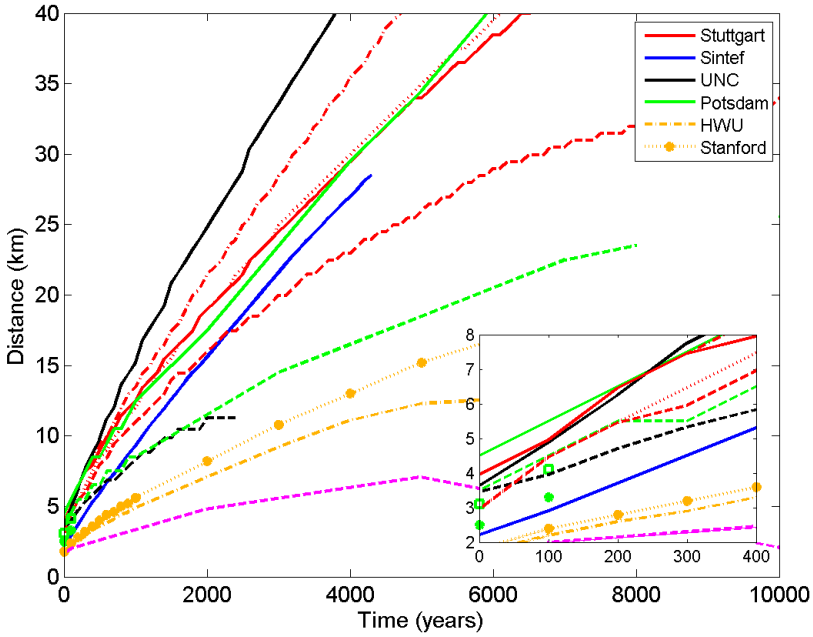

Figure 9.2: Furthest updip extent of CO_2 plume measured from the injection point, as a function of time since injection stop. Colors represent different participating groups, while different line styles represent different runs within the same group.

The furthest updip tip of the plume is a measure that is sensitive to horizontal and vertical grid resolution. In addition, other physical effects such as fluid properties and solubility may affect this metric. We note that a large range of variability in the results is present already at the end of the injection phase (see inset), with a spread of 2.5 km between the different model predictions, and continues increasing throughout the post-injection period. Interpreting the various results from the different groups as a single sensitivity study, we see none of the data from a single group captures the spread in results (and presumably the uncertainty) from the ensemble. The results from Stuttgart (red lines), which represent the broadest intra-group sensitivity study in terms of physical complexity, show a much smaller spread in results than the full ensemble.

We may compare models with similar complexity – lower complexity refers to results with hysteresis but no solubility (solid lines) and higher complexity refers to results that include both solubility and hysteresis (dashed lines). For the lowest complexity, there is relatively good agreement between Stuttgart, UNC and Potsdam at early time, while Sintef reports the lowest updip extent of the 4 models. At later times the UNC results deviate while the results from Sintef converge to the remaining two. An explanation for this may lie in the fact that the vertically integrated model used by UNC contains essentially infinite vertical resolution, allowing for fast tip movement, while the remaining groups are dependent on finite vertical resolution. For higher complexity, the Stuttgart, UNC and Potsdam results again agree at early time, indicating a significant reduction in tip speed when solubility is included. However, the Stuttgart results diverge, showing a less pronounced effect than the latter two models after 500 years. One notable aspect are the results from Stanford, which display metrics consistent with a high degree of dissolution compared to the other modeling groups. This leads to the tip of free-phase CO_2 receding at later times. The effective rate of dissolution is dependent on density-driven convective mixing, a phenomena that is very sensitive to grid resolution in numerical models, which may explain why other groups do not observe the receding plume tip. It is also worth noting that the Stanford results were reported using Peng-Robinson EOS, with the component properties taken to be the default values in WinProp, a software of Computer Modelling Group (CMG). A sensitivity study to the effect of choice of PVT data (not shown in figures) indicates that the Stanford results are in line with the reported results from Potsdam if National Institute of Standards and Technology (NIST) PVT data are used.

The effect of grid resolution is clear in the case of Potsdam and HWU, which are the only participants that reported the sensitivity to this modeling choice. From Potsdam, only two data points are available for the refined model (see inset), the results indicates that the model has not converged for the plume extent. Interestingly, HWU sees less sensitivity to grid refinement, although their results consistently report lower migration distances than the other groups.

9.5.2 Plume Center

To understand the dependency of the predictive capability on the questions asked, we consider an integral measure of upslope migration in addition to the point measure (tip location) studied in the previous subsection. Here, we consider the center of mass of mobile free-phase CO_2 in the system, as reported in Figure 9.3.

For minimum physical complexity (solid lines), we see a remarkable agreement for all time between the highly resolved model of Sintef and the results of Unc-imm, and a very good agreement also for Stu-imm for the first 1000 years. Furthermore, these results exhibit the

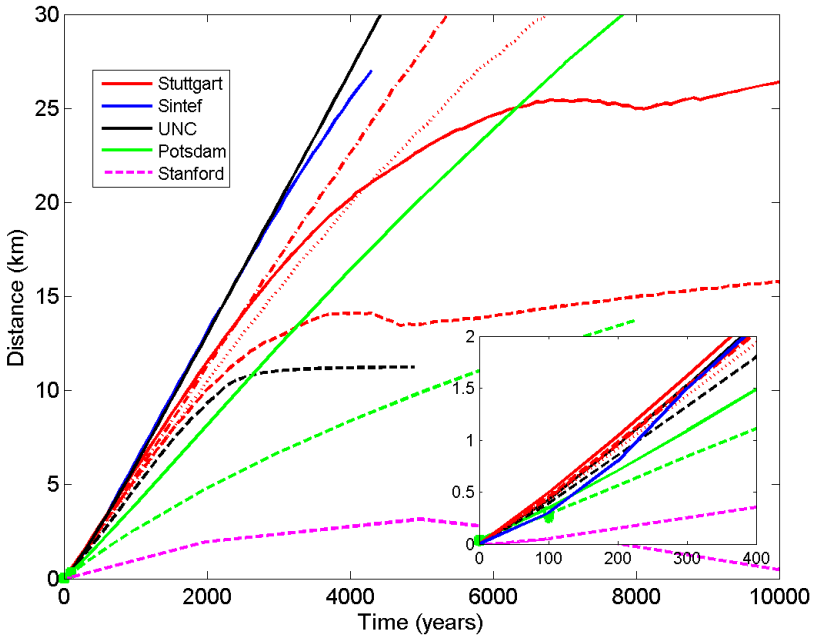

Figure 9.3: Updip extent of the center of mass of mobile CO_2 measured from the injection point, as a function of time since injection stop. Colors represent different participating groups, while different lines styles represent different runs within the same group.

near-constant velocity expected for this problem (the deviation at late time is attributed by the investigators to limited vertical resolution) [Hess 08]. We see that the results from Pot-imm are not in agreement, where a significantly different velocity is predicted. This is in part due to interpretation issues related to not distinguishing between mobile and residual CO_2 saturation, although additional affects must be considered to fully understand the different velocities. These observations carry over to the results including solubility (dashed lines), although the data reported from Stanford again shows the significant impact of choice of PVT data.

9.5.3 Plume Spread

To complement the buoyant migration measures of plume center and tip, along-slope and cross-slope standard deviation of the mobile CO_2 plume was adopted as a measure of interest. Physically speaking this can be associated with the spatial footprint of the plume, and thus correlates with leakage risk through the caprock, as reported in Figure 9.4.

There is a remarkable agreement between the reported results for the first 500 to 1,000 years, from the majority of groups. This indicates both that the standard deviations are reasonably robust measures for spread of the CO_2 plume, but also that unlike the upslope migration of the plume tip, the spreading is less affected by the physical processes modeled.

At later times, the results diverge significantly. This is in part due to different modeling assumptions (i.e. solubility) leading to different immobilization times for CO_2. As the CO_2 plume is nearly immobilized, it is present at low saturations over a large domain, and the standard deviation becomes sensitive to small variations in the saturation field. This likely explains why the standard deviation diverges in some models while it converges to

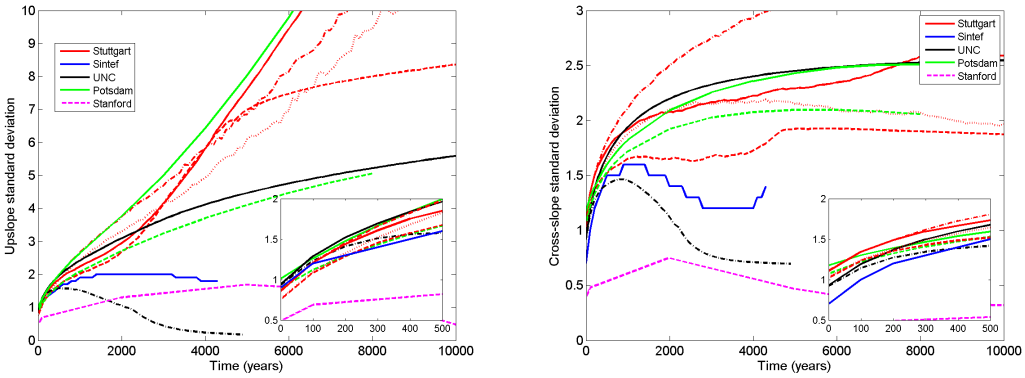

Figure 9.4: Along-slope (left) and cross-slope standard deviation of the mobile CO_2 plume as a function of time since injection stop. Colors represent different participating groups, while different lines styles represent different runs within the same group.

zero in others. An additional sensitivity study was carried out by Potsdam (not shown in figures), concluding that the distinction between free and immobile CO_2, which affects the calculations of residually trapped CO_2, accounts for as much as 20% variation in the reported results.

9.5.4 Phase Distribution of CO_2

The final reported measure was the distribution of CO_2 as a function of time. For the simplest models, this amounts to distinguishing between residually trapped and mobile free-phase CO_2, while for the models with solubility, dissolved CO_2 in the brine phase must also be accounted for. The reported results are shown in Figure 9.5, with the immiscible models shown in the left panel and the soluble models in the right panel. We note that after preliminary discussions where Potsdam only reported dissolved fractions, we have included data from Potsdam using the same interpretation of residually trapped as used by Stuttgart.

Considering first the immiscible runs shown in the left panel of Figure 9.5, we can can make some interesting observations regarding the sources of discrepancy between the reported data. At end of injection (time equal to zero in the figure), Stu-hys-imm and Potsdam-imm already reports that 30% of the injected CO_2 is trapped at residual saturation, while Sintef and Unc-imm report virtually no trapped CO_2. This is due to a difference in interpretation of what residually trapped means, where Stuttgart and Potsdam reported residually trapped CO_2 interpreted as all CO_2 at less than residual saturation as trapped, while the other groups interpreted CO_2 to be trapped at a location only if it was immobile. As time evolves, the Stuttgart and UNC models converge, while the Sintef results show a significantly faster time to immobilization than the other models.

For the soluble runs, we include results also from the remaining two participant groups (Stanford and HWU). It is interesting to note that these two groups get very similar results for the free-phase CO_2. However, they are in less agreement with regard to the dissolved fraction. Again, the values from Stu-imm and Potsdam are presented with a different interpretation of residually trapped. The values from Unc-sol predict a significantly faster dissolution of the CO_2 into the brine than any of the other models. This result is possibly

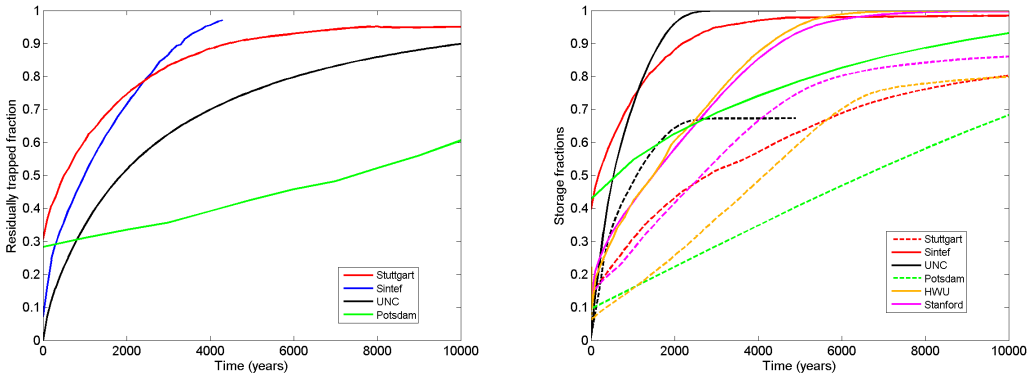

Figure 9.5: Storage fractions, defined as ratios of trapped CO_2. Left are responses without dissolution, to the right are model responses with dissolution. Colors represent different participating groups, while solid lines separate free (fraction above the curve) and residually trapped (fraction below the curve) CO_2, and dashed lines in the right figure separate residually trapped (fraction above the dashed curve but below the solid curve) and dissolved (below the dashed curve) CO_2.

due to the upscaling of convective mixing used by Unc-sol. In the other models convective mixing was not upscaled, and the coarse grids employed may have suppressed this trapping mechanism. This is also evident when comparing the reported data from Stuttgart and UNC, where we see that solubility only leads to small changes in the ultimate trapping time in the runs of Stuttgart, whereas a much greater impact is seen in the data from UNC. Finally, we note that although trapped CO_2 is often considered to be immobilized, the results of the Potsdam and HWU groups show a remobilization shortly after injection stop where the amount of trapped CO_2 decreases. This occurs, because pressure decreases rapidly after injection stop and therefore also the density of the residual CO_2 decreases, resulting in a slight mobilization.

9.6 Discussion

This model comparison study was designed with the objective of understanding the realistic variability in model predictions that could be expected from independent research groups applying different modeling approaches to the same problem. Hence, the benchmark problem was purposely simplified so that the variability due to differences in modeling choices would be maximized. We are interested in the effect of modeling choices because, even for an idealized problem such as this, decisions are made either due to necessity, posed by time constraints or available resources, or due to the independent interpretation of the problem. In addition, no problem statement is defined perfectly, therefore the modeler must also make choices due to this natural degree of uncertainty.

Despite having posed a relatively simple, idealized problem, the variability in model predictions from inter-group and intra-group comparison presented in Section 5 was greater than expected. Several interesting points are worthy of further discussion. We choose to focus on four different sources of this variability, all of which are a result of the modeling choices made by each of the participating groups. The sources are categorized as follows:

- the specific *physical processes* modeled,

- the *numerical modeling*,
- the type of *upscaling* employed, if at all, and
- the *interpretation* of the problem definition and metrics.

Based on the results from Section 5, we address the impact of these sources on the current modeling study by drawing attention to observations that span the full data set. Note that this study has been a comparative study, aimed at considering the interaction between a suite of uncertainties. As such, we will in some cases see that further data could possibly have highlighted certain aspects better.

9.6.1 Physical Processes, Numerical Modeling, Upscaling, and Interpretation

- **Upscaling** The only group attempting to use upscaling combined with numerical methods for this study was UNC. The upscaling methodology applied was a sharp interface segregation with vertically equilibrated pressure distribution. When comparing immiscible runs, we see that this estimates a plume tip velocity which is up to 50% greater than the responses that report 3D simulations, however the mean plume velocity is consistent with the other models. When further upscaling of convective mixing is applied, the upscaled model reports consistent trends compared to the 3D models, with results that are within the spread of the 3D models both for measures of velocity. In terms of the other measures reported, the effect of upscaling is much more pronounced, where we observe that in particular after the first few centuries, the models diverge significantly. This is due to the upscaled models having either significantly longer (without solubility) or significantly shorter (with solubility) times to immobilization than the 3D models without upscaling. However, due to the limited resolution spatial of the 3D models, it is not clear if the upscaled simulations or the 3D simulations are closer to the true solution for the problem.

- **Numerical modeling** Stuttgart, Potsdam, HWU and Stanford have largely comparable modeling approaches, with comparable physical processes and no upscaling. The main differences lie in interpretation and numerical implementation. Disregarding interpretation differences, which strongly affects the Stanford results, we may consider the impact of numerical modeling for this problem. In terms of plume extent, we see from Figure 2that Potsdam and Stuttgart report deceptively similar results for the immiscible calculation (solid lines). However, the interpretation that numerical modeling has relatively little impact is invalidated by the grid refinement study reported by Potsdam, where we see that at least at early time, there is a factor 2 uncertainty due to numerical modeling. This conclusion is supported in the reported soluble runs (dashed lines). In terms of integral features, as reported in the remaining figures, we see apparently less impact of numerical modeling. This is evidenced by the close agreement between Stuttgart and Potsdam in Figures 4 and between HWU and Stanford in Figure 5b. In the latter figure, the disparity in the results of Stuttgart and Potsdam is caused by interpretation, as we will consider below. The SINTEF calculations used the simplest physics and focused on grid resolution. They found that to get reliable results for plume migration in the post injection period, it was necessary to extrapolate from the two finest z-resolution calculation to get reliable

results. The center of mass of their calculation has the fastest movement of the 3D simulations and is the only group which report that the width of the plume decreases for late times.

- **Physical Processes** The impact of physical processes is addressed by sensitivity studies by three of the participating groups; Stuttgart, Potsdam and UNC. The results are interesting, in particular from a qualitative standpoint. Considering the results of Stuttgart and Potsdam (red and green in the figures), we see that the conclusion is that added physics has a relatively minor impact on the measures reported. In contrast, UNC finds a significant impact of including fluid solubility. To understand this, we must return to a fundamental challenge in modeling CO_2 storage. Firstly, the large domain and computational limitations necessitates coarse grids. Secondly, important non-linear processes require a fine grid, or careful upscaling, to be modeled correctly. For this problem, convection cells with length scales of meters enhance dissolution of CO_2 into brine [Riaz 06, Elen 12], a process that is distorted by the coarser grids utilized by Stuttgart and Potsdam. We may therefore expect that the impact of physical processes is underestimated in those simulations. As the upscaling methodology adopted by UNC is still not extensively validated, it is unclear how accurate these results can be expected to be. We note that contrary to the numerical modeling, which has a greater impact on plume extent than on integral measurements, the uncertainty associated with the physical processes included affect all reported measures.

- **Interpretation** We have two main differences in interpretation of data between the groups. The first is on the topic of residual saturation of CO_2, where three different interpretations were given. In the first iteration, Potsdam chose to not account for free versus residually trapped CO_2. Thus, the reported mean plume location in Figure 3 is averaged over the whole CO_2 phase. Since the lower trail of CO_2 is considered trapped by the remaining groups, Potsdam therefore reports significantly slower plume migration. Secondly, Stuttgart and HWU implemented a threshold where all CO_2 at saturations below residual saturation is considered trapped, even if CO_2 is at a higher saturation. Thus, they consider a significant fraction of CO_2 trapped already during the injection phase, as evidenced in Figures 5. This interpretation also impacts the standard deviations in Figures 4,where the center of mass of CO_2 becomes weighted less than for the remaining groups, leading to a relatively larger spread of the plume. Finally, the remaining groups interpret CO_2 as residually trapped only if CO_2 is present at a saturation no higher than the residual saturation. Thus, no CO_2 is residually trapped during the injection phase, and when the relative permeability is non-zero, all CO_2 at that point is considered mobile. In response to the different interpretations of residually trapped CO_2, Potsdam reported a set of results with all three interpretations, validating in part the observations described above.

  The second data interpretation issue lies in the choice of PVT data. This has a very strong influence, as evidenced by the submitted results from Stanford. Notably, the default PR-EOS data in WinProp predict significantly denser CO_2, thus eliminating much of the buoyant drive, which is the main source of dynamics in the system. Consequently, the plume travels a shorter distance and remains more compact. Clearly, these results highlight the need for consolidating the various PVT data sets available.

Fundamental issues of interpretation combine into what can collectively be referred to as an institutional bias. As was noted in Section 5.1, the reported data from Stuttgart, HWU, and Stanford indicate an institutional bias that is sufficiently large that in general, the collected reported results from one group does not overlap with the results from the other groups. Giving the various results reported by Stuttgart and HWU the interpretation of an internal sensitivity study, the observation is that the variation between groups exceeds the variability of results obtained by a single group.

From the summarizing discussion above, we can only strongly conclude that all four categories of uncertainty impact the results. We also try to report to what extent which cause dominates the variability reported: In particular, we observe that accurate accounting of solubility and convective mixing is dominated by upscaling and numerical modeling. Assessment of storage fractions is most dependent on physical processes and interpretation. Furthest updip plume extent (and thus tip velocity), is crucially dependent on numerical resolution, and possibly on physical processes (based on the upscaled results of UNC). Finally, integral measures of plume spread are highly variable at late time, depending strongly on upscaling, physical processes, and interpretation, but apparently less on numerical modeling.

9.6.2 Impact of Aspects Not Considered in this Study

Any single modeling study, such as this one, will come to conclusions which may lack generality. Here, we try to highlight some processes and aspects that may alter the findings.

- **Heterogeneity and anisotropy** This comparison study did not include challenges related to heterogeneity. Introducing heterogeneity, and in particular where the heterogeneity has significant small-scale structure with long correlation length, may increase the realism of the study for several potential storage sites. For this scenario, the study will be impacted as challenges of numerical resolution and upscaling increase, and consequently also their importance. However, the basic physical challenges remain unaltered, although some length and time scales will be changed due to the increased mixing associated with more tortuous flow paths.

  In contrast, we expect anisotropy in permeability (which also includes structured layering) to significantly alter the numerical challenges of this benchmark. In particular, we expect lower vertical permeability (which is realistic for most geological formations), to significantly reduce the role of convective mixing as an enhancer of dissolution. As such, it becomes less critical to capture the small-wavelength instabilities, and we expect the numerical challenges to be reduced, and similarly the importance of upscaling for soluble processes.

- **Caprock topography** The strong buoyant drive of CO_2 relative to water is the primary driving force for dynamics in the current benchmark. This makes the modeling results strongly sensitive to the topography of the caprock. Two effects can be expected: The presence of dome structures will lead to local trapping, known as structural trapping. Secondly, valley features will focus and lead the CO_2 upslope with less cross-slope spreading. Both of these effects are reasonably easy to calculate, and it can therefore be expected that caprock topography will simplify this modeling

study, and reduce the reported variability in the results. However, there is little reason to expect that the qualitative results would change, as long as structural trapping remains a modest trapping mechanism.

- **Boundary conditions** Boundary conditions influence the model in three important aspects. Firstly, non-hydrostatic boundary conditions may impose a regional flow of brine. This background flow both creates a competing force to the buoyant drive, which may alter the migration path of free-phase CO_2, and can also impact the time-scale of dissolution as fresh brine replaces CO_2 saturated brine. Secondly, confining boundary conditions (no-flow), will lead to increased pressure buildup in the formation, in particular for relatively smaller aquifers. This will heighten the importance of fluid property modeling, as well as possible geomechanical responses. Finally, the boundary condition imposed to model the caprock, here chosen as impermeable, crucially impacts the pressure field during injection. Furthermore, the boundary between the aquifer and the caprock is the primary feature determining the magnitude and characteristics of leakage. As such, aspects related to predicting leakage are not addressed by this study.

- **Uncertainty in problem specification** The properties of real geological media are usually estimated based on sparse measurement data obtained over a range of length scales. The assimilation of this data into meaningful parameters for simulation is a complex process which is designed to lead to a range of possible parameters consistent with the measurements. As such, the problem specification will be inherently uncertain. Understanding the relative impact of geological uncertainty as compared to the topics highlighted herein is an ongoing field of research.

9.7 Conclusion

Here we consider a highly simplified model for CO_2 storage, which nevertheless is demanding enough that no exact solution is known. We have attempted to assess the relative impacts of different simplifications introduced to obtain a reasonable approximation of the solution. Our primary attention has been drawn toward the interplay between the four topics modeling, upscaling, simulation, and data interpretation.

Our observations lead us to conclude that all four topics investigated lead to significant uncertainty in model prediction. The extent to which various approximations are appropriate is not only dependent on the physical problem at hand, but also on the properties of the solution we wish to address. Overall, the combined results of this benchmark study do not allow us to conclude, within any reasonable certainty, a common answer to basic questions such as migration distance, plume footprint, or storage fractions. However, we should emphasize that the large variation in model prediction due to modeling choices may be exaggerated by the simplicity of the benchmark problem. A more realistic problem may be dominated by uncertainty in the system parameters such as permeability, porosity and structural effects. Nevertheless, this study points to a fundamental challenge of modeling, that perfectly valid approaches to the same problem lead to divergent solutions.

We interpret the variation in modeling philosophies displayed by the participants, together with the large variability in reported results for key metrics, as an important statement about the predictability of CO_2 storage systems and the role of modeling. More precisely, it is our claim that basic questions with respect to CO_2 storage may not be

answerable with today's technology and knowledge, even under the assumption that the geological description is known. Therefore, the usual response to uncertain model predictions, which is to collect more data to improve the model parameters, may be inadequate. It thus appears that integrated time-lapse monitoring together with history matching and model updating during the life-time of the storage operation will be essential to enhance the long-term assessment of the ultimate fate of injected CO_2.

It is important that the scientific community, along with policy makers and regulators, recognize this fundamental limitation in terms of predictive modeling. This does not imply that modeling is a useless exercise. On the contrary, models for CO_2 are valuable tools for increasing our understanding, providing first estimates, and giving qualitative insight, which is valuable in the decision making process. However, they should not be mistaken for accurate prognostic tools. Furthermore, advances in numerical simulation capabilities, upscaling methodology, model description, or data understanding may narrow the gap in modeling philosophies, but essential uncertainty will still persist. In the end, only close collaboration between several participating groups will reduce the uncertainty towards acceptable bounds.

Conclusion and Outlook

This habilitation thesis is devoted to discussing several challenges facing the development of coupled numerical models for flow and transport processes in porous media. Most of the chapters have a dedicated conclusion. In the following, these conclusions are summarized and put into the context of this thesis. Moreover, several suggestions for future research are given.

Part A *Model Coupling* deals with uncoupled and coupled porous-media models in general and describes some of these models in detail. Chapter 1 *Mathematical and Numerical Models for Porous Media* primarily serves as an introduction to the terminology that is associated with flow and transport processes in porous media. In addition, two specific coupled models are presented: a multi-scale model for immiscible two-phase flow and a multi-physics approach for compositional two-phase flow. In the future, we aim to combine these two approaches and build up a multi-scale, multi-physics toolbox. Only a successful combination of both techniques will allow us to model highly complex processes in large domains at reasonable computational cost. Moreover, the applicability of semi-implicit IMPES-like approaches has to be reconsidered in view of the targeted applications such as underground gas storage or atomic waste disposal. Since simulations have to cover huge time intervals, the multi-scale multi-physics concepts should be extended to fully-implicit approaches which are expected to admit substantially larger time steps than the semi-implicit ones.

Chapter 2 *Classification and Review of Model Coupling Approaches* broadens the scope beyond multi-scale, multi-physics methods and highlights the relevance and diversity of coupling concepts for compositional multi-phase flow and transport processes. A general classification of coupled models is suggested. To this end, coupling methods are divided into temporal and spatial coupling, the latter of which is subdivided into volume and surface coupling methods. A further classification of the spatial concepts yields multi-process, multi-scale, multi-dimension, and multi-compartment techniques. Each category is reviewed by means of particular examples. Two main challenges for the future can be identified: the integration of multiple coupling schemes for a particular application and the adaptive selection of the required physics and scales of consideration. Especially the integration challenge poses problems not only on the conceptual but also on the practical and technical level, for example, the coupling of different software packages.

A specific coupled model for domains composed of a porous part and an adjacent free-flow region is described in Chapter 3 *Free-Flow – Porous-Media Coupling*. The model is developed for the case of non-isothermal compositional one- and two-phase systems. It accounts for mass, momentum and energy transfer across the interface, and allows the detailed description of evaporation processes, where the gas phase of the atmosphere interacts with a gas-water system in the subsurface. Numerical examples show that transfer of heat and gas across the interface and evaporation of water at the interface can be described as well as vaporization and condensation within the porous medium. In addition to the description in the chapter, several numerical tests have already been carried out and documented in, for example, [Babe 12]. Moreover, a detailed comparison with experimental data is at the

focus of our current and future work. The agreement between model and experiment could be substantially improved by adding zeroth-order terms for the description of turbulence effects. Based on this observation, we aim at including state-of-the art turbulence models for the free-flow region in the future.

Part B of this thesis focuses on *Locally Conservative Discretization Methods* (LCM) and starts with a *Review of LCM* in Chapter 4. Grouped into control volume, finite difference and finite element methods, several state-of-the-art LCM are introduced and reviewed by means of their traditional description. Some of the methods are interpreted within the framework of mixed finite element and mimetic finite difference methods. Moreover, a comparison of the methods is given. Especially for practical applications from subsurface engineering, the mesh requirements of one method provides an important criterion for preferring it over another method. Mimetic finite differences and discontinuous Galerkin schemes are most promising with respect to this criterion, since they do not rely on global interpolation properties like continuous Galerkin methods or the definition of dual grids – like vertex-centered control volume methods or multi-point flux approximation schemes. The chapter only presents the methods for the single-phase stationary pressure equation, and indeed, many schemes are mainly developed for this case. Extensions to multi-phase flow and other more complex processes are mainly based on semi-implicit approaches, while fully-implicit approaches often employ rather simple spatial discretizations. The extension of state-of-the-art LCM towards such problem formulations is a most promising topic for future research. Several methods are already investigated, like discontinuous Galerkin [Epsh 09], mimetic finite differences [Alpa 10], or vertex-centered control volumes [Eyma 12], but much more research is needed to cope with the requirements of practical applications.

A specific LCM is presented in Chapter 5 *An MPFA Method for the Treatment of Tensorial Relative Permeabilities*. The general case of an anisotropic, full tensor phase permeability and the consequences of splitting this tensor into the product of absolute and relative phase permeability are discussed. A new numerical method is developed that uses a cell centered finite volume technique with multipoint flux approximation and includes a special upwinding strategy. Numerical experiments are carried out and it has been shown that the proposed method properly accounts for the anisotropy, also in the case of a full tensor. The next step here is the employment of the method for a closer investigation of different upscaling concepts, in order to obtain a better understanding of the effects of anisotropic structures on different scales. First steps have already been undertaken in this direction, [Wolf 13b].

Another LCM is the topic of Chapter 6 *Numerical Investigation of a Mimetic Finite Difference Method*. The proposed mimetic method solves the majority of the benchmark problems with convincing accuracy and robustness. Mimetic methods are most promising for tackling real subsurface applications, since they are able to handle very rough grids and are also comparatively easy to implement. As already stated above, an extension of the method to fully-implicit approaches is of great scientific interest, [Alpa 10].

A numerical model is realized by its implementation in the form of computer code. Part C *Open-Source Porous-Media Simulation* deals with the idea of developing such a computer code by means of open-source development techniques. It starts with Chapter 7 *Open Source in Computational Science and Engineering*. A motivation for developing open-source code in academia is provided, consisting of three basic arguments: providing access to source code is mandatory as reproducibility is fundamental to the scientific method, code quality and applicability can be expected to increase, and collaborations with industrial

or academic partners are greatly facilitated. Definitions of free and open-source software are discussed and an overview of existing porous media simulators is given. The recent evolution of new open-source simulators such as MRST and DuMu^{x} and the change of licensing policies towards open source for some established codes such as OpenGeoSys and PFloTran are very promising for the future. The coupling of two numerical models is greatly facilitated if both underlying codes are open source. Moreover, only code inter-comparison will allow reliable predictions based on simulations, and open source is the only way for a detailed understanding of such comparisons.

Chapter 8 presents *DuMu^{x}: an Open-Source Porous-Media Simulator*. In particular, the vision, concept and design ideas are presented. The common base of all DuMu^{x} models is outlined, most importantly, the employed framework provided by DUNE, the Distributed and Unified Numerics Environment, as well as the flexible and extendable material system, the advanced simulation control, and the alternative to traits classes. The available models are described, distinguishing between semi-implicit and fully-implicit approaches and briefly sketching the multi-scale and multi-physics capabilities. Two examples are presented, one discussing the multi-scale framework in more detail and one focusing on a large-scale application. In the future, the modeling capabilities will be further extended. Increased emphasis will be laid on the efficiency and robustness of the implemented numerical models. Within the Open Porous Media (OPM) initiative, DuMu^{x} will become part of a simulation suite integrating the expertise of several academic and industrial partners.

The necessity for open-source simulators is illustrated from a different point of view in Chapter 9 *Uncertainties in the Practical Simulation of CO_2 Storage*. A highly simplified model for CO_2 storage is considered, which is nevertheless so demanding that no exact solution is known. An attempt is made to assess the relative impacts of different simplifications introduced to obtain a reasonable approximation of the solution. All simplifications lead to significant uncertainty in model prediction; the combined results of this benchmark study did not provide a common answer to basic questions such as migration distance, plume footprint, or storage fractions. It thus appears that integrated time-lapse monitoring together with history matching and model updating during the life-time of the storage operation will be essential to enhance the long-term assessment of the ultimate fate of injected CO_2. Moreover, only close collaboration between several participating groups will reduce the uncertainty to within acceptable limits. As already outlined above, collaboration is greatly facilitated if open-source principles are followed.

Bibliography

[Aarn 06] J. E. Aarnes, S. Krogstad, and K.-A. Lie. A hierarchical multiscale method for two-phase flow based upon mixed finite elements and nonuniform coarse grids. *Multiscale Model. Sim.*, Vol. 5, No. 2, pp. 337–363, 2006.

[Aarn 07] J. E. Aarnes, V. L. Hauge, and Y. Efendiev. Coarsening of three-dimensional structured and unstructured grids for subsurface flow. *Adv. Water Resour.*, Vol. 30, No. 11, pp. 2177–2193, 2007.

[Aarn 08a] J. E. Aarnes, Y. Efendiev, and L. Jiang. Mixed multiscale finite element methods using limited global information. *Multiscale Model. Sim.*, Vol. 7, No. 2, pp. 655–676, 2008.

[Aarn 08b] J. E. Aarnes, S. Krogstad, and K.-A. Lie. Multiscale mixed/mimetic methods on corner-point grids. *Computat. Geosci.*, Vol. 12, No. 3, pp. 297–315, 2008.

[Aava 01] I. Aavatsmark, E. Reiso, and R. Teigland. Control-Volume Discretization Method for Quadrilateral Grids with Faults and Local Refinements. *Computat. Geosci.*, Vol. 5, No. 1, pp. 1–23, 2001.

[Aava 02] I. Aavatsmark. An introduction to multipoint flux approximations for quadrilateral grids. *Computat. Geosci.*, Vol. 6, No. 3-4, pp. 405–432, 2002.

[Aava 06a] I. Aavatsmark and G. T. Eigestad. Numerical convergence of the MPFA O-method and U-method for general quadrilateral grids. *Int. J. Numer. Meth. Fl.*, Vol. 51, pp. 939–961, 2006.

[Aava 06b] I. Aavatsmark, G. T. Eigestad, and R. A. Klausen. Numerical convergence of the MPFA O-method for general quadrilateral grids in two and three dimensions. In: D. N. Arnold, P. B. Bochev, R. B. Lehoucq, R. A. Nicolaides, and M. Shashkov, Eds., *Compatible Spatial Discretizations*, pp. 1–21, Springer, New York, 2006.

[Aava 07] I. Aavatsmark. Interpretation of a two-point flux stencil for skew parallelogram grids. *Computat. Geosci.*, Vol. 11, No. 4, pp. 199–206, 2007.

[Aava 08] I. Aavatsmark, G. T. Eigestad, B. T. Mallison, and J. M. Nordbotten. A compact multipoint flux approximation method with improved robustness. *Numer. Meth. Part. D. E.*, Vol. 24, No. 5, pp. 1329–1360, 2008.

[Aava 96] I. Aavatsmark, T. Barkve, Ø. Bøe, and T. Mannseth. Discretization on non-orthogonal, quadrilateral grids for inhomogeneous anisotropic media. *J. Comput. Phys.*, Vol. 127, pp. 2–14, 1996.

[Aava 98] I. Aavatsmark, T. Barkve, Ø. Bøe, and T. Mannseth. Discretization on unstructured grids for inhomogeneous, anisotropic media. Part I: Derivation of the methods. Part II: Discussion and numerical results. *SIAM J. Sci. Comput.*, Vol. 19, No. 5, pp. 1700–1736, 1998.

[Acos 06] M. Acosta, C. Merten, G. Eigenberger, H. Class, R. Helmig, B. Thoben, and H. Müller-Steinhagen. Modeling non-isothermal two-phase multicomponent flow in the cathode of PEM fuel cells. *J. Power Sources*, Vol. 159, No. 2, pp. 1123–1141, 2006.

[Acs 85] G. Ács, S. Doleschall, and E. Farkas. General Purpose Compositional Model. *Soc. Petrol. Eng. J.*, Vol. 25, No. 4, pp. 543–553, 1985.

[Agel 10a] L. Agélas, C. Guichard, and R. Masson. Convergence of finite volume MPFA O type schemes for heterogeneous anisotropic diffusion problems on general meshes. *Int. J. Finite Vol.*, Vol. 7, No. 2, 2010.

[Agel 10b] L. Agélas, D. A. Di Pietro, and J. Droniou. The G method for heterogeneous anisotropic diffusion on general meshes. *M2AN Math. Model. Numer. Anal.*, Vol. 44, No. 4, pp. 597–625, 2010.

[Ains 00] M. Ainsworth and J. T. Oden. *A Posteriori Error Estimation in Finite Element Analysis*. Wiley-Interscience, New York, 2000.

[Alaz 01] B. Alazmi and K. Vafai. Analysis of fluid flow and heat transfer interfacial conditions between a porous medium and a fluid layer. *Int. J. Heat Mass Tran.*, Vol. 44, pp. 1735–1749, 2001.

[Albo 99] C. Albon, J. Jaffre, J. Roberts, X. Wang, and C. Serres. Domain decompositioning for some transition problems in flow in porous media. In: Z. Chen, R. E. Ewing, and Z.-C. Shi, Eds., *Numerical Treatment of Multiphase Flow in Porous Media*, Springer, 1999.

[Alle 92] M. B. Allen, R. E. Ewing, and P. Lu. Well-conditioned iterative schemes for mixed finite-element models of porous-media flows. *SIAM J. Sci. Statist. Comput.*, Vol. 13, No. 3, pp. 794–814, 1992.

[Alpa 10] F. O. Alpak. A Mimetic Finite Volume Discretization Method for Reservoir Simulation. *SPE J.*, Vol. 15, No. 2, pp. 436–453, 2010.

[Anon 12] Anonymous Contributors. start — Flyspray - The Bug Killer! 2012. `http://flyspray.org/doku.php?id=start&rev=1355516002`, [Online; accessed 27-February-2013].

[Apac 13] Apache Subversion. 2013. `http://subversion.apache.org/`, [Online; accessed 27-February-2013].

[Arbo 07] T. Arbogast, G. Pencheva, M. F. Wheeler, and I. Yotov. A multiscale mortar mixed finite element method. *Multiscale Model. Sim.*, Vol. 6, No. 1, pp. 319–346, 2007.

[Arbo 89] T. Arbogast. Analysis of the simulation of single phase flow through a naturally fractured reservoir. *SIAM J. Numer. Anal.*, Vol. 26, No. 1, pp. 12–29, 1989.

[Asst 05] A. Assteerawatt, P. Bastian, A. Bielinski, T. Breiting, H. Class, A. Ebigbo, H. Eichel, S. Freiboth, R. Helmig, A. Kopp, J. Niessner, S. Ochs, A. Papafotiou, M. Paul, H. Sheta, D. Werner, and U. Ölmann. MUFTE-UG: structure, applications and numerical methods. *Newsletter, International Groundwater Modeling Centre, Colorado School of Mines*, Vol. 23, No. 2, 2005.

[Asst 08] A. Assteerawatt. *Flow and Transport Modelling of Fractured Aquifers Based on a Geostatistical Approach*. PhD thesis, Universität Stuttgart, 2008.

[Atki 94] P. W. Atkins. *Physical Chemistry*. Oxford University Press, Fifth Ed., 1994.

[Aziz 79] K. Aziz and A. Settari. *Petroleum Reservoir Simulation*. Elsevier Applied Science, 1979.

[Aziz 89] K. Aziz and T. W. Wong. Considerations in the development of multipurpose reservoir simulation models. In: *Proceedings First and Second International Forum on Reservoir Simulation*, pp. 77–208, Steiner, P., 1989.

[Babe 12] K. Baber, K. Mosthaf, B. Flemisch, R. Helmig, and S. Müthing. Numerical scheme for coupling two-phase compositional porous-media flow and one-phase compositional free flow. *IMA J. Appl. Math.*, Vol. 77, No. 6, pp. 1–23, 2012.

[Babu 01] I. Babuska and T. Strouboulis. *The Finite Element Method and its Reliability*. Oxford University Press, New York, 2001.

[Bala 12] S. Balay, J. Brown, , K. Buschelman, V. Eijkhout, W. D. Gropp, D. Kaushik, M. G. Knepley, L. C. McInnes, B. F. Smith, and H. Zhang. PETSc Users Manual. Tech. Rep. ANL-95/11 - Revision 3.3, Argonne National Laboratory, 2012.

[Bank 87] R. E. Bank and D. J. Rose. Some error estimates for the box method. *SIAM J. Numer. Anal.*, Vol. 24, No. 4, pp. 777–787, 1987.

[Barb 05] F. Barbir. *PEM Fuel Cells: Theory and Practice*. Elsevier, Academic press, Burlington, 2005.

[Bare 60] G. I. Barenblatt and I. P. Zheltov. Fundamental equations for the filtration of homogeneous fluids through fissured rocks. *Doklady Akademii Nauk SSSR*, Vol. 132, No. 3, pp. 545–548, 1960.

[Bark 97] J. Barker and S. Thibeau. A critical review of the use of pseudorelative permeabilities for upscaling. *SPE Reservoir Eng.*, Vol. 12, No. 2, pp. 138–143, 1997.

[Basq 05] R. Basquet, C. E. Cohen, and B. Bourbiaux. Fracture flow property identification: an optimized implementation of discrete fracture network models. *14th SPE Middle East Oil and Gas Show and Conference*, 2005.

[Bast 03] P. Bastian and B. Rivière. Superconvergence and $H(\mathrm{div})$ projection for discontinuous Galerkin methods. *Int. J. Numer. Meth. Fl.*, Vol. 42, No. 10, pp. 1043–1057, 2003.

[Bast 08a] P. Bastian, M. Blatt, A. Dedner, C. Engwer, R. Klöfkorn, R. Kornhuber, M. Ohlberger, and O. Sander. A generic grid interface for parallel and adaptive scientific computing. II. Implementation and tests in DUNE. *Computing*, Vol. 82, No. 2-3, pp. 121–138, 2008.

[Bast 08b] P. Bastian, M. Blatt, A. Dedner, C. Engwer, R. Klöfkorn, M. Ohlberger, and O. Sander. A generic grid interface for parallel and adaptive scientific computing. I. Abstract framework. *Computing*, Vol. 82, No. 2-3, pp. 103–119, 2008.

[Bast 10] P. Bastian, F. Heimann, and S. Marnach. Generic implementation of finite element methods in the Distributed and Unified Numerics Environment DUNE. *Kybernetika*, Vol. 46, No. 2, pp. 294–315, 2010.

[Batt 11] I. Battiato, D. Tartakovsky, A. Tartakovsky, and T. Scheibe. Hybrid models of reactive transport in porous and fractured media. *Adv. Water Resour.*, Vol. 34, No. 9, pp. 1140–1150, 2011.

[Beav 67] G. S. Beavers and D. D. Joseph. Boundary conditions at a naturally permeable wall. *J. Fluid Mech.*, Vol. 30, pp. 197–207, 1967.

[Berk 02] B. Berkowitz. Characterizing flow and transport in fractured geological media: A review. *Adv. Water Resour.*, Vol. 25, No. 8-12, pp. 861–884, 2002.

[Bern 01] M. Berndt, K. Lipnikov, D. Moulton, and M. Shashkov. Convergence of mimetic finite difference discretizations of the diffusion equation. *East-West J. Numer. Math.*, Vol. 9, No. 4, pp. 265–284, 2001.

[Bern 05] M. Berndt, K. Lipnikov, M. Shashkov, M. F. Wheeler, and I. Yotov. Superconvergence of the velocity in mimetic finite difference methods on quadrilaterals. *SIAM J. Numer. Anal.*, Vol. 43, No. 4, pp. 1728–1749, 2005.

[Biel 06] A. Bielinski. *Numerical Simulation of CO_2 Sequestration in Geological Formations*. PhD thesis, Department of Hydromechanics and Modeling of Hydrosystems, Universität Stuttgart, 2006.

[Binn 99] P. Binning and M. A. Celia. Practical implementation of the fractional flow approach to multi-phase flow simulation. *Adv. Water Resour.*, Vol. 22, No. 5, pp. 461–478, 1999.

[Biot 55] M. A. Biot. Theory of elasticity and consolidation for a porous anisotropic solid. *J. Appl. Phys.*, Vol. 25, pp. 182–185, 1955.

[Boch 08] P. B. Bochev and M. D. Gunzburger. A locally conservative least-squares method for Darcy flows. *Commun. Numer. Meth. En.*, Vol. 24, No. 2, pp. 97–110, 2008.

[Boch 09] P. B. Bochev and M. D. Gunzburger. *Least-Squares Finite Element Methods*. Vol. 166 of *Applied Mathematical Sciences*, Springer, New York, 2009.

[Boeh 81] B. Boehm. *Software Engineering Economics*. Prentice-Hall, 1981.

[Bram 93] J. H. Bramble. *Multigrid Methods*. Vol. 294 of *Pitman Research Notes in Mathematics Series*, Longman Scientific & Technical, Harlow, 1993.

[Brau 05] C. Braun, R. Helmig, and S. Manthey. Determination of constitutive relationships for two-phase flow processes in heterogeneous porous media with emphasis on the relative permeability-saturation-relationship. *J. Contam. Hydrol.*, Vol. 76, No. 1-2, pp. 47–85, 2005.

[Brez 05a] F. Brezzi, K. Lipnikov, and M. Shashkov. Convergence of the mimetic finite difference method for diffusion problems on polyhedral meshes. *SIAM J. Numer. Anal.*, Vol. 43, No. 5, pp. 1872–1896, 2005.

[Brez 05b] F. Brezzi, K. Lipnikov, and V. Simoncini. A family of mimetic finite difference methods on polygonal and polyhedral meshes. *Math. Mod. Meth. Appl. S.*, Vol. 15, No. 10, pp. 1533–1551, 2005.

[Brez 91] F. Brezzi and M. Fortin. *Mixed and Hybrid Finite Element Methods*. Vol. 15 of *Springer Series in Computational Mathematics*, Springer-Verlag, New York, 1991.

[Brig 00] W. L. Briggs, V. E. Henson, and S. F. McCormick. *A Multigrid Tutorial*. Society for Industrial and Applied Mathematics (SIAM), Philadelphia, PA, second Ed., 2000.

[Brin 47] H. Brinkman. A calculation of the viscous force exerted by a flowing fluid on a dense swarm of particles. *Appl. Sci. Res. A*, Vol. 1, pp. 27–34, 1947.

[Broo 64] R. Brooks and A. Corey. Hydraulic properties of porous media. *Hydrology Paper*, No. 3, 1964. Civil Engineering Department, Colorado State University, Fort Collins, CO.

[Cai 91] Z. Q. Cai, J. Mandel, and S. F. McCormick. The finite volume element method for diffusion equations on general triangulations. *SIAM J. Numer. Anal.*, Vol. 28, No. 2, pp. 392–402, 1991.

[Cai 97] Z. Cai, J. E. Jones, S. F. McCormick, and T. F. Russell. Control-volume mixed finite element methods. *Computat. Geosci.*, Vol. 1, No. 3-4, pp. 289–315 (1998), 1997.

[Calo 11] V. Calo, Y. Efendiev, and J. Galvis. A note on variational multiscale methods for high-contrast heterogeneous porous media flows with rough source terms. *Adv. Water Resour.*, Vol. 34, No. 9, pp. 1177–1185, 2011.

[Cao 02] H. Cao. *Development of Techniques for General Purpose Simulators*. PhD thesis, Department of Petroleum Engineering, Stanford University, 2002.

[Cao 08] Y. Cao, R. Helmig, and B. Wohlmuth. The influence of the boundary discretization on the multipoint flux approximation *L*-method. In: *Finite Volumes for Complex Applications V*, pp. 257–263, ISTE, London, 2008.

[Cao 09] Y. Cao, R. Helmig, and B. Wohlmuth. Geometrical interpretation of the multipoint flux approximation L-method. *Int. J. Numer. Meth. Fl.*, Vol. 60, No. 11, pp. 1173–1199, 2009.

[Cao 11] Y. Cao, R. Helmig, and B. Wohlmuth. Convergence of the multipoint flux approximation L-method for homogeneous media on uniform grids. *Numer. Meth. Part. D. E.*, Vol. 27, No. 2, pp. 329–350, 2011.

[Carr 04] J. Carrayrou, R. Mose, and P. Behra. Operator-splitting procedures for reactive transport and comparison of mass balance errors. *J. Contam. Hydrol.*, Vol. 68, No. 3-4, pp. 239–268, 2004.

[Cart 10] J. N. Carter, P. J. Ballester, Z. Tavassoli, and P. R. King. Our calibrated model has poor predictive value: An example form the petroleum industry. *Reliab. Eng. Syst. Safe.*, Vol. 91, No. 10–11, pp. 1373–1381, 2010.

[Catt 03] C. Cattani and E. Laserra. Wavelets in the transport theory of heterogeneous reacting solutes. *Int. J. Fluid Mech. Res.*, Vol. 30, No. 2, pp. 147–152, 2003.

[CDas 13] CDash software testing server. 2013. `http://www.cdash.org/`, [Online; accessed 27-February-2013].

[Celi 09] M. A. Celia and J. M. Nordbotten. Practical modeling approaches for geological storage of carbon dioxide. *Ground Water*, Vol. 47, No. 5, pp. 627–638, 2009.

[Chan 06] M. Chandesris and D. Jamet. Boundary conditions at a planar fluid-porous interface for a Poiseuille flow. *Int. J. Heat Mass Tran.*, Vol. 49, pp. 2137–2150, 2006.

[Chan 07] M. Chandesris and D. Jamet. Boundary conditions at a fluid-porous interface: An a priori estimation of the stress jump coefficients. *Int. J. Heat Mass Tran.*, Vol. 50, pp. 3422–3436, 2007.

[Chan 09] M. Chandesris and D. Jamet. Jump conditions and surface-excess quantities at a fluid/porous interface: A multi-scale approach. *Transport Porous Med.*, Vol. 78, pp. 419–438, 2009.

[Chav 76] G. Chavent. *A New Formulation of Diphasic Incompressible Flows in Porous Media*, pp. 258–270. Springer, Berlin, 1976.

[Chav 86] G. Chavent and J. Jaffré. *Mathematical Models and Finite Elements for Reservoir Simulation*. North-Holland, Amsterdam, 1986.

[Chav 91] G. Chavent and J. Roberts. A unified physical presentation of mixed, mixed-hybrid finite elements and standard finite difference approximations for the determination of velocities in waterflow problems. *Adv. Water Resour.*, Vol. 14, No. 6, pp. 329–348, 1991.

[Chen 02] Z. Chen, R. E. Ewing, Q. Jiang, and A. M. Spagnuolo. Degenerate two-phase incompressible flow. V. Characteristic finite element methods. *J. Numer. Math.*, Vol. 10, No. 2, pp. 87–107, 2002.

[Chen 03a] Y. Chen, L. J. Durlofsky, M. Gerritsen, and X. H. Wen. A coupled local-global upscaling approach for simulating flow in highly heterogeneous formations. *Adv. Water Resour.*, Vol. 26, No. 10, pp. 1041–1060, 2003.

[Chen 03b] Z. Chen and T. Y. Hou. A mixed multiscale finite element method for elliptic problems with oscillating coefficients. *Math. Comput.*, Vol. 72, No. 242, pp. 541–576, 2003.

[Chen 06a] Y. Chen and L. J. Durlofsky. Adaptive local-global upscaling for general flow scenarios in heterogeneous formations. *Transport Porous Med.*, Vol. 62, No. 2, pp. 157–185, 2006.

[Chen 06b] Y. Chen and L. J. Durlofsky. Efficient incorporation of global effects in upscaled models of two-phase flow and transport in heterogeneous formations. *Multiscale Model. Sim.*, Vol. 5, No. 2, pp. 445–475, 2006.

[Chen 06c] Z. Chen, G. Huan, and Y. Ma. *Computational Methods for Multiphase Flows in Porous Media*. SIAM, Computational Science & Engineering, 2006.

[Chen 08] Q.-Y. Chen, J. Wan, Y. Yang, and R. T. Mifflin. Enriched multi-point flux approximation for general grids. *J. Comput. Phys.*, Vol. 227, No. 3, pp. 1701–1721, 2008.

[Chen 09] Y. Chen and Y. Li. Local-global two-phase upscaling of flow and transport in heterogeneous formations. *Multiscale Model. Sim.*, Vol. 8, No. 1, pp. 125–153, 2009.

[Chen 13] Y. Chen, Y. Li, and Y. Efendiev. Time-of-flight (TOF)-based two-phase upscaling for subsurface flow and transport. *Adv. Water Resour.*, Vol. 54, pp. 119–132, 2013.

[Chen 96] Z. Chen. Equivalence between and multigrid algorithms for nonconforming and mixed methods for second-order elliptic problems. *East-West J. Numer. Math.*, Vol. 4, No. 1, pp. 1–33, 1996.

[Chen 97] Z. X. Chen and R. E. Ewing. From single-phase to compositional flow: Applicability of mixed finite elements. *Transport Porous Med.*, Vol. 27, No. 2, pp. 225–242, 1997.

[Chou 91] S.-H. Chou and Q. Li. Mixed finite element methods for compressible miscible displacement in porous media. *Math. Comput.*, Vol. 57, No. 196, pp. 507–527, 1991.

[Chri 01] M. A. Christie and M. J. Blunt. Tenth SPE comparative solution project : a comparison of upscaling techniques. *SPE Reserv. Eval. Eng.*, Vol. 4, pp. 308–317, 2001.

[Ciar 02] P. G. Ciarlet. *The Finite Element Method for Elliptic Problems*. Vol. 40 of *Classics in Applied Mathematics*, Society for Industrial and Applied Mathematics (SIAM), Philadelphia, PA, 2002.

[Clas 02] H. Class, R. Helmig, and P.Bastian. Numerical simulation of non-isothermal multiphase multicomponent processes in porous media. 1. An efficient solution technique. *Adv. Water Resour.*, Vol. 25, pp. 533–550, 2002.

[Clas 08] H. Class, R. Helmig, and I. Neuweiler. Sequential coupling of models for contaminant spreading in the vadose zone. *Vadose Zone J.*, Vol. 7, No. 2, pp. 721–731, 2008.

[Clas 09] H. Class, A. Ebigbo, R. Helmig, H. K. Dahle, J. M. Nordbotten, M. A. Celia, P. Audigane, M. Darcis, J. Ennis-King, Y. Fan, B. Flemisch, S. E. Gasda, M. Jin, S. Krug, D. Labregere, A. N. Beni, R. J. Pawar, A. Sbai, S. G. Thomas, L. Trenty, and L. Wei. A benchmark study on problems related to CO_2 storage in geologic formations: Summary and discussion of the results. *Computat. Geosci.*, Vol. 13, No. 4, pp. 409–434, 2009.

[Coat 03a] K. H. Coats. IMPES stability: Selection of stable timesteps. *SPE J.*, Vol. 8, pp. 181–187, 2003.

[Coat 03b] K. H. Coats. IMPES stability: The CFL limit. *SPE J.*, Vol. 8, pp. 291–297, 2003.

[Cock 07] B. Cockburn, J. Gopalakrishnan, and H. Wang. Locally conservative fluxes for the continuous Galerkin method. *SIAM J. Numer. Anal.*, Vol. 45, No. 4, pp. 1742–1776, 2007.

[Cock 89a] B. Cockburn, S. Y. Lin, and C.-W. Shu. TVB Runge-Kutta local projection discontinuous Galerkin finite element method for conservation laws. III. One-dimensional systems. *J. Comput. Phys.*, Vol. 84, No. 1, pp. 90–113, 1989.

[Cock 89b] B. Cockburn and C.-W. Shu. TVB Runge-Kutta local projection discontinuous Galerkin finite element method for conservation laws. II. General framework. *Math. Comput.*, Vol. 52, No. 186, pp. 411–435, 1989.

[Codi 01] R. Codina. A stabilized finite element method for generalized stationary incompressible flows. *Comput. Method. Appl. M.*, Vol. 190, No. 20-21, pp. 2681–2706, 2001.

[Comp 06] Computer Modelling Group. GEM User Guide. 2006.

[Core 94] A. T. Corey. *Mechanics of Immiscible Fluids in Porous Media*. Water Resources Publications, 1994.

[Coud 10] Y. Coudière and G. Manzini. The discrete duality finite volume method for convection-diffusion problems. *SIAM J. Numer. Anal.*, Vol. 47, No. 6, pp. 4163–4192, 2010.

[Dahl 08] H. K. Dahle, G. T. Eigestad, J. M. Nordbotten, and K. Pruess. A model-oriented benchmark problem for CO2 storage. 2008. Princeton-Bergen Series on Carbon Storage, `http://arks.princeton.edu/ark:/88435/dsp01pn89d657g`.

[Dam 00] J. C. van Dam and R. A. Feddes. Numerical simulation of infiltration, evaporation and shallow groundwater levels with the Richards equation. *J. Hydrol.*, Vol. 233, pp. 72–85, 2000.

[DAng 08] C. D'Angelo and A. Quarteroni. On the coupling of 1d and 3d diffusion-reaction equations: application to tissue perfusion problems. *Math. Mod. Meth. Appl. S.*, Vol. 18, No. 8, pp. 1481–1504, 2008.

[Darc 11] M. Darcis, H. Class, B. Flemisch, and R. Helmig. Sequential model coupling for feasibility studies of CO_2 storage in deep saline aquifers. *Oil Gas Sci. Technol.*, Vol. 66, No. 1, pp. 93–103, 2011.

[Darc 12] M. Darcis. *Coupling Models of Different Complexity for the Simulation of CO_2 Storage in Saline Aquifers*. PhD thesis, Department of Hydromechanics and Modeling of Hydrosystems, Universität Stuttgart, 2012.

[Darm 02] N. H. Darman, G. E. Pickup, and K. S. Sorbie. A comparison of two-phase dynamic upscaling methods based on fluid potentials. *Computat. Geosci.*, Vol. 6, No. 1, pp. 5–27, 2002.

[Daws 89] C. N. Dawson, T. F. Russell, and M. F. Wheeler. Some improved error estimates for the modified method of characteristics. *SIAM J. Numer. Anal.*, Vol. 26, No. 6, pp. 1487–1512, 1989.

[Denn 96] J. E. Dennis, Jr. and R. B. Schnabel. *Numerical Methods for Unconstrained Optimization and Nonlinear Equations*. Vol. 16 of *Classics in Applied Mathematics*, Society for Industrial and Applied Mathematics (SIAM), Philadelphia, PA, 1996.

[Dent 11] M. Dentz, T. L. Borgne, A. Englert, and B. Bijeljic. Mixing, spreading, and reactions in heterogeneous media: A brief review. *J. Contam. Hydrol.*, Vol. 120–121, pp. 1–17, 2011.

[Deut 98] Deutsche Forschungsgemeinschaft. *Proposals for Safeguarding Good Scientific Practice*. Wiley-VCH, Weinheim, 1998.

[Diet 05] P. Dietrich, R. Helmig, M. Sauter, H. Hötzl, J. Köngeter, and G. Teutsch, Eds. *Flow and Transport in Fractured Porous Media*. Springer, 2005.

[Disc 02] M. Discacciati, E. Miglio, and Q. A. Mathematical and numerical models for coupling surface and groundwater flows. *Appl. Numer. Math.*, Vol. 43, pp. 57–74, 2002.

[Doga 09] M. O. Dogan, H. Class, and R. Helmig. Different concepts for the coupling of porous-media flow with lower-dimensional pipe flow. *CMES-Comp. Model. Eng.*, Vol. 53, No. 3, pp. 207–234, 2009.

[Doug 83] J. Douglas, Jr., R. E. Ewing, and M. F. Wheeler. A time-discretization procedure for a mixed finite element approximation of miscible displacement in porous media. *RAIRO Anal. Numér.*, Vol. 17, No. 3, pp. 249–265, 1983.

[Doug 99] J. Douglas, Jr., C.-S. Huang, and F. Pereira. The modified method of characteristics with adjusted advection. *Numer. Math.*, Vol. 83, No. 3, pp. 353–369, 1999.

[Dous 06] C. Doussan, A. Pierret, E. Garrigues, and L. Pagès. Water uptake by plant roots: II – modelling of water transfer in the soil root-system with explicit account of flow within the root system – comparison with experiments. *Plant and Soil*, Vol. 283, No. 1–2, pp. 99–117, 2006.

[Dron 10] J. Droniou, R. Eymard, T. Gallouët, and R. Herbin. A unified approach to mimetic finite difference, hybrid finite volume and mixed finite volume methods. *Math. Mod. Meth. Appl. S.*, Vol. 20, No. 2, pp. 265–295, 2010.

[DuMu 13] DuMu^x website. 2013. `http://dumux.org/`, [Online; accessed 27-February-2013].

[DUNE 13] DUNE website. 2013. `http://www.dune-project.org/`, [Online; accessed 27-February-2013].

[Durl 91] L. J. Durlofsky. Numerical calculation of equivalent grid block permeability sensors for heterogeneous porous media. *Water Resour. Res.*, Vol. 27, No. 5, pp. 699–708, 1991.

[Durl 94] L. Durlofsky. Accuracy of mixed and control volume finite element approximations to darcy velocity and related quantities. *Water Resour. Res.*, Vol. 30, No. 4, pp. 965–973, 1994.

[E 03a] W. E, B. Engquist, and Z. Huang. Heterogeneous multiscale method: A general methodology for multiscale modeling . *Phys. Rev.*, Vol. 67, 2003.

[E 03b] W. E and B. Engquist. The heterogeneous multiscale methods. *Commun. Math. Sci.*, Vol. 1, No. 1, pp. 87–132, 2003.

[E 03c] W. E and B. Engquist. Multiscale modeling and computation. *Notices Amer. Math. Soc.*, Vol. 50, No. 9, pp. 1062–1070, 2003.

[E 07] W. E, B. Engquist, X. Li, W. Ren, and E. Vanden-Eijnden. Heterogeneous multiscale methods: a review. *Commun. Comput. Phys.*, Vol. 2, No. 3, pp. 367–450, 2007.

[Edwa 02] M. G. Edwards, R. D. Lazarov, and I. Yotov, Eds. *Locally Conservative Numerical Methods for Flow in Porous Media*. Springer, Dordrecht, 2002. *Computat. Geosci.*, Vol. 6, No. 3-4.

[Edwa 98] M. G. Edwards and C. F. Rogers. Finite volume discretization with imposed flux continuity for the general tensor pressure equation. *Computat. Geosci.*, Vol. 2, No. 4, pp. 259–290, 1998.

[Efen 00] Y. Efendiev, L. J. Durlofsky, and S. H. Lee. Modeling of subgrid effects in coarse-scale simulations of transport in heterogeneous porous media. *Water Resour. Res.*, Vol. 36, No. 8, pp. 2031–2041, 2000.

[Efen 02] Y. Efendiev and L. J. Durlofsky. Numerical modeling of subgrid heterogeneity in two phase flow simulations. *Water Resour. Res.*, Vol. 38, No. 8, pp. 3–1–3–11, 2002.

[Efen 04] Y. Efendiev and L. J. Durlofsky. Accurate subgrid models for two-phase flow in heterogeneous reservoirs. *SPE J.*, Vol. 9, pp. 219–226, 2004.

[Efen 07] Y. Efendiev and T. Hou. Multiscale finite element methods for porous media flows and their applications. *Appl. Numer. Math.*, Vol. 57, No. 5-7, pp. 577–596, 2007.

[Eich 05] H. Eichel, R. Helmig, I. Neuweiler, and O. A. Cirpka. Upscaling of two-phase flow processes in porous media. In: D. B. Das and S. M. Hassanizadeh, Eds., *Upscaling Multiphase Flow in Porous Media*, pp. 237–257, Springer, 2005.

[Eige 05] G. T. Eigestad and R. A. Klausen. On the convergence of the multi-point flux approximation O-method: numerical experiments for discontinuous permeability. *Numer. Meth. Part. D. E.*, Vol. 21, No. 6, pp. 1079–1098, 2005.

[Eige 09] G. T. Eigestad, H. K. Dahle, B. Hellevang, W. T. Johansen, F. Riis, and E. Øian. Geological modeling and simulation of CO2 injection in the Johansen formation. *Computat. Geosci.*, Vol. 13, No. 4, pp. 435–450, 2009.

[Elen 12] M. T. Elenius, J. M. Nordbotten, and H. Kalisch. Effects of a capillary transition zone on the stability of a diffusive boundary layer. *IMA J. Appl. Math.*, Vol. 77, No. 6, pp. 771–787, 2012.

[Enwo 10] M. E. Enwongulu. *The CIPR CO_2 Benchmark Study.* Master's thesis, Heriot-Watt University, 2010.

[Epsh 09] Y. Epshteyn and B. Rivière. Analysis of *hp* discontinuous Galerkin methods for incompressible two-phase flow. *J. Comput. Appl. Math.*, Vol. 225, No. 2, pp. 487–509, 2009.

[Erbe 12] K. Erbertseder, J. Reichold, R. Helmig, P. Jenny, and B. Flemisch. A coupled discrete/continuum model for describing cancer therapeutic transport in the lung. *PLoS ONE*, Vol. 7, No. 3, e31966, 2012.

[Ewin 84] R. E. Ewing, T. F. Russell, and M. F. Wheeler. Convergence analysis of an approximation of miscible displacement in porous media by mixed finite elements and a modified method of characteristics. *Comput. Method. Appl. M.*, Vol. 47, No. 1-2, pp. 73–92, 1984.

[Ewin 94] R. E. Ewing and H. Wang. Eulerian-Lagrangian localized adjoint methods for variable-coefficient advective-diffusive-reactive equations in groundwater contaminant transport. In: *Advances in optimization and numerical analysis (Oaxaca, 1992)*, pp. 185–205, Kluwer Acad. Publ., Dordrecht, 1994.

[Ewin 96] R. E. Ewing and H. Wang. An optimal-order estimate for Eulerian-Lagrangian localized adjoint methods for variable-coefficient advection-reaction problems. *SIAM J. Numer. Anal.*, Vol. 33, No. 1, pp. 318–348, 1996.

[Eyma 00] R. Eymard, T. Gallouët, and R. Herbin. Finite volume methods. In: *Handbook of Numerical Analysis, Vol. VII*, pp. 713–1020, North-Holland, Amsterdam, 2000.

[Eyma 07] R. Eymard, T. Gallouët, and R. Herbin. A new finite volume scheme for anisotropic diffusion problems on general grids: convergence analysis. *C. R. Math. Acad. Sci. Paris*, Vol. 344, No. 6, pp. 403–406, 2007.

[Eyma 10] R. Eymard, T. Gallouët, and R. Herbin. Discretization of heterogeneous and anisotropic diffusion problems on general nonconforming meshes SUSHI: a scheme using stabilization and hybrid interfaces. *IMA J. Numer. Anal.*, Vol. 30, No. 4, pp. 1009–1043, 2010.

[Eyma 11] R. Eymard, G. Henry, R. Herbin, F. Hubert, R. Klöfkorn, and G. Manzini. 3D benchmark on discretization schemes for anisotropic diffusion problems on general grids. In: *Finite Volumes for Complex Applications VI*, pp. 895–930, Springer, Berlin Heidelberg, 2011.

[Eyma 12] R. Eymard, C. Guichard, R. Herbin, and R. Masson. Vertex-centred discretization of multiphase compositional Darcy flows on general meshes. *Computat. Geosci.*, Vol. 16, No. 4, pp. 987–1005, 2012.

[Faig 13] B. Faigle, R. Helmig, I. Aavatsmark, and B. Flemisch. Efficient multi-physics modelling with adaptive grid-refinement using a MPFA method. *Computat. Geosci.*, 2013. Submitted.

[Favo 81] A. Favorskii, A. Samarskii, M. J. Shashkov, and V. Tishkin. Operational finite-difference schemes. *Differential Equations*, Vol. 17, pp. 854–862, 1981.

[Fjae 08] E. Fjaer, R. Holt, P. Horsrud, A. Raaen, and R. Risnes. *Petroleum Related Rock Mechanics. Developments in Petroleum Science*, Elsevier, second Ed., 2008.

[Flec 10] J. H. Fleckenstein, S. Krause, D. M. Hannah, and F. Boano. Groundwater-surface water interactions: New methods and models to improve understanding of processes and dynamics. *Adv. Water Resour.*, Vol. 33, No. 11, pp. 1291–1295, 2010.

[Flem 07] B. Flemisch, J. Fritz, R. Helmig, J. Niessner, and B. Wohlmuth. DUMUX: a multi-scale multi-physics toolbox for flow and transport processes in porous media. In: A. Ibrahimbegovic and F. Dias, Eds., *ECCOMAS Thematic Conference on Multi-scale Computational Methods for Solids and Fluids*, pp. 82–87, Cachan, France, November 28-30, 2007.

[Flem 08] B. Flemisch and R. Helmig. Numerical investigation of a mimetic finite difference method. In: R. Eymard and J. Hérard, Eds., *Finite Volumes for Complex Applications V – Problems and Perspectives*, pp. 815–824, Wiley - VCH, 2008.

[Flem 11] B. Flemisch, M. Darcis, K. Erbertseder, B. Faigle, A. Lauser, K. Mosthaf, S. Müthing, P. Nuske, A. Tatomir, M. Wolff, and R. Helmig. DUMUX: DUNE for Multi-{Phase, Component, Scale, Physics,...} Flow and Transport in Porous Media. *Adv. Water Resour.*, Vol. 34, No. 9, pp. 1102–1112, 2011.

[Frit 12] J. Fritz, B. Flemisch, and R. Helmig. Decoupled and multiphysics models for non-isothermal compositional two-phase flow in Porous Media. *Int. J. Numer. Anal. Mod.*, Vol. 9, No. 1, pp. 17–28, 2012.

[Fugg 03] A. Fuggetta. Open source software – an evaluation. *J. Syst. Software*, Vol. 66, pp. 77–90, 2003.

[Galv 10] J. Galvis and Y. Efendiev. Domain decomposition preconditioners for multiscale flows in high contrast media. *Multiscale Model. Sim.*, Vol. 8, No. 4, pp. 1461–1483, 2010.

[Gasd 09] S. Gasda, J. M. Nordbotten, and M. Celia. Vertical Equilibrium with Sub-scale Analytical Methods for Geological CO2 Sequestration. *Computat. Geosci.*, Vol. 13, No. 4, pp. 469–481, 2009.

[Gasd 11a] S. Gasda, J. M. Nordbotten, and M. Celia. Vertically-averaged approaches to CO2 injection with solubility trapping. *Water Resour. Res.*, Vol. 47, W05528, 2011.

[Gasd 11b] S. Gasda, M. Farthing, C. Kees, and C. Miller. Adaptive split-operator methods for modeling transport phenomena in porous medium systems. *Adv. Water Resour.*, Vol. 34, pp. 1268–1282, 2011.

[Gaus 08] I. Gaus, P. Audigane, L. André, J. Lions, N. Jacquemet, P. Durst, I. Czernichowski-Lauriol, and M. Azaroual. Geochemical and solute transport modelling for CO2 storage, what to expect from it? *Int. J. Greenh. Gas Con.*, Vol. 2, pp. 605–625, 2008.

[Geba 02] S. Gebauer, L. Neunhäuserer, R. Kornhuber, S. Ochs, R. Hinkelmann, and R. Helmig. Equidimensional modelling of flow and transport processes in fractured porous systems I. *Dev. Water Sci.*, Vol. 47, pp. 335–342, 2002.

[Gerr 05] M. Gerritsen and L. Durlofsky. Modeling fluid flow in oil reservoirs. *Annu. Rev. Fluid Mech.*, Vol. 37, pp. 211–238, 2005.

[Ghos 09] R. Ghostine, G. Kesserwani, R. Mosé, J. Vazquez, and A. Ghenaim. An improvement of classical slope limiters for high-order discontinuous Galerkin method. *Int. J. Numer. Meth. Fl.*, Vol. 59, No. 4, pp. 423–442, 2009.

[Gira 06] L. Giraud, J. Langou, and G. Sylvand. On the parallel solution of large industrial wave propagation problems. *J. Comput. Acoust.*, Vol. 14, No. 1, pp. 83–111, 2006.

[Gira 09] V. Girault and B. Rivière. DG approximation of coupled Navier-Stokes and Darcy equations by Beaver-Joseph-Saffman interface condition. *SIAM J. Numer. Anal.*, Vol. 47, pp. 2052–2089, 2009.

[GNU 91] GNU General Public License version 2. 1991. `http://www.gnu.org/licenses/old-licenses/gpl-2.0.html`, [Online; accessed 27-February-2013].

[Gong 09] B. Gong, M. Karimi-Fard, and L. J. Durlofsky. Upscaling discrete fracture characterizations to dual-porosity, dual-permeability models for efficient simulation of flow with strong gravitational effects. *SPE J.*, Vol. 13, No. 1, pp. 58–67, 2009.

[Gonz 13] J. M. González-Barahona, J. S. Pascual, and G. Robles. *Introduction to Free Software*. Free Technology Academy, 2013.

[Goye 03] B. Goyeau, D. Lhuillier, D. Gobin, and M. Velarde. Momentum transport at a fluid-porous interface. *Int. J. Heat Mass Tran.*, Vol. 46, pp. 4071–4081, 2003.

[Gray 93] W. Gray, A. Leijnse, L. Randall, and C. Blain. *Mathematical tools for changing spatial scales in the analysis of physical systems*. CRC Press, 1993.

[Hack 89] W. Hackbusch. On first and second order box schemes. *Computing*, Vol. 41, No. 4, pp. 277–296, 1989.

[Haeg 07] H. Hægland, H. Dahle, G. Eigestad, K.-A. Lie, and I. Aavatsmark. Improved streamlines and time-of-flight for streamline simulation on irregular grids. *Adv. Water Resour.*, Vol. 30, No. 4, pp. 1027–1045, 2007.

[Haeg 09] H. Hægland, A. Assteerawatt, H. K. Dahle, G. T. Eigestad, and R. Helmig. Comparison of cell-and vertex-centered discretization methods for flow in a two-dimensional discrete-fracture-matrix system. *Adv. Water Resour.*, Vol. 32, No. 12, pp. 1740–1755, 2009.

[Haji 08] H. Hajibeygi, G. Bonfigli, M. A. Hesse, and P. Jenny. Iterative multiscale finite-volume method. *J. Comput. Phys.*, Vol. 227, No. 19, pp. 8604–8621, 2008.

[Hame 99] K. Hameyer, J. Driesen, H. De Gersem, and R. Belmans. The classification of coupled field problems. *IEEE T. Magn.*, Vol. 35, No. 3, pp. 1618–1621, 1999.

[Hass 89] S. M. Hassanizadeh and W. G. Gray. Derivation of conditions describing transport across zones of reduced dynamics within multiphase systems. *Water Resour. Res.*, Vol. 25, pp. 529–539, 1989.

[Hauk 01] G. Hauke and A. García-Olivares. Variational subgrid scale formulations for the advection-diffusion-reaction equation. *Comput. Method. Appl. M.*, Vol. 190, No. 51-52, pp. 6847–6865, 2001.

[He 08] Y. He and B. Han. A wavelet finite-difference method for numerical simulation of wave propagation in fluid-saturated porous media. *Appl. Math. Mech. (English Ed.)*, Vol. 29, No. 11, pp. 1495–1504, 2008.

[Hell 60] G. Hellwig. *Partielle Differentialgleichungen*. Teubner, Stuttgart, 1960.

[Helm 10] R. Helmig, J. Niessner, B. Flemisch, M. Wolff, and J. Fritz. Efficient modelling of flow and transport in porous media using multi-physics and multi-scale approaches. In: W. Freeden, Z. Nashed, and T. Sonar, Eds., *Handbook of Geomathematics*, Chap. 37, pp. 417–458, Springer, 2010.

[Helm 13] R. Helmig, B. Flemisch, M. Wolff, A. Ebigbo, and H. Class. Model coupling for multiphase flow in porous media. *Adv. Water Resour.*, Vol. 51, pp. 52–66, 2013.

[Helm 97] R. Helmig. *Multiphase Flow and Transport Processes in the Subsurface: A Contribution to the Modeling of Hydrosystems*. Springer, Berlin, 1997.

[Herb 08] R. Herbin and F. Hubert. Benchmark on discretization schemes for anisotropic diffusion problems on general grids. In: R. Eymard and J. Hérard, Eds., *Finite Volumes for Complex Applications V*, pp. 659–692, ISTE, London, 2008.

[Herm 03] F. Hermeline. Approximation of diffusion operators with discontinuous tensor coefficients on distorted meshes. *Comput. Method. Appl. M.*, Vol. 192, No. 16-18, pp. 1939–1959, 2003.

[Herr 93] I. Herrera, R. E. Ewing, M. A. Celia, and T. F. Russell. Eulerian-Lagrangian localized adjoint method: the theoretical framework. *Numer. Meth. Part. D. E.*, Vol. 9, No. 4, pp. 431–457, 1993.

[Hess 08] M. A. Hesse, F. M. Orr, and H. A. Tchelepi. Gravity currents with residual trapping. *J. Fluid Mech.*, Vol. 611, pp. 35–60, 2008.

[Hest 08] J. S. Hesthaven and T. Warburton. *Nodal Discontinuous Galerkin Methods*. Vol. 54 of *Texts in Applied Mathematics*, Springer, New York, 2008.

[Heyw 96] J. G. Heywood, R. Rannacher, and S. Turek. Artificial boundaries and flux and pressure conditions for the incompressible Navier-Stokes equations. *Int. J. Numer. Meth. Fl.*, Vol. 22, No. 5, pp. 325–352, 1996.

[Holm 10] R. Holm, M. van Dijke, and S. Geiger. Three-phase flow modelling using pore-scale capillary pressure and relative permeabilities for mixed-wet media at the continuum scale. *Transport Porous Med.*, Vol. 81, No. 3, pp. 423–442, 2010.

[Hote 04] H. Hoteit, P. Ackerer, R. Mosé, J. Erhel, and B. Philippe. New two-dimensional slope limiters for discontinuous Galerkin methods on arbitrary meshes. *Int. J. Numer. Meth. Eng.*, Vol. 61, No. 14, pp. 2566–2593, 2004.

[Hote 08] H. Hoteit and A. Firoozabadi. Numerical modeling of two-phase flow in heterogeneous permeable media with different capillarity pressures. *Adv. Water Resour.*, Vol. 31, No. 1, pp. 56–73, 2008.

[Hou 97] T. Y. Hou and X.-H. Wu. A multiscale finite element method for elliptic problems in composite materials and porous media. *J. Comput. Phys.*, Vol. 134, No. 1, pp. 169–189, 1997.

[Hris 97] D. Hristopulos and G.Christakos. An analysis of hydraulic conductivity upscaling. *Nonlinear Analysis*, Vol. 30, No. 8, pp. 4979–4984, 1997.

[Huan 00] C.-S. Huang. Convergence analysis of a mass-conserving approximation of immiscible displacement in porous media by mixed finite elements and a modified method of characteristics with adjusted advection. *Computat. Geosci.*, Vol. 4, No. 2, pp. 165–184, 2000.

[Hube 00] R. Huber and R. Helmig. Node-centered finite volume discretizations for the numerical simulation of multiphase flow in heterogeneous porous media. *Computat. Geosci.*, Vol. 4, No. 2, pp. 141–164, 2000.

[Hube 99] R. Huber and R. Helmig. Multiphase flow in heterogeneous porous media: a classical finite element method versus an implicit pressure–explicit saturation-based mixed finite element–finite volume approach. *Int. J. Numer. Meth. Fl.*, Vol. 29, No. 8, pp. 899–920, 1999.

[Hugh 00] T. J. R. Hughes, G. Engel, L. Mazzei, and M. G. Larson. The continuous Galerkin method is locally conservative. *J. Comput. Phys.*, Vol. 163, No. 2, pp. 467–488, 2000.

[Hugh 87] T. J. R. Hughes. *The Finite Element Method*. Prentice Hall Inc., Englewood Cliffs, NJ, 1987.

[Hugh 95] T. J. R. Hughes. Multiscale phenomena: Green's functions, the Dirichlet-to-Neumann formulation, subgrid scale models, bubbles and the origins of stabilized methods. *Comput. Method. Appl. M.*, Vol. 127, No. 1-4, pp. 387–401, 1995.

[Hugh 98] T. J. R. Hughes, G. R. Feijóo, L. Mazzei, and J.-B. Quincy. The variational multiscale method—a paradigm for computational mechanics. *Comput. Method. Appl. M.*, Vol. 166, No. 1-2, pp. 3–24, 1998.

[Hyma 02] J. Hyman, J. Morel, M. Shashkov, and S. Steinberg. Mimetic finite difference methods for diffusion equations. *Computat. Geosci.*, Vol. 6, No. 3-4, pp. 333–352, 2002.

[IAPW 09] IAPWS. Revised release on the IAPWS formulation 1995 for the thermodynamic properties of ordinary water substance for general and scientific use. 2009. `http://www.iapws.org`.

[Ince 10] D. Ince. If you're going to do good science, release the computer code too. *The Guardian*, 2010. `http://www.guardian.co.uk/technology/2010/feb/05/science-climate-emails-code-release`.

[Inge 10] S. E. Ingebritsen, S. Geiger, S. Hurwitz, and T. Driesner. Numerical simulation of magmatic hydrothermal systems. *Rev. Geophys.*, Vol. 48, RG1002, 2010.

[Ingh 98] D. B. Ingham and I. I. Pop. *Transport Phenomena in Porous Media*. Elsevier Science, 1998.

[IPCC 05] IPCC. *Carbon Dioxide Capture and Storage. Special Report of the Intergovernmental Panel on Climate Change*. Cambridge University Press, 2005.

[Jack 09] A. S. Jackson, C. T. Miller, and W. G. Gray. Thermodynamically constrained averaging theory approach for modeling flow and transport phenomena in porous medium systems: 6. Two-fluid-phase flow. *Adv. Water Resour.*, Vol. 32, pp. 779–795, 2009.

[Jaeg 07] J. Jaeger, N. Cook, and R. Zimmerman. *Fundamentals of Rock Mechanics*. Blackwell Publishing, fourth Ed., 2007.

[Jage 00] W. Jäger and A. Mikelic. On the interface boundary condition of Beavers, Joseph and Saffman. *SIAM J. Appl. Math.*, Vol. 60, pp. 1111–1127, 2000.

[Jage 09] W. Jäger and A. Mikelić. Modeling effective interface laws for transport phenomena between an unconfined fluid and a porous medium using homogenization. *Transport Porous Med.*, Vol. 78, pp. 489–508, 2009.

[Jame 09] D. Jamet, M. Chandesris, and B. Goyeau. On the equivalence of the discontinuous one- and two-domain approaches for the modeling of transport phenomena at a fluid/porous interface. *Transport Porous Med.*, Vol. 78, pp. 403–418, 2009.

[Jang 04] G.-W. Jang, J. E. Kim, and Y. Y. Kim. Multiscale Galerkin method using interpolation wavelets for two-dimensional elliptic problems in general domains. *Int. J. Numer. Meth. Eng.*, Vol. 59, No. 2, pp. 225–253, 2004.

[Jenn 03] P. Jenny, S. H. Lee, and H. Tchelepi. Multi-scale finite-volume method for elliptic problems in subsurface flow simulations. *J. Comput. Phys.*, Vol. 187, pp. 47–67, 2003.

[Jenn 06] P. Jenny, S. H. Lee, and H. A. Tchelepi. Adaptive fully implicit multi-scale finite-volume method for multi-phase flow and transport in heterogeneous porous media. *J. Comput. Phys.*, Vol. 217, No. 2, pp. 627–641, 2006.

[Jian 07] Y. Jiang. *Techniques for Modeling Complex Reservoirs and Advanced Wells.* PhD thesis, Department of Petroleum Engineering, Stanford University, 2007.

[Jian 98] B.-N. Jiang. *The Least-Squares Finite Element Method. Scientific Computation*, Springer-Verlag, Berlin, 1998.

[Juan 05] R. Juanes. A variational multiscale finite element method for multiphase flow in porous media. *Finite Elem. Anal. Des.*, Vol. 41, No. 7-8, pp. 763–777, 2005.

[Juan 08a] R. Juanes and F.-X. Dub. A locally conservative variational multiscale method for the simulation of porous media flow with multiscale source terms. *Computat. Geosci.*, Vol. 12, pp. 273–295, 2008.

[Juan 08b] R. Juanes and K.-A. Lie. Numerical modeling of multiphase first-contact miscible flows. II. Front-tracking/streamline simulation. *Transport Porous Med.*, Vol. 72, No. 1, pp. 97–120, 2008.

[Kann 03] J. Kanney, C. Miller, and C. Kelley. Convergence of iterative split-operator approaches for approximating nonlinear reactive transport problems. *Adv. Water Resour.*, Vol. 26, No. 3, pp. 247–261, 2003.

[Kavi 95] M. Kaviany. *Principles of Heat Transfer in Porous Media.* Springer, 1995.

[Kees 08] C. E. Kees, M. Farthing, and C. N. Dawson. Locally conservative, stabilized finite element methods for variably saturated flow. *Comput. Method. Appl. M.*, Vol. 197, No. 51-52, pp. 4610–4625, 2008.

[Keil 12] E. Keilegavlen, J. M. Nordbotten, and A. Stephansen. Tensor relative permeabilities: Origins, modeling and numerical discretization. *Int. J. Numer. Anal. Mod.*, Vol. 9, No. 3, pp. 701–724, 2012.

[Kim 07] M.-Y. Kim, E.-J. Park, S. G. Thomas, and M. F. Wheeler. A multiscale mortar mixed finite element method for slightly compressible flows in porous media. *J. Korean Math. Soc.*, Vol. 44, No. 5, pp. 1103–1119, 2007.

[Kim 11a] J. Kim, H. A. Tchelepi, and R. Juanes. Stability and convergence of sequential methods for coupled flow and geomechanics: Drained and undrained splits. *Comput. Method. Appl. M.*, Vol. 200, pp. 2094–2116, 2011.

[Kim 11b] J. Kim, H. A. Tchelepi, and R. Juanes. Stability and convergence of sequential methods for coupled flow and geomechanics: Fixed-stress and fixed-strain splits. *Comput. Method. Appl. M.*, Vol. 200, pp. 1591–1606, 2011.

[Kipp 08] V. Kippe, J. E. Aarnes, and K.-A. Lie. A comparison of multiscale methods for elliptic problems in porous media flow. *Computat. Geosci.*, Vol. 12, No. 3, pp. 377–398, 2008.

[Klau 04] R. A. Klausen and T. F. Russell. Relationships among some locally conservative discretization methods which handle discontinuous coefficients. *Computat. Geosci.*, Vol. 8, No. 4, pp. 341–377, 2004.

[Klau 06a] R. A. Klausen and R. Winther. Convergence of multipoint flux approximations on quadrilateral grids. *Numer. Meth. Part. D. E.*, Vol. 22, No. 6, pp. 1438–1454, 2006.

[Klau 06b] R. A. Klausen and R. Winther. Robust convergence of multi point flux approximation on rough grids. *Numer. Math.*, Vol. 104, No. 3, pp. 317–337, 2006.

[Klau 08] R. A. Klausen and A. F. Stephansen. Mimetic MPFA. In: *11th European Conference on the Mathematics of Oil Recovery*, EAGE, Bergen, Norway, 2008.

[Kold 12] O. Kolditz, U.-J. Görke, H. Shao, and W. Wang. *Thermo-Hydro-Mechanical-Chemical Processes in Porous Media: Benchmarks and Examples*. Springer, 2012.

[Koll 10] S. Kollet, R. Maxwell, C. Woodward, S. Smith, J. Vanderborght, H. Vereecken, and C. Simmer. Proof-of-concept of regional scale hydrologic simulations at hydrologic resolution utilizing massively parallel computer resources. *Water Resour. Res.*, Vol. 46, W04201, 2010.

[Kyte 75] J. R. Kyte and D. W. Berry. New pseudo functions to control numerical dispersion. *SPE J.*, Vol. 15, No. 4, pp. 269–276, 1975.

[Laus 11] A. Lauser, C. Hager, R. Helmig, and B. Wohlmuth. A new approach for phase transitions in miscible multi-phase flow in porous media. *Adv. Water Resour.*, Vol. 34, No. 8, pp. 957–966, 2011.

[Layt 03] W. J. Layton, F. Schieweck, and I. Yotov. Coupling fluid flow with porous media flow. *SIAM J. Numer. Anal.*, Vol. 40, pp. 2195–2218, 2003.

[Lee 01] J. van der Lee and L. De Windt. Present state and future directions of modeling of geochemistry in hydrogeological systems. *J. Contam. Hydrol.*, Vol. 47, No. 2–4, pp. 265–282, 2001.

[Lee 08] S. H. Lee, C. Wolfsteiner, and H. A. Tchelepi. Multiscale finite-volume formulation of multiphase flow in porous media: black oil formulation of compressible, three-phase flow with gravity. *Computat. Geosci.*, Vol. 12, No. 3, pp. 351–366, 2008.

[Lee 09] S. H. Lee, H. Zhou, and H. A. Tchelepi. Adaptive multiscale nite-volume method for nonlinear multiphase transport in heterogeneous formations. *J. Comput. Phys.*, Vol. 228, pp. 9036–9058, 2009.

[Lehm 08] P. Lehmann, S. Assouline, and D. Or. Characteristic lengths affecting evaporative drying of porous media. *Phys. Rev. E*, Vol. 77, pp. 1–16, 2008.

[Lerd 05] T. Lerdahl, A. Rustad, T. Theting, J. Stensen, P. Oren, S. Bakke, T. Boassen, and B. Palatnik. Pore- to field-scale multi-phase upscaling for IOR. *Proc. SPE Europec / EAGE Annual Conference, Madrid, Spain*, SPE94191, 2005.

[LeVe 02] R. J. LeVeque. *Finite Volume Methods for Hyperbolic Problems. Cambridge Texts in Applied Mathematics*, Cambridge University Press, Cambridge, 2002.

[Leve 41] M. Leverett. Flow of Oil-Water Mixtures through Unconsolidated Sands. *Petroleum Trans. AIME*, Vol. 142, pp. 152–169, 1941.

[Levy 75] T. Levy and E. Sanchez-Palencia. On boundary conditions for fluid flow in porous media. *Int. J. Eng. Sci.*, Vol. 13, pp. 923–940, 1975.

[Lewi 91] R. Lewis, B. Schrefler, and L. Simoni. Coupling versus uncoupling in soil consolidation. *Int. J. Numer. Anal. Met.*, Vol. 15, pp. 533–548, 1991.

[Lich 96] P. C. Lichtner. Continuum formulation of multicomponent-multiphase reactive transport. *Rev. Mineral. Geochem.*, Vol. 34, No. 1, pp. 1–81, 1996.

[Lie 10] K.-A. Lie, S. Krogstad, I. S. Ligaarden, J. R. Natvig, H. M. Nilsen, and B. Skaflestad. Discretisation on complex grids – Open source MATLAB implementation. In: *Proceedings of ECMOR XII, Oxford, UK*, 2010.

[Lie 12] K.-A. Lie, S. Krogstad, I. S. Ligaarden, J. R. Natvig, H. M. Nilsen, and B. Skaflestad. Open source MATLAB implementation of consistent discretisations on complex grids. *Computat. Geosci.*, Vol. 16, No. 2, pp. 297–322, 2012.

[Lipn 09a] K. Lipnikov, D. Svyatskiy, and Y. Vassilevski. Interpolation-free monotone finite volume method for diffusion equations on polygonal meshes. *J. Comput. Phys.*, Vol. 228, No. 3, pp. 703–716, 2009.

[Lipn 09b] K. Lipnikov, M. Shashkov, and I. Yotov. Local flux mimetic finite difference methods. *Numer. Math.*, Vol. 112, No. 1, pp. 115–152, 2009.

[Lipn 11] K. Lipnikov, J. D. Moulton, and D. Svyatskiy. Adaptive strategies in the multilevel multiscale mimetic (M^3) method for two-phase flows in porous media. *Multiscale Model. Sim.*, Vol. 9, No. 3, pp. 991–1016, 2011.

[Long 02] P. Longuemare, M. Mainguy, P. Lemonnier, A. Onaisi, C. Gerard, and N. Koutsabeloulis. Geomechanics in reservoir simulation: overview of coupling methods and field case study. *Oil Gas Sci. Technol.*, Vol. 57, No. 5, pp. 471–483, 2002.

[Lude 00] C. Lüdecke and D. Lüdecke. *Thermodynamik*. Springer, Berlin, 2000.

[Luna 06] I. Lunati and P. Jenny. Multiscale finite-volume method for compressible multiphase flow in porous media. *J. Comput. Phys.*, Vol. 216, No. 2, pp. 616–636, 2006.

[Luna 07] I. Lunati and P. Jenny. Treating highly anisotropic subsurface flow with the multiscale finite-volume method. *Multiscale Model. Sim.*, Vol. 6, No. 1, pp. 308–318, 2007.

[Luna 08] I. Lunati and P. Jenny. Multiscale finite-volume method for density-driven flow in porous media. *Computat. Geosci.*, Vol. 12, No. 3, pp. 337–350, 2008.

[Mart 05] V. Martin, J. Jaffré, and J. E. Roberts. Modeling fractures and barriers as interfaces for flow in porous media. *SIAM J. Sci. Comput.*, Vol. 26, No. 5, pp. 1667–1691, 2005.

[Matr 06] S. F. Matringe, R. Juanes, and H. A. Tchelepi. Robust streamline tracing for the simulation of porous media flow on general triangular and quadrilateral grids. *J. Comput. Phys.*, Vol. 219, No. 2, pp. 992–1012, 2006.

[Maxw 10] R. Maxwell, S. Kollet, S. Smith, C. Woodward, R. Falgout, I. Ferguson, C. Baldwin, W. Bosl, R. Hornung, and S. Ashby. ParFlow Users Manual. Tech. Rep., 2010. International Ground Water Modeling Center Report GWMI 2010-01.

[Mazz 06] A. Mazzia and M. Putti. Three-dimensional mixed finite element-finite volume approach for the solution of density-dependent flow in porous media. *J. Comput. Appl. Math.*, Vol. 185, No. 2, pp. 347–359, 2006.

[McDo 03] M. McDonald and A. Harbaugh. The history of MODFLOW. *Ground Water*, Vol. 41, No. 2, pp. 280–283, 2003.

[Mich 07] M. Michelsen and J. Mollerup. *Thermodynamic Models: Fundamentals & Computational Aspects*. Tie-Line Publications, Denmark, 2007.

[Mill 60] R. Millington and J. Quirk. Permeability of porous solids. *Trans. Faraday Soc.*, Vol. 57, pp. 1200–1207, 1960.

[Mill 93] C. Miller and A. Rabideau. Development of split-operator, PetrovGalerkin methods to simulate transport and diffusion problems. *Water Resour. Res.*, Vol. 29, No. 7, pp. 2227–2240, 1993.

[Mill 98] C. Miller, G. Christakos, P. Imhoff, J. McBride, J. Pedit, and J. Trangenstein. Multiphase flow and transport modeling in heterogeneous porous media: challenges and approaches. *Adv. Water Resour.*, Vol. 21, No. 2, pp. 77–120, 1998.

[Mori 12] A. Morin, J. Urban, and P. Sliz. A quick guide to software licensing for the scientist-programmer. *PLoS Comput. Biol.*, Vol. 8, No. 7, e1002598, 2012.

[Most 11] K. Mosthaf, K. Baber, B. Flemisch, R. Helmig, T. Leijnse, I. Rybak, and B. Wohlmuth. A coupling concept for two-phase compositional porous-medium and single-phase compositional free flow. *Water Resour. Res.*, Vol. 47, W10522, 2011.

[Mull 03] S. Müller. *Adaptive Multiscale Schemes for Conservation Laws*. Vol. 27 of *Lecture Notes in Computational Science and Engineering*, Springer-Verlag, Berlin, 2003.

[Muth 12] S. Müthing and P. Bastian. DUNE-Multidomaingrid: A metagrid approach to subdomain modelling. In: A. Dedner, B. Flemisch, and R. Klöfkorn, Eds., *Advances in DUNE: Proceedings of the DUNE User Meeting 2010, Stuttgart*, pp. 59–76, Springer, 2012.

[Neun 03] L. Neunhäuserer. *Diskretisierungsansätze zur Modellierung von Strömungs- und Transportprozessen in geklüfteten-porösen Medien*. PhD thesis, Universität Stuttgart, 2003.

[Nghi 84] L. Nghiem and Y.-K. Li. Computation of multiphase equilibrium phenomena with an equation of state. *Fluid Phase Equilibr.*, Vol. 17, No. 1, pp. 77–95, 1984.

[Niel 06] D. A. Nield and A. Bejan. *Convection in Porous Media*. Springer, 2006.

[Nies 07] J. Niessner and R. Helmig. Multi-Scale Modeling of Three-Phase–Three-Component Processes in Heterogeneous Porous Media. *Adv. Water Resour.*, Vol. 30, No. 11, pp. 2309–2325, 2007.

[Nies 09] J. Niessner and S. M. Hassanizadeh. Modeling kinetic interphase mass transfer for two-phase flow in porous media including fluid-fluid interfacial area. *Transport Porous Med.*, Vol. 80, pp. 329–344, 2009.

[Nils 10a] H. M. Nilsen and J. R. Natvig. Improved gravity splitting for streamline and reordering methods. In: *Proceedings of ECMOR XII, Oxford, UK*, 2010.

[Nils 10b] H. M. Nilsen, K. Lie, and J. R. Natvig. Accurate modelling of faults by multipoint, mimetic, and mixed methods. *SPE J.*, Vol. 149690, 2010.

[Nord 05a] J. M. Nordbotten and I. Aavatsmark. Monotonicity conditions for control volume methods on uniform parallelogram grids in homogeneous media. *Computat. Geosci.*, Vol. 9, No. 1, pp. 61–72, 2005.

[Nord 05b] J. M. Nordbotten and G. T. Eigestad. Discretization on quadrilateral grids with improved monotonicity properties. *J. Comput. Phys.*, Vol. 203, No. 2, pp. 744–760, 2005.

[Nord 07] J. M. Nordbotten, I. Aavatsmark, and G. T. Eigestad. Monotonicity of control volume methods. *Numer. Math.*, Vol. 106, No. 2, pp. 255–288, 2007.

[Nord 08] J. M. Nordbotten and P. E. Bjørstad. On the relationship between the multiscale finite-volume method and domain decomposition preconditioners. *Computat. Geosci.*, Vol. 12, No. 3, pp. 367–376, 2008.

[Nord 09a] J. M. Nordbotten. Adaptive variational multiscale methods for multiphase flow in porous media. *Multiscale Model. Sim.*, Vol. 7, No. 3, 1455, 2009.

[Nord 09b] J. M. Nordbotten, D. Kavetski, M. A. Celia, and S. Bachu. A semi-analytical model estimating leakage associated with CO_2 storage in large-scale multi-layered geological systems with multiple leaky wells. *Environ. Sci. Technol.*, Vol. 43, No. 3, pp. 743–749, 2009.

[Nord 12] J. M. Nordbotten, B. Flemisch, S. E. Gasda, H. M. Nilsen, Y. Fan, G. E. Pickup, B. Wiese, M. A. Celia, H. K. Dahle, G. T. Eigestad, and K. Pruess. Uncertainties in practical simulation of CO2 storage. *Int. J. Greenh. Gas Con.*, Vol. 9, pp. 234–242, 2012.

[Ocho 95] J. A. Ochoa-Tapia and S. Whitaker. Momentum transfer at the boundary between a porous medium and a homogeneous fluid – I. Theoretical development. *Int. J. Heat Mass Tran.*, Vol. 38, No. 14, pp. 2635–2646, 1995.

[Oden 98] J. T. Oden, I. Babuska, and C. E. Baumann. A discontinuous *hp* finite element method for diffusion problems. *J. Comput. Phys.*, Vol. 146, No. 2, pp. 491–519, 1998.

[Odyc 08] D. E. A. van Odyck, J. B. Bell, F. Monmont, and N. Nikiforakis. The mathematical structure of multiphase thermal models of flow in porous media. In: *Proceedings of the Royal Society A: Mathematical, Physical and Engineering Sciences*, pp. 523–549, 2008.

[Of 07] G. Of. Fast multipole methods and applications. In: *Boundary element analysis*, pp. 135–160, Springer, Berlin, 2007.

[Olad 08] S. Oladyshkin, J.-J. Royer, and M. Panfilov. Effective solution through the streamline technique and HT-splitting for the 3D dynamic analysis of the compositional flows in oil reservoirs. *Transport Porous Med.*, Vol. 74, No. 3, pp. 311–329, 2008.

[Open 13a] Open Porous Media Initiative. 2013. `http://www.opm-project.org`, [Online; accessed 27-February-2013].

[Open 13b] OpenGeoSys project. 2013. `http://www.opengeosys.org`, [Online; accessed 27-February-2013].

[Pal 06] M. Pal, M. G. Edwards, and A. R. Lamb. Convergence study of a family of flux-continuous, finite-volume schemes for the general tensor pressure equation. *Int. J. Numer. Meth. Fl.*, Vol. 51, No. 9-10, pp. 1177–1203, 2006.

[Pal 11] M. Pal and M. G. Edwards. Non-linear flux-splitting schemes with imposed discrete maximum principle for elliptic equations with highly anisotropic coefficients. *Int. J. Numer. Meth. Fl.*, Vol. 66, No. 3, pp. 299–323, 2011.

[Panf 00] M. Panfilov. *Macroscale models of flow through highly heterogeneous porous media*. Kluwer Academic Publishers, 2000.

[Pau 12] G. S. H. Pau, J. B. Bell, A. S. Almgren, K. M. Fagnan, and M. J. Lijewski. An adaptive mesh refinement algorithm for compressible two-phase flow in porous media. *Computat. Geosci.*, Vol. 16, No. 3, pp. 577–592, 2012.

[Pebe 98] J. E. Pebesma and C. G. Wesseling. Gstat: a program for geostatistical modelling, prediction and simulation. *Computers & Geosciences*, Vol. 24, pp. 17–31, 1998.

[Pers 08] M. Person, A. Banerjee, J. Rupp, P. Lichtner, R. Pawar, and M. A. Celia. Basin-scale Impacts of CO_2 Sequestration within the Mt. Simon Formation, Illinois Basin: Scaling Calculations using Sharp-Interface Theory. In: *American Geophysical Union, Fall Meeting*, 2008. Abstract H12C-01.

[Pesz 00] M. Peszynska, Q. Lu, and M. Wheeler. Multiphysics coupling of codes. In: *Computational Methods in Water Resources*, pp. 175–182, A. A. Balkema, 2000.

[Pesz 02] M. Peszynska, M. F. Wheeler, and I. Yotov. Mortar upscaling for multiphase flow in porous media. *Computat. Geosci.*, Vol. 6, pp. 73–100, 2002.

[Pick 10] G. E. Pickup, M. Kiatskulphan, and J. Mills. Analysis of grid resolution for simulations of CO_2 storage in deep saline aquifers. In: *Proceedings of ECMOR XII, Oxford, UK*, 2010.

[Pick 96] G. E. Pickup and K. Sorbie. The scaleup of two-phase flow in porous media using phase permeability tensors. *SPE J.*, Vol. 1, No. 4, pp. 369–381, 1996.

[Prat 90] M. Prat. Modelling of heat transfer by conduction in a transition region between a porous medium and an external fluid. *Transport Porous Med.*, Vol. 5, pp. 71–95, 1990.

[Prau 67] J. M. Prausnitz, R. N. Lichtenthaler, and E. G. Azevedo. *Molecular Thermodynamics of Fluid-Phase Equilibria*. Prentice-Hall, 1967.

[Prei 11] M. Preisig and J. Prevost. Coupled multi-phase thermo-poromechanical effects. Case study: CO_2 injection at In Salah, Algeria. *Int. J. Greenh. Gas Con.*, Vol. 5, pp. 1055–1064, 2011.

[Prue 04] K. Pruess. The TOUGH codes – a family of simulation tools for multiphase flow and transport processes in permeable media. *Vadose Zone J.*, Vol. 3, pp. 738–746, 2004.

[Prue 85] K. Pruess and T. N. Narasimhan. A practical method for modeling fluid and heat flow in fractured porous media. *SPE J.*, Vol. 25, No. 1, pp. 14–26, 1985.

[Prue 92] K. Pruess. Brief guide to the MINC-method for modeling flow and transport in fractured media. Tech. Rep., Lawrence Berkeley Lab., CA (United States), 1992.

[Pude 00] A. Puder. Ubiquitous Computing Environments through Open Systems. In: D. Patel, I. Choudhury, S. Patel, and S. de Cesare, Eds., *OOIS'2000, 6th International Conference on Object Oriented Information Systems, London, UK*, pp. 200–210, Springer, 2000.

[Quin 88] M. Quintard and S. Whitaker. Two-phase flow in heterogeneous porous media: The method of large-scale averaging. *Transport Porous Med.*, Vol. 3, No. 4, pp. 357–413, 1988.

[Rami 09] B. Ramirez, H. Kazemi, M. Al-Kobaisi, E. Ozkan, and S. Atan. A critical review for proper use of water/oil/gas transfer functions in dual-porosity naturally fractured reservoirs: Part I and II. *SPE Reserv. Eval. Eng.*, Vol. 12, No. 2, pp. 200–217, 2009.

[Reic 06] V. Reichenberger, H. Jakobs, P. Bastian, and R. Helmig. A mixed-dimensional finite volume method for two-phase flow in fractured porous media. *Adv. Water Resour.*, Vol. 29, No. 7, pp. 1020–1036, 2006.

[Reid 87] R. C. Reid, J. M. Prausnitz, and B. E. Poling. *The Properities of Gases & Liquids.* McGraw-Hill, 1987.

[Rena 97] P. Renard and G. de Marsily. Calculating effective permeability: a review. *Adv. Water Resour.*, Vol. 20, pp. 253–278, 1997.

[Rhod 09] M. Rhodes, B. Bijeljic, and M. Blunt. A rigorous pore-to-field-scale simulation method for single-phase flow based on continuous time random walks. *SPE J.*, Vol. 14, pp. 88–94, 2009.

[Riaz 06] A. Riaz, M. Hesse, H. A. Tchelepi, and F. M. Orr. Onset of convection in a gravitationally unstable diffusive boundary layer in porous media. *J. Fluid Mech.*, Vol. 548, pp. 87–111, 2006.

[Rivi 00] B. Rivière, M. F. Wheeler, and V. Girault. Part II. Discontinuous Galerkin method applied to a single phase flow in porous media. *Computat. Geosci.*, Vol. 4, No. 4, pp. 337–349, 2000.

[Rivi 08] B. Rivière. *Discontinuous Galerkin methods for solving elliptic and parabolic equations.* Vol. 35 of *Frontiers in Applied Mathematics*, Society for Industrial and Applied Mathematics (SIAM), Philadelphia, PA, 2008. Theory and implementation.

[Robi 00] B. Robinson, H. Viswanathan, and A. Valocchi. Efficient numerical techniques for modeling multi-component groundwater transport based upon simultaneous solution of strongly coupled subsets of chemical components. *Adv. Water Resour.*, Vol. 23, pp. 307–324, 2000.

[Robi 03] N. Robidoux. Mimetic discretizations bibliography homepage. 2003. `http://www.cs.laurentian.ca/robidoux/mimetic/mimetic2.pdf`.

[Rohm 10] J. Rohmer and D. M. Seyedi. Coupled large scale hydromechanical modelling for caprock failure risk assessment of CO_2 storage in deep saline aquifers. *Oil Gas Sci. Technol.*, Vol. 65, No. 3, pp. 503 – 517, 2010.

[Rose 07] R. Rosenzweig and U. Shavit. The laminar flow field at the interface of a Sierpinski carpet configuration. *Water Resour. Res.*, Vol. 43, W10402, 2007.

[Russ 89] T. F. Russell. Stability Analysis and Switching Criteria for Adaptive Implicit Methods Based on the CFL Condition. In: *Proceedings of SPE Symposium on Reservoir Simulation*, pp. 97–107, Society of Petroleum Engineers, 1989.

[Russ 90] T. F. Russell. Eulerian-Lagrangian localized adjoint methods for advection-dominated problems. In: *Numerical analysis 1989 (Dundee, 1989)*, pp. 206–228, Longman Sci. Tech., Harlow, 1990.

[Rutq 03] J. Rutqvist and C.-F. Tsang. TOUGH-FLAC: A numerical simulator for analysis of coupled thermal-hydrologic-mechanical processes in fractured and porous geological media under multi-phase flow conditions. In: *TOUGH Symposium*, Lawrence Berkeley National Laboratory, Earth Sciences Division, Berkeley, CA 945 30, USA, 2003.

[Ryzh 07] V. Ryzhik. Spreading of a NAPL lens in a double-porosity medium. *Computat. Geosci.*, Vol. 11, No. 1, pp. 1–8, 2007.

[Saad 95] N. Saad, A. S. Cullick, M. M. Honarpour, and M. E. T. Center. Effective relative permeability in scale-up and simulation. *SPE J.*, 29592, 1995.

[Saez 89] A. E. Sáez, C. J. Otero, and I. Rusinek. The effective homogeneous behavior of heterogeneous porous media. *Transport Porous Med.*, Vol. 4, No. 3, pp. 213–238, 1989.

[Saff 71] R. Saffman. On the boundary condition at the surface of a porous medium. *Stud. Appl. Math.*, Vol. 50, pp. 93–101, 1971.

[Sand 11] A. Sandvin, J. M. Nordbotten, and I. Aavatsmark. Multiscale mass conservative domain decomposition preconditioners for elliptic problems on irregular grids. *Computat. Geosci.*, Vol. 15, No. 3, pp. 587–602, 2011.

[Sand 12] T. H. Sandve and J. M. Nordbotten. An efficient multi-point flux approximation based approach for discrete fracture matrix simulations. *J. Comput. Phys.*, Vol. 231, No. 9, pp. 3784–3800, 2012.

[Sche 04] O. Schenk and K. Gärtner. Solving unsymmetric sparse systems of linear equations with PARDISO. *Journal of Future Generation Computer Systems*, Vol. 20, No. 3, pp. 475–487, 2004.

[Sche 74] A. Scheidegger. *The Physics of Flow Through Porous Media*. University of Toronto Press, Third Ed., 1974.

[Schl 09] Schlumberger. *ECLIPSE technical description*. 2009.

[Schm 93] T. Schmidt. Box schemes on quadrilateral meshes. *Computing*, Vol. 51, No. 3-4, pp. 271–292, 1993.

[Schn 10] K. Schneider-Zapp, O. Ippisch, and K. Roth. Numerical study of the evaporation process and parameter estimation analysis of an evaporation experiment. *Hydrol. Earth Syst. Sc.*, Vol. 14, pp. 765–781, 2010.

[Seri 91] V. B. Serikov. Porous phase model of the lung interstitial fluid motion. *Microvasc. Res.*, Vol. 42, No. 1, pp. 1–16, 1991.

[Sett 01] A. Settari and D. A. Walters. Advances in coupled geomechanical and reservoir modeling with application to reservoir compaction. *SPE J.*, Vol. 6, No. 3, pp. 334–342, 2001.

[Shas 96] M. Shashkov. *Conservative Finite-Difference Methods on General Grids*. CRC Press, Boca Raton, FL, 1996.

[Shav 09] U. Shavit. Special Issue: Transport phenomena at the interface between fluid and porous domains. *Transport Porous Med.*, Vol. 78, No. 3, pp. 327–540, 2009.

[Shel 59] J. W. Sheldon and W. T. Cardwell. One-dimensional, incompressible, noncapillary, two-phase fluid in a porous medium. *Petroleum Trans. AIME*, Vol. 216, pp. 290–296, 1959.

[Shen 10] C. Shen and M. S. Phanikumar. A process-based, distributed hydrologic model based on a large-scale method for surfacesubsurface coupling. *Adv. Water Resour.*, Vol. 33, No. 12, pp. 1524–1541, 2010.

[Slee 93] B. E. Sleep and J. F. Sykes. Compositional simulation of groundwater contamination by organic-compounds. 1. Model developement and verification. *Water Resour. Res.*, Vol. 29, No. 6, pp. 1697–1708, 1993.

[Smit 07] J. Smith and A. Humphrey. Interstitial transport and transvascular fluid exchange during infusion into brain and tumor tissue. *Microvasc. Res.*, Vol. 73, No. 1, pp. 58–73, 2007.

[Smit 99] E. H. Smith and M. S. Seth. Efficient solution for matrix-fracture flow with multiple interacting continua. *Int. J. Numer. Anal. Met.*, Vol. 23, No. 5, pp. 427–438, 1999.

[Some 74] W. Somerton, A. El-Shaarani, and S. Mobarak. High temperature behavior of rocks associated with geothermal type reservoirs. *SPE J.*, 4897, 1974.

[Span 09] K. Spanoudaki, A. I. Stamou, and A. Nanou-Giannarou. Development and verification of a 3-D integrated surface watergroundwater model. *J. Hydrol.*, Vol. 375, pp. 410–427, 2009.

[Spol 00] J. Spolsky. The Joel Test: 12 Steps to Better Code. 2000. `http://www.joelonsoftware.com/articles/fog0000000043.html`, [Online; accessed 27-February-2013].

[Spyc 05] N. Spycher and K. Pruess. CO_2-H_2O mixtures in the geological sequestration of CO_2. II. Partitioning in chloride brines at 12–100°C and up to 600 bar. *Geochim. Cosmochim. Ac.*, Vol. 69, No. 13, pp. 3309–3320, 2005.

[Srin 92] C. Srinivas, B. Ramaswamy, and M. F. Wheeler. Mixed finite element methods for flow through unsaturated porous media. In: *Computational Methods in Water Resources, IX, Vol. 1 (Denver, CO)*, pp. 239–246, Comput. Mech., 1992.

[Stal 13] R. Stallman. Why open source misses the point of free software. 2013. `http://www.gnu.org/philosophy/open-source-misses-the-point.html`.

[Stau 85] D. Stauffer. *Introduction to Percolation Theory.* Taylor & Francis, London, 1985.

[Sten 93] E. H. Stenby and P. Wang. Noniterative phase equilibrium calculation in compositional reservoir simulation. *SPE J.*, 26641, 1993.

[Ston 61] H. L. Stone and A. O. Garder Jr. Analysis of gas-cap or dissolved-gas reservoirs. *Petroleum Trans. AIME*, Vol. 222, pp. 92–104, 1961.

[Ston 91] H. L. Stone. Rigorous black oil pseudo functions. In: *SPE Symposium on reservoir simulation, Anaheim, California*, 1991.

[Stov 12] K. H. Støverud, M. Darcis, R. Helmig, and S. M. Hassanizadeh. Modeling concentration distribution and deformation during convection-enhanced drug delivery into brain tissue. *Transport Porous Med.*, Vol. 92, No. 1, pp. 119–143, 2012.

[Stub 01] K. Stüben. A review of algebraic multigrid. *J. Comput. Appl. Math.*, Vol. 128, No. 1-2, pp. 281–309, 2001.

[Suk 08] H. Suk and G.-T. Yeh. Multiphase flow modeling with general boundary conditions and automatic phase-configuration changes using a fractional-flow approach. *Computat. Geosci.*, Vol. 12, No. 4, pp. 541–571, 2008.

[Suli 10] M. Sulis, S. B. Meyerhoff, C. Paniconi, R. M. Maxwell, M. Putti, and S. J. Kollet. A comparison of two physics-based numerical models for simulating surface water-groundwater interactions. *Adv. Water Resour.*, Vol. 33, No. 4, pp. 456–467, 2010.

[Thom 11] S. G. Thomas and M. F. Wheeler. Enhanced velocity mixed finite element methods for modeling coupled flow and transport on non-matching multiblock grids. Analysis and applications to transport of reactive species in multiphase flow through porous media. *Computat. Geosci.*, Vol. 15, No. 4, pp. 605–625, 2011.

[Torn 08] A.-K. Tornberg and L. Greengard. A fast multipole method for the three-dimensional Stokes equations. *J. Comput. Phys.*, Vol. 227, No. 3, pp. 1613–1619, 2008.

[Tran 89] J. Trangenstein and J. Bell. Mathematical structure of compositional reservoir simulation. *SIAM J. Sci. Stat. Comput.*, Vol. 10, No. 5, pp. 817–845, 1989.

[Tref 07] M. Trefry and C. Muffels. FEFLOW: a finite-element ground water flow and transport modeling tool. *Ground Water*, Vol. 45, No. 5, pp. 525–528, 2007.

[Trot 01] U. Trottenberg, C. W. Oosterlee, and A. Schüller. *Multigrid*. Academic Press Inc., San Diego, CA, 2001.

[Truc 96] E. Truckenbrodt. *Fluidmechanik*. Springer, 1996.

[Urba 09] K. Urban. *Wavelet Methods for Elliptic Partial Differential Equations*. Oxford University Press, Oxford, 2009.

[US D 02] U.S. Department of Energy. Final Environmental Impact Statement for a Geologic Repository for the Disposal of Spent Nuclear Fuel and High-Level Radioactive Waste at Yucca Mountain, Nye County, Nevada. 2002.

[Vafa 00] K. Vafai, Ed. *Handbook of Porous Media*. Marcel Dekker, New York, 2000.

[Vald 06] F. J. Valdés-Parada, B. Goyeau, and J. A. Ochoa-Tapia. Diffusive mass transfer between a microporous medium and an homogeneous fluid: Jump boundary condition. *Chem. Eng. Sci.*, Vol. 61, pp. 1692–1740, 2006.

[Vald 07] F. J. Valdés-Parada, J. A. Ochoa-Tapia, and J. A. Alvarez-Ramirez. Diffusive mass transport in the fluid-porous medium inter-region: Closure problem solution for the one-domain approach. *Chem. Eng. Sci.*, Vol. 62, pp. 6054–6068, 2007.

[Vald 09a] F. J. Valdés-Parada, J. A. Alvarez-Ramirez, B. Goyeau, and J. A. Ochoa-Tapia. Computation of jump coefficient for momentum transfer between a porous medium and a fluid using a closed generalized transfer equation. *Transport Porous Med.*, Vol. 78, pp. 439–457, 2009.

[Vald 09b] F. J. Valdés-Parada, J. A. Alvarez-Ramirez, B. Goyeau, and J. A. Ochoa-Tapia. Jump condition for diffusive and convective mass transfer between a porous medium and a fluid involving adsorption and chemical reaction. *Transport Porous Med.*, Vol. 78, pp. 459–476, 2009.

[Vida 09] S. Vidal-Gilbert, J. F. Nauroy, and E. Brosse. 3D geomechanical modelling for CO_2 geologic storage in the dogger carbonates of the Paris basin. *Int. J. Greenh. Gas Con.*, Vol. 3, No. 3, pp. 288–299, 2009.

[Vohr 06] M. Vohralík. Equivalence between lowest-order mixed finite element and multi-point finite volume methods on simplicial meshes. *M2AN Math. Model. Numer. Anal.*, Vol. 40, No. 2, pp. 367–391, 2006.

[Wall 02a] T. C. Wallstrom, M. A. Christie, L. J. Durlofsky, and D. H. Sharp. Effective flux boundary conditions for upscaling porous media equations. *Transport Porous Med.*, Vol. 46, No. 2, pp. 139–153, 2002.

[Wall 02b] T. C. Wallstrom, S. Hou, M. A. Christie, L. J. Durlofsky, D. H. Sharp, and Q. Zou. Application of effective flux boundary conditions to two-phase upscaling in porous media. *Transport Porous Med.*, Vol. 46, No. 2, pp. 155–178, 2002.

[Wang 02] H. Wang, D. Liang, R. E. Ewing, S. L. Lyons, and G. Qin. An ELLAM approximation for highly compressible multicomponent flows in porous media. *Computat. Geosci.*, Vol. 6, No. 3-4, pp. 227–251, 2002.

[Wang 95] P. Wang and J. W. Barker. Comparison of flash calculations in compositional reservoir simulation. *SPE J.*, 30787, 1995.

[Weat 08] D. Weatherill, T. Graf, C. T. Simmons, P. G. Cook, R. Therrien, and D. A. Reynolds. Discretizing the fracture-matrix interface to simulate solute transport. *Ground Water*, Vol. 46, No. 4, pp. 606–615, 2008.

[Weil 11] S. Weill, A. Mazzia, M. Putti, and C. Paniconi. Coupling water flow and solute transport into a physically-based surfacesubsurface hydrological model. *Adv. Water Resour.*, Vol. 34, No. 1, pp. 128–136, 2011.

[Wen 03] X. H. Wen, L. J. Durlofsky, and M. G. Edwards. Use of border regions for improved permeability upscaling. *Math. Geol.*, Vol. 35, No. 5, pp. 521–547, 2003.

[Whee 01] J. Wheeler and M. F. Wheeler. Integrated parallel and accurate reservoir simulator. Tech. Rep., 2001. TICAM01-25, CSM, University of Texas at Austin.

[Whee 02] M. F. Wheeler and M. Peszynska. Computational engineering and science methodologies for modeling and simulation of subsurface applications. *Adv. Water Resour.*, Vol. 25, No. 8-12, pp. 1147–1173, 2002.

[Whee 99] M. F. Wheeler, T. Arbogast, S. Bryant, J. Eaton, Q. Lu, M. Peszynska, and I. Yotov. A parallel multiblock/multidomain approach to reservoir simulation. In: *Fifteenth SPE Symposium on Reservoir Simulation, Houston, Texas*, SPE51884, Society of Petroleum Engineers, 1999.

[Whit 00] M. White and M. Oostrom. STOMP Subsurface Transport Over Multiple Phases: Theory Guide. Tech. Rep. PNNL-12030 (UC-2010), Pacific Northwest National Laboratory, Richland, Washington, 2000.

[Whit 03] F. White. *Fluid Mechanics.* McGraw-Hill, 2003.

[Whit 98] S. Whitaker. *The Method of Volume Averaging*. Kluwer Academic Publishers, 1998.

[Wiki 13a] Wikipedia. Comparison of issue-tracking systems — Wikipedia, The Free Encyclopedia. 2013. `en.wikipedia.org`, [Online; accessed 27-February-2013].

[Wiki 13b] Wikipedia. Copyleft — Wikipedia, The Free Encyclopedia. 2013. `en.wikipedia.org`, [Online; accessed 21-April-2013].

[Wiki 13c] Wikipedia. MODFLOW — Wikipedia, The Free Encyclopedia. 2013. `en.wikipedia.org`, [Online; accessed 1-March-2013].

[Wiki 13d] Wikipedia. Regression testing — Wikipedia, The Free Encyclopedia. 2013. `en.wikipedia.org`, [Online; accessed 27-February-2013].

[Wiki 13e] Wikipedia. Test automation — Wikipedia, The Free Encyclopedia. 2013. `en.wikipedia.org`, [Online; accessed 27-February-2013].

[Will 11] J. I. Williams and R. Maxwell. Propagating subsurface uncertainty to the atmosphere using fully-coupled, stochastic simulations. *J. Hydrometeorol.*, Vol. 12, pp. 690–701, 2011.

[Wolf 12] M. Wolff, B. Flemisch, R. Helmig, and I. Aavatsmark. Treatment of tensorial relative permeabilities with multipoint flux approximation. *Int. J. Numer. Anal. Mod.*, Vol. 9, No. 3, pp. 725–744, 2012.

[Wolf 13a] M. Wolff, Y. Cao, B. Flemisch, R. Helmig, and B. Wohlmuth. Multi-point flux approximation L-method in 3D: Numerical convergence and application to two-phase flow through porous media. In: P. Bastian, J. Kraus, R. Scheichl, and M. Wheeler, Eds., *Simulation of Flow in Porous Media - Applications in Energy and Environment*, De Gruyter, 2013.

[Wolf 13b] M. Wolff, B. Flemisch, and R. Helmig. An adaptive multi-scale approach for modeling two-phase flow in porous media including capillary pressure. *Water Resour. Res.*, 2013. Submitted.

[Xu 01] T. Xu and K. Pruess. Modeling multiphase non-isothermal fluid flow and reactive geochemical transport in variably saturated fractured rocks: 1. Methodology. *Am. J. Sci.*, Vol. 301, No. 1, pp. 16–33, 2001.

[Yao 08] Z.-H. Yao, H.-T. Wang, P.-B. Wang, and T. Lei. Investigations on fast multipole BEM in solid mechanics. *J. Univ. Sci. Technol. China*, Vol. 38, No. 1, pp. 1–17, 2008.

[Yoto 02] I. Yotov. Advanced techniques and algorithms for reservoir simulation IV. Multiblock solvers and preconditioners. In: J. Chadam, A. Cunningham, R. E. Ewing, and M. F. Ortoleva, P. Wheeler, Eds., *IMA Volumes in Mathematics and its Applications, Volume 131: Resource Recovery, Confinement, and Remediation of Environmental Hazards*, Springer, 2002.

[Yu 10] C. Yu and C. Zheng. HYDRUS: software for flow and transport modeling in variably saturated media. *Ground Water*, Vol. 48, No. 6, pp. 787–791, 2010.

[Zoba 07] M. Zoback. *Reservoir Geomechanics*. Cambridge University Press, 2007.

[Zyvo 07] G. A. Zyvoloski. FEHM: A control volume finite element code for simulating subsurface multi-phase multi-fluid heat and mass transfer. Tech. Rep., 2007. LA-UR-3359, Los Alamos National Laboratory.